UNIVERSITY OF LEEDS

Solid State Growth of Piezoelectric Single Crystals

Danielle Charlotte Woodruff

Submitted in accordance with the requirements for the degree of

Doctor of Philosophy

The University of Leeds

School of Chemical and Process Engineering

Faculty of Engineering

January 2022

The candidate confirms that the work submitted is her own and that appropriate credit has been given where reference has been made to the work of others.

Acknowledgments

I would firstly like to thank my Supervisor Professor Andrew Bell for this opportunity and for all his invaluable help and guidance over the course of this work.

I would like to acknowledge Thales and the EPSRC who provided funding for this work. Special thanks go to my industrial supervisor Dr Laura Stoica for all the help and guidance as well as proof reading and providing feedback.

I would like to thank Rob Simpson for his help with optical microscopy as well as his general technical support. Greatly appreciated are Stuart Micklethwaite and John Harrington for their help with scanning electron microscopy and Chloe Fisher for her help with X-ray diffraction.

I would also like to thank everyone in the Electroceramics group at the University of Leeds: Chloe, Ashleigh, Stephen, Sam, Tom, Yang, Richard and Anton.

Finally, thanks to all my family and friends especially my dad and Mike for all your support over the years.

Abstract

Solid state single crystal growth (SSCG) is a promising alternative to melt growth methods for obtaining single crystals. SSCG has many benefits including cost effectiveness, producing crystals with no composition gradient and allowing the growth of crystals that are difficult to obtain due to incongruent melting points. This method is based on the abnormal grain growth that occurs naturally when only a small amount of liquid phase is introduced upon sintering. Therefore, as the material does not have to be completely in liquid form the temperature required is reduced. Abnormal grain growth allows a few large grains to grow at a much higher rate, scavenging the matrix grains. This accelerated growth is only stopped when the large grains impinge upon one another. Crystal seeds may be used in the place of abnormal grains and if abnormal grain growth in the matrix is prevented the crystal may grow without impingement for the time allowed.

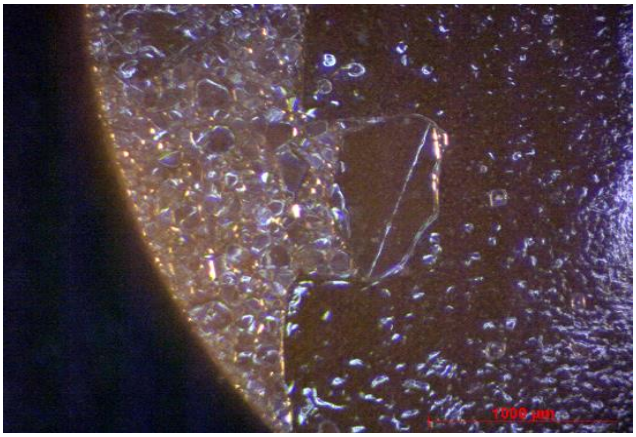

An optical micrograph taken at 1.5 x magnification showing a large twinned grain impinging upon a single crystal grown via the solid state method.

Here, the results of both grain growth and crystal growth experiments using $BaTiO_3$, $(Ba_x,Ca_{x-1})(Ti_y,Zr_{y-1})O_3$ and $Ba(Ti_x,Zr_{x-1})O_3$ are presented. BaTiO3 single crystals have been successfully grown and crystal growth has been observed in $(Ba_x,Ca_{x-1})(Ti_y,Zr_{y-1})O_3$, $Ba(Ti_x,Zr_{x-1})O_3$ and in preliminary experiments using $Pb(Ti_x,Zr_{x-1})O_3$.

Contents

List of Figures

List of Tables

List of Abbreviations

PZT - ($PbZr_{1-x}\ Ti_xO_3$)

SSCG – Solid State Crystal growth

AGG – Abnormal grain growth

PT - $PbTiO_3$

MPB - Morphotropic phase boundary

PMN - $Pb(Mg_{1/3}Nb_{2/3})O_3$

PMN-PT - $Pb(Mg_{1/3}Nb_{2/3})O_3$-$PbTiO_3$

PZN-PT - $Pb(Zn_{1/3}Nb_{2/3})O_3$-$PbTiO_3$

PMN-PZT - $Pb(Mg_{1/3}Nb_{2/3})O_3$ - $PbZr_{1-x}\ Ti_xO_3$

PIN-PMN-PT - $Pb(In_{0.5}Nb_{0.5})$-$Pb(Mg_{1/3}Nb_{2/3})O_3$-$PbTiO_3$

BCTZ – $(Ba_x,Ca_{1-x})(Ti_y,Zr_{1-y})O_3$

BZT - $Ba(Zr_x,Ti_{1-x})O_3$

TPRE - Twin plane re-entrant edge mechanism

IPA - Isopropyl alcohol

XRD - X-ray diffraction

ICDD - The International centre for diffraction data

SEM - Scanning electron microscopy

EDX - Energy dispersive X-ray spectroscopy

SE(U) - Upper secondary electron detector

SE(L) - Lower secondary electron detector

PDBSE - Plate detector for back scattered electron

Chapter 1 Introduction

1.1 Background and Motivation

Relaxor based piezoelectric single crystals are gaining popularity in a range of applications and have already replaced PZT ($PbZr_{1-x}Ti_xO_3$) in medical imaging. This increase in popularity is due to their exceptionally high piezoelectric coefficient, which is up to five times larger than that of PZT, as well as their very high coupling coefficient [1]. These materials also display a broader bandwidth and resolution leading to higher sensitivity. Their properties mean a smaller size of material is needed and power consumption is reduced [2].

These materials do however have their drawbacks these include costly growth methods, such methods still result in a composition gradient throughout the crystal. Such growth methods involve freezing a crystal from the melt which involves very high temperatures, a long period of time in order to produce one crystal and expensive platinum crucibles. Platinum crucibles often cannot be reused as they must be cut open to free the crystal. Titanium concentration is also an issue as its segregation coefficient is low, leading to a concentration gradient and varying piezoelectric properties throughout the crystal. Efforts have been made to improve uniformity such as continuous top feeding, however this still only results in two thirds of a grown crystal having uniform properties [2].

There is however an alternative method of crystal growth that is much cheaper, avoids compositional gradients throughout crystals grown, enables the growth of crystals that are difficult to grow from the melt due to incongruent melting and allows the growth of net-shaped crystals using preformed ceramics. This promising alternative to melt growth techniques is known as solid state crystal growth or SSCG. SSCG is based on the abnormal grain growth (AGG) that occurs naturally upon sintering. Therefore, as the material does not have to be completely in liquid form the temperature required is reduced to typical ceramic sintering temperatures. AGG allows a few large grains to grow at a much higher rate, scavenging the matrix grains. This accelerated growth is only stopped when the large grains impinge upon one another. Crystal seeds may be used in the place of abnormal grains and if AGG in the matrix is prevented the crystal may grow without impingement for the time allowed [2]. Previous research of this method has been undertaken in South Korea leading to the development of Ceracomp [3], a company that produces single crystals via this

method. However, not enough information has been published in order to replicate the process and there is no generally accepted method.

1.2 Aims and Objectives

A reproducible method for obtaining single crystals via the solid state would be invaluable, therefore this work will initially focus on understanding grain growth and solid state crystal growth in barium titanate $BaTiO_3$. $BaTiO_3$ has been chosen as grain growth and microstructural characteristics in this material are well documented, there are no volatile components such as PbO, and the $BaO\text{-}TiO_2$ eutectic at 1320^oC can be used to introduce varying amounts of liquid phase by differing concentration of TiO_2. Various parameters will be investigated including differing sintering temperatures, sintering times and compositional differences including dopants. Scanning electron microscopy, optical microscopy and electron back scatter diffraction will be used to test and observe the aforementioned parameters.

When a method for SSCG in $BaTiO_3$ has been developed, the viability of the solid state crystal growth method will be tested using $(Ba,Ca)(Ti,Zr)O_3$ and $Ba(Ti,Zr)O_3$. Experiments using these materials began with grain growth studies. Again, various parameters were investigated including varying TiO_2 concentration, the addition of sintering aids and varying sintering temperature. After which various crystal growth experiments were performed to determine the optimum conditions for solid state crystal growth.

Chapter 2 – Introduction to Piezoelectricity

The piezoelectric effect was first discovered in 1880 by J Curie and P Curie. They found that when certain materials were placed under a mechanical stress, they developed an electric charge. Soon after it was discovered that the reverse is true, and these materials respond to an applied voltage with a mechanical strain. These two effects are now known as the direct piezoelectric affect and the inverse piezoelectric effect respectively. This effect was firstly described in some limited materials such as Rochelle salts and Quartz. Since then many piezoelectric materials have been discovered for a variety of applications, some of which will be discussed later in this chapter [4].

2.1 History and Applications

The Curie brothers first discovered the direct piezoelectric effect in 1880, the following year the indirect effect was predicted by Lippman and verified by the Curie brothers. However, it wasn't until World War I that piezoelectric materials were put to use. During the war there became a need to detect German U boats, therefore Langevin had the idea to use quartz plates as underwater transducers. Later quartz was replaced by Rochelle salt for underwater applications, which was used until the discovery of $BaTiO_3$ and PZT. Quartz found a new role as a piezoelectric resonator and is still used in clocks today.

In the 1940's during the second world war $BaTiO_3$ was discovered independently by the US, Russia and Japan. $BaTiO_3$ was discovered for use in capacitors and is still used today in multilayer capacitors. In 1947 it was discovered that $BaTiO_3$ had piezoelectric properties. Research into transducer applications began as $BaTiO_3$ ceramics were easy to produce and had a larger electromechanical coupling coefficient than any previously discovered materials except for Rochelle salt, it is also more stable than Rochelle salt and is not water soluble. However, $BaTiO_3$ has a low Curie temperature so in order to rectify this researchers at the time began studying different ion replacements including Ca and Pb. This led to the discovery of PZT and its superior piezoelectric properties in the 1950's. From here many other applications of piezoelectric materials have become apparent. Today piezoelectric materials are still used as underwater transducers, in medical imaging, as sensors, in inkjet printing, autofocusing cameras and much more some examples can be seen in Table 2.1. The development of further materials and the ability to adjust properties by making

compositional changes means that materials can be tailor made for individual applications. More recently the improved properties of relaxor-PT, such as $Pb(Mg_{1/3}Nb_{2/3})O_3$ - $PbTiO_3$ single crystals has lead to the replacement of PZT in applications such as medical imaging [5][6].

Table 2. 1 Table showing some of the applications of piezoelectric materials *[7]*.

Piezoelectric effect used	Applications

Direct piezoelectric effect	**Gas igniter**
	
	Sensors
	
	• ***Pressure sensor***
	  ▪ ***Blood pressure monitor***
	• ***Sound sensor***
	  ▪ ***Hydrophone***
	  ▪ ***Piezoelectric microphone***
	• ***Tactile sensor***
	  ▪ ***Scalpel and grasper for keyhole surgery***
	• ***Vibration sensor***
	  ▪ ***Accelerometer***
	  ▪ ***Pacemaker control***

Converse piezoelectric effect	**Actuators**
	
	• ***Piezoelectric pump***
	  ▪ ***Insulin pump***
	  ▪ ***Fuel injection systems***
	  ▪ ***Inkjet printer***
	• ***Ultrasonic drill***
	• ***Ultrasonic cleaner***
	• ***Ultrasonic generator***
	• ***Electronic buzzer***

Both direct and converse effects	**Quartz resonator** **Transducers** • ***SONAR*** • ***Ultrasonic non-destructive testing*** • ***Medical imaging (ultrasound scanners)*** • ***Bone density measurements***

2.2 Crystallography

2.2.1 Crystal structures

The crystal structures have an important role in determining physical and electrical properties of crystalline materials. Atoms in such materials are packed together forming organised structures. The simplest method of describing these structures is by the unit cell. A unit cell is the smallest repeating arrangement of atoms. These unit cells are described using the 7 crystal systems shown in Figure 2.1, these can then be further divided into 14 Bravais lattices [8]. These Bravais lattices can further be divided by their symmetry characteristics in 32 crystal point groups. These point groups describe the symmetry of the atoms within the unit cell and have an effect on the properties of the materials as a whole. Piezoelectric materials are non- centrosymmetric which enables them to develop a polarisation in the presence of a mechanical stress and a mechanical strain with an applied electric field. Of the 32 point groups 21 are non-centrosymmetric, of these 20 are piezoelectric. The exception displays other symmetry elements which align to cancel out positive and negative charges within the material and thus meaning the piezoelectric effect can not occur. The 20 piezoelectric point groups include the 10 polar point groups. These polar point groups are piezoelectric and pyroelectric. All polar materials possess a spontaneous polarisation, in pyroelectric materials the polarisation will be changed by variations in temperature. Some of the pyroelectric materials can also be described as ferroelectric meaning that a change in polarisation can be induced and reversed by the application of an electric field. Pyroelectric and ferroelectric materials do not have crystallographic differences and the ferroelectric properties of a material must be determined experimentally [5], [9].

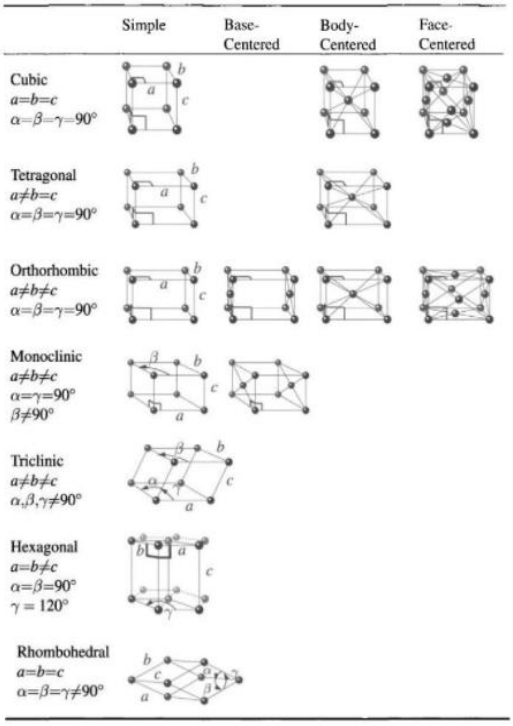

Figure 2. 1 The seven crystal systems and fourteen Bravais lattices*[10]*

2.2.2 The Perovskite Structure

The perovskite structure (ABO_3) is demonstrated by the unit cell shown in Figure 2.2. It is comprised of a cation (A) on the corner sites and a smaller cation (B) in the centre with face centred oxygen atoms. Most of the commonly used piezoelectric materials have the perovskite structure. The perovskite structure is often distorted by the size of the A and B ions meaning this structure is often not simply cubic as it appears in Figure 2.2 but can be rhombohedral, tetragonal or orthorhombic.

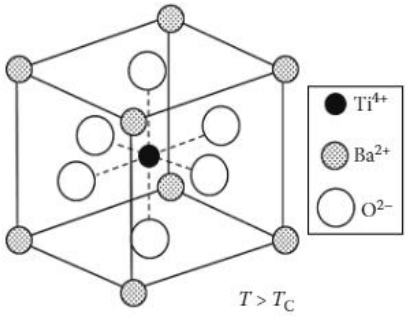

Figure 2. 2 The perovskite structure of $BaTiO_3$ above its Curie temperature*[11]*.

The Goldschmidt tolerance factor can be used to describe the relationship of the anions and cations in the perovskite structure [4]: where t is the Goldschmidt tolerance factor, R_A, R_B and R_0 are the ionic radius of the A cation, B cation and O anion respectively.

$$t = \frac{(R_A + R_0)}{\sqrt{2}\ (R_B + R_0)} \qquad (2.2.1)$$

When the tolerance factor (t) is equal to 1 the perovskite structure is cubic, when t is slightly lower than 1 the structure is distorted and for example rhombohedral structure is formed, a tolerance factor slightly above 1 indicates the structure is tetragonal. These distortions (where t is < or >1) can lead to ferroelectricity [4], [9].

2.3 Electrical properties

2.3.1 Dielectric properties

When placed under an electric field dielectric materials do not conduct electricity and instead small structural changes take place leading to the creation of a dipole moment i.e. the material is polarised. A dipole moment (p) is defined as equal positive and negative charges (Q) separated by a distance (δx) as shown in Equation 2.3.1 [9].

$$p = Q\delta x \qquad (2.3.1)$$

Various polarisation processes occur these include atomic, ionic, dipolar and space charge polarisation. Atomic polarisation is a process that occurs in all materials as the negatively charged electrons within an atom are displaced relative to its nucleus. Ionic polarisation occurs when negative anions and positive cations are displaced within a material. Dipolar materials, as the name suggests, have a permanent dipole moment. These dipoles are randomly oriented with charges cancelling each other out in the material. When these materials are placed under an electric field the dipoles are orientated and thus the material becomes polarised. Finally, space charge polarisation occurs when charge accumulates on either side of a barrier such as a grain boundary. These processes are demonstrated in Figure 2.3 [9].

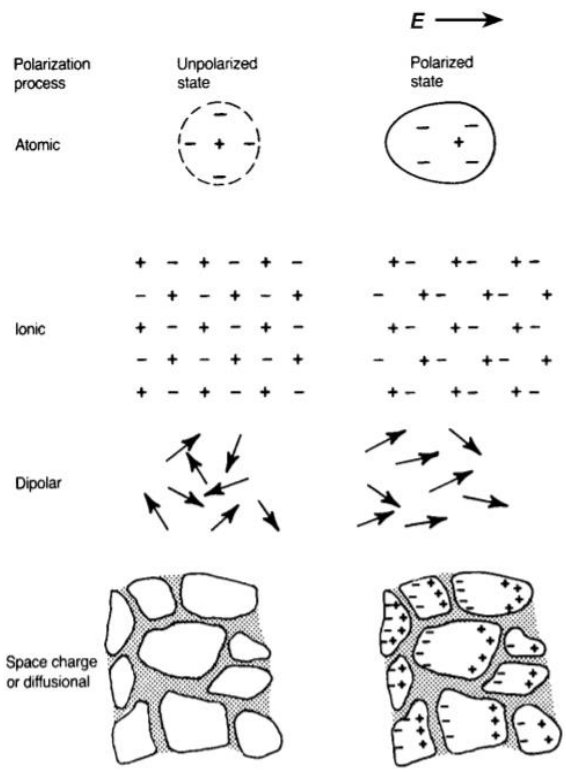

Figure 2. 3 The various polarisation processes. *[9]*

Relative permittivity is a ratio of the charged stored on parallel plate capacitor containing a dielectric material to that stored on two identical parallel plates separated by vacuum, when both are brought to a given voltage. Figure 2.4 shows a comparison of these two scenarios

where U is the applied potential difference, E is the electric field, P is polarisation, h is the distance between the plates, A is the area of the plates and σ is the charge density on the plates. In Figure 2.4(b) σ_p is the charge density on the dielectric material and σ_T is the charge density on the plates [9], [12].

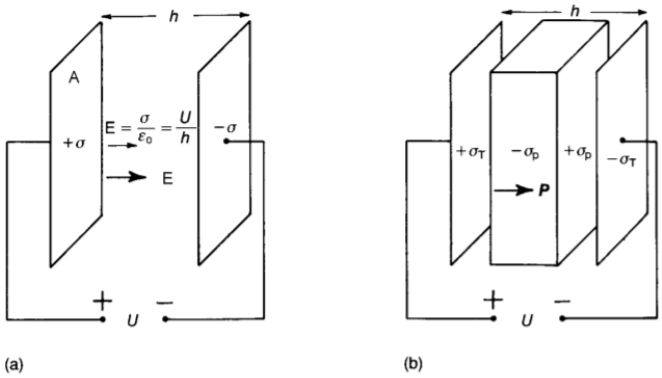

Figure 2. 4 Demonstrating parallel plate capacitors separated by a vacuum (a) and a dielectric (b)*[9]*.

As polarisation occurs in the dielectric, the charge on the dielectric opposes the charge on the parallel plates therefore the charge density of the system is reduced. This is demonstrated by Equation 2.3.2:

$$E = \frac{\sigma_T - \sigma_P}{\varepsilon_0} \tag{2.3.2}$$

Where ε_0 is the permittivity of free space and is 8.854 x 10^{-12} F m^{-1}.

When the plates are separated by a vacuum capacitance (C) can be calculated by:

$$C_0 = \frac{Q_T}{U} = (1 + x_e)\varepsilon_0 \frac{A}{h} \tag{2.3.3}$$

Where x_e is electric susceptibility and Q_T is the total charge on the plates. When a dielectric material is present then the capacitance is by the permittivity of the dielectric ε where:

$$\varepsilon = \varepsilon_0 (1 + x_e) \tag{2.3.4}$$

So capacitance in this scenario can be calculated by:

$$C = (1 + x_e)\varepsilon_0 \frac{A}{h} = \varepsilon \frac{A}{h} \tag{2.3.5}$$

And:

$$\varepsilon_r = 1 + x_e = \frac{\varepsilon}{\varepsilon_0} \tag{2.3.6}$$

Where ε_r is the relative permittivity. [9]

In reality some conduction occurs as well as other energy losses due to the rotation of charges or atoms. The effect of these losses is accounted for by the introduction of complex relative permittivity. Where ε_r* is the complex relative permittivity, ε_r' is the real part, ε_r'' is the lossy imaginary part and j is $\sqrt{(-1)}$ [9].

$$\varepsilon_r^* = \varepsilon_r' - j\varepsilon_r'' \tag{2.3.7}$$

The dissipation or loss factor is given by the ratio of the imaginary and real components of the relative permittivity [9]:

$$tan\delta = \frac{\varepsilon_r''}{\varepsilon_r'} \tag{2.3.8}$$

2.3.2 Piezoelectric Properties

Piezoelectric materials are defined as materials that react to the application of mechanical stress or of an electric field, by producing a polarisation or mechanical strain respectively. The production of polarisation by application of mechanical stress is known as the direct piezoelectric effect and the production of mechanical strain by application of an electric field is known as the converse effect [9]. Figure 2.5 illustrates these effects, 2.5 (a) shows a

compressive force causing the material to become polarised. Polarisation will also occur if a tensile stress is applied. 2.5 (b) shows a mechanical strain caused by the presence of an electric field. Contraction or expansion can occur depending on the orientation of the electric field [9].

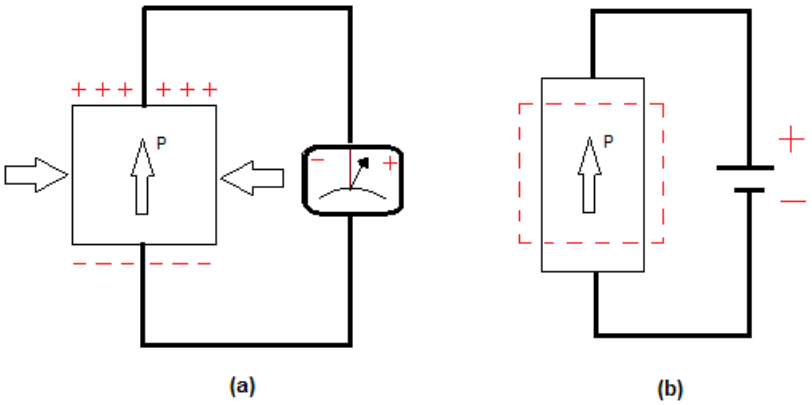

Figure 2. 5 Demonstrating the direct (a) and converse (b) piezoelectric effects *[13]*.

The equations that describe the piezoelectric effects are shown below. Equation 2.3.9 defines the direct effect. Where P is polarisation, d is the piezoelectric charge coefficient, X is applied stress, ε^X is the dielectric permittivity at constant stress and E is electric field. Equation 2.3.10 defines the indirect effect. Where x refers to strain produced and s^E is the elastic compliance at constant field [12].

$$P = dX + \varepsilon^X E \tag{2.3.9}$$

$$x = s^E X + dE \tag{2.3.10}$$

2.3.2.1 Piezoelectric charge coefficient (d)

A high piezoelectric charge coefficient (d) is often desirable and is useful in applications that require motion such as sonar. The charge coefficient can be related to the direct or indirect

effect and has units of pC/N when describing the direct effect and pm/V when describing the indirect effect. However, the numerical value for both the direct and converse effect remains the same.

Two subscripts are used to describe the direction of the electric field and the mechanical strain. Convention dictates that the direction of polarisation is defined as the 3 axis. Therefore, for example d_{31} is the coefficient used when electric field is parallel to the polar axis and mechanical strain is perpendicular to it. This example along with d_{33} and d_{15} can be seen in Figure 2.6 [9], [12].

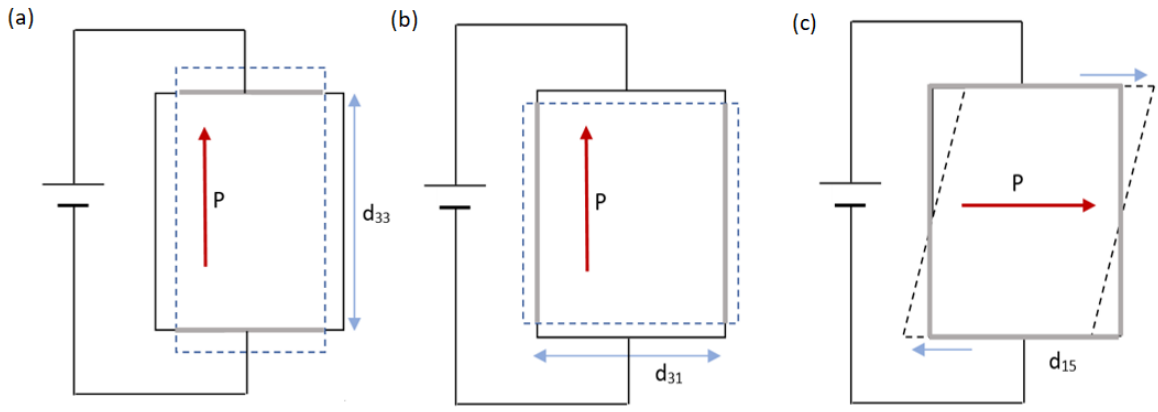

Figure 2. 6 Demonstrating the longitudinal (a), transverse (b) and shear (c) piezoelectric modes.

2.3.2.2 The electromechanical coupling factor (k)

The electromechanical coupling coefficient (k) is an important measure of the strength of the piezoelectric effect in a material. It measures the amount of energy which can be converted to electrical or mechanical energy by the material. This relationship can be seen in Equation 2.3.11 in terms of k^2. As complete conversion of energy is not possible, some of the energy will always be stored as mechanical energy then k and k^2 will always be less than 1 [12].

$$k^2 = \frac{electrical\ energy\ converted\ to\ mechanical\ energy}{input\ electrical\ energy}$$

or

$$k^2 = \frac{mechanical\ energy\ converted\ to\ electrical\ energy}{input\ mechanical\ eneergy} \quad (2.3.11)$$

The electromechanical coupling coefficient can also be described in terms of the piezoelectric charge coefficient, the elastic compliance and dielectric permittivity [12].

$$k^2 = d^2 / s^E \varepsilon^X \quad (2.3.12)$$

2.3.3 Ferroelectric properties

2.3.3.1 Phase Transitions

Piezoelectric perovskites have temperature dependant polymorphic forms and undergo phase transitions due to temperature. This is important in application as above a piezoelectric materials Curie temperature (T_C) the material becomes cubic, as discussed previously symmetrical crystal structures do not allow for a dipole moment and any piezoelectric properties are lost. Other phase transitions also occur due to temperature. $BaTiO_3$ for example (Figure 2.7) is cubic at temperatures above its Curie temperature of ~ 130°C. When it is cooled below this temperature it adopts a tetragonal structure which transitions to an orthorhombic structure at ~ 0°C and again to a rhombohedral form at ~ -90°C. In the tetragonal, orthorhombic and rhombohedral forms the direction of polarisation will be parallel to the elongation of the unit cell [4], [9].

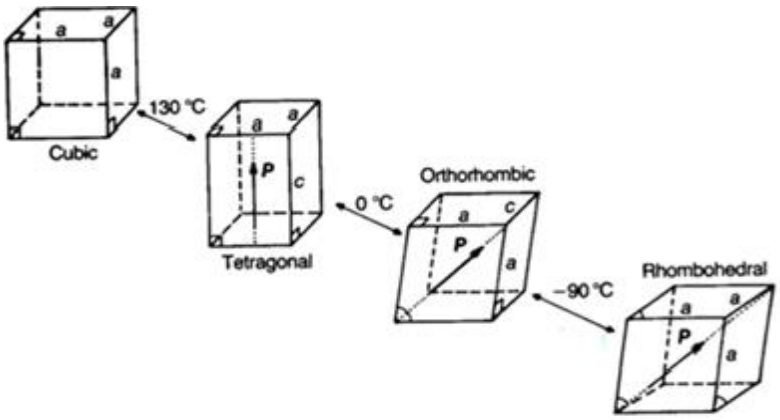

Figure 2. 7 The polymorphic phase transitions of $BaTiO_3$ *[9]*.

Phase changes can also be composition dependant, these transitions are shown by a vertical line known as a morphotropic phase boundary (MPB) on a phase diagram (Figure 2.8). In compositions at or near this line different phases coexist in the material which gives rise to improved piezoelectric properties. In PZT extrinsic contributions due to the motion of domain walls (extrinsic contributions) are responsible for up to 50% of the piezoelectric effect. The MPB aids these contributions as transformations between tetragonal/rhombohedral phases can occur [9][4].

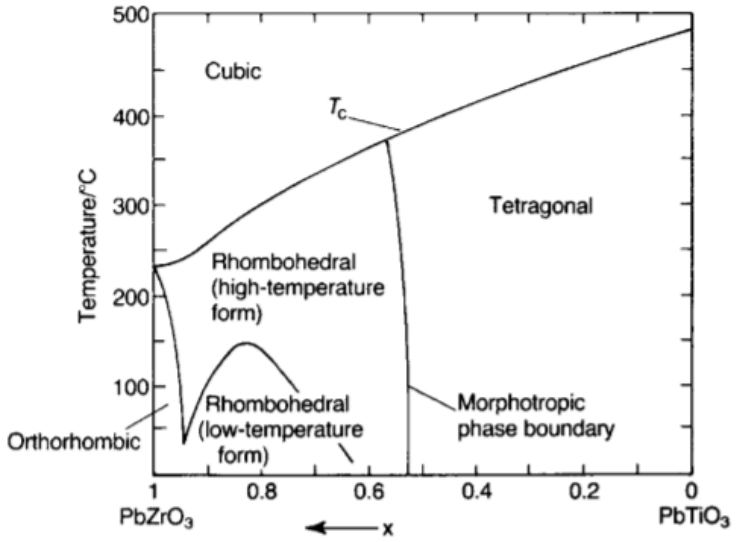

Figure 2. 8 Phase diagram of PZT showing the morphotropic phase boundary *[9]*

2.3.3.2 Ferroelectric Domains

As a paraelectric material is cooled through its Curie temperature it undergoes a phase transition and becomes ferroelectric. During this phase transition areas which have the same direction of polarisation are formed, these areas are called ferroelectric domains. No net polarisation occurs throughout the material as polarisation direction varies between domains and grains. If a tetragonal ferroelectric is formed upon cooling 90° and 180° domains are formed. A micrograph and schematic of these domains can be seen in Figures 2.9 and 2.10. 90° domains are formed to reduce strain due to the mechanical stresses caused by the deformation of the unit cell during the phase transition. As spontaneous polarisation occurs in the ferroelectric material surface charge builds and causes a depolarising field to form, the energy associated with these processes is reduced by the formation of 180° domains. In a rhombohedral ferroelectric 109°, 71° and 180° occur in order to reduce surface charge and stresses and no 90° domains are present [9], [12], [14].

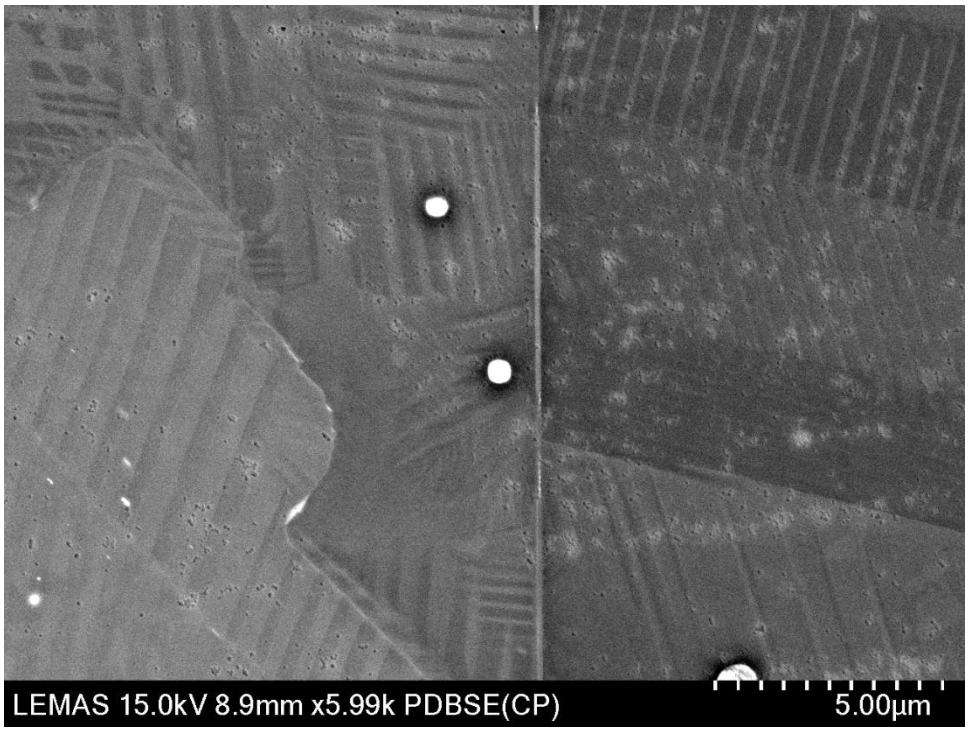

Figure 2. 9 A scanning electron micrograph of $BaTiO_3$ where ferroelectric domain patterns can be seen as the striped regions within grains. This image was taken as part of this work.

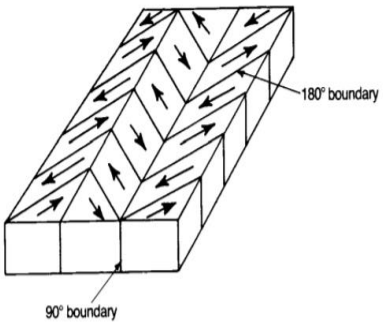

Figure 2. 10 A schematic diagram showing 180° and 90° domains in a tetragonal ferroelectric material *[9]*.

As there is no net polarisation the material is non-piezoelectric, in order to create a net polarisation a sufficiently large electric field must be applied. Upon application of this electric field domains align with the field. In practice complete poling does not happen due to intergranular stress and stresses caused by reorientation of 90° domains. Ideally 180° domain switching should be completed whilst limiting 90° domain switching in order to reduce mechanical stresses as shown in Figure 2.11 [12].

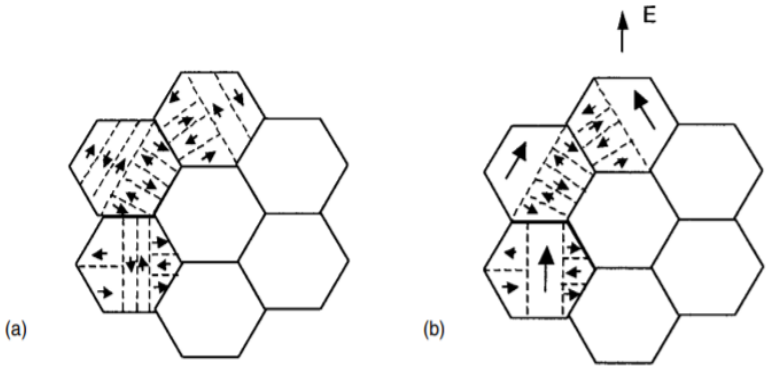

Figure 2. 11 A schematic diagram showing (a) an unpoled ferroelectric showing random domain orientation and (b) after poling and subsequent 180° domain switching. Please note the blank grains would contain similar domain patterns and polarisation directions *[9]*.

Intrinsic contributions to piezoelectricity are due to the elongation of the unit cell and resulting displacement of the central atom as it cooled through the Curie temperature. However, extrinsic contributions are also responsible for a large part of the piezoelectric effect. This extrinsic piezoelectric effect is due to the motion of domain walls, where upon

application of an electric field the domains aligned with the electric field grow at the expense of those that are not aligned with the field. Defects and dopants can interfere with this domain wall motion and the polarisation within the domains. Acceptor dopants are dopants with a lower positive charge than those they these dopants are compensated by oxygen vacancies. Defects and oxygen vacancies within the domain wall can pin the domain walls in place and acceptor dopants or impurities form dipoles with oxygen vacancies. These dipoles then align themselves in the polarisation direction by movement of the oxygen vacancies which provides an internal electric field stabilising the domain walls. These domain clamping effects can be manufactured with the addition of acceptor dopants for example in the production of 'hard' PZT. Donor dopants are dopants with a higher positive charge than those they replace and are compensated by cation vacancies. Both acceptor and donor dopants supress the vacancies that the other promotes. Hence, donor doping can also be used to increase domain wall mobility for example in the production of 'soft' PZT. This increased domain wall mobility is due to a decrease in oxygen vacancy concentration and therefore a decrease in the concentration of domain stabilising defect pairs [9].

2.3.3.3 Hysteresis Loops

In order to measure the degree of polarisation and thus ferroelectricity D/E hysteresis loops are obtained, where D is displacement and D ≈ P. An example of a hysteresis loop can be seen in Figure 2.12. Before an electric field is applied to an unpoled material there is no net polarisation as domains are randomly orientated. As the electric field increases the domains begin to reorientate themselves in alignment with the electric field. P_{sat} is reached when domain reorientation is complete. When the electric field is decreased back to zero there is a remnant polarisation (P_r), in crystals P_r can be equal to P_{sat}. Large P_r values generally demonstrate the usability of a piezoelectric material. The coercive field (E_c) is the electric field needed to reverse the direction of polarisation causing domains to switch again to align themselves in the opposite direction. Spontaneous polarisation (P_s) can also be extrapolated from hysteresis loops by following a tangent from P_{sat} back to zero [9], [12].

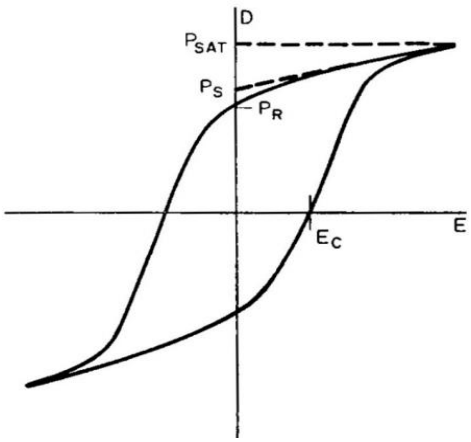

Figure 2. 12 An example of a typical hysteresis loop *[12]*.

2.4 Piezoelectric Materials

2.4.1 Barium Titanate ($BaTiO_3$)

Barium Titanate was the first piezoelectric ceramic to be developed and commercialised, for use as an acoustic generator and ultrasonic detector. Today it is less commonly used due to the development of materials such as PZT, which has better piezoelectric properties and can be used over a wider temperature range. However, $BaTiO_3$ is still commonly used in multilayer ceramic capacitors due to its high dielectric constant [12]. The lead free composition of $BaTiO_3$ is however beneficial in terms of health, safety and the environment [9].

The crystal structure and polymorphic transitions of $BaTiO_3$ are well documented. At temperatures below approximately -97°C $BaTiO_3$ exists in rhombohedral form, as the temperature is increased to above -97°C the material undergoes a phase transition and the structure becomes orthorhombic. Another phase transition takes place when the temperature is increased to 0°C where barium titanate becomes tetragonal. The Curie temperature (T_c) of Barium titanate is 120°C at this temperature there is a tetragonal to cubic phase transition and the material loses its spontaneous polarisation. Barium titanate can take stable hexagonal form at high temperature (>1460°C), below this temperature it loses stability but can exist in a metastable state at room temperature although this is not usual. Normally the hexagonal form will transition to a cubic perovskite when temperature is reduced. The hexagonal phase can sometimes be present in ceramics due to impurities or a

disequilibrium due to fast sintering and processing techniques [12]. Doping $BaTiO_3$ can be useful in order to adjust the properties and microstructure to fit with an intended application. For example, the Curie temperature can be adjusted by substitution of Sr^{2+} or Pb^{+} for Ba^{2+} (A-site doping). With addition of Sr^{2+} the T_c is reduced and with the addition of Pb^{+} T_c can be increased; this means that the peak in permittivity can be brought in line with the temperature range at which the material is going to be used. Another variation of this involves the addition of $CaZrO_3$ which leads to the development of a core-shell structure. The core and shell regions have different Curie temperatures, which leads to a broadening of the permittivity peak in a plot of permittivity vs temperature and thus a larger range of temperature across which high permittivity can be taken advantage of. Domain wall pinning can also be induced with the addition of acceptor dopants such as the addition of Co^{3+} in place of Ti^{4+}. This reduction in domain wall motion leads to a decrease in the dissipation factor, which leads to less energy being lost as heat and more consistent properties over time. Grain growth can also be restricted with the addition of certain donor dopants such as Nb^{5+} in place of Ti^{4+}, at concentrations above 0.5%, this increases permittivity below T_c [9].

As a small amount of liquid phase present between a growing single crystal and the polycrystalline matrix is seen to have an important role in solid state crystal growth (SSCG), an important feature of barium titanate is the BaO-TiO_2 eutectic (1320°C) where the melting point of barium titanate is lowered significantly with the addition of TiO_2, as is shown in Figure 2.13. This means that the liquid phase present at the crystal/polycrystalline matrix interface can be controlled by TiO_2 addition at temperatures above 1320°C [14]. $BaTiO_3$ also forms a eutectic system with SiO_2 which leads to liquid formation at 1260°C. SiO_2 has also been used as an additive to promote densification in $BaTiO_3$ and in SSCG [15].

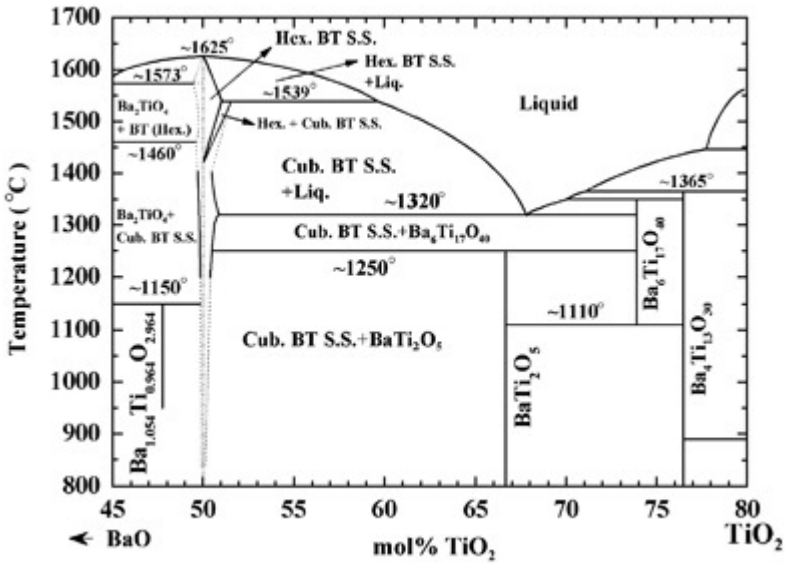

Figure 2. 13 Showing the BaO-TiO_2phase diagram. [16]

Single crystals of Barium titanate cannot be obtained from melt growth techniques such as the Bridgman and Czochralski methods. This is due to the hexagonal to cubic phase transition at 1460°C mentioned previously, which is below the temperature at which $BaTiO_3$ solidifies (1618°C). As the hexagonal phase can then exist metastabily at room temperature it is best avoided. Other methods of crystal growth however have been more successful. The usual methods for growth of $BaTiO_3$ single crystals are Remeika's method of flux growth [17] and Sasaki's method of melt growth.[18] The Remeika method produces crystals of the 'butterfly twin' shape. These crystals are triangular with (001) broad faces and are joined together at their hypotenuse. The crystals are produced using a small amount (0.2%) of iron oxide mixed with (30%) $BaTiO_3$ which is placed into a platinum crucible and covered by (69.8%) potassium fluoride (KF). The mixture is then heated to 1150°C - 1200°C for 8 hours before being slowly cooled to 850°C - 900°C at which point the KF liquid can be carefully removed. Boiling water can then remove any left-over KF [19]. The method developed by Sasaki takes advantage of the BaO-TiO_2 eutectic shown in Figure 2.13 Crystals can be produced by this method using a mixture of 65% TiO_2 and 35% $BaTiO_3$. This reduces the melting point to around 1400°C. The mixture is placed into a platinum crucible which is then heated to 1450°C in order to ensure complete melting. The crucible is then cooled slowly to around the eutectic temperature, to enable crystallisation, at which point the cooling can be accelerated. Adjustments to this method have since been made and include removal of the TiO_2 rich liquid before the cooling rate is increased and by using top seeding for added control of crystal growth [20].

2.4.2 Lead Zirconate Titanate (PZT)

Lead Titanate ($PbTiO_3$ or PT) has a large tetragonal distortion and very high Curie temperature but is difficult to produce as it breaks apart due to internal stresses when cooled. However, lead zirconate ($PbZrO_3$or PZ) is orthorhombic with a lower Curie temperature [9]. When a portion of the titanium ions in PT are replaced with zirconium ions tetragonality is reduced, in addition to this a ferroelectric rhombohedral phase is produced. $PbZr_{1-x}$ Ti_xO_3 or PZT shows very good piezoelectric properties around the tetragonal/rhombohedral phase boundary known as the morphotropic phase boundary (MPB). Which can be seen in Figure 2.14 at around 50 mol % $PbTiO_3$ [12].

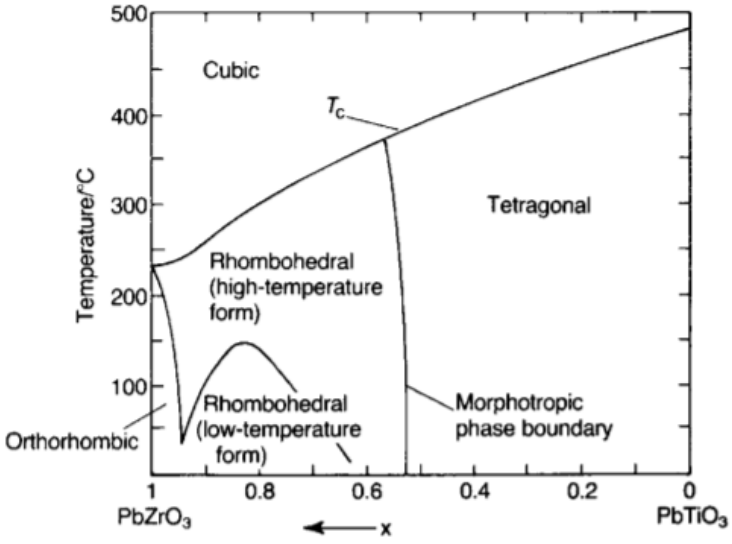

Figure 2. 14 Displaying the possible phases in PZT with variations of mol% PT, mol%PZ and temperature *[9]*

In PZT extrinsic contributions due to the motion of domain walls (extrinsic contributions) are responsible for up to 50% of the piezoelectric effect. The MPB aids these contributions as transformations between tetragonal/rhombohedral phases can occur. The extrinsic contributions to the piezoelectric effect can also be enhanced by the addition of donor dopants in the production of 'soft' PZT. 'Soft' PZT has increased permittivity and piezoelectric coefficients making it useful for converting mechanical energy into electrical energy such as in pressure sensors. 'Hard' PZT can also be produced using acceptor dopants, this type of PZT has a lower piezoelectric coefficient and electromechanical coupling factor. However hard PZT also has a lower dissipation factor which results in less energy being lost as heat and

more consistent properties over time, making it suitable for other applications such as wave filters [9].

2.4.3 Lead-free Piezoelectrics

Due to the introduction of regulations from 2002, such as the Waste Electrical and Electronic Equipment (WEEE), the Restriction of Hazardous Substances (RoHS) and the Registration, Evaluation, Authorisation and Restriction of Chemicals (REACH), there has been an increased interest in discovering a viable lead-free alternative to PZT[21]–[24]. Some of the materials studied in this search include alkaline niobates such as: $(K,Na)NbO_3$ (or KNN), alkaline bismuth titanates such as $(Na,Bi)TiO_3$ (or NBT) and those based on $BaTiO_3$ such as $(Ba,Ca)(Ti,Zr)O_3$ (or BCTZ). Of these KNN would be one of the most promising lead-free alternatives in terms of piezoelectric properties and temperature stability. However, life-cycle assessments have demonstrated that the environmental impact of this KNN is several times higher than that of PZT due to the mining and extraction processes necessary to obtain niobium[25]. NBT based materials have lower piezoelectric coefficients than KNN but still have good temperature stability. Life-cycle analysis of NBT has demonstrated some environmental drawbacks with this material due to the bismuth content. The authors noted that up to 95% of Bi_2O_3 is the product of lead smelting and there are higher energy costs associated with obtaining and refining Bi_2O_3 as well as recycling when compared to PbO[26]. BCTZ has a high d_{33} however, the Curie temperature is very low (~85°C). The Curie temperature is often lower than device manufacturing temperatures therefore in-situ poling would be necessary, and applications would be limited by temperature[27]–[29]. Barium is also known to be toxic, but it does not have the same level of human toxicity as lead so could still be beneficial from a health and safety point of view.

2.4.4 Perovskite Relaxor Ferroelectrics

Perovskite Relaxor ferroelectrics with a formula of $Pb(B'B'')O_3$, B'' is the cation with the highest valence of the two and B' is the cation with lower valence (e.g. PMN or $Pb(Mg_{1/3}Nb_{2/3})O_3$). The materials have been found to display unusual properties. These materials have excellent electrostriction coefficients which are useful for generating mechanical energy from electrical energy (e.g. for use in actuation). Addition of PT to these systems introduced more conventional ferroelectric behaviour as opposed to highly

electrostrictive behaviour, as well as an increased Curie temperature. Various compositions of the PMN-PT system have been investigated leading to the discovery of a MPB (Figure 2.15) at which the piezoelectric properties are amplified, much like in PZT [2].

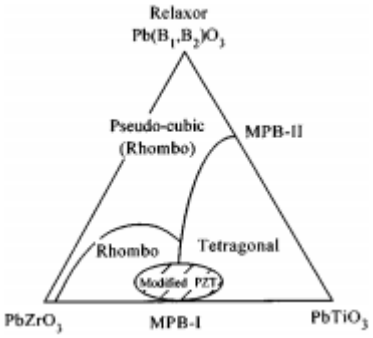

Figure 2. 15 Showing the MPB between a relaxor ferroelectric and PT (labelled MPB-II) [30].

2.4.5 Relaxor-PT Single Crystals

Attempts have been made to produce PZT single crystals, which has been difficult due to incongruent melting behaviours. However, relaxor-PT single crystals can be grown with little difficulty, using Flux growth methods. These single crystals have increased piezoelectric coefficients as well as much higher coupling factors, making them very attractive for use in various applications. As an example of the large piezoelectric coefficients observed in these materials, a d_{33} of around 2500 pC/N is observed in <001> orientated rhombohedral crystals of PZN-PT ($Pb(Zn_{1/3}Nb_{2/3})O_3$-$PbTiO_3$). This material also has a high coupling factor (k_{33}) of 0.94 [30]. Due to these crystals having greater piezoelectric properties resulting in higher sensitivity, as well as an increased bandwidth, they have already been commercialised as medical ultrasonic transducers. There are however some drawbacks to single crystals of this type. The low T_C and ferroelectric phase transition temperatures of first-generation crystals posed problems for usage at higher temperature ranges or where heat may be generated. Reliability is also an issue as problems with polarisation stability have been raised due to the low electric coercivity measured. Efforts to produce more reliable crystals have been successful resulting in second generation single crystals such as PMN-PZT and PIN-PMN-PT ($Pb(In_{1/2}Nb_{1/2})$-$Pb(Mg_{1/3}Nb_{2/3})O_3$-$PbTiO_3$) . These crystals are classified by their ability to withstand greater temperatures, mechanical stresses and electric fields. There is also a third generation of single crystals that are a result of doping in order to adjust crystals properties

to better fit their purpose, as with PZT doping. For example relaxor-PT materials produced for use as sonar transducers have been doped with Mn in order to enhance their electromechanical properties [2].

Chapter 3 – Introduction to Single Crystal Growth

As relaxor-PT single crystals have replaced PZT in various applications such as medical imaging, growth methods that produce good quality crystals that are time and cost efficient are important. Single crystals can be obtained from solution, via the solid state or from the melt. These methods along with their benefits and drawbacks will be outlined here.

3.1 Melt Growth Methods

Crystals can be obtained directly from the melt using methods such as the Czochralski or Bridgman methods. These methods are not suitable for compounds that are incongruently melting or those which have high temperature phase transitions.

3.1.1 The Czochralski Method

The Czochralski method or crystal pulling is widely used to produce certain crystals, for example lithium niobate. For this method the material to be crystalised is heated until melting and then held at high temperature. A rotating rod with a seed crystal attached is then lowered into the melt. The rod is then slowly withdrawn to initiate crystallisation. Cooling can be aided by controlled air flow through the rod [9]. It can be difficult to produce crystals with volatile components such as bismuth or potassium using this method [31]. Figure 3.1 shows a schematic of the Czochralski method experimental arrangement.

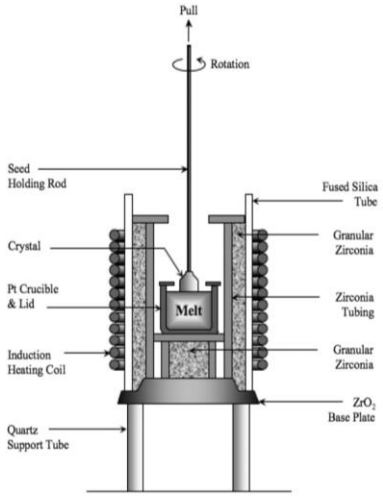

Figure 3. 1 Experimental schematic showing the Czochralski method [32]

3.1.2 The Bridgman Method

The Bridgman method was first described by P. Bridgman in 1924. The starting materials are placed into a crucible and heated to melting, the crucible is then moved slowly through a temperature gradient in order to slowly freeze the melt along the length [33].

Building on Bridgman's work Stockbarger employed the use of two furnaces with one stacked vertically in order to create two distinct temperature zones. The top furnace was set above the melting point and the lower below the freezing point. The crucible could then be slowly lowered to the bottom furnace enabling controlled crystallisation of the melt [34]. Due to Stockbargers work the modern Bridgman method is sometimes referred to as the Bridgman-Stockbarger method or the modified Bridgman method. Figure 3.2 shows a typical modified-Bridgman experimental set up.

Today specialised furnaces are commercially available with separate temperature zones combined with a mechanism to lower the crucible to lower temperature zones at a given rate. This method is commonly used commercially to produce relaxor-PT single crystals. However, this method is not without drawbacks for instance it involves very high temperatures, a long period of time in order to grow one crystal and expensive platinum crucibles. Such crucibles cannot be reused as they have to be cut open to free the crystal. Titanium concentration is also an issue as its segregation coefficient is low, leading to a concentration gradient and varying piezoelectric properties throughout the crystal. Efforts

have been made to improve uniformity such as continuous top feeding, however this still only results in two thirds of a grown crystal having uniform properties [2], [35], [36].

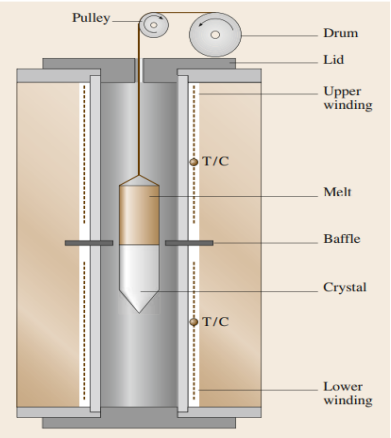

Figure 3. 2 A schematic demonstrating a typical Bridgman growth system [35]

3.2 Solution growth methods

This method is useful for growing crystals that cannot be obtained from the melt due to factors such as incongruent melting and materials that undergo phase transitions at temperatures cooler than their melting point. As the name of this method suggests starting materials are dissolved into a solution. Nucleation is then prompted as the solution becomes supersaturated which occurs as the solvent evaporates or the solution is carefully cooled.

3.2.1 Flux Method

The Flux method is a type of solution growth in which the starting composition along with a flux are placed into a platinum crucible within a sealed alumina crucible in order to minimise loss of volatile components. Some variations of this set up can also be used in order to provide a nucleation point at the bottom of the platinum crucible. These variations include the use of an alumina rod (Figure 3.3) or the introduction of oxygen gas flowing to the bottom of the crucible, both of which cause a temperature variation which induces nucleation and allows for larger size crystals to be grown. [37] The crucibles are placed into a furnace and heated to a suitable temperature. The furnace is then held at this temperature for several

hours to ensure complete melting before being slowly cooled. During this cooling process crystallisation occurs. Once crystal growth is complete cooling is allowed to occur at a faster rate down to room temperature. Once removed from the furnace the flux is removed using an acid solution such as nitric acid [2].

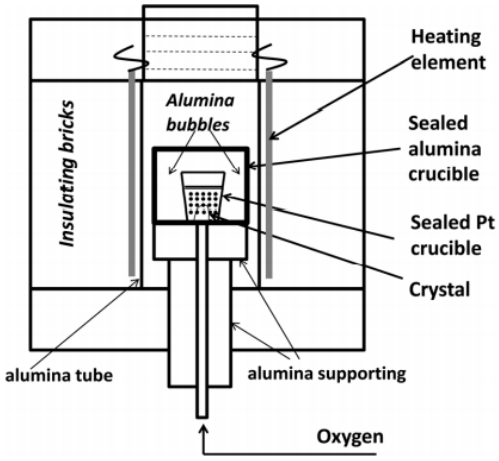

Figure 3. 3 Showing an experimental set up for the flux method which uses an oxygen gas cooling system *[2]*

This method has the advantage of allowing crystal growth to occur at a relatively low temperature when compared to melt growth techniques. However, this method is unsuitable for commercialisation due to small crystal size, nucleation occurring at multiple points, variations in dopant distribution throughout the crystal and impurities due to solvent inclusion in the resulting crystal. This method also requires platinum crucibles which are expensive and can sometimes not be reused, due to the crucible having to be cut to free the crystal making this a less economical method [1], [2].

3.2.2 The Flux-Bridgman method

As the name suggests the Flux-Bridgman method is a combination of the two previously described crystal growth methods. The experimental procedure for this method involves placing starting materials and flux into a Pt crucible which is subsequently placed into an alumina crucible containing additional alumina packing powder for additional stability and in order to inhibit the loss of PbO in Pb containing materials. Like the flux method this flux-

Bridgman method also utilises an additional cooling mechanism such as a cooling rod [38] or oxygen gas flow beneath the crucible to initiate nucleation [2]. Analogous with the Bridgman method the crucible is placed into a furnace with various temperature zones and moved slowly from high to low temperature.

3.2.2 Top seeded solution growth method

Top seeded solution growth (TSSG) involves melting the starting materials and flux in a Pt crucible and placing a seed crystal on the top of the molten mixture. The seed crystal is suspended via a Pt wire from an alumina rod as shown in Figure 3.4. This method is also using a temperature gradient at the surface of the melt to induce crystallisation.[39] This method offers some advantages in terms of preventing compositional segregation and enabling control of crystallographic growth direction. However, large boule shaped crystals cannot be obtained by this method, the growth rate is slow and again this method is costly requiring a specialised furnace, high temperatures and Pt crucibles [1].

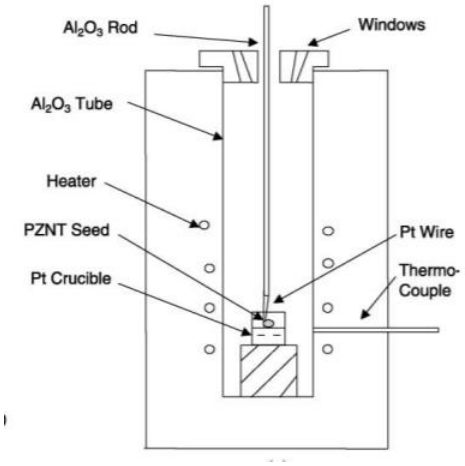

Figure 3. 4 Showing a typical set up used for the TSSG method [39]

3.3 Solid State Crystal growth

Theoretically solid state crystal growth (SSCG) takes advantage of abnormal grain growth in a polycrystal. A single crystal seed is placed onto the body of a polycrystal. When annealed this seed crystal then acts as a large abnormal grain, which grows at the expense of the fine-

grained matrix. This method of grain growth has been used for several different materials and has the advantage of being compatible with incongruently melting materials. This method is also a cost-effective choice when growing single crystals as it is simply an adaptation of traditional ceramic processing. There are however some difficulties related to this processing route. The largest difficulty being microstructure control. In order for the seed crystal to be able to grow to a relatively large size its growth has to be exaggerated whilst growth in the rest of the matrix must be kept normal and minimal to allow the seed to scavenge as many grains as possible. Figure 3.5 is a low magnification photograph of a seeded single crystal that has grown by scavenging surrounding grains. Abnormal grains can be seen below the single crystal, these grains eventually halt crystal growth by impingement therefore their growth must be controlled.

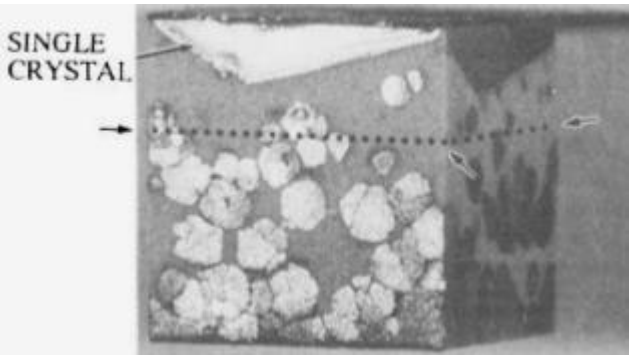

Figure 3. 5 Showing an SSCG arrangement, with a single crystal grown from a seed crystal [19]

This method has several advantages over conventional crystal production methods such as melt growth (Bridgman and Czochralski) and solution growth methods. It is difficult to grow crystals via melt growth if the material has volatile components, high melting points, have phase transitions at high temperatures, are particularly reactive or have incongruent melting points. As SSCG uses temperatures that are usual to the production of polycrystalline ceramics these problems are minimised or eliminated. The solution growth method has addressed some of the problems with the melt growth method and is suitable for materials with volatile components or phase transitions at high temperature however this is at the cost of crystal size and purity. Growing crystals from the melt also requires more costly equipment whereas solution growth of crystals and SSCG do not [40].

3.3.1 Microstructure and Grain Growth

Upon annealing a polycrystal, changes in microstructure can occur as a result of grain growth. There are two types of grain growth, the first is normal grain growth (NGG), when grain growth occurs without a large change in the distribution of grain sizes it is said to be normal. The second type of grain growth is abnormal grain growth (AGG). When some larger grains grow at an accelerated rate in comparison to the surrounding matrix of fine grains, as shown in Figure 3.6. As there are a variety of variables which can affect grain growth mechanisms, predicting behaviour and controlling the microstructure can be complex.

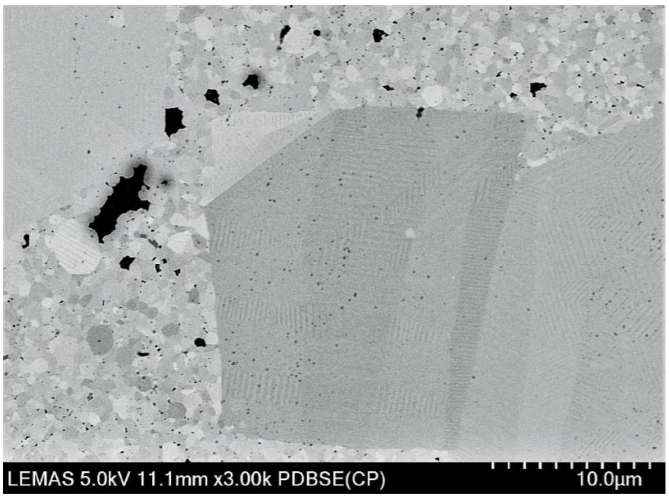

Figure 3. 6 A scanning electron microscopy image of $BaTiO_3$ with 2 mol% excess Ti sintered at 1300°C produced during this work, showing an example of abnormal grain growth resulting in bimodal grain distribution.

Grain growth occurs in order to enable a reduction in grain boundary energy of the polycrystal, this occurs as the grain boundary area throughout the polycrystal is reduced as the total number of grains are reduced. This is demonstrated by Eq. 3.3.1 where ΔG is the reduction in free energy that occurs when atoms diffuse across boundaries (causing grain growth) or "driving force" of grain growth, γ is the grain boundary energy and A_2 and A_1 are the final and initial total grain boundary areas respectively. [14]

$$\Delta G = \int_{A_1}^{A_2} \gamma \, dA = \gamma(A_2 - A_1) \tag{3.3.1}$$

3.3.1.1 Normal grain growth

Normal grain growth is dependent upon the curvature of the grain boundaries. Grain boundaries that are curved tend to move toward their centre of curvature driven by the difference in free energy of the two grains in question. This means that when viewed in two dimensions the direction of growth and subsequent disappearance of neighbouring grains can be predicted from the location of the centre of curvature of the grain boundary (Figure 3.7). Grains with a larger number of sides (>6) have boundaries that are curved inwards towards the centre of the grain (convex in relation to the centre). These are the grains that are likely to grow and eliminate neighbour grains with fewer sides (whose centre of curvature is towards the centre of the grain).

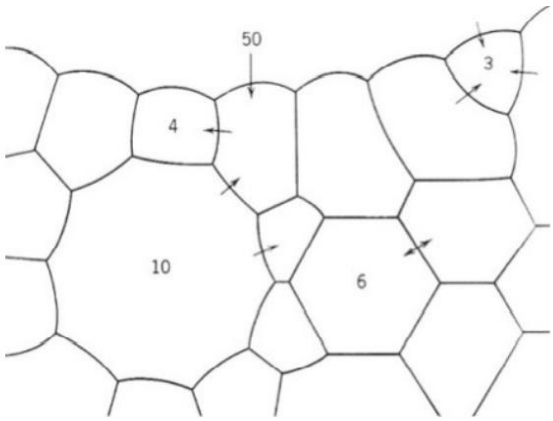

Figure 3. 7 A two-dimensional schematic of a polycrystalline matrix, showing how grain boundary curvature varies depending on the number of sides. Arrows indicate the direction of grain growth.

The boundary velocity (V) is therefore determined by the driving force resulting from boundary curvature (F) and boundary mobility (M) as shown in Eq. 3.3.2. [14]

$$\mathrm{V} = \mathrm{MF} \tag{3.3.2}$$

The parabolic law of normal grain growth is shown in Eq. 3.3.3 where g is grain size, g_0 is grain size at t=0 and t is time.

$$g^2 - g_0^2 = 2M\gamma t \tag{3.3.3}$$

Not all NGG follows this kinetic law however, this can be for a number of reasons such as changes in grain mobility with grain size or there not being a large difference between the grain size at t=0 and the final grain size. [14]

Normal or intrinsic grain growth occurs when the diffusion of atoms is the rate limiting step of grain growth; however various impurities such as solutes and pores or the presence of a liquid film within the matrix can influence this. Abnormal grain growth is much more common as most ceramics contain some impurities [14].

3.3.1.2 Solute drag

Solute drag has been found to be a reason for the occurrence of AGG. Solute drag occurs when there are interactions between a solute and a moving grain boundary. The interactions present cause the solute to be moved along with the boundary, as the solutes cannot migrate as easily as the boundary this causes a drag force on grain boundary movement [14]. If such solutes or impurities are not homogenously spread throughout the grains this can lead to the development of AGG, as the growth of only some of the grains is slowed.

3.3.1.3 Pore and second phase inclusion drag

Pore and second phase inclusion drag also slows grain growth leading to AGG. Some inclusions can be considered stationary, therefore as the boundaries move, they come into contact with these inclusions. The inclusion then exerts an opposing force on the moving boundary. This opposing force can only be overcome if the driving force for grain growth is larger than the opposing force exerted by the inclusion, if this is the case the inclusion will be left behind. Zener analysis is shown in Eq. 3.3.4 where R is the limiting grain size, r is the radius of the inclusion and V_f is the inclusion volume fraction. From this equation it can be seen that grain growth is limited by inclusion volume [14].

$$\frac{R}{r} = \frac{4}{3V_f} \tag{3.3.4}$$

During annealing of ceramics, pores shrink as densification occurs. Initially, pore volume will be large; from Eq. 3.3.4 it would be thought that grain growth would be restricted whilst the pores are relatively large. Grain growth in this scenario is determined by the rate at which the material densifies and pore shrinkage occurs, this phenomena is known as pore pinning. Approximations can only be made from Eq. 3.3.4, as to assume second phase particles are immobile is a large simplification especially as the most inclusions in ceramics are pores, which are not entirely spherical or immobile. Mobile pores can become attached to grain boundaries. This can exert a drag force on grain boundaries that opposes the driving force of grain growth. If pore mobility is low then more of a drag force is exerted and when pore mobility is high the grain growth is less restricted. Pores have a maximum velocity of which they cannot surpass, if the grain boundary and attached pore surpass this velocity then the pore will detach. Pore size also plays a role in pore drag as smaller pores are more mobile and exert less drag force and larger pores exert a larger drag force. As the size of pores change during grain growth the limits placed on grain growth can change throughout the process. Inclusions can also become concentrated at intersections if they do not become free of the boundary [14].

3.3.1.4 Liquid film enhanced AGG

The presence of a liquid film has also been thought to aid AGG, this is said to occur by a solution segregation process. The larger grains were shown to be less soluble leading to the smaller grains being dissolved. Material dissolved from smaller grains are then thought to diffuse through the liquid layer and deposit on the larger grains due to the lower solubility displayed by the larger grains [41].

3.3.1.5 Mixed control mechanism

Recent investigations discussed by Kang, Ko and Moon propose that grain growth is not governed purely by diffusion but can also be controlled by interface reaction [42]. It has been suggested that abnormal grain growth only occurs in faceted systems. The migration kinetics and driving force of grain growth in faceted systems was studied and the presence of a critical driving force confirmed. This critical driving force Δg_c was shown to be related to the degree

of faceting in the system. It can be deduced from this that grains behave in a similar way to single crystals during growth. Single crystals grown from melts or vapour are known to follow different growth kinetics depending on their morphology. Single crystals that are spherical, i.e. have disordered surface structure and surface defects have growth rates determined by diffusion. This is because the disorder and energy differences at the surface give rise to rapid interface reactions. This type of growth is comparable to normal grain growth in a polycrystal. In faceted single crystals however surface structure is much more ordered and therefore interface reactions are much slower. This results in a non-linear plot of growth rate vs driving force and is known as the step growth mechanism. The growth of faceted single crystals has been shown to be comparable to the abnormal grain growth of faceted grains. Another important aspect of this mechanism is the maximum driving force for grain growth, Δg_{max}, as different grains in a polycrystal have different driving forces with the largest crystal having largest driving force, the maximum driving force of the complete system is dependent on grain size distribution and average grain size. It follows that grain growth behaviour can then be predicted by observing the magnitudes of Δg_c and Δg_{max} [42].

Normal grain growth is expected when $\Delta g_c = 0$

Pseudo normal grain growth is expected when $0 < \Delta g_c << \Delta g_{max}$

Abnormal grain growth is expected when $\Delta g_c \leq \Delta g_{max}$

Stagnant grain growth (virtually no grain growth) when $\Delta g_{max} << \Delta g_c$

Chapter 4 - Literature Review

4.1 Barium Titanate ($BaTiO_3$)

4.1.1 Previous investigations of grain growth behaviour in ($BaTiO_3$)

It is well known that abnormal grain growth occurs in TiO_2 excess containing $BaTiO_3$, above and below the eutectic temperature (Figure 4.1). This abnormal grain growth occurs more readily above the eutectic temperature [43]. Barium titanate is usually sintered above the eutectic temperature with excess TiO_2, despite this excess being associated with AGG, as the liquid formed at this temperature aids densification which, without the liquid, is very slow. Different types of grain growth are reported for temperatures above and below the eutectic.

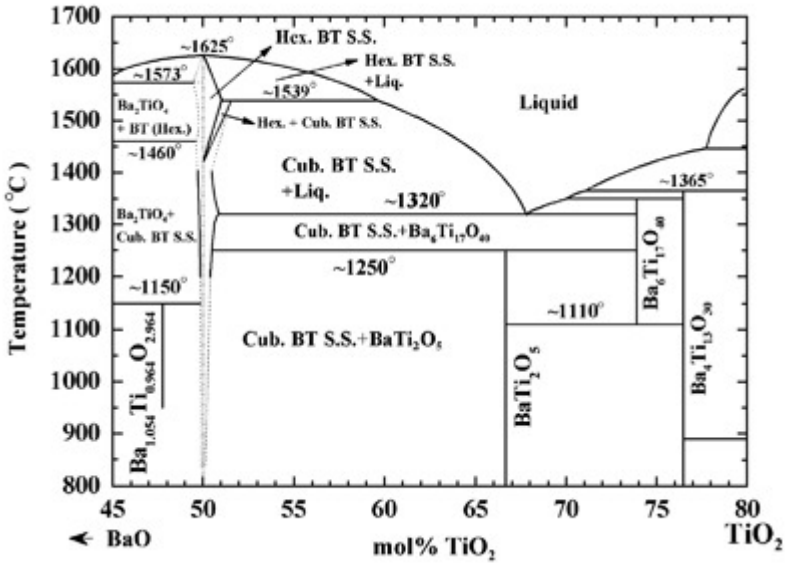

Figure 4. 1 Showing the BaO-TiO2phase diagram [44].

A study by Hennings, Janssen and Reynen, in 1987 [41] reported that below the eutectic temperature twinned crystals appear and grow abnormally, with the addition of TiO_2 the growth of these twinned crystals is exaggerated and when sintered for long periods the barium titanate is made up entirely of these large twinned grains. Above the eutectic not all of the abnormal grains are twinned as demonstrated at lower temperatures therefore these twins are not thought to be necessary for the abnormal grain growth observed in the presence of a liquid phase. When more than 2 mol % excess TiO_2 is added the larger liquid

phase causes a reduction in grain growth rates. 2 mol % excess TiO_2 was found to have the largest corresponding growth rate in this study, this is likely to be because at this excess more grains are in contact with a relatively thin liquid film. This study reported that the abnormal grain growth in barium titanate was likely due to liquid phase enhanced AGG. Grains that grew rapidly were found to be faceted. The finer grains that are dissolved in this process were found to have spherical characteristics [41].

Grain growth behaviour has been found to be dependent on grain boundary structure in a number of studies such as the one conducted by Lee, Chung and Kang [45]. This study was performed below the eutectic temperature (1250°C) and found that grain boundaries can be defaceted when sintered in a reducing H_2 atmosphere. The defaceting of the grain boundaries led to normal grain growth and therefore suggests that the abnormal grain growth is dependent on faceting which is enhanced by the presence of twinned crystals. It was also found that in the reducing atmosphere the double twins began to grow isotropically rather than elongating further, this is despite the presence of {111} twinned crystals. Further studies by Jung, Choi and Kang confirmed this behaviour [46], [47]. In 2003 the authors found that sintering in only air, with no prior sintering in an atmosphere of reduced oxygen partial pressure, led to AGG irrespective of whether the sintering temperature was above or below the BaO/TiO_2 eutectic. Pre-sintering in a reducing hydrogen rich atmosphere however affected grain growth mechanisms when subsequently sintering in air at temperatures of 1250°C or 1350°C (below or above the eutectic temperature). The effect of the hydrogen pre-sinter depended on its length; samples that were sintered in hydrogen for only 30 minutes displayed different types of abnormal grain growth when sintered in air. The samples sintered in air below the eutectic temperature displayed elongated abnormal grains with the sample sintered above the eutectic displaying approximately equal amounts of growth in all directions. When the hydrogen pre-sinter was prolonged for 10 hours, no AGG occurred when sintered in air at either 1250°C or 1350°C. Normal grain growth also appeared to be stunted in these conditions. The 2006 study used 4 different types of sintering atmosphere chosen for their variety of oxygen partial pressures. Air was used to study effects of grain growth in high oxygen partial pressures (0.2 atm), a mixture of CO and CO_2 for an oxygen partial pressure of above ~10^{-14} atm followed by a mixture of H_2 and N_2 which reduced oxygen partial pressure to below ~ 10^{-15} atm and finally using increasing amounts H_2 in the H_2 / N_2 mixture which reduced the oxygen partial pressure to ~10^{-19} atm. Different concentration combinations of the gases described were used so a broad range of oxygen partial pressures could be created. Samples were all sintered at 1250°C (below the eutectic

temperature). As described previously when sintered in air, at this temperature, AGG assisted by {111} twins occurred. All of the grain boundaries observed after sintering in air were found to be faceted. As the oxygen partial pressure was reduced {111} twin formation was reduced and eventually stopped. At the same time the grain boundaries were defaceted. At an oxygen partial pressure of ~10^{-11} to 10^{-17} twin formation was stopped and some boundaries were defaceted, this led to stagnant grain growth. When oxygen partial pressure was reduced again abnormal grain growth resumed however, twin formation was still not present and more of the boundaries were rough. Finally at the lowest oxygen partial pressures, a significant amount of grain boundaries were defaceted and normal grain growth began. Leading to the deduction that increased oxygen vacancy concentration at boundaries leads to roughening and thus inhibits AGG. The authors thought this change in grain growth behaviour was due to the re-entrant edge mechanism, which states that twin planes provide edges for fast atom attachment in $BaTiO_3$ below the eutectic temperature, being promoted or suppressed by faceting or defaceting [48]. The twin plane re-entrant edge mechanism (TPRE) however was disputed by Eibl, Pongratz and Skalicky in 1987 as the existence of twins does not always equate to AGG. [49] It was noted that grains grew quickly parallel to the twins in undoped $BaTiO_3$ however these twins were present in Nb doped $BaTiO_3$ and did not grow abnormally.

4.1.2 Solid state crystal growth in ($BaTiO_3$)

Growth of barium titanate crystals is difficult due to the phase transition at 1460°C, meaning crystals cannot be produced from Bridgman growth. Other techniques have been employed to obtain $BaTiO_3$ single crystals. Yamamoto and Sakuma [19] produced a $BaTiO_3$ single crystal of dimensions 3mm x 3mm x 0.5mm via SSCG. AGG was controlled in the study by limiting the annealing temperature at which the single crystal was formed. It was found that grain growth was very slow up to 1300°C after which AGG began. The onset of AGG was found to be detrimental to the growth of the single crystal seed. At 1300°C abnormal grains were found to grow in the matrix, when these grains came into contact with the single crystal its growth was supressed. A lower temperature would slow the growth of the abnormal grains however this would result in slowing the growth of the single crystal as well. The authors of this study found 1300°C to be the best compromise and the crystal of 3mm x 3mm x 0.5mm dimensions was annealed at this temperature for 30 hours. This crystal however was not

without impurities, the crystal was translucent due to the presence of pores and island crystals. Suggestions presented in the paper to enhance the purity and size of the crystal produced were maximising the temperature used without promoting AGG in the polycrystalline matrix and to optimise the sintering conditions to produce very dense $BaTiO_3$ with small, close to uniformly sized grains.

$BaTiO_3$ single crystals measuring up to 1.5cm in size were produced by Yoo et al [15]. The method used here took advantage of the exaggerated grain growth of $BaTiO_3$, when a liquid phase is introduced to the matrix, by addition of SiO_2.The type of exaggerated grain growth used here was secondary abnormal grain growth (SAGG) or secondary recrystallization. This type of accelerated grain growth occurs after primary AGG is completed and the abnormal grains have impinged on one another, resulting in grain size being once again uniform [50]. In a paper previous to this Yoo, Kim and Kim [15] observed the effects of the presence of a liquid phase on the grain growth of $BaTiO_3$. For these experiments SiO_2 and TiO_2 were used to create the two liquid phases. Each of these additives was placed at the top of a $BaTiO_3$ compact, which already contained a small excess of TiO_2 (the Ba/Ti ratio was 0.999) and sintering was performed at 1350°C. It was found that the SiO_2, which forms a eutectic with $BaTiO_3$ at 1260°C, promoted the formation of twin lamellas in the top portion of the compact this then increased the rate of SAGG by what was deduced to be the twin plane re-entrant edge mechanism (TPRE). In contrast to this the addition of TiO_2 slowed exaggerated grain growth, as the temperature of 1350°C was reached, very soon after the microstructure appeared uniform. The microstructure of this sample remained uniform even when sintered for long periods. Yoo et al took advantage of the effects of SiO_2 addition in order to grow single crystals [51]. This was performed by again dropping a small amount SiO_2 on to the top of $BaTiO_3$ a compact. As SiO_2 was observed to promote the development of twin lamellae, using only a small amount meant that only a few grains containing lamellae would develop. These grains would then act as seeds without impinging on one another. Sintering was performed at 1370°C for up to 80 hours after which time crystals of 1.5cm were obtained. All the crystals produced were again not transparent due to the presence of pores.

Lee et al furthered the research undertaken by Yoo et al[15], [52]. As it is not necessary for SiO_2 to be present in $BaTiO_3$ in order for {111} double twins to form it only enhances formation, as stated previously. Lee et al found that these twins were present in lower quantities in $BaTiO_3$ and questioned the possibility of SAGG occurring by TPRE in pure $BaTiO_3$. This was then investigated by sintering $BaTiO_3$ at a range of temperatures for various times.

It was found that primary AGG was completed after sintering for 1 hour at 1355°C and when the $BaTiO_3$ sample was kept at this temperature for up to 50 hours no significant changes were observed. However, when the temperature was increased to 1360°C the onset of SAGG occurred. After 15 hours very large grains could be observed easily and after 50 hours the grains were approximately 1 cm in size. This effect was even more pronounced at a temperature of 1365°C and after sintering for 50 hours the structure became uniform consisting of only the grains affected by SAGG. At 1370°C these effects were still notable but not as pronounced as the effect at 1365°C and at even higher temperatures no evidence of SAGG was observed. This demonstrates the temperature dependence of SAGG. As a large percentage of the abnormal grains were found to have a {111} double twin it was deemed likely that TPRE was the cause of SAGG. At temperatures higher than 1370°C the grains were found to be rough and as such prevented SAGG occurring via TPRE and below 1360°C growth via TPRE, which occurs when material transfer is similar to 2-D nucleation, was negligible. Lee et al were then able to use the information gathered on SAGG in $BaTiO_3$ to produce single crystals. This was done using a two-step heat treatment. As no SAGG was observed in the first 5 hours of sintering at any temperature it was assumed that the nuclei of the grains that became abnormal after a longer period were formed in this time. As such the first heat treatment step consisted of heating to 1365°C for 1-3 hours to allow these nuclei to develop. As would be expected less nuclei developed after 1 hour than 3 hours. The second heat treatment step consisted of heating to 1355°C for 20 hours and then 100 hours. In this time the nuclei developed in the first stage of heat treatment grew and no further secondary abnormal grains developed. The grains continued to grow for the 100 hours and the length the heat treatment was used to dictate the size of the crystal. The size of the single crystal obtained was around 2cm. {111} double twins were however present in the single crystals grown by this method as would be expected. The optical quality of the crystals grown by this method appears better than the crystals presented by Yamomoto and Sakuma and Yoo et al [19], [51].

The work performed by Lee, Chung and Kang and furthered by Jung, Choi and Kang discussed previously has been of use in the production of $BaTiO_3$ single crystals. A study performed by Choi, Yoon and Kang in 2004 used a H_2 pre sinter in order to control grain growth in the matrix in conjunction with a seed crystal [45], [47], [53]. This was done by placing single crystals into $BaTiO_3$ powders prior to pressing. These compacts were then pre-sintered in a H_2 rich environment for 10 hours prior to sintering in air at 1350°C for 5, 20 or 50 hours. Crystal growth was said to be enabled in this environment, as the driving force of crystal

growth was in excess of a critical value; whilst grain growth is supressed due to a driving force smaller than a critical value. Growth of the crystal increased alongside sintering time. Different excesses of TiO_2 were used in the initial powder in order to evaluate the behaviour of the liquid phase. It was found that liquid film formed at the crystal/matrix boundary, the reason stated for this was build-up of TiO_2 segregate. The appearance of the liquid film was followed by thickening due to redistribution from triple junctions as the crystal grew. As would be expected the film was thinner at lower levels of TiO_2 excess and these lower levels correspond to greater crystal growth. After sintering for 50 hours the largest crystal that grew in length by 919µm was formed at 0.1 mol% excess TiO_2. At higher excesses of TiO_2, 0.4 mol% and 1 mol%, the crystals grew by 722 µm and 537 µm respectively.

This method of crystal growth has now been commercialised and the two step heat treatment method described by Lee et al in 1999 as well as the method described by Choi, Yoon and Kang are described in a patent assigned to Ceracomp [3], [16], [52], [54]. The patent also describes a variation on the original work of Lee et al where a seed crystal is embedded after the first heat treatment. The seed crystal will then grow and scavenge the matrix grains. The patent states that primary and secondary abnormal grain growth is determined by several factors including the ratio of Ba/Ti used, temperature and any additional substances present in the powder. The temperature required in the first stage of heat treatment can be reduced with addition of substance soluble in a $BaTiO_3$. Analogous to the work of Yoo et al [15], [51] such additives (for example SiO_2) can be used in specific areas to trigger the growth of secondary abnormal grains, at a lower temperature. Such grains then grow freely in the 2^{nd} heat treatment. For the methods described that take advantage of the seed crystal the patent states that the crystal can be placed onto a powder body or a polycrystal or placed into loose powder that is subsequently pressed. A temperature gradient is also said to be used and the temperature of the seed single crystal is kept higher than that of the polycrystal or an additive is placed at the seed/polycrystal interface to promote seed growth. The methods stated that use seed crystals rather than secondary grains have the advantage of allowing determination of crystal orientation as the seed crystal can be ground before placement and the resulting crystal will have the same orientation. As so many methods are described covering a lot of the work previously done on SSCG in $BaTiO_3$, it is unclear which method Ceracomp have utilised for commercialisation. As discussed previously a reproducible method of growing single crystals by SSCG is the objective of this study and would be a valuable alternative to other more costly crystal growth methods. For this to be

achieved many of the methods described in this section could be explored, especially as there is no method that poses more advantages than the others.

4.2 Barium Zirconate Titanate ($Ba(Zr_x,Ti_{1-x})O_3$

4.2.1 Previous investigations of grain growth behaviour in($Ba(Zr_x,Ti_{1-x})O_3$.

A study performed by Mahesh, Bhanu Prasaad and James investigated the effect of sintering temperature on the microstructure and electrical properties of $Ba(Zr_{0.85,}Ti_{0.15})O_3$. The prepared ceramics were sintered at temperatures ranging from 1350°C to 1450°C for 5 hours. The authors concluded that grain size increased with increasing sintering temperature due to enhanced grain boundary mobility. It was noted that at the sintering temperature of 1450°C grain boundaries were not as prominent in the micrographs the authors theorised that this was likely due to 1450°C being more than 90% of the melting temperature of BZT and that small areas around the grain boundaries had liquified during sintering. It was concluded that although grain size and density were increased with increasing temperature, this resulted in reduced piezoelectric properties and it was therefore suggested that 1350°C was the optimum sintering temperature [55]. A study performed by Sun et al came to the same conclusion after performing similar experiments on $Ba(Ti_{0.2},Zr_{0.8})O_3$. In these experiments samples were sintered for 4 hours at 1325°C, 1350°C, 1375°C and 1400°C. Average grain sizes in these ceramics were found to be 25µm, 30 µm, 47 µm, 70µm with size increasing with sintering temperature.

Experiments into the effect of sintering time on the resulting grain size in $Ba(Ti_{0.2},Zr_{0.8})O_3$ were performed by Cai et al. Here, samples were all sintered at 1350°C for 0.5, 2, 4 and 8 hours. Coarse microstructures were developed with grain size increasing with time were developed. Reported average grain sizes were 25µm, 40µm, 45µm and 80µm[56].

Investigations into the additions of various sintering aids to BZT have also been performed. One study performed by Zheng et al investigated the effects of CuO addition to $Ba(Zr_{0.0377},Ti_{0.9625})O_3$. Two samples were produced for these investigations one was pure $Ba(Zr_{0.0377},Ti_{0.9625})O_3$ and the other was $Ba(Zr_{0.0377},Ti_{0.9625})O_3$ with 1mol% CuO addition. The sample with no CuO additions was sintered at 1450°C for 2 hours in line with previous literature [57] and the sample containing 1 mol% CuO was sintered at 1300°C for 2 hours. The microstructure of the pure $Ba(Zr_{0.0377},Ti_{0.9625})O_3$ was found to display bimodal grain

growth with large grains having a size of ~45µm and small grains measuring 9µm. Whereas the CuO modified sample had a fine grained microstructure with average grain size of 2µm [58]. Another study continued this work and produced samples of $Ba(Zr_{0.05},Ti_{0.95})O_3$ with CuO additions ranging from 0 to 4 mol% CuO. Sintering was performed at temperatures ranging from 1200°C to 1350°C and the sample with no CuO addition was sintered at 1400°C only. This study found that when sintering at low temperatures with up to 0.2 mol% CuO addition, the microstructure was very fine grained and porous as the sintering process was incomplete. However, as CuO concentration was increased, denser ceramics were obtained. 4 mol% CuO addition produced very coarse grains that were of a similar size to grains in the 0% CuO sample that was sintered at 1400°C. The authors also noted that AGG occurred in the samples sintered at 1250°C and below, however at higher temperatures AGG was complete and these large grains had proliferated at the expense of all the smaller grains within the matrix [59].

4.2.2 Solid state crystal growth in $(Ba(Zr_x,Ti_{1-x})O_3)$

Rehrig et al have investigated SSCG in $Ba(Zr_x,Ti_{1-x})O_3$, various compositions were studied in these experiments where x = 0.04,0.05 or 0.085. 3 mol% excess TiO_2 was also added to each of these compositions in order to facilitate growth by the introduction of an intergranular liquid phase. Experiments began by sintering these compositions at 1300-1350°C for 2 hours. Grain sizes in the sintered pellets were then examined and found to be 15µm in the 4 and 5 mol% Zr samples and 25µm in the sample containing 8.5 mol% Zr. After this initial sintering one side of the pellets was polished and an (001) $BaTiO_3$ crystal seed was placed on top of the pellets with no pressure. The seed crystals and pellets were then annealed at 1350°C for 8 – 30 hours. Single crystal growth had occurred in all of the samples but details of only the 5 mol% Zr sample were included in the literature. In this sample, a single crystal with a maximum growth length of 825µm and a growth rate of 27.5µm/hr had grown. Matrix porosity had however been transferred to the crystal during growth. Figure 4.2 shows a micrograph of the grown crystal [57].

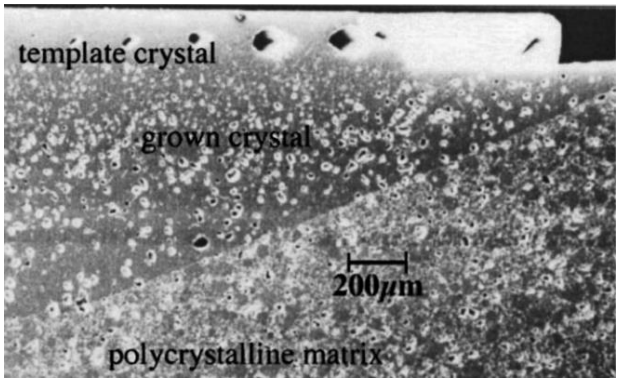

Figure 4. 2 A scanning electron micrograph showing a $BaTiO_3$ template crystal and a grown $Ba(Zr_{0.05},Ti_{0.95})O_3$ crystal. [57]

4.3 Barium calcium zirconate titanate ($Ba(Zr_{x,}Ti_{1-x})O_3$)

4.3.1 Previous investigations of grain growth behaviour in barium calcium zirconate titanate

Barium calcium zirconate titante (BCTZ) is a promising alternative to lead based ceramics. Lui and Ren discovered that $(Ba_{0.85}Ca_{0.15})(Ti_{0.90}Zr_{0.10})O_3$ had a high d_{33} of ~620 pC/N in 2009 [60]. Since then there has been an expanding amount of research into this material, although much of this research is focused on studying the effect of varying composition on piezoelectric properties [22], [61]. There is currently much less literature regarding the microstructure and grain growth of this material.

Sun et al conducted a study looking at the correlation between grain size and piezoelectric properties in $(Ba_{0.85}Ca_{0.15})(Ti_{0.90}Zr_{0.10})O_3$ [62]. Experiments were conducted over a range of sintering temperatures from 1320°C to 1560°C, the researchers also varied the sintering times at both 1360°C and 1480°C. It was found that samples had decreased density with visible porosity and small grain size in SEM images when sintering temperatures were below 1400°C. The grain size and density increased with increasing sintering temperature up to 1480°C, at this temperature average grain size was 20.57μm this then decreased with further increase in temperature down to 17.81μm at 1560°C. This decrease in grain size was theorised to be due to the appearance of a small amount of second phase that appeared in the XRD spectra at sintering temperatures over 1520°. The authors then chose to investigate the effects of sintering time on the microstructure, they chose to carry out these further experiments at 1360°C and 1480°C. The average grain size in the samples sintered at 1360°C

were found to steadily increase from 8.91µm to 18.38µm at sintering times of 2 hours and 22 hours respectively. However, at 1480°C there was no obvious increase in grain size with increasing time. The aforementioned secondary phase was also reported when dwell time was increased above 8 hours in the samples sintered at 1360°C and 16 hours for the samples sintered at 1480°C.

In contrast to the reports of Sun et al, an earlier investigation performed by Wu et al found that the optimal sintering temperature for $(Ba_{0.85}Ca_{0.15})(Ti_{0.90}Zr_{0.10})O_3$ ceramics was 1440°C [63]. In these experiments samples were sintered for 2 hours at temperatures ranging from 1300°C to 1500°C. Wu et al found that the samples sintered at 1440°C displayed improved piezoelectric properties whereas Sun et al found that the sintering temperature of 1480°C produced ceramics with the best properties. Both papers attributed the enhanced electrical properties to the increased density and grain size in their respective samples. Wu et al stated that grain size increased with increasing sintering temperature from 5.2µm to 20.1µm, with the largest average grain size reported at 1410°C after which there is a small decrease in average grain size with increasing temperature to slightly under 20µm. The increase in piezoelectric properties in the samples sintered at 1440°C was due to these samples displaying peak splitting, in the XRD results, of the peak corresponding to ~45° 2θ this signifies the presence of an MPB between the tetragonal and rhombohedral phases.

A third study [23] into the effects of sintering and microstructure on the piezoelectric properties of $(Ba_{0.85}Ca_{0.15})(Ti_{0.90}Zr_{0.10})O_3$ reports a larger d_{33} of 650 pC/N, compared to the two previously mentioned articles which reported d_{33} measurements of 416 pC/N [62] and 442 pC/N [63]. This large d_{33} occurred in ceramics sintered at 1540°C and made from powders calcined at 1300°C. These experiments investigated the effects of different calcining temperatures on grain growth and found that grain growth was promoted with increasing calcination temperature due to a narrowing of the grain boundary. These effects were reported to be small but grain size measurements were not given. Sintering was performed at temperatures ranging from 1500°C to 1550°C for 2 hours. Average grain size was said to increase with increasing temperatures, although measurements were only given for the samples calcined at 1200°C. These averages sizes have a maximum of ~14.5µm so are smaller than those reported at lower sintering temperature at the same calcination temperature.

Due to the addition of zirconia the sintering temperature of BCTZ is significantly higher than that of barium titanate and temperatures of above 1400°C are needed for effective sintering. This has led to research into sintering aids and thus some studies reporting their effects on

the microstructure are available. In one such study performed by Shin and Yu [64], ZnO was added to $(Ba_{0.85}Ca_{0.15})(Ti_{0.919}Zr_{0.085})O_3$ in amounts ranging from 0 – 0.4 wt%. These ceramics were sintered for 5 hours at 1360°C. Results stated that grain size increased with ZnO addition up to 0.2 wt% and then decreased with further addition. The largest reported average grain size in these experiments was 2.09µm. This grain size also corresponds to the best piezoelectric properties of the samples produced in this study. It is fairly small compared to the literature discussed previously, which is likely due to the low sintering temperature. However, the density was improved with increasing ZnO content and porosity was reduced suggesting that ZnO is a viable sintering aid in BCTZ.

Other experiments have been performed by Lee et al [65], for these SiO_2 was added to $(Ba_{0.96}Ca_{0.04})(Ti_{0.85}Zr_{0.15})O_3$. As described earlier SiO_2 has been shown to encourage grain growth in $BaTiO_3$ due to the formation of a eutectic liquid at 1260°C. The addition of SiO_2 was found to reduce the feasible sintering temperature to 1220°C in a reducing atmosphere which was followed by annealing at 1000°C. Various concentrations of SiO_2 were used ranging from 0.075 mol % up to 3 mol %. The results showed that when the amount of SiO_2 increased above 1% there was a detectable $BaTiSiO_5$ second phase. The grain size increased with SiO_2 concentration and there was a notable difference between the sample with no SiO_2 and just 0.15 mol %. The pure BCTZ sample was very porous and ineffectively sintered. With increasing amounts of SiO_2 grain size was significantly increased from 3µm in the sample containing 0.3 mol% to 21µm in the 5 mol % sample. No bimodal grain growth was reported in this study this could be due to being sintered in a reducing atmosphere as described earlier for $BaTiO_3$.

It has been demonstrated by Chen et al [66] that CuO is also an effective sintering aid in $(Ba_{0.85}Ca_{0.15})(Ti_{0.90}Zr_{0.10})O_3$ ceramics. Average grain size was increased from ~9µm to ~17µm with increasing amounts of CuO (from 0 mol % to 3 mol%) when sintered at 1400°C for 2 hours. This is due to the addition of CuO leading to the development of a small amount of liquid phase which as discussed previously accelerates grain growth. Larger grain sizes, in the samples containing 0.5 mol % CuO, could be obtained by increasing the sintering temperature up to 1500°C or increasing the sintering time up to 6 hours. Unfortunately no average grain size measurements were reported for the further sintering time and temperature experiments as the study was primarily focused on optimising the d_{33} and other electrical properties alongside reducing sintering temperature. The authors found that d_{33} and other electrical properties were reduced with increasing CuO and increased with

temperature and dwell time. However, if a reduction in sintering temperature is necessary, a trade-off of sorts can be made as good piezoelectric properties (e.g. a d_{33} of 403 pC/N) were displayed with a CuO concentration of 0.5 mol%, sintered at 1400°C with an increased sintering time of 6 hours.

4.4 Lead zirconate titanate ($Pb(Zr_{(1-x)}Ti_{(x)})O_3$)

4.4.1 Previous investigations of grain growth behaviour in ($Pb(Zr_{(1-x)}Ti_{(x)})O_3$)

Liquid phase sintering is known to be an important factor in SSCG and the addition of excess PbO is known to provide this intergranular liquid phase. A study performed by Kingon and Clark [67] investigated the effects of this liquid phase on the sintering and densification in $Pb(Zr_{0.525}Ti_{0.475})O_3$. PbO addition ranged from 19mol% excess down to 1.6 mol% deficiency. Excess PbO was found to accelerate grain growth and densification in the initial stages of sintering ~4mins at 1200°C. Longer sintering times however showed that the grain growth rate of the samples containing large amounts of excess PbO (19mol%) were slower than the samples that were PbO deficient. It was hypothesised that this initial increase in grain size was due to the solution-precipitation mechanism described in chapter 1. As discussed previously, larger amounts of intergranular liquid phase can itself become rate limiting, as transfer through the liquid film is slowed which could be the case in this example.

Due to the volatility of PbO, measures need to be taken during sintering of PZT to maintain composition and density, these include but aren't limited to the use of atmosphere powder, crucible arrangement and the addition of excess PbO into the initial powders as discussed by Kingon and Clark. Due to this research groups have investigated ways to reduce the sintering temperature of PZT. One such experiment performed by Wittmer and Buchanan in 1981 [68] used V_2O_5 as a sintering aid. V_2O_5 was introduced in quantities ranging from 0.1 to 6 wt%. This was done by introducing the V_2O_5 both before and after calcination. For pre calcination additions, calcining temperature was reduced to prevent sintering from 800°C down to 550°C. There was a notable change in the microstructure when additions were made pre-calcine with the appearance of bimodal grain distribution and an overall smaller grain size. This was due to the reduced calcination temperature causing the initial particle size to be reduced and because V^{4+} would have diffused into the lattice upon calcination causing a reduction of the V_2O_5 available to form an intergranular liquid phase and thus reducing grain size. Both pre and post calcine addition did however cause average grain size to be increased at a lower temperature when compared to stoichiometric PZT. For example, for the sample

with a post calcine V_2O_5 addition of 0.25% sintered at 960°C grain size was found to be ~6.5µm, whereas stoichiometric PZT sintered at 1100°C for the same time (4 hours) average grain size was reduced to ~2µm. Grain size was found to decrease with increased V_2O_5 (>0.25 wt%) especially for the samples where the addition was made before calcination. Rate of grain growth was accelerated with post calcination addition of V_2O_5 when compared to the pure PZT samples. These investigations demonstrate that V_2O_5 could be used to introduce an intergranular liquid that could promote the growth of a seed single crystal in SSCG experiments.

In 2006 Kim et al [69] performed investigations into the grain growth of PZT, in the hope that AGG could be enhanced to enable the possibility of PZT single crystal growth via the solid state. This crystal growth would theoretically be performed via a similar method to that used by Yoo et al in $BaTiO_3$. For these experiments $Pb(Zr_{0.53}Ti_{0.47})O_3$ was used alone and with additives of 7mol% excess PbO, 7 mol % PbO with 0.7 mol% MgO and finally 7 mol% excess PbO with both 0.7 mol% MgO and 2 mol% SiO_2. All of these compositions were prepared by sintering at 1200°C for 1hour. The pure PZT displayed a finely grained microstructure with uniform average grain size of 2µm grains. The ceramics containing MgO and excess PbO displayed a larger grain size (14.3µm). The grains in this sample were also all faceted and angular, which as discussed previously for $BaTiO_3$, is known to encourage grain growth and thus AGG when only a few grains display this structure. As SiO_2 is known to encourage twin grain formation in some grains in $BaTiO_3$ the authors then added SiO_2 as well as MgO and excess PbO. The SiO_2 addition caused large abnormal twinned grains to form in PZT, this was due to the twinned structure of these grains providing “steps” at which nucleation can take place as discussed for $BaTiO_3$. These large grains were found to be up to 100µm in size and had the structure of so called penetration twins. If solid state crystal growth was successfully performed using SiO_2 to provide large grains the resulting twins would be difficult to separate. The formation of abnormal grains in PZT is however promising demonstrating that conditions could be provided that allow for accelerated growth, a seed crystal would however be preferable to large twinned grains.

4.5 Other Materials

4.5.1 PMN-PT ($Pb(Mn_{1/3}Nb_{2/3})O_3$-$PbTiO_3$)

Due to the current expensive growth methods (Bridgman and flux methods) and the strong piezoelectric properties displayed by PMN-PT, discussed previously, there is interest in developing alternative growth methods for this material. Ceracomp is currently producing PMN-PT single crystals via SSCG [40] demonstrating that it is very possible although again there is not a clear, reproducible method available, which produces crystals of a usable size and quality.

In 1999 Khan et al [70] succeeded in growing PMN-35PT (35 mol% PT) single crystals using a seed crystal and $PbZrO_3$ atmosphere powder. Unlike barium titanate, which has no volatile components, suitable conditions for controlling the loss, of PbO, from PMN-PT must be devised and a suitable atmosphere powder used. Experiments were also performed using an atmosphere powder of the same composition, but these were less successful. It was found that maximum growth occurred in the <111> direction (1.4mm). The $PbZrO_3$ powder is thought to have enhanced growth of the seed crystal by enhancing PbO absorption from the vapour phase, formed due the atmosphere powder. $PbZrO_3$ increased the vapour pressure in the surrounding atmosphere more effectively than PMN-35PT powder. This had the effect of creating a liquid PbO phase between boundaries, which in turn enhances exaggerated growth of the seed crystal by solute segregation as was discussed in relation to barium titanate with excess TiO_2. However, the excess PbO observed was found to be responsible for inclusions in the crystal.

King et al presented a study into the kinetics of PMN-35PT single crystals grown by SSCG in 2003 [71]. This work looked closely at the effects of a PbO liquid phase. In order to find an optimum amount of PbO excess that would aid in growth of the seed crystal, King et al used a range of additions from 0 – 5 vol% PbO. The additions were this time mixed into the PMN-35PT powders. It was found that when a small amount (1.5 vol%) of PbO was added the growth rate of the single crystal is substantially increased where and its growth constant is increased to ~100 times larger than the growth constant of the matrix grains. The magnitude difference between the growth constants is reported to be due to the seed crystal being a much larger size than the smaller grains. However, one issue with this is that if AGG is allowed and large grains can freely grow in the matrix their growth constants will also increase until it is comparable with that of the seed crystal. It was found that crystal growth increased in

rate with addition of PbO up to 3 vol% displaying liquid phase enhanced grain growth; the growth rate is limited by atom diffusion through the liquid film. At higher volumes of PbO growth rate of the single crystal began to slow. This slowing of growth was more distinct in the matrix grains than the single crystal. The authors concluded that the growth mechanisms changed above this point and that single crystal growth became interface reaction controlled and the grain growth in the matrix appeared to be diffusion controlled with the liquid layer too large for fast diffusion.

Another study into SSCG of PMN-35PT was performed by Kim et al In 2006 [72]. This study used Li_2O as a dopant as well as varying the amounts of PbO excess, with the hope of promoting the growth of the seed crystal whilst restricting AGG in the bulk. The additions used were 8 mol% PbO, 7mol % PbO with 1 mol% Li_2O, 6mol % PbO with 2 mol% Li_2O and 4mol % PbO with 4 mol% Li_2O. It was found these compositions displayed different types of grain growth with AGG initially increasing in the sample with 7mol % PbO and 1 mol% Li_2O. However, this behaviour varied substantially with the 6mol % PbO and 2 mol% Li_2O sample which displayed less AGG than the samples including a higher mol% PbO excess. The sample with 4mol % PbO and Li_2O displayed no AGG. Temperature effects were also studied and the prevalence of AGG in the various samples. It was found that for the sample containing 8mol % PbO and the sample containing 7mol % PbO with 1 mol% Li_2O the amount of AGG observed increased alongside sintering temperature. However, for the sample with 6 mol % PbO and 2 mol% Li_2O AGG actually decreased. The final sample with 4mol % PbO and Li_2O displayed no AGG at any of the three temperatures (1000^{o}C, 1100^{o}C or 1200^{o}C). In the latter sample however, all grains were much coarser when sintering at 1200^{o}C. SSCG was then performed using a barium titanate seed crystal embedded in polycrystals of PMN-35PT with the same additions of PbO and Li_2O, used in the previous experiment. It was found that the seed crystal grew significantly in the sample containing 6 mol % PbO and 2 mol% Li_2O. This was reported to be due to the reduction of AGG in the matrix however the seed crystal did not grow significantly in the sample containing the most Li_2O even though no abnormal grains were observed. This was thought to be due to the increased amount of coarsening in the matrix and has previously been observed when grains are mainly rough and spherical. In the two systems with the largest amounts of PbO the seed crystal did grow but AGG was prevalent in the matrix. With the seed crystal being impinged upon in the sample containing additions of 7mol % PbO and 1 mol% Li_2O. This is in agreement with the initial grain growth experiments where the maximum amount of AGG was observed in this sample. In addition to this Kim et al investigated the effects of dislocations on the seed crystal surface. These

dislocations increased the rate of growth of the seed crystal by providing attachment sites. The dislocations were produced either by grinding or heat treatment. Grinding produced the larger number of dislocations and thus the seed crystal grew at a higher rate. This study displays the various ways in which growth of the seed crystal can be accelerated and microstructural control can be gained.

Another study into the growing 70PMN-30PT crystals performed by Yamada (2006) [73] introduced a liquid PbO layer between the seed crystal and the polycrystal and hypothesised that this enabled crystal growth by an Oswald ripening mechanism. There was no excess PbO in the bulk ceramic as PbO liquid is associated with abnormal grain growth. The author heated the ceramics in air to 800°C before sintering in pure O_2 at 1000°C - 1050°C and finally using a hot isotactic press in an Ar-O_2 atmosphere at 1000°C for 2 hours before applying the seed crystal. This method produced a high density and minimised AGG. These experiments were successful in producing single crystals of a few millimetres in size. Further examination of the crystals via permittivity measurements found them to be comparable to crystals produced using the Bridgman method [74].

4.5.2 Potassium sodium niobate ($(K_{0.5}Na_{0.5})NbO_3$)

Fisher et al performed SSCG experiments on $(K_{0.5}Na_{0.5})NbO_3$ or KNN in 2007 [75]. They performed these experiments using a $KTaO_3$ crystal seed that was pressed into the KNN powder. $K_4CuNb_8O_{32}$ was used as a sintering aid and to introduce a small amount of intergranular liquid phase. The first sample was then sintered for 10 hours at 1100°C. Growth of the seed crystal had occurred with a maximum growth length observed of 160µm. However, a large amount of porosity was visible in the SEM images. It was concluded that the porosity was due to growth of the crystal boundary occurring a faster rate than densification causing the pores to become entrapped within the crystal, as discussed in chapter 1. A second experiment was performed with the sample being prepared in the same way except hot pressing was performed before sintering. Hot pressing was performed at 1025°C and pressure was maintained at 50MPa.The maximum growth length of this crystal was reduced significantly (35µm). As expected, there was a reduction in porosity, although there were still some smaller pores present. In 2008 the authors continued with this research and grew two more KNN single crystals via the SSCG method. One of these crystals was grown in a box furnace at 1100°C for 100 hours without being hot-pressed. The resulting

crystal has a maximum growth length of 1650µm but again was very porous. The second crystal was grown entirely in a hot press using a two-step regime. Initially the sample was hot pressed at 975°C and 50MPa for 2 hours to allow densification prior to single crystal growth. The second step included a maintained pressure of 50MPa but had an increased temperature of 1100°C for 100 hours. The maximum growth of this crystal was 1890µm. There was still a small amount of porosity present although this was much improved. A drawback of this method is that AGG of the matrix grains had occurred in the hot-pressed sample. Some of these grains were 1000µm in size and had impinged upon the growing single crystal and prevented further growth. A comparison of the crystals grown in these studies can be seen in Figure 4.3.

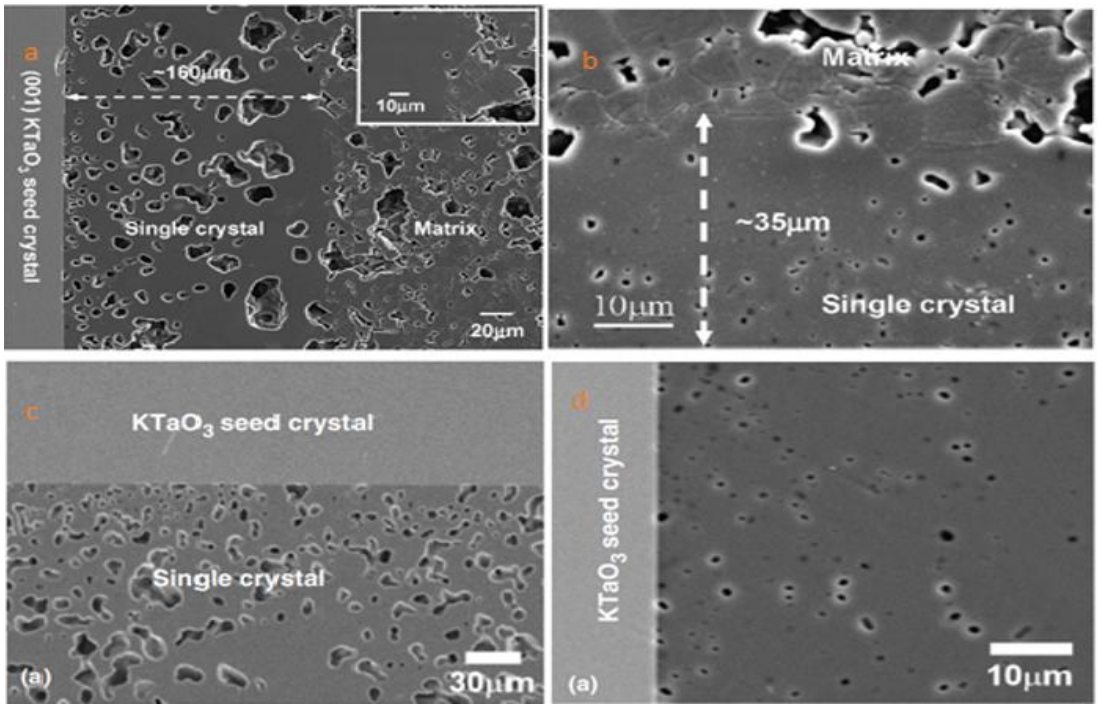

Figure 4. 3 SEM secondary electron images showing the various KNN single crystals grown by Fisher et al. (a) shows the sample sintered for 10 hours with no hot press treatment. (b) shows the sample sintered for 10 hours that had undergone hot-pressing [75].

4.6 Conclusions

This research aims to develop a reproducible method of growing single crystals via the solid state. From the literature it can be concluded that this is possible although there are various issues that will need to be overcome. Firstly, grain growth in the matrix must be controlled to allow a single crystal to grow without impingement. Secondly conditions that allow growth of a seed crystal must be maintained in order to allow single crystals to grow at an appreciable rate. Problems with porosity have also been highlighted and this work attempts to outline a solution by studying the effects of hot-pressing and varying composition on the single crystals obtained.

The presence of intergranular liquid phase has been concluded to be an important factor in SSCG therefore this work will investigate different sintering aids and additives and their effects on grain and single crystal growth as well as the absence of any liquid phase. Temperature and time effects on grain growth will also be studied in various materials in order to achieve conditions where single crystal growth is possible. Dopants known to reduce grain growth will be investigated and used to prevent AGG in the matrix grains.

As there is a large amount of literature available regarding grain growth in $BaTiO_3$, as well as several studies demonstrating that SSCG is possible, $BaTiO_3$ was chosen as the initial material for these investigations. As mentioned previously the presence of a BaO-TiO_2 eutectic makes the addition of varying amounts of liquid phase relatively simple. $BaTiO_3$ also has the additional benefit of having no volatile components making the lengthy sintering much easier than some of the other materials mentioned.

Chapter 5 Experimental Procedures

5.1 Sample Preparation

All powder samples were prepared using the traditional mixed oxide method. This method was used as it is relatively simple and both cost and time efficient. Other methods of producing higher purity ceramics exist however they are more expensive and timely, especially to produce large batches, therefore any results from these experiments may not be easily reproduced in an industrial setting [12]. Commercially available raw materials were used, these can be viewed in Table 5.1.

Table 5. 1 Showing a list of the raw materials used in this work

Reagent	Source and purity
$BaCO_3$	Alfa Aesar (99%)
TiO_2	Sigma-Aldrich (99.9%)
Nb_2O_5	Sigma-Aldrich (99.9%)
ZrO_2	Sigma-Aldrich (99%)
$CaCO_3$	Sigma-Aldrich (99%)
SiO_2	Sigma-Aldrich (99.5%)
ZnO	Sigma-Aldrich (99.9%)

5.1.1 Drying and Weighing

The raw materials mentioned in the previous section were dried initially in a drying oven at 150°C for at least 24 hours to ensure that any water absorbed from the atmosphere was removed prior to weighing.

Powders were then weighed according to the desired stoichiometry of the products and placed into a high-density polyethylene bottle. Weighing boats were rinsed into the bottle using isopropyl alcohol (IPA) to ensure all of the starting material required was transferred to the bottle.

5.1.2 Ball Milling

Ball milling is necessary in order to thoroughly mix the raw materials and create a homogenous mixture of uniform particle size. In order to ball mill 9mm yttrium- stabilised zirconia milling media were added to a container along with IPA and the starting materials. The mixture produced had a similar viscosity and appearance to double cream and milling was ensured by monitoring the bottle on the ball mill, checking for cascading milling media and ensuring that at no time were the milling media immobile at the bottom of the bottle. The bottle was placed on the ball mill for 24 hours and removed immediately prior to drying.

5.1.3 Drying and Sieving

After ball milling was complete, the bottle was removed and the contents drained into a container using a colander. The beads were moved and washed with IPA in order to ensure that most of the starting materials were recovered. After this the mixture was dried using a Kenwood KMO80. The Kenwood was initially heated to just under 90°C whilst continually stirring to remove much of the IPA. When the mixture became the consistency of a paste the temperature was lowered to 55°C. When the IPA was fully removed, the starting materials were transferred into a pre-weighed glass beaker and weighed again.

The powder was then sieved using 300µm mesh before being transferred into an alumina crucible. The sieving step ensures that any powder agglomerations were removed prior to the calcination step.

5.1.4 Calcination

The starting materials and alumina crucible were then placed in a conventional box furnace and heated to a temperature that will allow the solid state reaction to take place but not so high that subsequent ball-milling and sieving became too difficult. Initially, upon heating any volatile components such as CO_2 and other volatile impurities are lost from the mixture and the remaining materials react to form the desired products. As a consequence of this reaction and loss of the volatile starting materials, volume loss is evident upon removal of the

crucible. All of the compositions produced were heated at a rate of 300°C/hour and held for 4 hours to allow the reagents to react. The calcination temperatures used for each material produced are shown below in Table 5.2.

Table 5. 2 Showing the different materials produced and their calcination temperatures.

Final Product	Calcination Temperature °C
$BaTiO_3$	1100
$Ba(Ti_x,Nb_{1-x})O_3$	1100
$(Ba_x,Ca_{1-x})(Ti_y,Zr_{1-y})O_3$	1250
$Ba(Ti_x,Zr_{1-x})O_3$	1150

5.1.5 Pressing and Sintering

After the powder samples had been removed from the furnace they were weighed and ball-milled again with IPA, this time including 2% PVA binder (by weight). After ball-milling was complete, the powder was dried and sieved as described in section 5.1.3. The final powder product was then transferred into a container for storage.

In order to produce sample pellets approximately 0.75g of powder was weighed and transferred to a 10mm pressing die. Uniaxial pressing at 1 tonne for 20 seconds was then performed in order to obtain green pellets. The added binder ensures that the green pellets do not crumble apart after pressing.

The green pellets were then placed on a zirconia tile and covered with an alumina crucible before being placed into a box furnace for sintering. Sintering regimes vary throughout this project but all samples were heated at a rate of 50°C/hour up to 550°C and then held for 4 hours, this ensures complete removal of the binder prior to sintering. The samples were then heated at 300°C an hour up to their sample specific sintering temperature and held for a specified time. The samples were all then cooled to room temperature at a maximum rate of 300°C/hour. During sintering grain growth occurs and subsequent densification as pores close. The grain size of a piezoelectric can affect its properties; when grains are too small and sufficient sintering has not been performed the ferroelectric polarisation is reduced. However, if the ceramic has been sintered for too long or at too high of a temperature SAGG can occur which lead to pores developing and growing which means reduced permittivity

and can cause issues when poling [12]. Various sintering regimes using different times and temperatures were performed throughout this project in order to determine the best conditions for SSCG to occur in the various samples prepared and will be discussed in greater detail in the following chapters.

5.1.6 Solid State Crystal Growth Experiments

In order to perform SSCG experiments 001 $BaTiO_3$ single crystals with 1 side polished were obtained from MaTeck. These seeds were 10mm x 10mm x 1mm therefore they were cut into 9 sections prior to crystal growth experiments. Initial cutting was done using a diamond scribe, however, this led to some breakage and unevenly cut pieces. A precision cutter (Struers Accotom-5) was subsequently used. Prior to cutting, crystals were mounted onto an aluminium substrate. The blade speed used was 3000rpm and the feed was 0.025mm/s.

The seed crystal was then thoroughly cleaned and placed into a 10mm pressing die and covered with the desired powder composition before sintering.

After sintering pellets were examined using optical microscopy and then cut using the Accutom into quarters. This was done so that cross sections of the sample could be viewed using optical and scanning electron microscopy. Figure 5.1 illustrates how cross sections were obtained in order to examine any crystal growth that may have occurred. The cross sections of these samples were held face side down with clips before setting in resin ready to be polished.

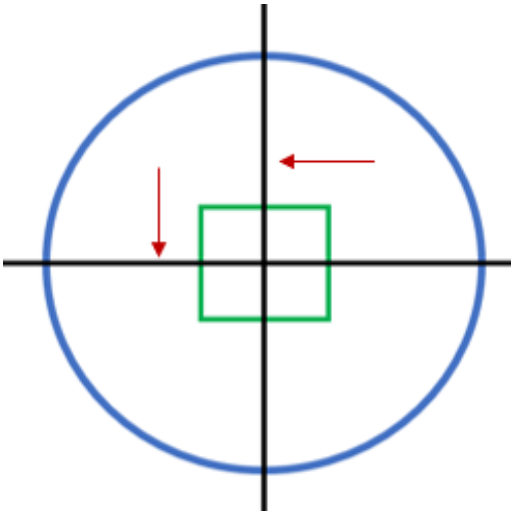

Figure 5. 1 A schematic showing the pellet (blue), crystal seed (green) and the cutting directions used to obtain cross sections. The red arrows show the faces examined by microscopy.

5.1.6 Grinding and polishing

In order to prepare the samples for optical microscopy and scanning electron microscopy (SEM) samples were ground and polished, this ensured that any grain structure or single crystal growth could be visualised easily. Samples were placed individually into pots and then a mixture of Epothin 2 epoxy resin and hardener (obtained from Buehler) was poured on top, to ensure the side of the sample to be examined would be exposed. The pots were left overnight to set and then the resin containing the pellet was removed. The pellet and surrounding resin was then ground in accordance with the instructions in Table 5.2, this ensured that the surface was level and there was no epoxy resin obscuring the underside of the pellet. The resin and pellets were then polished via the route displayed in Table 5.2. After polishing, pellets displayed a mirror like finish. After polishing pellets were ready to be examined by microscopy.

Table 5. 3 Polishing route and products as recommended by Buehler.

Step	Surface	Abrasive	Lubricant	Force (per sample)	Time (min:sec)	Platen speed (rpm)	Head speed (rpm)	Relative rotation
1	SiC	P600/P400	Water	4lbs	Until plane 0.40	150	60	Comp
2	TexMet P	9µm MetaDi supreme		4lbs	5.00	150	60	Contra
3	TexMet P	3µm MetaDi supreme		4lbs	5.00	150	60	Comp
4	TriDent	1µm MetaDi supreme		4lbs	3.00	150	60	Comp
5	ChemoMet	MasterMet colloidal silica		4lbs	1.20	100	60	Contra

5.2 Characterisation Techniques

5.2.1 X-Ray Diffraction

X-ray diffraction (XRD) is an important technique when analysing ceramic materials. It can be used to determine structure, composition and identify any impurities that are present in detectable quantities (> 1 wt.%). XRD works by firstly producing a collimated X-ray beam in a cathode ray tube. This is done using a heated filament which provides electrons that are then focused towards a target material. The X-ray diffractometers used in this case both use copper as the target material. When the electrons have built up enough energy, inner shell electrons are lost from the target material. The loss of an inner shell electron from an atom causes an electron from another shell, of higher energy, to fill the vacancy. As the electron drops to the lower energy shell an X-ray photon is emitted with energy equal to the difference in energy between the shells. The X-rays produced have wavelengths characteristic of the target material (copper) and are composed of Kα and Kβ x-rays. Kα X-rays comprise of two wavelengths $K\alpha_1$ and $K\alpha_2$. Monochromators can be used to produce an incident beam with a narrower range of wavelengths. Broad band and narrow band monochromators can be used so only Kα or $K\alpha_1$, respectively, are allowed to be incident on the sample. The X-rays produced are collimated and the beam is focused at the sample. Some x-rays are reflected back from the surface of the sample and others penetrate the sample and are reflected back by the various planes of atoms described by miller indices (hkl). When

Braggs law is satisfied the X-rays reflected back from successive planes are in phase with each other therefore a peak in intensity occurs. Bragg's law is show below (Eq 5.2.1) where λ is the wavelength of the X-rays, θ is the angle at which the X-rays impinge on the sample and d is the spacing between the planes of atoms [8], [76].

$$\lambda = 2\, d\, sin\, \theta \tag{5.2.1}$$

Structure of the samples produced was determined by examining peak splitting. For example if a substance has cubic structure and the unit cell axes and angles are equal (a=b=c and α = β = γ= 90°) then no peak splitting would be observed. At room temperature $BaTiO_3$ is known to have a tetragonal structure, as a tetragonal unit cell is elongated along its c axis the unit cell axes are no longer equal (a = b ≠ c). Due to the unequal axes peak splitting is observed between the 001 and 100 peaks, the 110 and 011 peaks and the 200 and 002 peaks. Often this splitting is easier to observe between the 200 and 002 peaks due to the smaller d spacing between these planes leading to the peaks being separated by a high angle 2θ. If the structure were orthorhombic (a ≠b ≠ c) this would be evident by the splitting of the same peaks as the tetragonal unit cell however as triplets displaying the additional 010, 101 and 020 peaks. In a rhombohedral unit cell the axes are of equal length however the angles no longer equal to 90° (α = β = γ ≠ 90°) due to elongation across the body diagonal. These changes cause XRD spectra to display the 110 and 011 peaks as a doublet and splitting of the 111 peak.

A D8 Bruker diffractometer or a PANaylitical X'Pert diffractometer were used for analysis of sintered pellets. Both of these diffractometers use CuKα radiations and use Bragg-Brentano geometry.

5.2.2 Optical Microscopy

Optical microscopy was used in order to check that the microstructure was easily visualised after polishing. Due to the lower magnification, compared to SEM, this technique was also useful for measuring any crystal growth that had occurred during the SSCG experiments.

Optical microscopy uses a system of convex lenses to produce a magnified image. Dark field illumination or polarised light can be used; both of which can make surface features such as

pores and scratches more apparent by increasing contrast between these features and the rest of the surface [77].

For analysis at low magnification a Motic SMZ-168 stereo microscope was used. For higher magnification images the microscope used was an Olympus BX51.

5.2.3 Scanning Electron Microscopy

Scanning Electron Microscopy (SEM) was also used to optically view the pellets. A greater degree of magnification can be achieved using SEM therefore more details in surface topography can be seen. This greater degree of magnification is due to an electron beam having a shorter wavelength than the visible light used in optical microscopy. In order to produce an image, a scanning electron microscope accelerates an electron beam at the sample, this beam continuously moves across the sample to gain a complete image. The electrons fired at the sample are known as primary electrons when these electrons interact with the sample secondary electrons are released. The secondary electrons are then detected using a positively charged secondary electron detector and thus an image is produced. As explained in the previous chapter when an electron is released from an atom an X-ray photon is also released. These X-rays are characteristic of the element they were produced by meaning they can be used for determination of elemental composition using energy dispersive X-ray spectroscopy (EDX). Back scattered electrons are also produced via elastic collisions between the primary electrons and atoms in the sample, these electrons can be detected using a backscattered electron detector. These backscattered electrons can be used to view larger atoms with a greater atomic number as they incur more of such collisions. As elements with a larger atomic number produce a stronger signal they can be viewed as bright areas on images produced by backscattered electron detectors. This can be useful in detecting a titanium or barium containing second phase between grain boundaries [8], [78].

SEM images were used to determine average grain size of the prepared ceramics. This was performed using the linear intercept method. In this method a line of known length is drawn across the micrograph and each occurrence of grain boundaries intercepting the line is counted. The length of the line is then divided by the number of interceptions and multiplied by a proportionality constant. A proportionality constant of 1.56 was proposed by

Mendelson in 1969 to account for grains being larger than can be seen via microscopy. This size difference is due to surrounding grains overlapping and obscuring part of the truncated octahedron shaped grains [79]. This was repeated using various lines across several parts of the microstructure and an average calculated.

The scanning electron microscope used for analysis in this case was a Hitachi SU8230 CFEG SEM (cold-field emission gun scanning electron microscope). The detectors used for secondary electrons were the upper and lower secondary electron detectors (SE(U) and SE(L)) and a plate detector for back scattered electrons (PDBSE). All samples were coated using with iridium prior to SEM and carbon paint was used to provide a path across the epoxy resin.

Chapter 6 Results and Discussion

6.1 $BaTiO_3$

6.1.1 X-ray Diffraction of $BaTiO_3$

After sintering for 2 hours both at 1300°C and 1340°C, the pellets were all analysed using a PANaylitical X'Pert diffractometer with scans ranging from 10 to 90° 2θ with a step size of 0.033 at a rate of 0.5s/step.

As mentioned in Chapter 5, XRD was used to determine the structure and which, if any, second phases were present. All of the spectra were matched to the ICDD (The International Centre of Diffraction Data) file for tetragonal $BaTiO_3$ using search match software.

Figure 6.1 shows the spectra corresponding to the pellets sintered at 1300°C. It can be seen that the XRD spectra all correspond to a tetragonal structure. Although the 002 peak is clearly visible in all the scans and the 111 peak is a well-defined singlet in all of the spectra ruling out the possibility of rhombohedral structure. Also, no triplets are observed in the positions mentioned previously that would point to an orthorhombic structure. Hence from the XRD patterns of the powders it can be confirmed that barium titanate with the tetragonal structure expected at room temperature, was produced. The peak positions and splitting correspond with tetragonal $BaTiO_3$. However, the 200 and 002 peaks in Figure 6.1 do not all display the 2:1 ratio expected in the spectra of a randomly orientated sample. This is deemed

to be due to preferred orientation along the surface of the pellet, this can be caused by domain switching during grinding the samples prior to XRD.

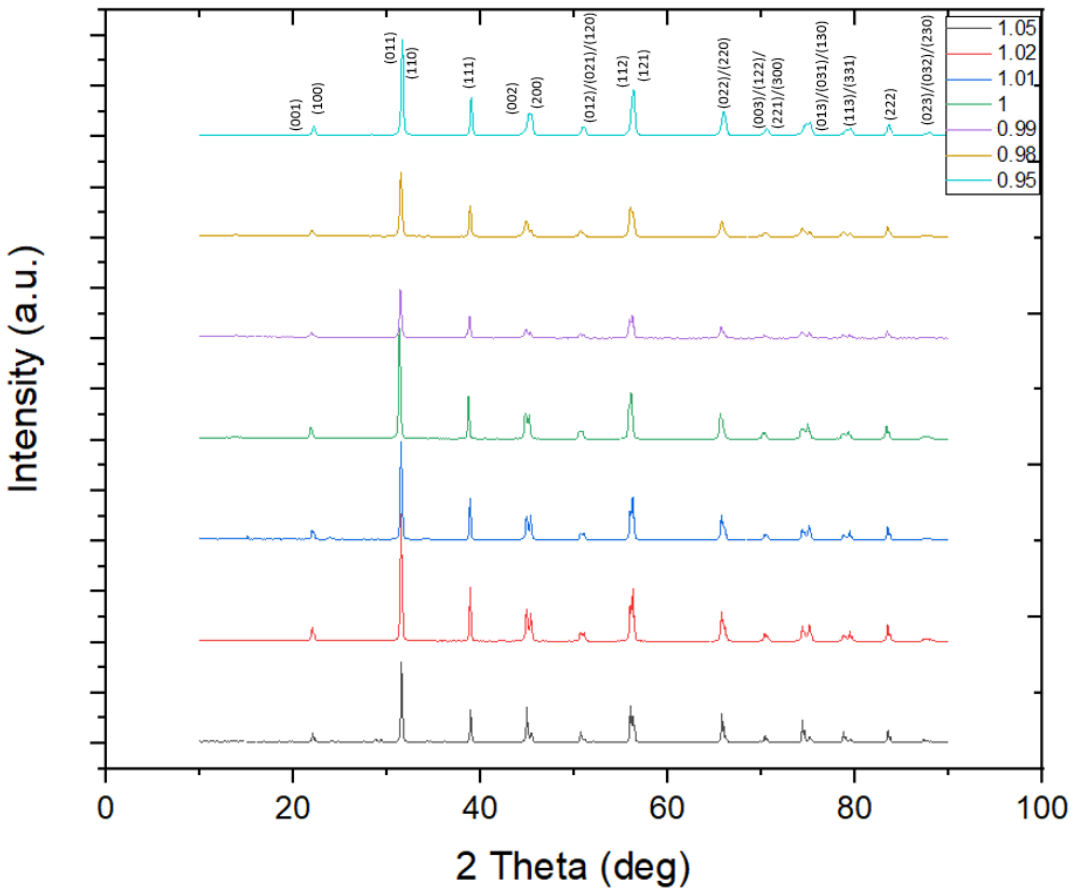

Figure 6. 1 Showing the XRD spectra for all of the $BaTiO_3$ compositions after sintering for 2 hours at 1300°C. The legend refers to Ba/Ti ratio.

From Figure 6.1 some small impurity peaks can be seen in some of the spectra. For the sample with 5 mol% TiO_2 deficiency (Ba/Ti = 1.05) these impurity peaks can be viewed in Figure 6.2. The peaks were identified using search match software and matched with ICDD files corresponding to TiO_2 (file number 01-070-2556) and Ba_2TiO_4 (file number 00-008-0277).

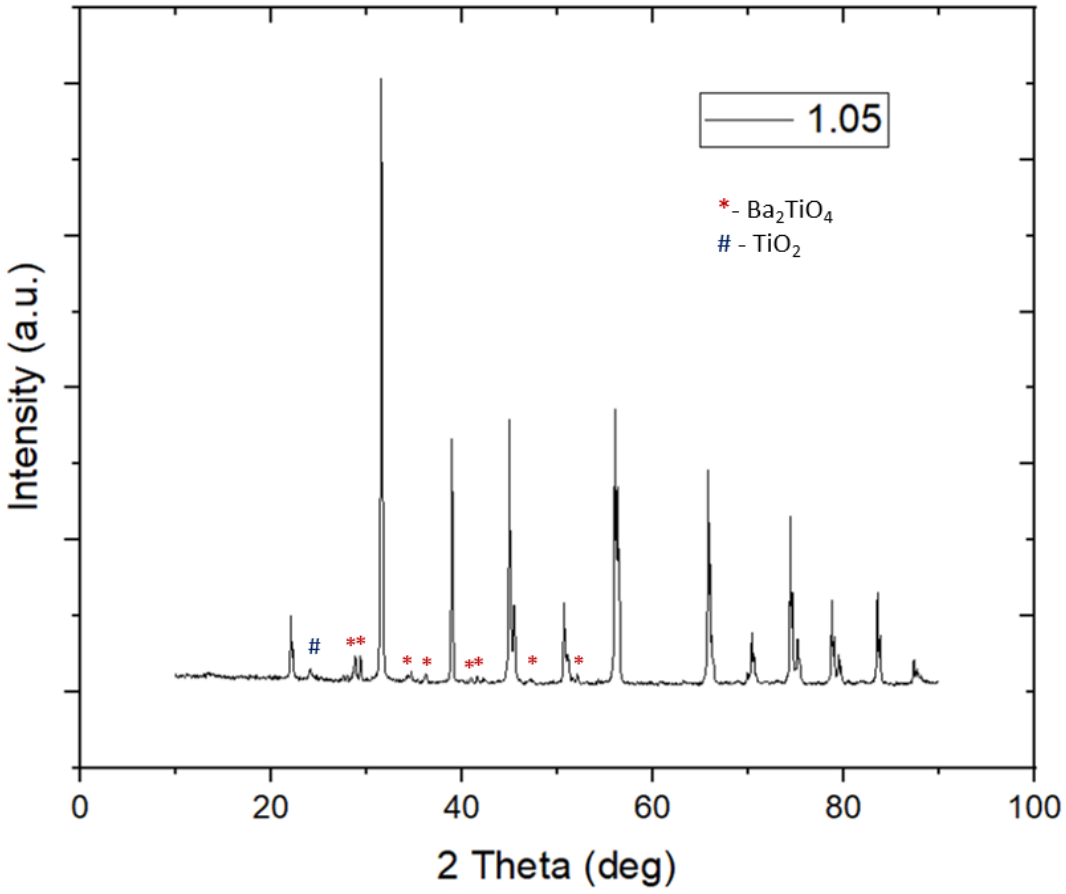

Figure 6. 2 Showing the XRD spectrum of 5 mol % TiO_2 deficient $BaTiO_3$ sintered at 1300°C for 2 hours with the multiple impurity peaks labelled.

Some evidence of second phase is also visible in the XRD spectrum of $BaTiO_3$ with a 1 mol % TiO_2 deficiency. These peaks have been labelled and can be viewed in Figure 6.3. They again correspond with Ba_2TiO_4 (ICDD file number 00-008-0277) and TiO_2 (ICDD file number 01-071-6414).

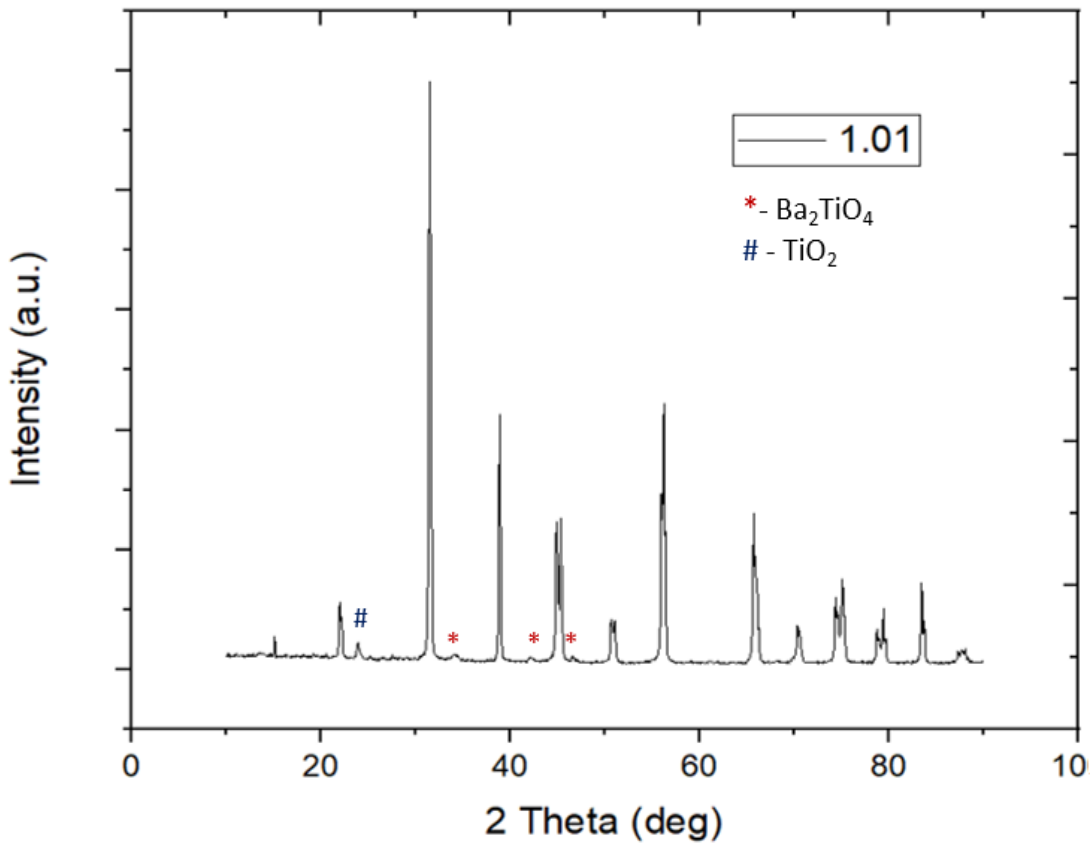

Figure 6. 3 Showing the XRD spectrum of 1 mol % TiO_2 deficient $BaTiO_3$ sintered at 1300°C for 2 hours with the multiple impurity peaks labelled.

Pellets sintered at 1340°C were also analysed using a PANaylitical X'Pert diffractometer with the same parameters as the pellets sintered at 1300°C. All sample patterns (Figure 6.4) were again matched with existing ICDD data files for tetragonal $BaTiO_3$.

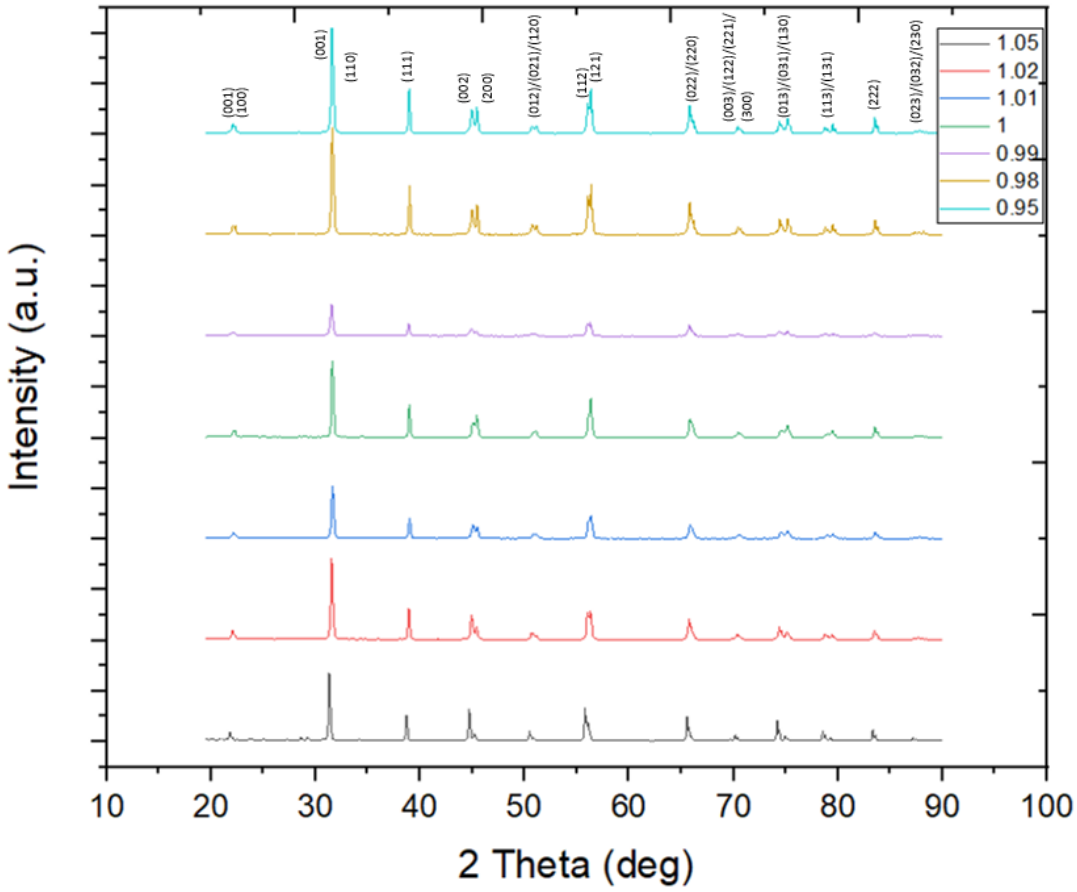

Figure 6. 4 Showing the XRD spectra for all of the $BaTiO_3$ compositions after sintering for 2 hours at 1340°C. The legend refers to Ba/Ti ratio.

When sintered at 1340°C there was still some evidence of second phase in the sample with a 5 mol% TiO_2 deficiency. The impurity peaks were identified as Ba_2TiO_4 (ICDD file 00-008-0277) and TiO_2 (ICDD file 04-014-5355) and can be seen in Figure 6.5.

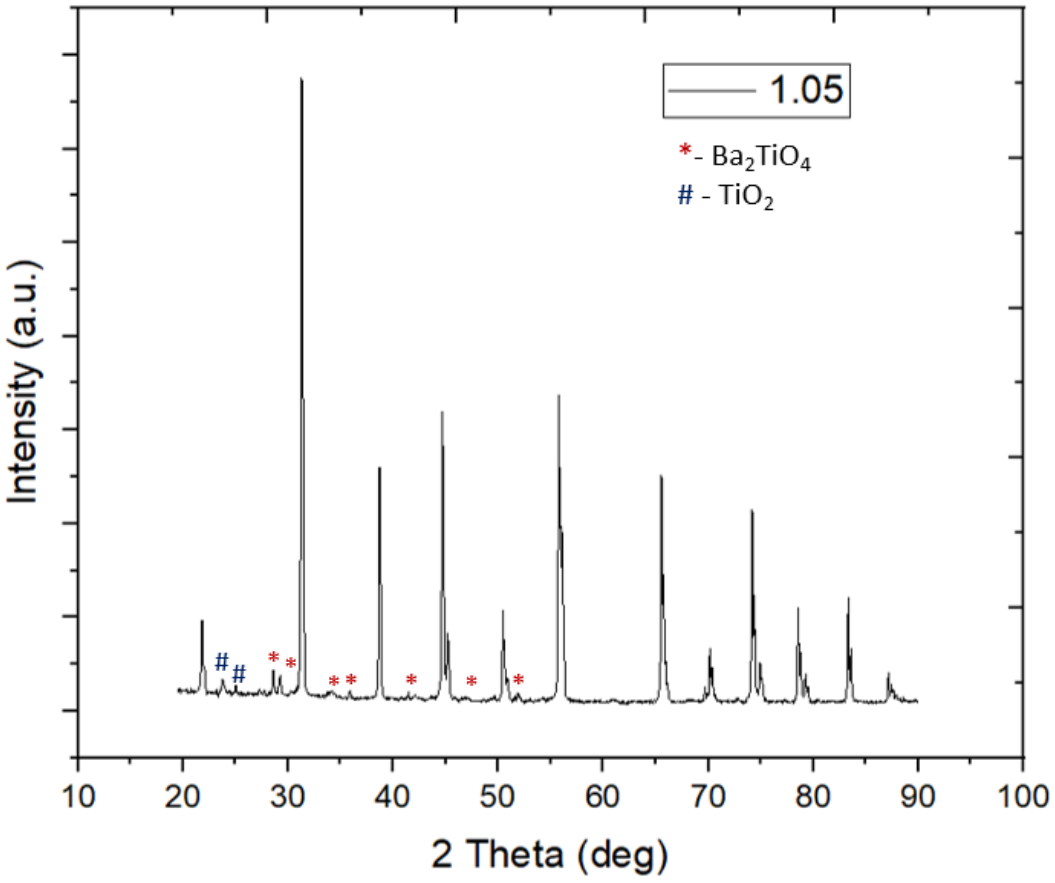

Figure 6. 5 Showing the XRD spectrum of 5 mol % TiO_2 deficient $BaTiO_3$ sintered at 1340°C for 2 hours with the multiple impurity peaks labelled.

6.1.2 Grain Growth in $BaTiO_3$

6.1.2.1 Grain Growth with Changes in Temperature

Both optical and scanning electron microscopy were performed in order to examine grain size and any notable characteristics in the microstructure. The results from this study would be used in order to determine the optimum conditions for single crystal growth experiments. As previously discussed, sintering temperature was either above (1340°C) or below (1300°C) the BaO-TiO_2 eutectic temperature of 1320°C. Sintering was performed at both these temperatures for 2 hours.

Table 6. 1 Showing the sintering temperature and average grain size of the various $BaTiO_3$ compositions.

Ba/Ti ratio	Average grain size (μm) after 2hrs at 1300°C	Average grain size (μm) After 2hrs at 1340°C
1.02	3.1	3.5
1.01	3.4	5.3
1	5.6	12.7
0.99	34	63
0.98	1.1 (with large grains ~33μm)	33
0.95	0.7	14.81 (with large grains measuring 39.5μm)

The results of the initial grain growth study can be seen in full in Table 6.1. It is clear that sintering above the eutectic temperature promotes grain growth. TiO_2 addition also encourages grain growth. However, grain size decreases when TiO_2 excess exceeds 1 mol %. This effect was deemed due to transport through an increased intergranular liquid becoming the rate limiting step.

Figure 6.6 shows scanning electron micrographs of the samples sintered at 1300°C for 2 hours. When sintered below the eutectic temperature the sample containing 1 mol% excess TiO_2 had the largest grain size. Bimodal grain growth was evident in the sample containing 2 mol% excess TiO_2 with some large grains being surrounded by a fine-grained matrix. When TiO_2 excess was increased to 5 mol % grain size was reduced. Stochiometric samples and

those with 1 and 2 mol% TiO_2 deficiency had a uniformly fine-grained microstructure. When TiO_2 deficiency was increased to 5 mol% grains did not grow and samples remained in powder form.

These results are similar to those reported by Hennings, Janssen and Reynan [80]. As can be seen in Figure 6.6, twinned grains are present in the stochiometric, 1 mol% and 2 mol % excess TiO_2 samples. With abnormal grain growth in these twinned grains being most obvious in the sample with 2 mol % excess TiO_2.

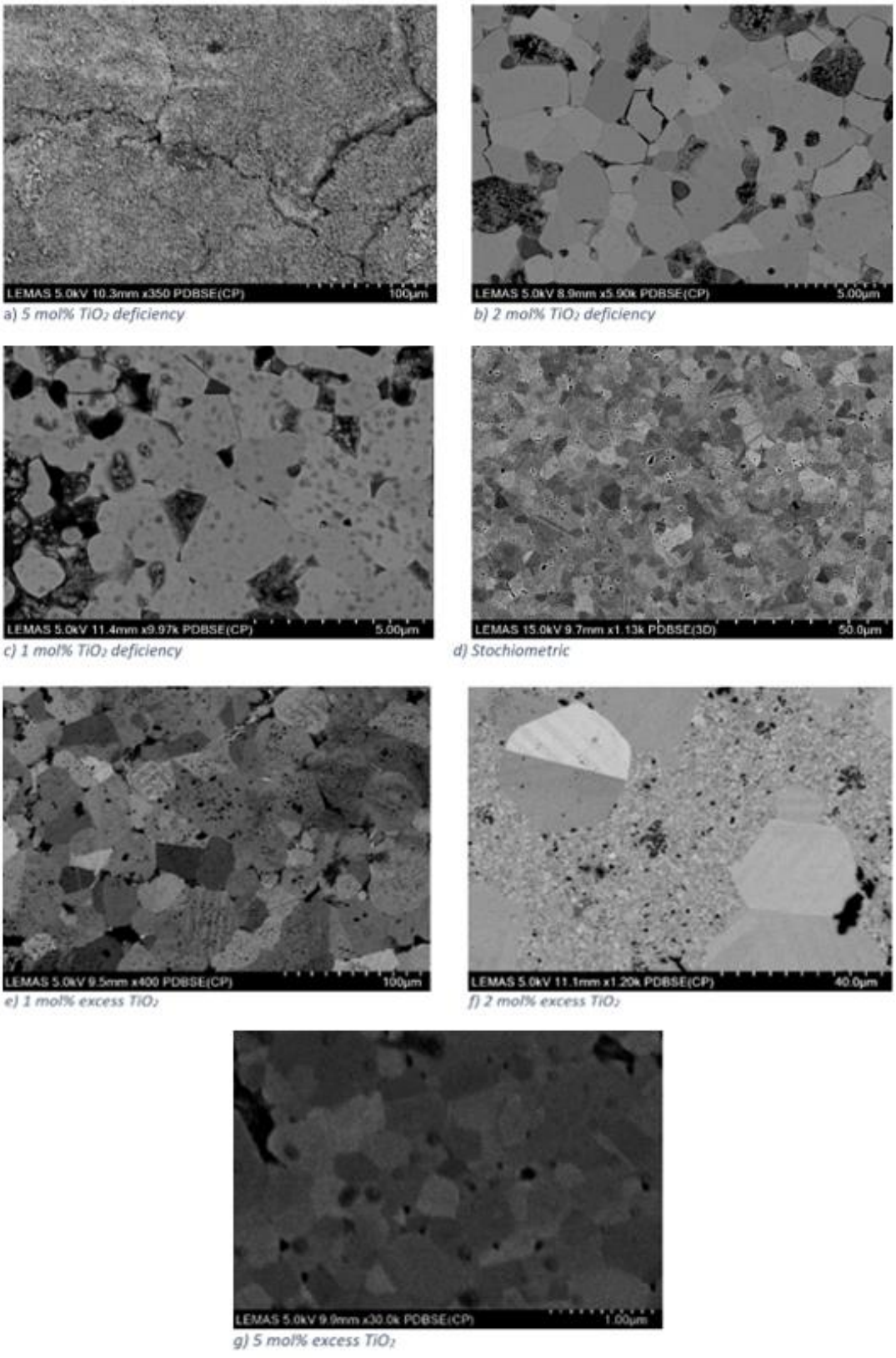

Figure 6. 6 Showing scanning electron micrographs of the $BaTiO_3$ sintered at 1300°C for 2 hours.

.

When sintered at the higher temperature (1340°C) further changes in the microstructure were apparent as shown in Figure 6.7. The sample with 5 mol% TiO_2 deficiency again remained in powder form. The other samples however, all demonstrated a larger grain size than those sintered below the eutectic temperature. This change was minor in the samples with TiO_2 deficiency as can be seen In Table 6.1. The largest grains were found in the sample with 1 mol% TiO_2. At this temperature grains in the pellet with 2 mol% excess TiO_2 were found to be uniform and of an average size equal to that of the abnormal grains when sintered at the lower temperature. In contrast to the results published by Hennings, Janssen and Reynan [80] the largest grains in these experiments were not in the 2 mol% excess TiO_2 samples. In these experiments the thickening of the intragranular liquid phase which begins to inhibit grain growth occurred between 1 and 2 mol% excess TiO_2. However, in contrast to when sintered below the eutectic temperature the sample with 5 mol% excess TiO_2 displayed bimodal grain growth with varying grain size. There was also clear evidence of a thick intergranular liquid phase between the smaller grains which likely contributed to their restricted growth. Some evidence of this intergranular phase can also be seen in the sample with 2 mol % excess TiO_2.

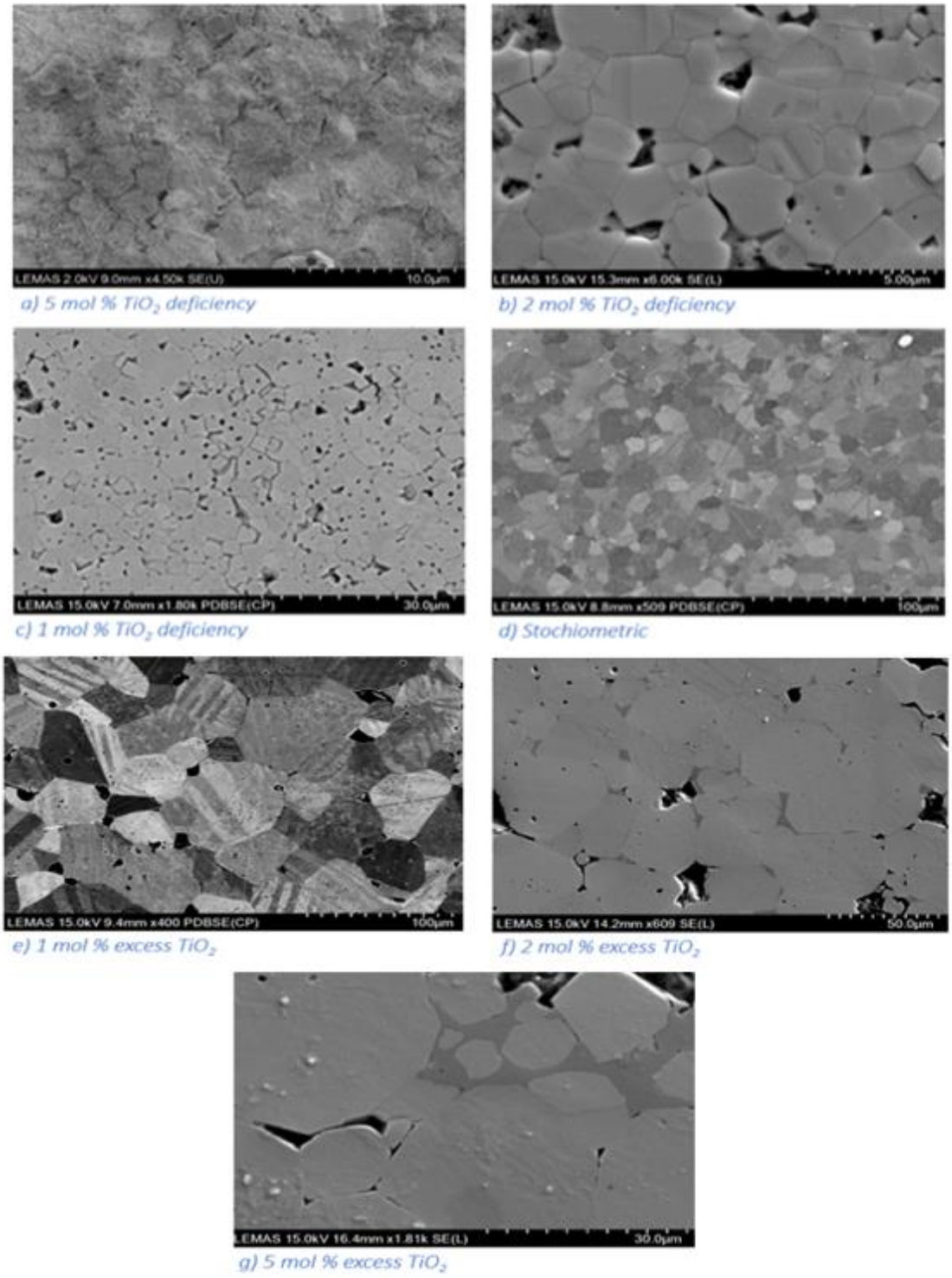

Figure 6. 7 Showing scanning electron micrographs of the $BaTiO_3$ sintered at 1340°C for 2 hours. Figure a was taken using the upper secondary electron detector, Figure b, f and g were taken using the lower secondary electron detector and the rest of the figures were taken with a backscattered electron detector.

6.1.2.2 Grain Growth with Changes in Sintering Time

In order to further understand grain growth rates samples containing 1 mol%TiO_2 deficiency, stochiometric and 1 mol % TiO_2 excess were compared by sintering at 1340°C for different lengths of time. These samples were all sintered for 0.5, 1, 2, 4, 8 and 16 hours. As expected, the $BaTiO_3$ containing TiO_2 excess was much larger across all sintering temperatures followed by the stochiometric sample and lastly the TiO_2 deficient sample. Figure 6.8 shows a plot of average grain size vs time for these samples, along with additional plots showing the standard deviation of grain size within these samples. The large standard deviation shown in the plot for the sample containing excess TiO_2 shows that grain growth in this sample was pseudo-normal and there was a relatively large variation in grain size.

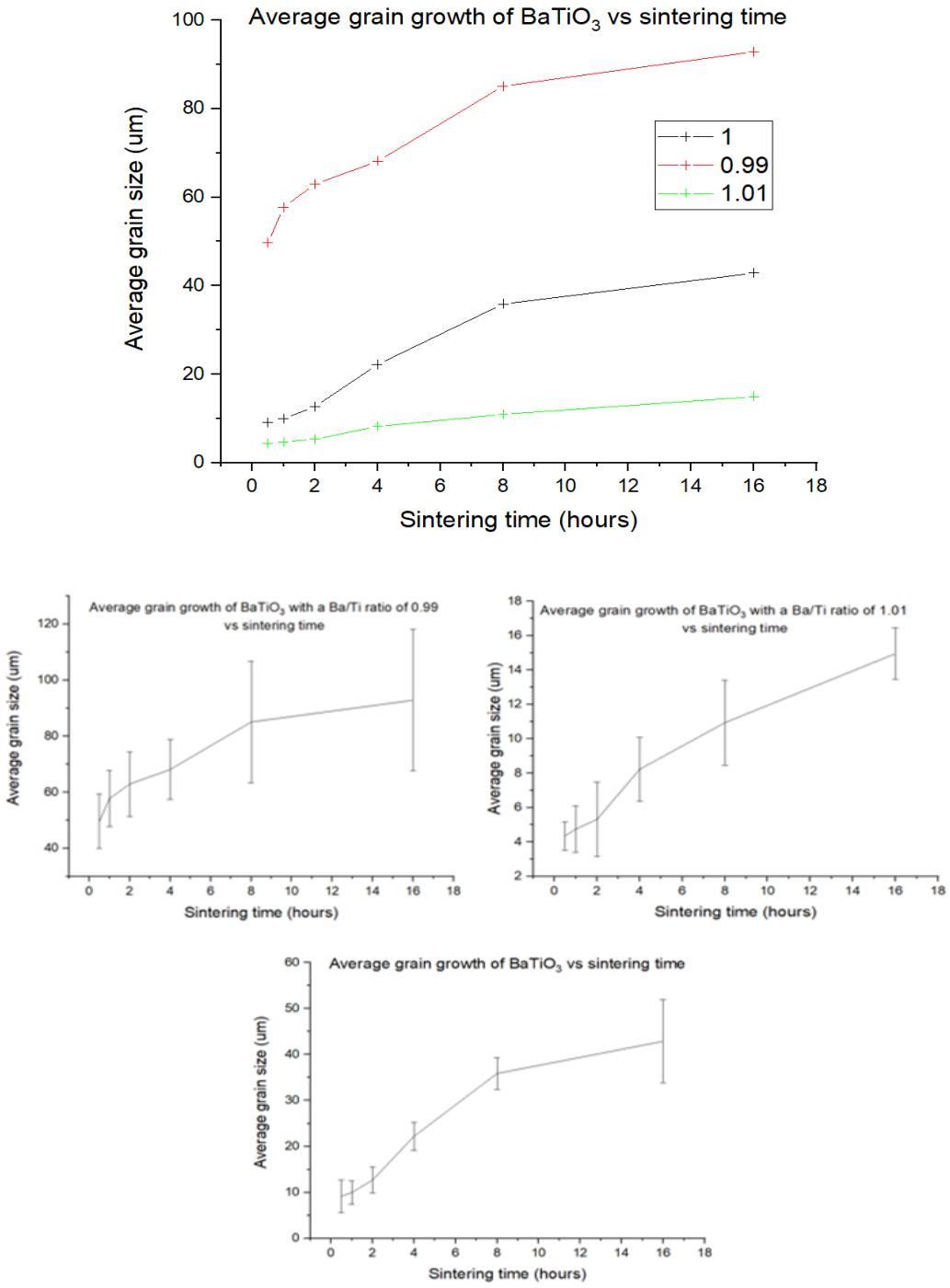

Figure 6. 8 Showing a plot of grain size (µm) vs sintering time (hours) for $BaTiO_3$ compositions with Ba/Ti ratios of 1.01, 1 and 0.99 sintered at 1340°C. The smaller plots also show the same data individually with the addition of error bars to demonstrate the standard deviation of the grain size measurements taken.

Figure 6.9 shows stoichiometric $BaTiO_3$ sintered at 1340°C for differing amounts of time. It is clear that grain size increased significantly with sintering time. Other microstructural features however remain the same. Twinned grains were common with this composition however no bimodal grain growth was observed.

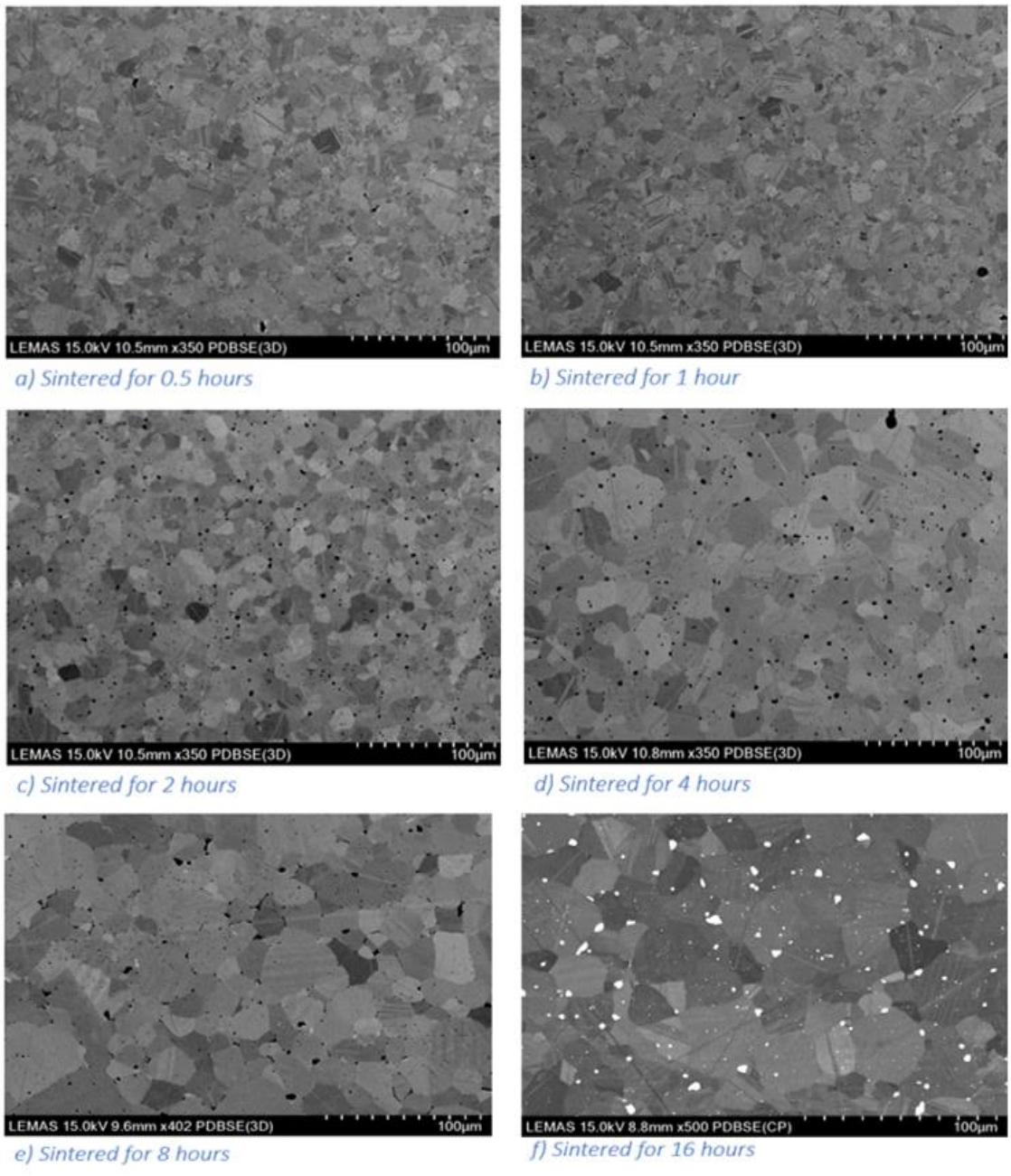

Figure 6. 9 Scanning electron micrographs of stoichiometric $BaTiO_3$ when sintered at 1340°C for various amounts of time. The bright areas in seen in Figure 6.9 f are due to some residual polishing material on the sample surface.

Figure 6.10 shows micrographs of the $BaTiO_3$ samples with 1 mol % TiO_2 deficiency sintered for varying amounts of time at 1340°C. Again, grain size is larger with increasing sintering time. This composition displayed faceted grains with some twinning. Large abnormal twinned grains can be seen occasionally as demonstrated by images 6.10 b and e.

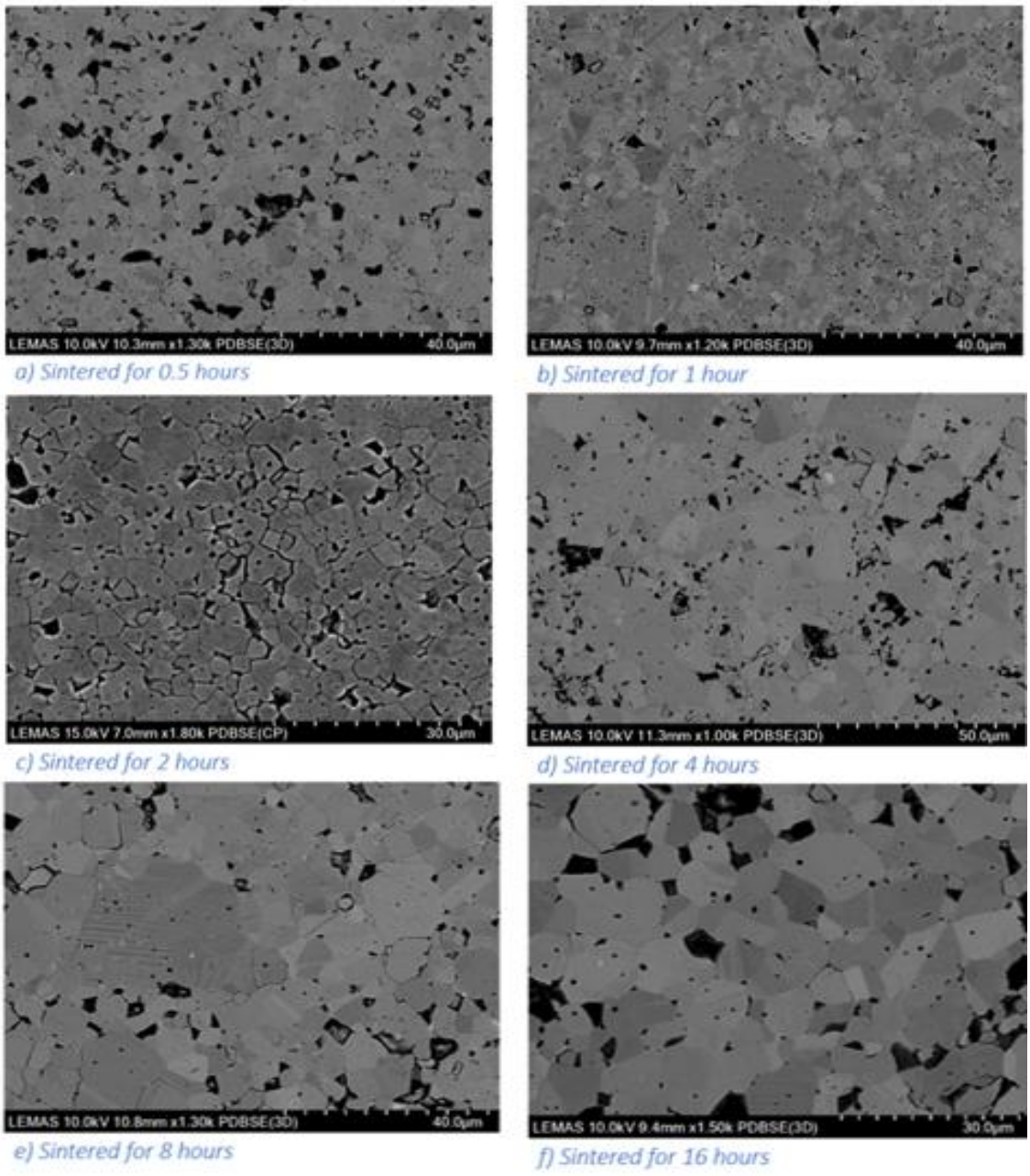

Figure 6. 10 Scanning electron micrographs of $BaTiO_3$ with a 1 mol% TiO_2 deficiency sintered at 1340°C for various amounts of time.

Figure 6.11 shows images of $BaTiO_3$ with 1 mol% excess TiO_2 sintered at 1340°C for varying lengths of time. These samples had the largest grains across all sintering times as clearly the addition of TiO_2 and the formation of a $Ba_6Ti_{17}O_{40}$ intergranular liquid phase has an accelerating effect on grain growth particularly above the eutectic temperature. The formation of this liquid phase can be explained by the BaO-TiO_2 phase diagram (Figure 4.1) Twinned grains were present as with the previous examples, but no abnormally large abnormal grains were noted on inspection.

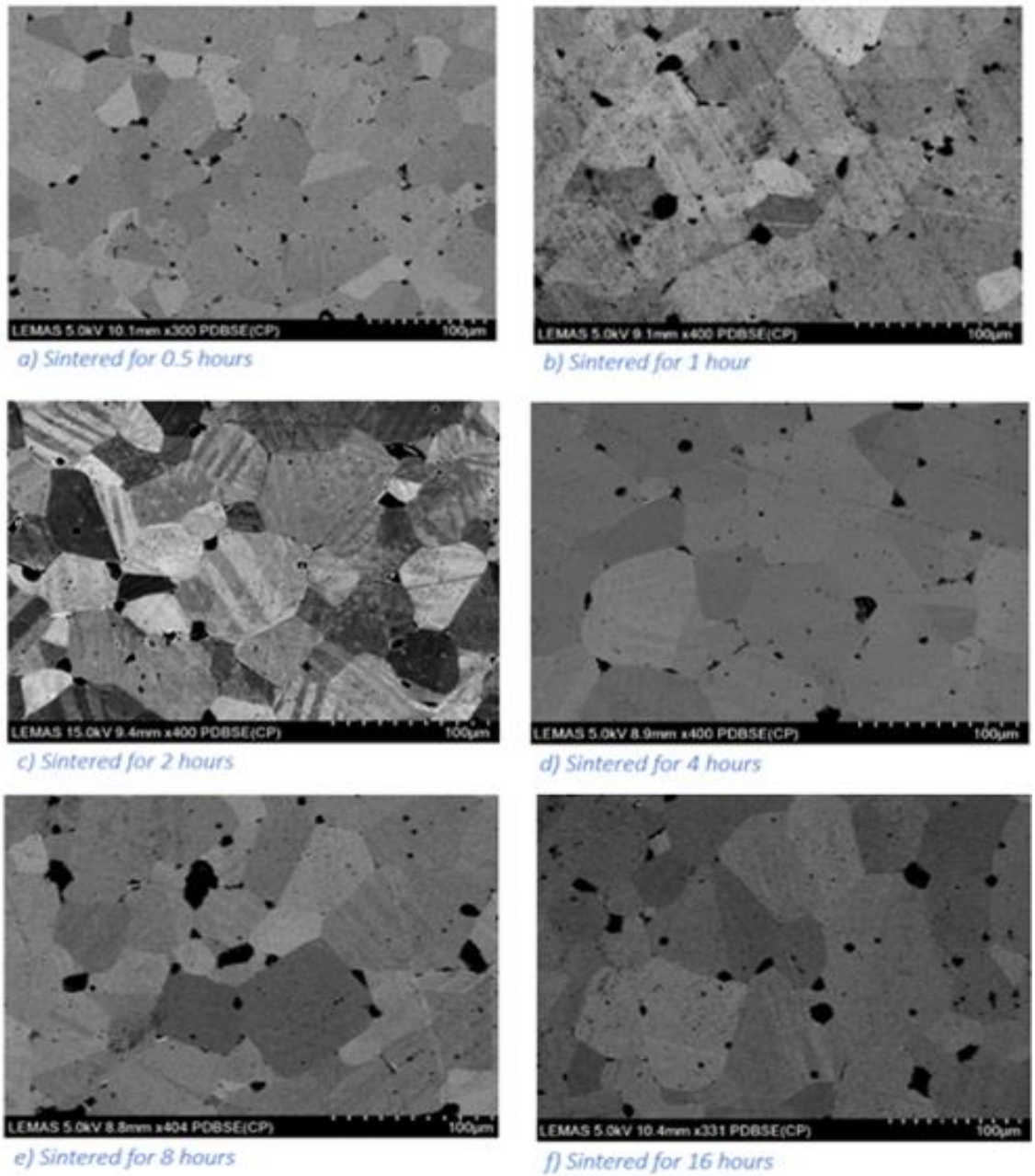

Figure 6. 11 Scanning electron micrographs showing $BaTiO_3$ with 1 mol % excess TiO_2 sintered at 1340°C for varying amounts of time.

It is clear from these results that intergranular liquid phase accelerates grain growth, it was therefore hypothesised that SSCG experiments would be more successful when using compositions of $BaTiO_3$ with excess TiO_2. Particularly 1 mol% excess as this composition produced the largest grains when compared to the other TiO_2 rich compositions.

6.1.3 Solid State Crystal Growth in $BaTiO_3$

6.1.3.1 Solid state crystal growth in $BaTiO_3$ containing 1 mol% excess TiO_2

It was determined from the grain growth experiments that crystal growth would be insufficient with a TiO_2 deficient $BaTiO_3$ although this would eliminate the problem of large grains arising and impinging on any growing crystal. Therefore, only stoichiometric and 1 mol% excess TiO_2 were used.

A relatively large crystal was grown using the $BaTiO_3$ containing 1 mol % excess TiO_2 sintered at 1340°C for 72 hours. This crystal had grown in various directions and was immediately visible to the naked eye as is shown in Figure 6.12 a. The maximum growth length of the crystal was found to be approximately 2075µm with a growth rate of 29µm/hr. However, a few large, twinned grains were found to have grown within the edges of the pellet which impinged on the growing single crystal. One of these grains is shown in Figure 6.12 b. The shape of the crystal seed in these images is a result of the seed crystal breaking when cutting was performed with a diamond scribe as detailed in Chapter 5.

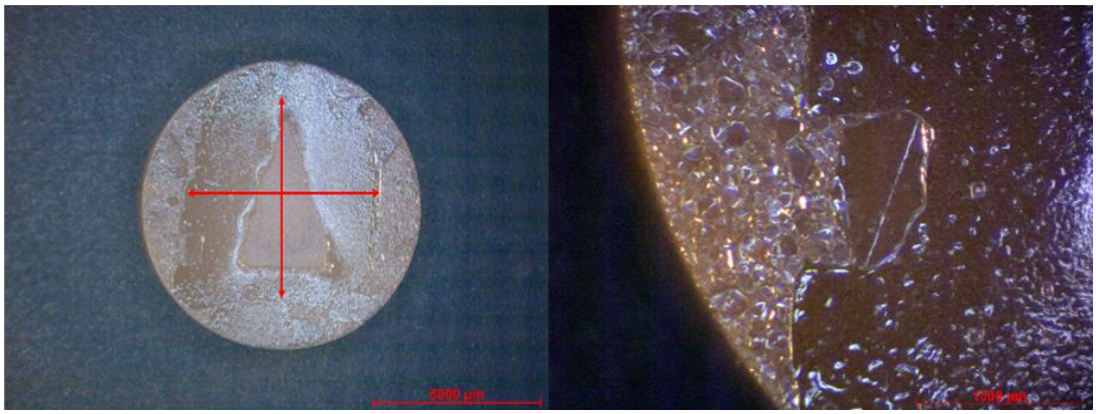

Figure 6. 12 a (above left) An optical micrograph taken at 0.75x magnification showing the single crystal grown using BaTiO3 containing 1 mol% excess TiO_2, sintered at 1340°C for 72 hours. The red lines indicate the growth length of the crystal and 5.1.8 b (above right) taken at 1.5 x magnification showing a large twinned grain that has grown within the matrix and impinged upon the growing crystal.

In order to examine the grown single crystal more closely, the crystal was cut in order to reveal cross sections and polished as discussed earlier before being examined using SEM. An example of one of these cross sections is shown in Figure 6.13. and Figure 6.14.

In both these images it can be seen that there is a clear difference in porosity between the seed crystal and the grown single crystal. The grown crystal is very porous and an area of dense porosity can be seen In Figure 6.13 and 6.14, in the optical micrograph this area of porosity can be seen as a whiter area. A close up of this area can be seen In Figure 6.15.

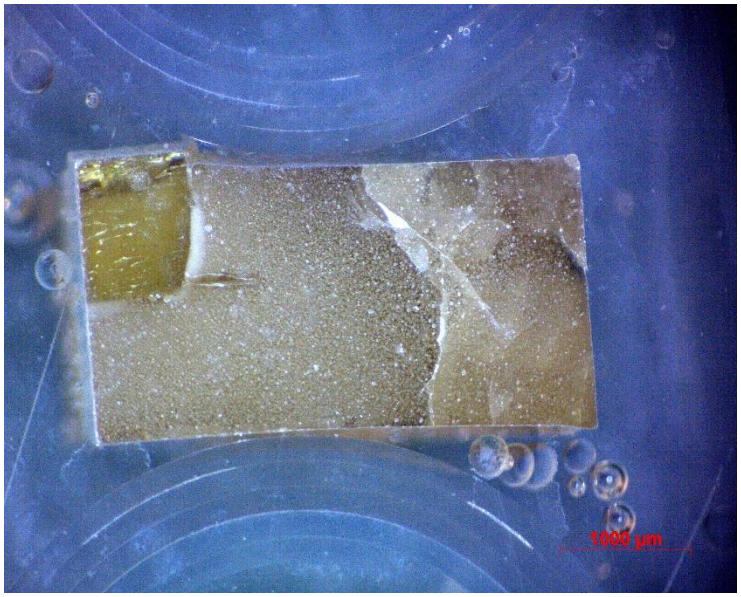

Figure 6. 13 Shows an optical micrograph of a cross section of the $BaTiO_3$ single crystal shown in Figure 6.11. This image was taken at 3x magnification

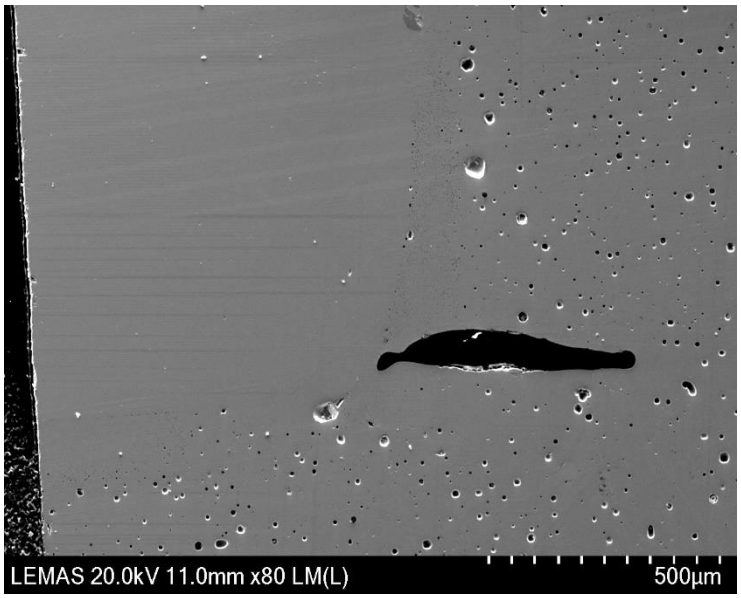

Figure 6. 14 A scanning electron micrograph of the cross section of the grown single crystal shown in Figure 6.13.

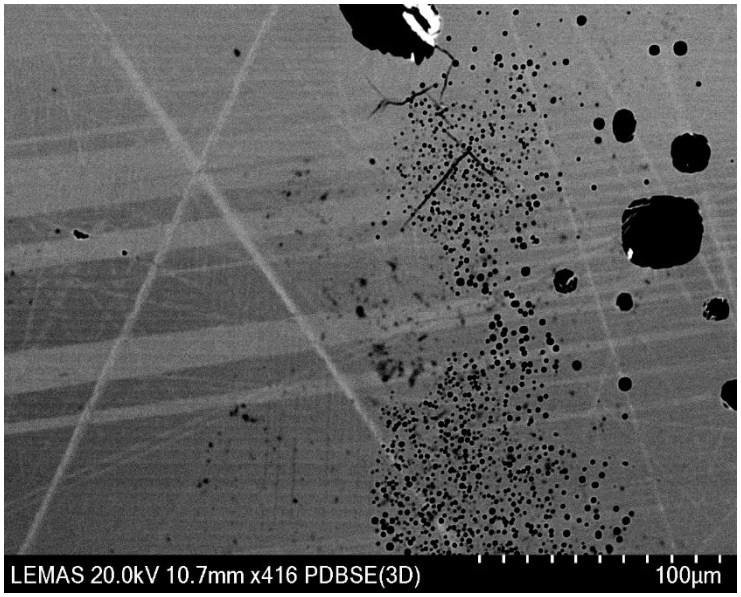

Figure 6. 15 A scanning electron micrograph showing a closer image of the porous section between the seen crystal and grown single crystal

EDX performed on the area shown in Figure 6.16 shows that there was no obvious compositional differences between the seed single crystal, the grown crystal and the area of porosity between. The 1 mol % excess TiO_2 is too small of a compositional difference to be picked up by the detector. The sample was coated with iridium prior to SEM and EDX analysis.

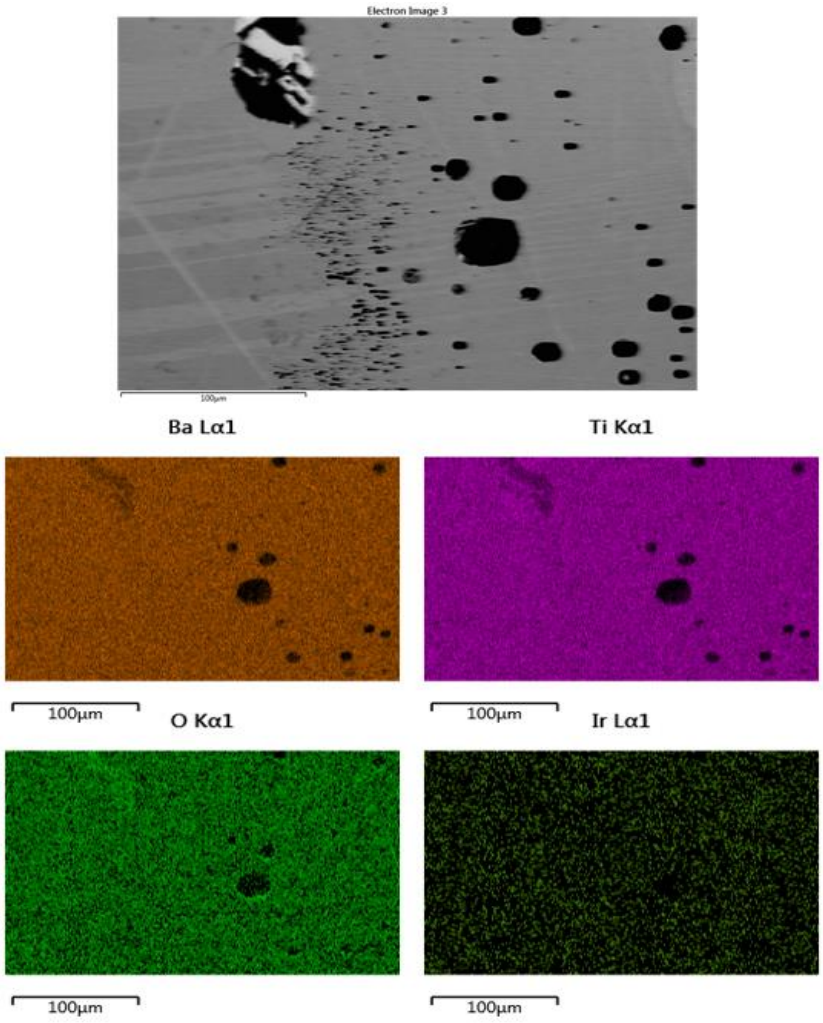

Figure 6. 16 Showing a scanning electron micrograph of the seed crystal and the single crystal grown using $BaTiO_3$ with 1 mol% excess TiO_2 and an elemental map of the same area produced using EDX.

In order to prove repeatability another crystal was grown using the same composition of $BaTiO_3$ (1 mol% excess TiO_2) this sample was prepared in the same way and sintered for the same time at the same temperature (72 hours at 1340°C). The resulting crystal can be seen in Figure 6.17. This crystal was larger in size with a maximum growth length of 2750µm and had grown at a rate of 38µm/hour. The larger size if this crystal was due to the fact that no large grains had grown in the path of crystal growth which led to impingement and restricted growth in the previous example.

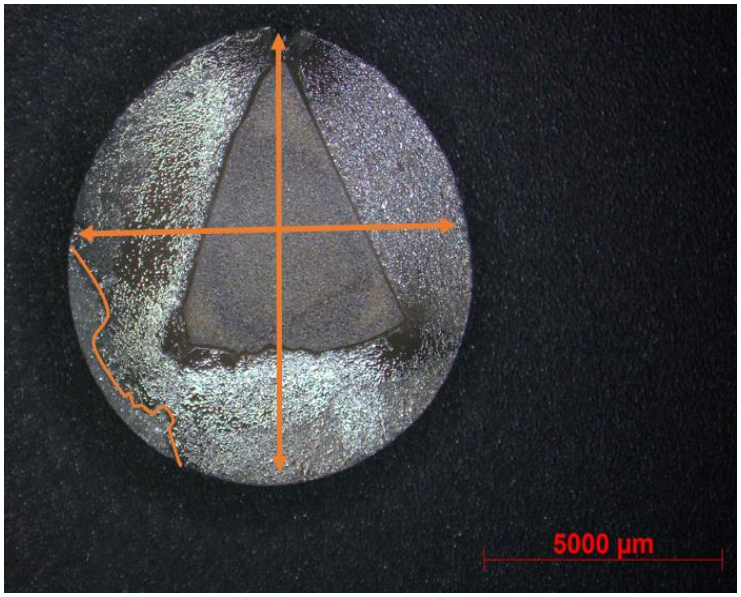

Figure 6. 17 An optical micrograph taken at 0.75x magnification showing the single crystal grown using BaTiO3 containing 1 mol% excess TiO_2 and sintered at 1340°C for 72 hours, the orange arrows indicate the growth length of the crystal. The outlined section at the bottom left of the pellet shows the section of the pellet that is polycrystalline.

A cross section of the second single crystal produced with a 1 mol % excess TiO_2 can be seen in Figure 6.18. This sample has the same issues with porosity as the sample discussed previously. The grown single crystal was again porous in comparison to the seed crystal and there was a particular pore dense area between the seed crystal and the grown crystal. This area can be seen in Figure 6.19a. The cross sections taken from this sample were found to be completely single crystal, bar a single small area shown in Figure 6.19b.

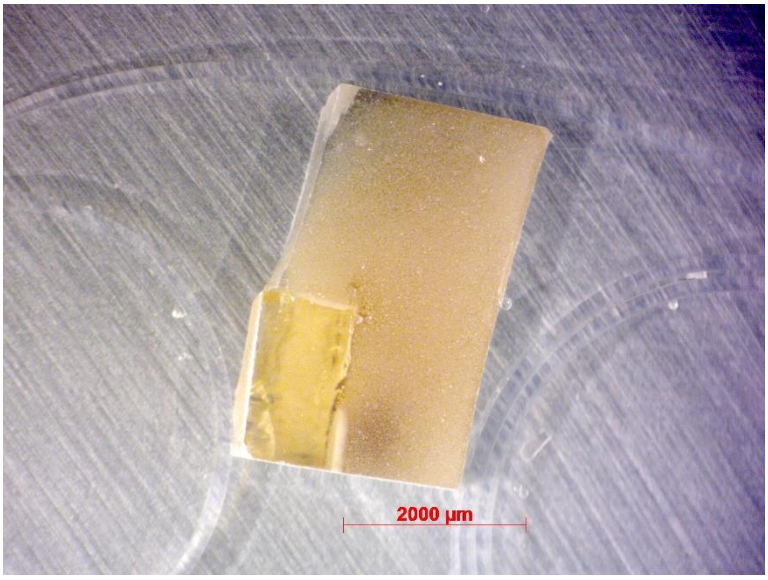

Figure 6. 18 Shows an optical micrograph of a cross section of the $BaTiO_3$ single crystal shown in Figure 6.17. This image was taken at 2x magnification.

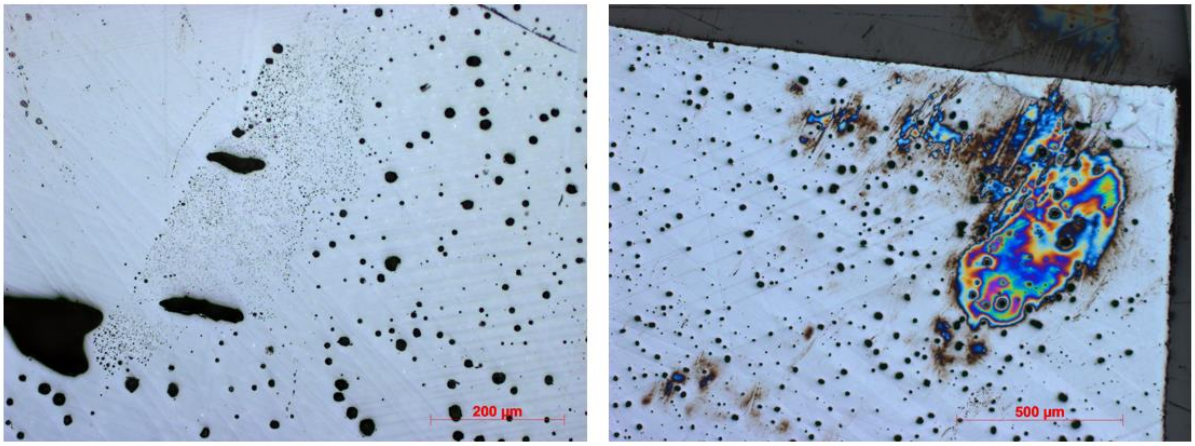

Figure 6. 19 a (left) and b (right) show bright field optical micrographs of the single crystal shown in Figures 6.17 and 6.18. Image a is taken at 10x magnification and image b is taken at 5x magnification.

6.1.3.2 Solid state crystal growth in stoichiometric $BaTiO_3$

SSCG was then attempted using stoichiometric $BaTiO_3$. The conditions were kept the same as for the previously discussed experiment with sintering taking place at 1340°C for 72 hours. No single crystal growth was initially apparent when the whole sample was viewed using optical microscopy as is shown in Figure 6.20.

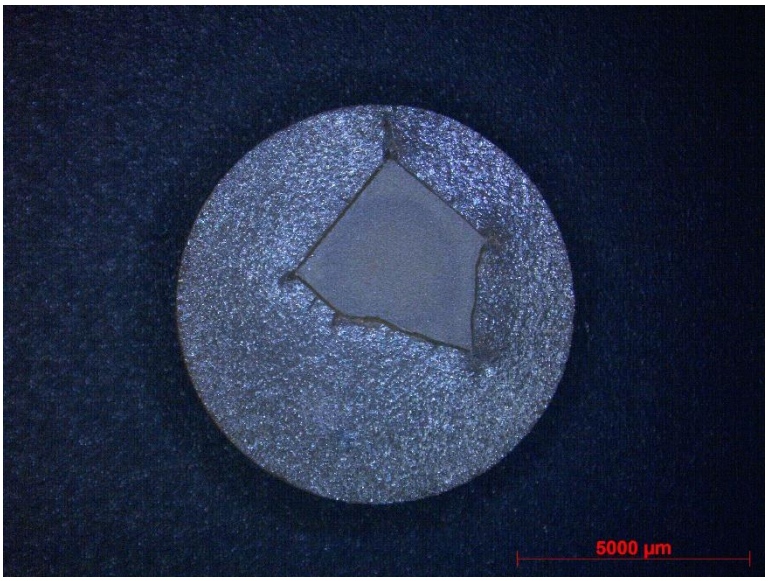

Figure 6. 20 An optical micrograph showing the seeded stochiometric $BaTiO_3$ following sintering for 72hours at 1340°C.

When the cross sections of the sample were viewed however, a single crystal was found to have grown from the seed slightly into the polycrystal. As expected, the amount of growth was much less significant than in the sample containing TiO_2 excess. The growth in this sample is shown below in Figures 6.21 a and b, the maximum growth length of the crystal was found to be approximately 550µm with a growth rate of 7µm/hr.

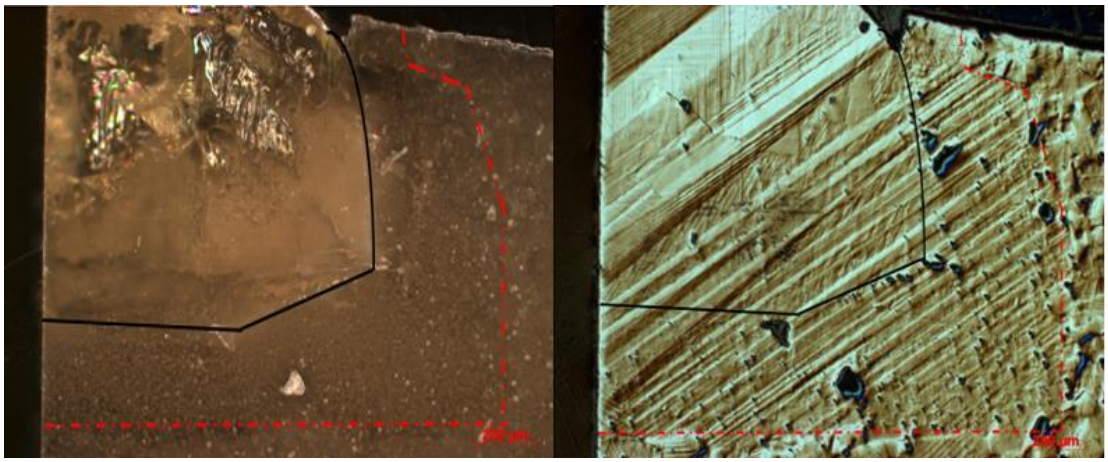

Figure 6. 21 a (above left) and 4b (above right) showing optical micrographs showing a cross section of seed crystal and the crystal grown using the stoichiometric $BaTiO_3$. Figure a is a dark field image and figure b is a bright field image taken using differential interference contrast, both images are of the same area and were taken at 5x magnification. The black line defines the edge of the seed crystal and the red lines border the grown single crystal.

This sample was then examined using SEM, as shown in Figure 6.22. The stochiometric sample appeared to be slightly less porous than the single crystal grown using the composition with 1 mol % excess TiO_2. However, there will still some obvious issues with porosity and one area along the edge of the seed crystal with more obvious porosity. Figure 6.22 a and b show two different areas where the seed crystal meets the grown single crystal.

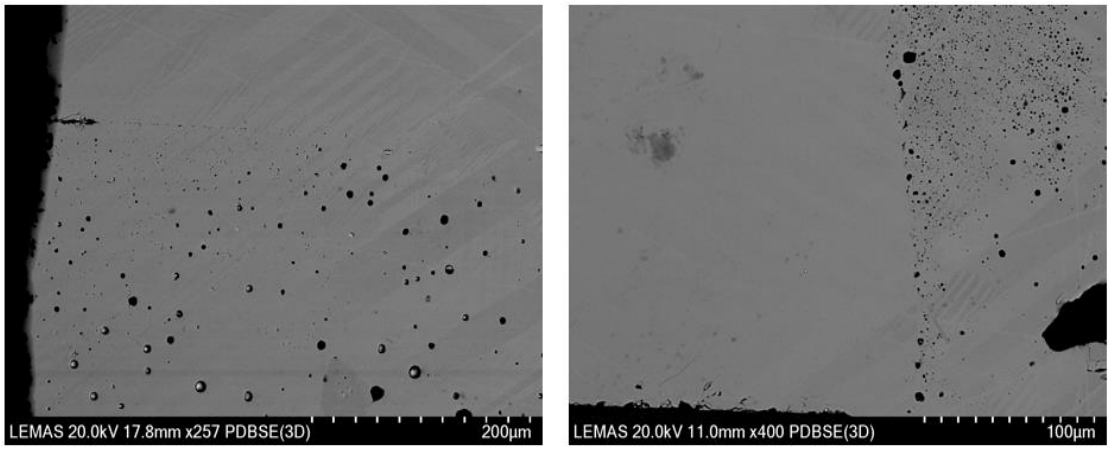

Figure 6. 22 a (left) and b (right) showing scanning electron micrographs of the seed crystal and single crystal grown using a stoichiometric $BaTiO_3$.

As expected, upon investigation using EDX there was no obvious compositional difference between the seed crystal and the grown single crystal. A composition map generated by EDX can be seen in Figure 6.23, the sample was also coated with iridium prior to SEM and EDX analysis.

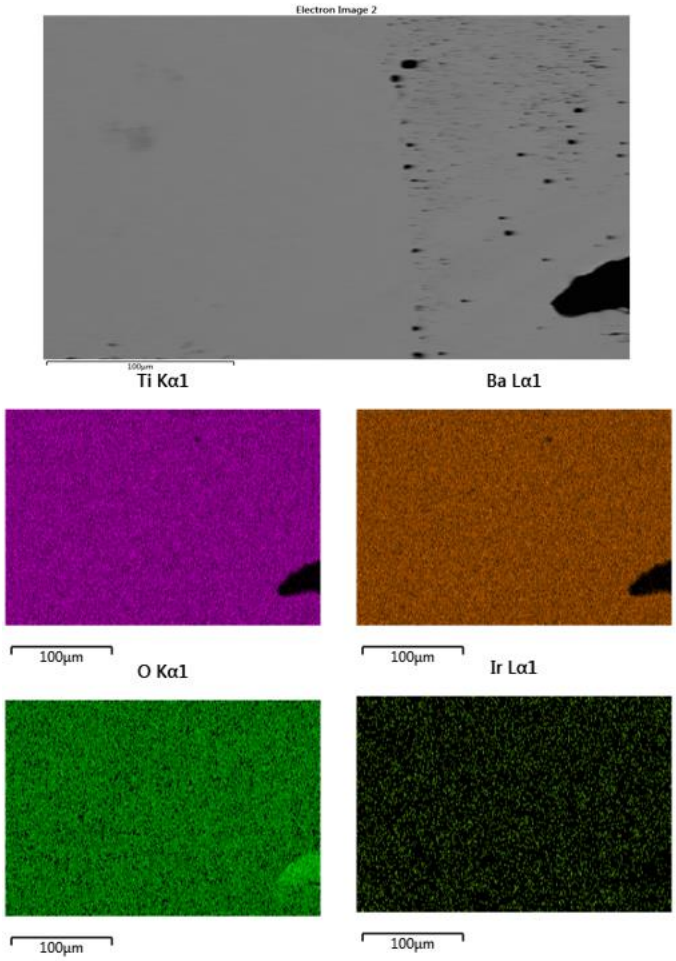

Figure 6. 23 Showing a scanning electron micrograph of the seed crystal and the single crystal grown using stoichiometric $BaTiO_3$ and an elemental map of the same area produced using EDX.

Further single crystal growth experiments investigated the use of a TiO_2 interlayer. This was done using nano-sized TiO_2 (primary particle size 21nm with a purity of 99.5%) obtained from Sigma Aldrich. The nano-sized TiO_2 was mixed with ipa and dropped on the surface of the crystal and allowed to dry. This crystal was then covered with stochiometric $BaTiO_3$ before sintering for 72 hours at 1340°C.

After sintering the sample was analysed using the Motic SMZ-168. There appeared to be a small amount of crystal growth surrounding the crystal seed this can be seen in Figure 6.24.

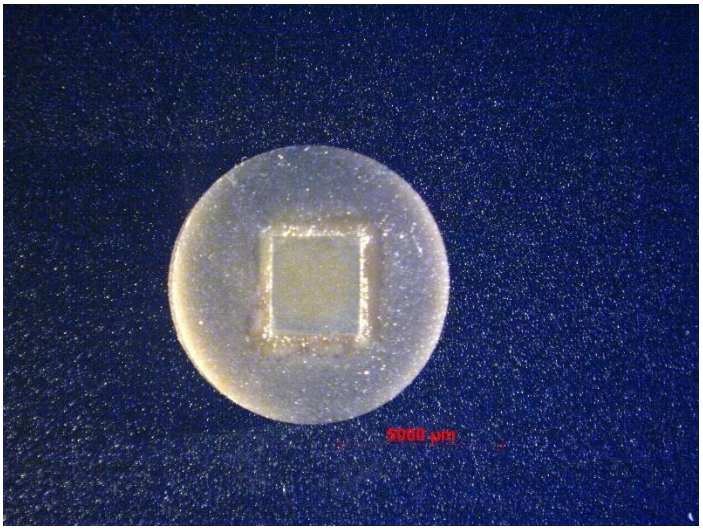

Figure 6. 24 Optical micrograph taken at 0.75x magnification of the $BaTiO_3$ crystal seed and sintered compact after sintering at 1340°C for 72hours.

This sample was subsequently cut into cross sections and polished. Figure 6.25 shows an optical microscope image of the polished cross section taken at 5x magnification. Some single crystal growth was evident, however a large matrix grain had grown and impinged on the growth, preventing further growth. The maximum growth length of the grown crystal was found to be ~790µm with a growth rate of ~11µm/hour. Therefore, the addition of a TiO_2 had improved the growth rate compared to the stochiometric $BaTiO_3$.

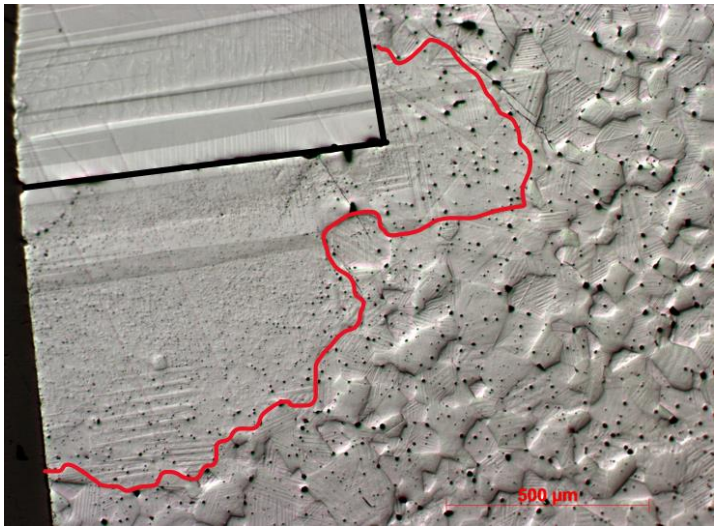

Figure 6. 25 An optical microscope image taken at 5x magnification in bright field showing the seed and grown $BaTiO_3$ single crystals. The grown single crystal is outlined with red.

SEM was then performed on the sample as well as EDX analysis and there was no evidence of a region of TiO_2 excess as can be seen in Figure 6.26.

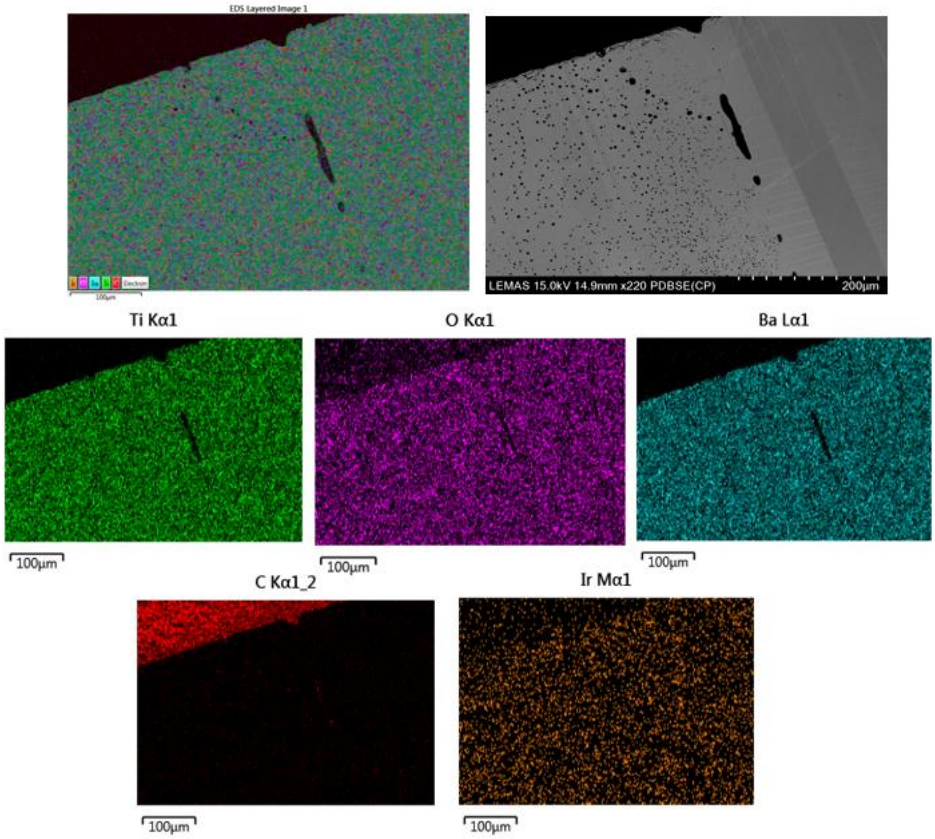

Figure 6. 26 Compositional map generated by EDX of the seed and grown single crystal. This sample was coated using iridium.

6.1.3.3 Discussion

6.1.3.1 Grain growth in $BaTiO_3$

It is evident that a TiO_2, excess in $BaTiO_3$ promotes grain growth with this effect maximised at 1 mol% excess. In the samples with 1 mol % TiO_2 grains were ~5x and ~6x larger than their stochiometric counterparts, at 1340°C and 1300°C respectively. The grains in this sample were nearly double the size as those with the same composition when sintered above the eutectic temperature. Promotion of grain growth in the presence of a small amount of liquid phase suggests a liquid phase enhanced grain growth mechanism. Further evidence of this is

seen as grain growth slowed when TiO_2 excess was increased further. This slowing of grain growth past a certain TiO_2 concentration occurs as the intergranular phase thickens and transport through this liquid becomes rate limiting. Evidence of a thick second phase is present in the electron micrographs of the sample containing 5 mol% excess TiO_2 sintered at 1340°C (Figure 6.7). Bimodal grain growth was also present in this sample, as atoms from the smaller grains were surrounded by an increased amount of second phase thus were not as easily transported and therefore these smaller grains remained present after sintering.

When the stoichiometric $BaTiO_3$, along with 1 mol% excess TiO_2 containing and 1 mol% TiO_2 deficient $BaTiO_3$ were sintered for a range of differing sintering times at 1340°C, grain size in all the samples increased with sintering time. The 1 mol% excess TiO_2 had a coarser microstructure after sintering for only 30 minutes with average grain size being nearly 5x that of its stochiometric counterpart. This shows that grain growth is rapid in the first 30 minutes of sintering and any abnormal grain growth that had occurred in this sample was completed in this time. This occurs when the small grains have been dissolved completely during the liquid phase enhanced grain growth and large grains begin to impinge on each other. After this initial rapid grain growth the grains in this sample followed a normal grain growth pattern similar to the stoichiometric and 1 mol% deficient samples. A consequence of this initial rapid grain growth was that pore entrapment had occurred in this sample as grain growth occurred at a rate greater than the rate of densification. This meant that densification was limited in this sample by the presence of intragranular pores shown in more detail in Figure 6.27

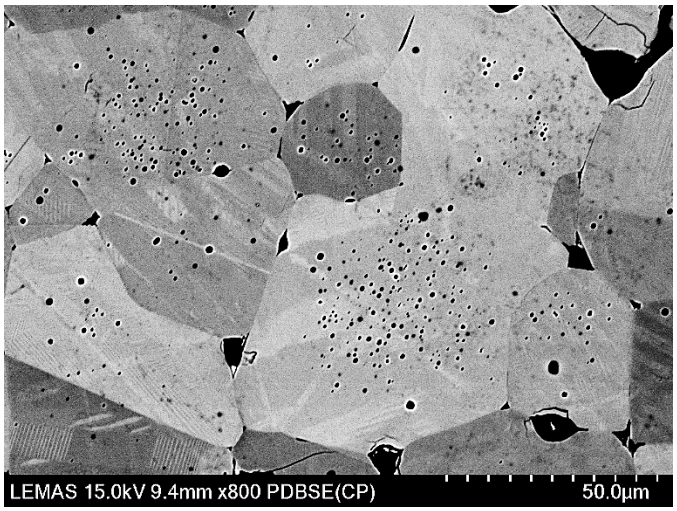

Figure 6. 27 A scanning electron micrograph of $BaTiO_3$ sintered at 1340°C for 2 hours showing intragranular porosity.

There was no significant abnormal grain growth noted in the stochiometric sample despite the presence of multiple growth twins. This shows that although abnormal growth is more likely in this grain it does not always occur. The 1 mol% TiO_2 deficient sample did however display some evidence of abnormal grain growth in some of the samples but these large twinned grains were not common throughout the microstructure, with some of these samples appearing to not have any large grains upon inspection.

6.1.3.2 Solid state crystal growth in $BaTiO_3$

The most successful crystal growth experiments in terms of crystal size were performed using 1 mol% excess TiO_2. This is likely due to the rapid grain growth and subsequent grain impingement in the matrix leading to normal grain growth while allowing the single crystal to continue to grow like a large abnormal grain. In the second experiment using this composition crystal growth rate was found to be 961.65µm/day, Bridgman grown single crystals have a growth rate of around 4.5mm/day [36]. While the SSCG growth rate is reduced in comparison, if this process can be successfully transferred to materials such as PMN-PT then a saving in cost and the possibility of growing several crystals in the same box furnace would make it worthwhile. In the first SSCG experiment using the excess TiO_2 some secondary abnormal grain growth was observed in the bulk which can be observed in Figure 6.12. The large, twinned grain imaged here had impeded growth of the single. The process, by which this grain had grown was likely a combination of the twin growth re-entrant edge mechanism combined with liquid phase enhanced growth. It was clear that the single crystal seeds in these experiments utilised the liquid phase enhanced grain growth mechanism as the experiment performed using stoichiometric $BaTiO_3$ resulted in a much smaller amount of crystal growth. Considerable levels of porosity was observed in all of the $BaTiO_3$ crystals grown. A pore dense area around the edge of the crystal seeds was observed in all of the crystal samples, this is likely due to the initial crystal growth occurring at a faster rate, crystal growth than begins to slow as the matrix grains increase in size which is evidence by the porosity gradient observed where pores further away from the crystal seen had coalesced prior to entrapment.

6.2. Nb_2O_5 doped $BaTiO_3$ ($Ba(Ti_x,Nb_{1-x})O_3$)

Due to the fact that large grains had impinged on one of the single crystals grown using $BaTiO_3$ containing 1 mol % excess TiO_2 and the single crystals were all porous, further investigations into microstructure control commenced. These investigations began by considering dopants. Niobium was chosen for further experiments as doping with Nb_2O_5 is known to restrict grain growth in $BaTiO_3$. [49] It was hoped that this restriction in grain growth could be utilised in order to prevent large grains growing in the matrix during solid state crystal growth and leading to impingement. Further grain growth experiments investigated how Nb_2O_5 doping alongside varying concentration of TiO_2 affects microstructure.

Compositions of $Ba(Ti_x,Nb_{1-x})O_3$ and $Ba_{0.99}(Ti_x,Nb_{1-x})O_3$ where x = 0.9925, 0.995 and 0.99 were prepared.

6.2.1 X-ray Diffraction of $Ba(Ti_x,Nb_{1-x})O_3$ and $Ba_{0.99}(Ti_x,Nb_{1-x})O_3$

After sintering for 2 hours at 1340°C, the pellets were all analysed using a Bruker D8 diffractometer with scans ranging from 20 to 80^o 2θ with a step size of 0.033 at a rate of 0.5s/step.

All of the spectra were matched to ICDD data files corresponding with tetragonal $BaTiO_3$. This is due to the dopant amounts not being present in large enough amounts for the diffractometer to detect. However, a second phase of Nb_2O_5 was detected in two of the samples. Figure 6.28 shows the x ray diffraction spectra of the Nb_2O_5 doped $BaTiO_3$ samples.

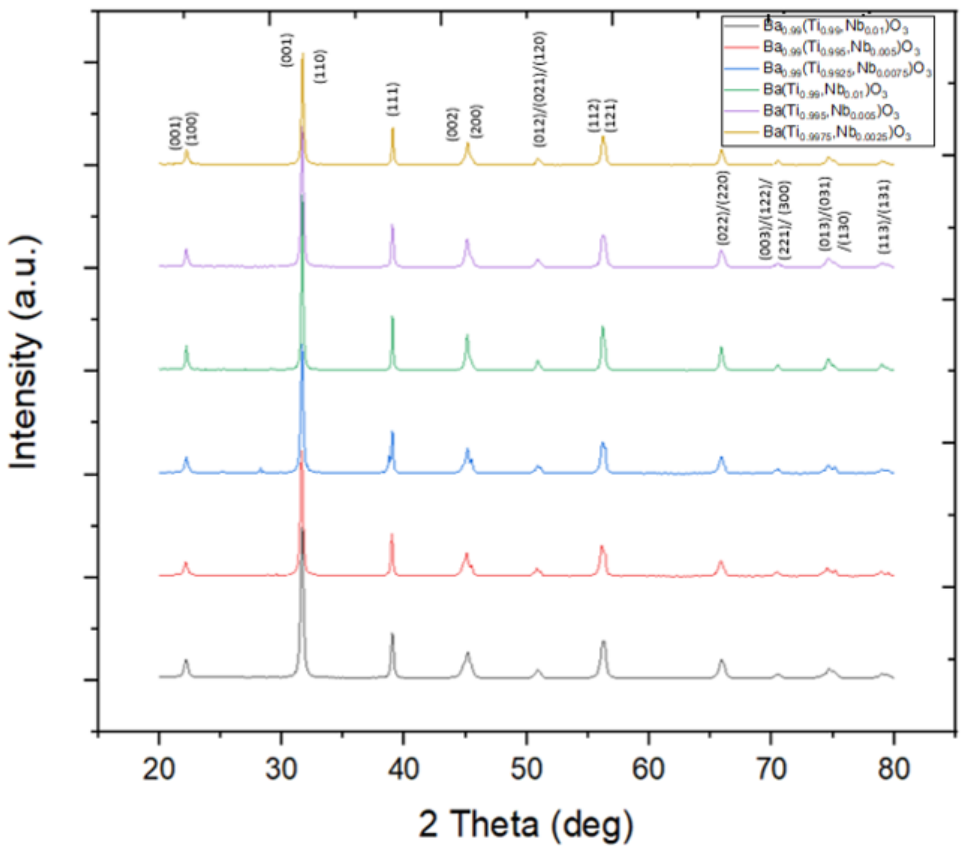

Figure 6. 28 Showing the XRD spectra for all of the $Ba(Ti_x,Nb_{1-x})O_3$ and $Ba_{0.99}(Ti_x,Nb_{1-x})O_3$ compositions after sintering for 2 hours at 1340°C.

From Figure 6.28 It can be seen that there are some small impurity peaks in the spectra of $Ba(Ti_{0.99},Nb_{0.01})O_3$ and $Ba_{0.99}(Ti_{0.9925},Nb_{0.0075})O_3$. Figures 6.29 and 6.30 show these spectra with labelled impurity peaks.

Figure 6.29 is the X-ray diffraction spectra of $Ba(Ti_{0.99},Nb_{0.01})O_3$. There are some small impurity peaks at ~ 29° 2θ, these peaks correspond with the ICDD data file 00-027-1313 for Nb_2O_5. The X-ray diffraction spectra of $Ba_{0.99}(Ti_{0.9925},Nb_{0.0075})O_3$, shown in Figure 6.30 shows several impurity peaks two of which also match the ICDD file for Nb_2O_5 with the remaining impurity peaks matching an ICDD file for TiO_2 (file number 04-014-5355).

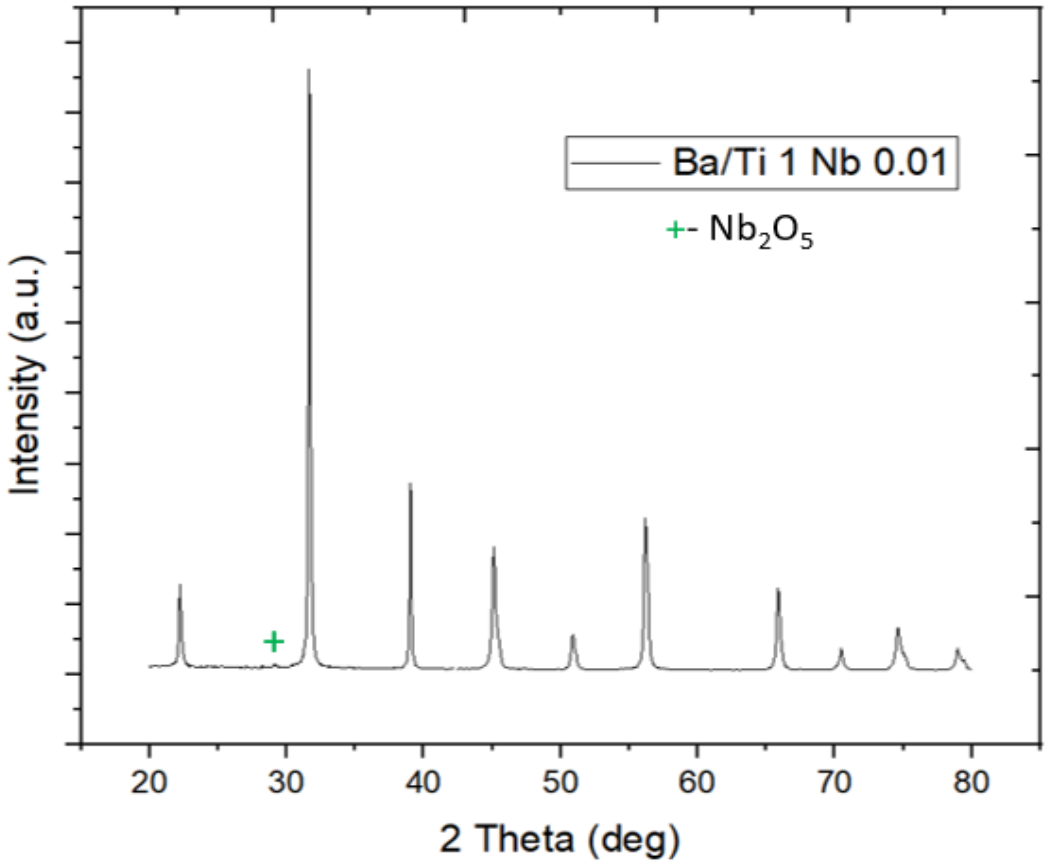

Figure 6. 29 Showing the XRD spectrum of $Ba(Ti_{0.99},Nb_{0.01})$ sintered at 1340°C for 2 hours with the impurity peaks labelled.

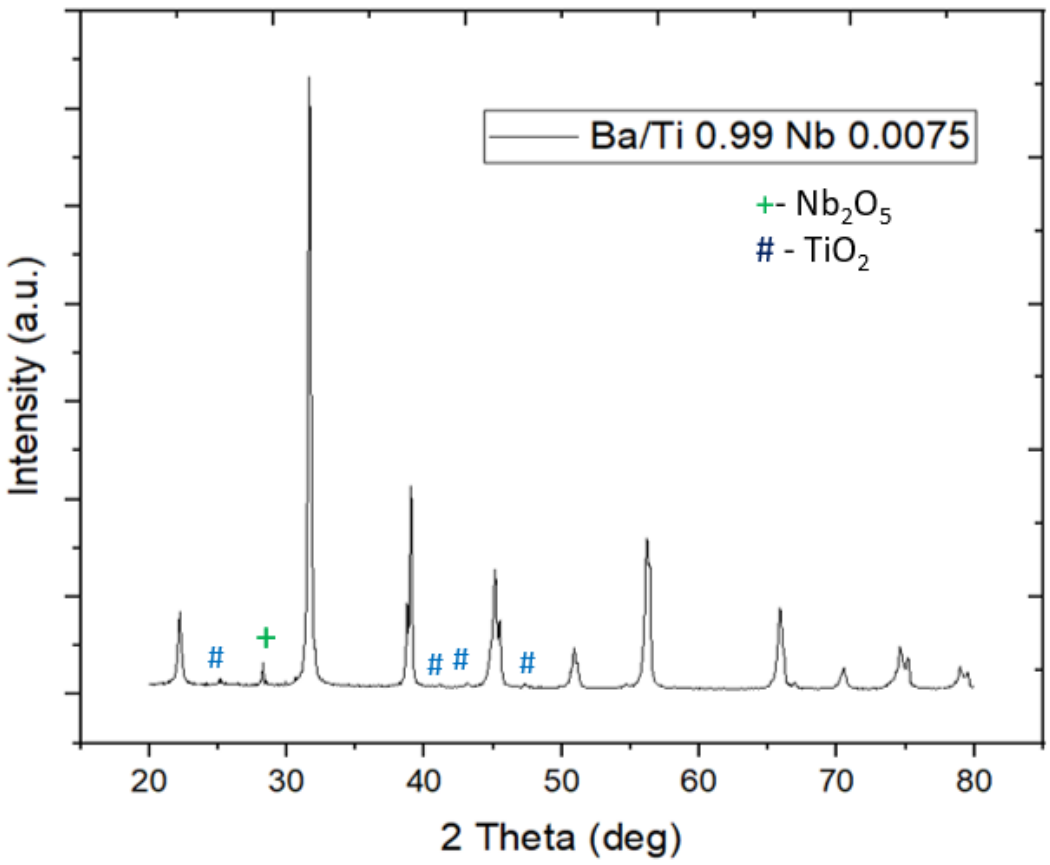

Figure 6. 30 Showing the XRD spectrum of $Ba_{0.99}(Ti_{0.9925},Nb_{0.0075})O_3$ sintered at 1340°C for 2 hours with the impurity peaks labelled.

6.2.2 Grain Growth in $Ba(Ti_x,Nb_{1-x})O_3$ and $Ba_{0.99}(Ti_x,Nb_{1-x})O_3$

The different composition of Nb_2O_5 doped $BaTiO_3$ were sintered at 1340°C in order to examine the effect of the eutectic liquid on grain growth. Different sintering times were used in order to understand the rate of grain growth in these samples. The sintering times used were 0.5, 1, 2, 4, 8 and 16 hours. Figure 6.31 shows a plot of average grain sizes vs sintering times for all the compositions produced along with plots showing the standard deviation of the grain size measurements. From this plot it can be seen that addition of Nb_2O_5 restricts grain growth and all the samples produced had a fine-grained microstructure and average grain size was found to be inversely proportional to Nb_2O_5 concentration in the samples. The addition of excess TiO_2 resulted in larger average grain size than any of the samples with a Ba/Ti ratio of 1.

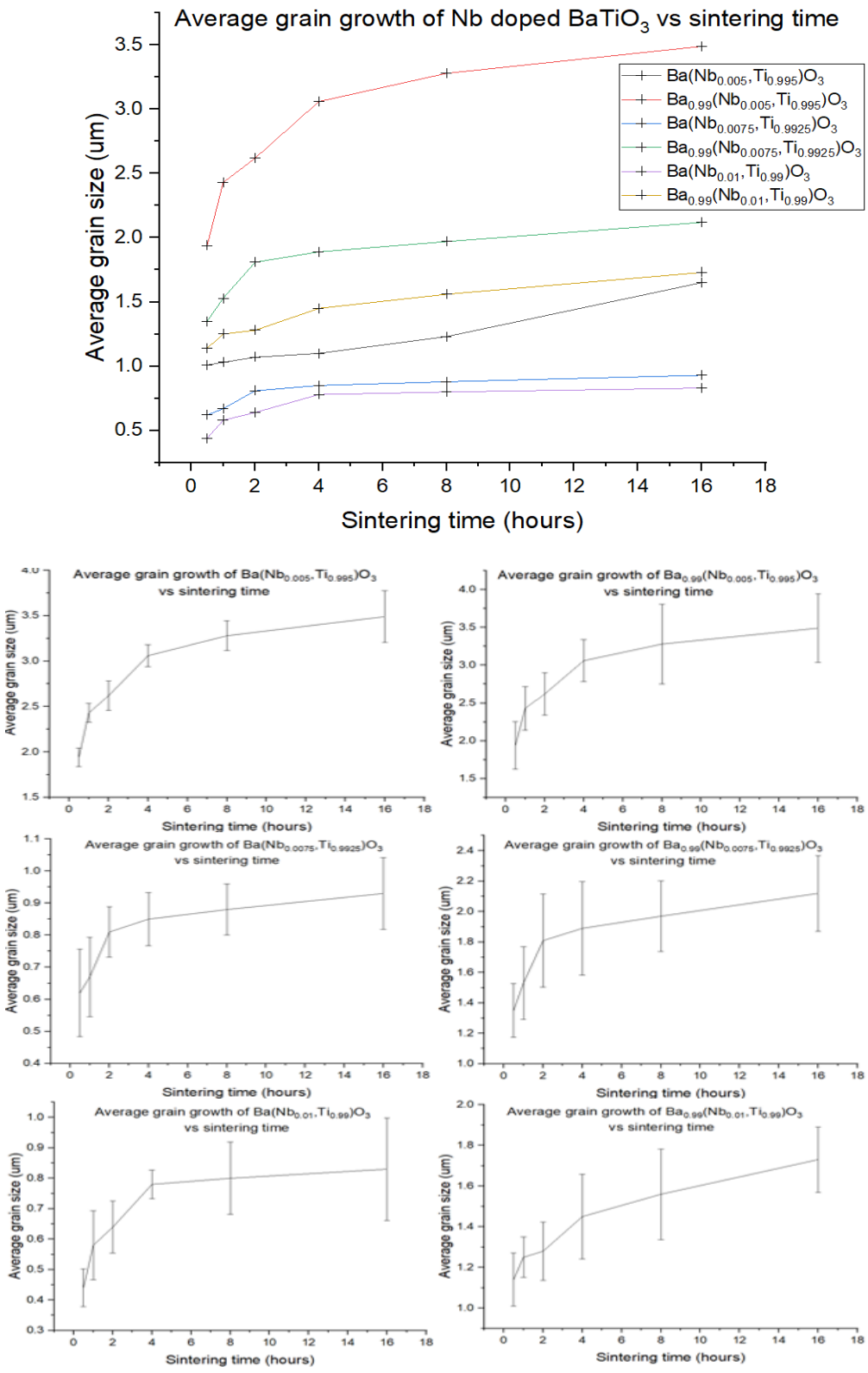

Figure 6. 31 Showing a plot of grain size (µm) vs sintering time (hours) for the Nb_2O_5 doped $BaTiO_3$ compositions with Ba/Ti ratios of 1 and 0.99 sintered at 1340°C. The smaller graphs display the same data with error bars to show the standard deviation of the grain growth measurements.

Figure 6.32 shows SEM images of the Nb_2O_5 doped samples when sintered for 2 hours at 1340°C. From these images it can be seen that the microstructures of Nb_2O_5 doped $BaTiO_3$ are considerably finer grained than $BaTiO_3$. Another important feature of these microstructures is the absence of intragranular porosity. This is thought to be due to the slower rate of growth in these samples resulting from Nb_2O_5 addition inducing the solute drag effect discussed in Chapter 3.

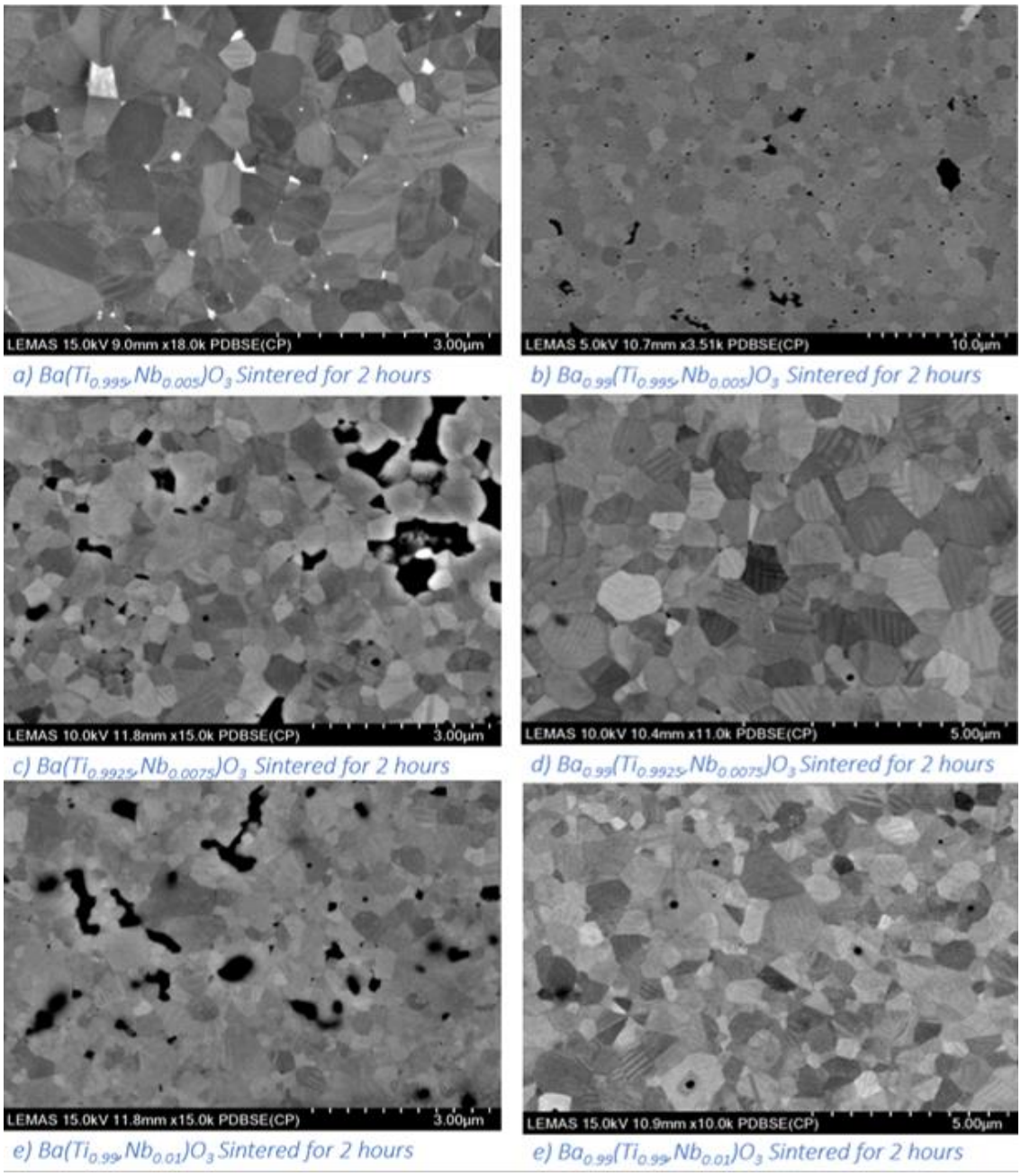

Figure 6. 32 Showing the different compositions of $BaTiO_3$ doped with Nb_2O_5 sintered at 1340°C for 2 hours.

Figure 6.33 shows scanning electron micrographs of the of $Ba(Ti_{0.995},Nb_{0.005})O_3$ samples across the various sintering times, all sintered at 1340°C. These samples had the third smallest average grain size across all the sintering times as shown in Figure 6.31. The grains are larger than the compositions containing higher Nb_2O_5 concentrations but smaller than the samples containing excess TiO_2. Again, it is clear the presence of grain twinning does not always equate to large abnormal grains.

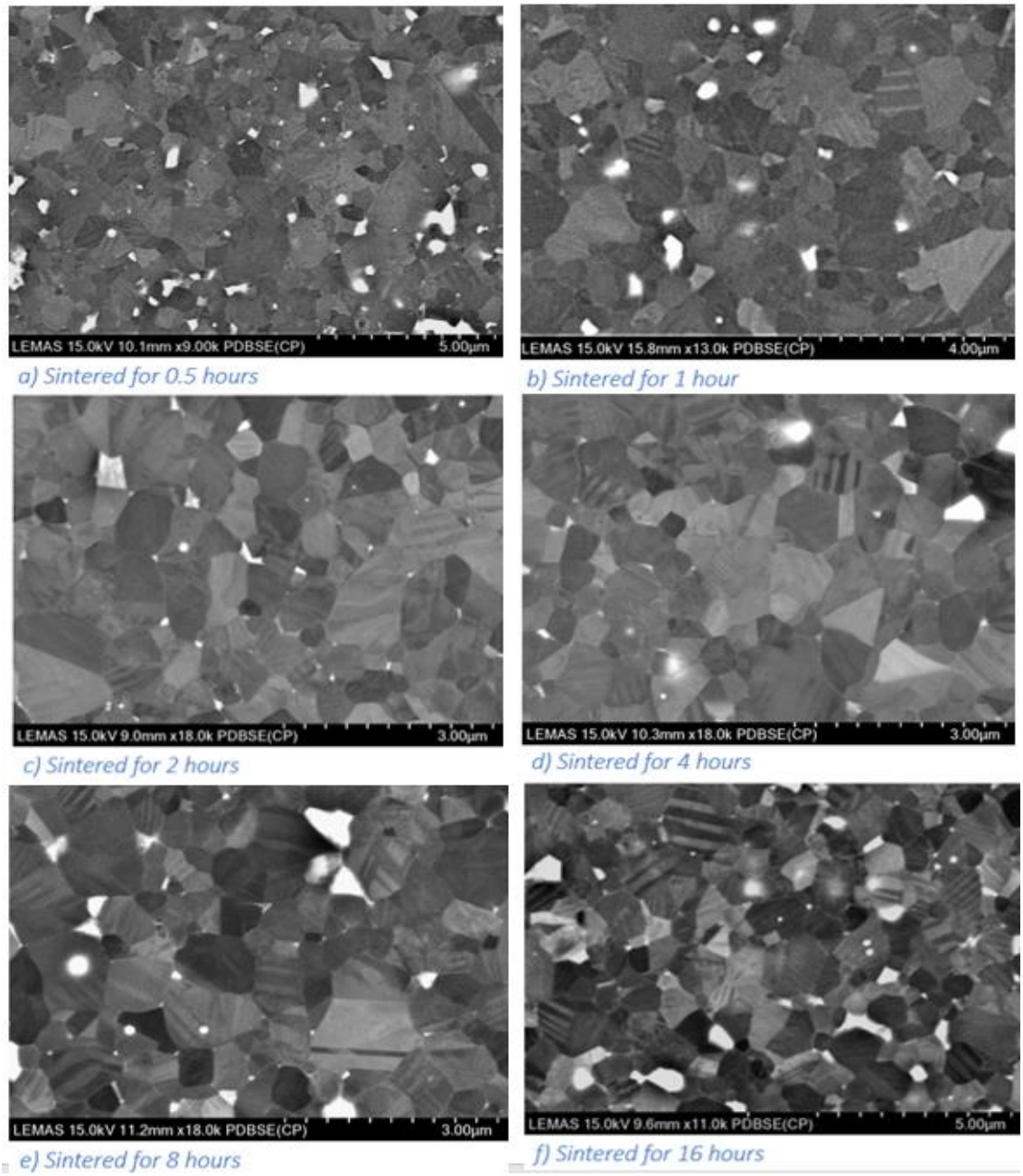

Figure 6. 33 Shows scanning electron micrographs of $Ba(Ti_{0.995},Nb_{0.005})O_3$ sintered at 1340°C for various lengths of time.

Figure 6.34 shows the scanning electron micrographs taken of $Ba_{0.99}(Ti_{0.995},Nb_{0.005})O_3$. This sample had the largest average grain size across the various sintering temperatures.

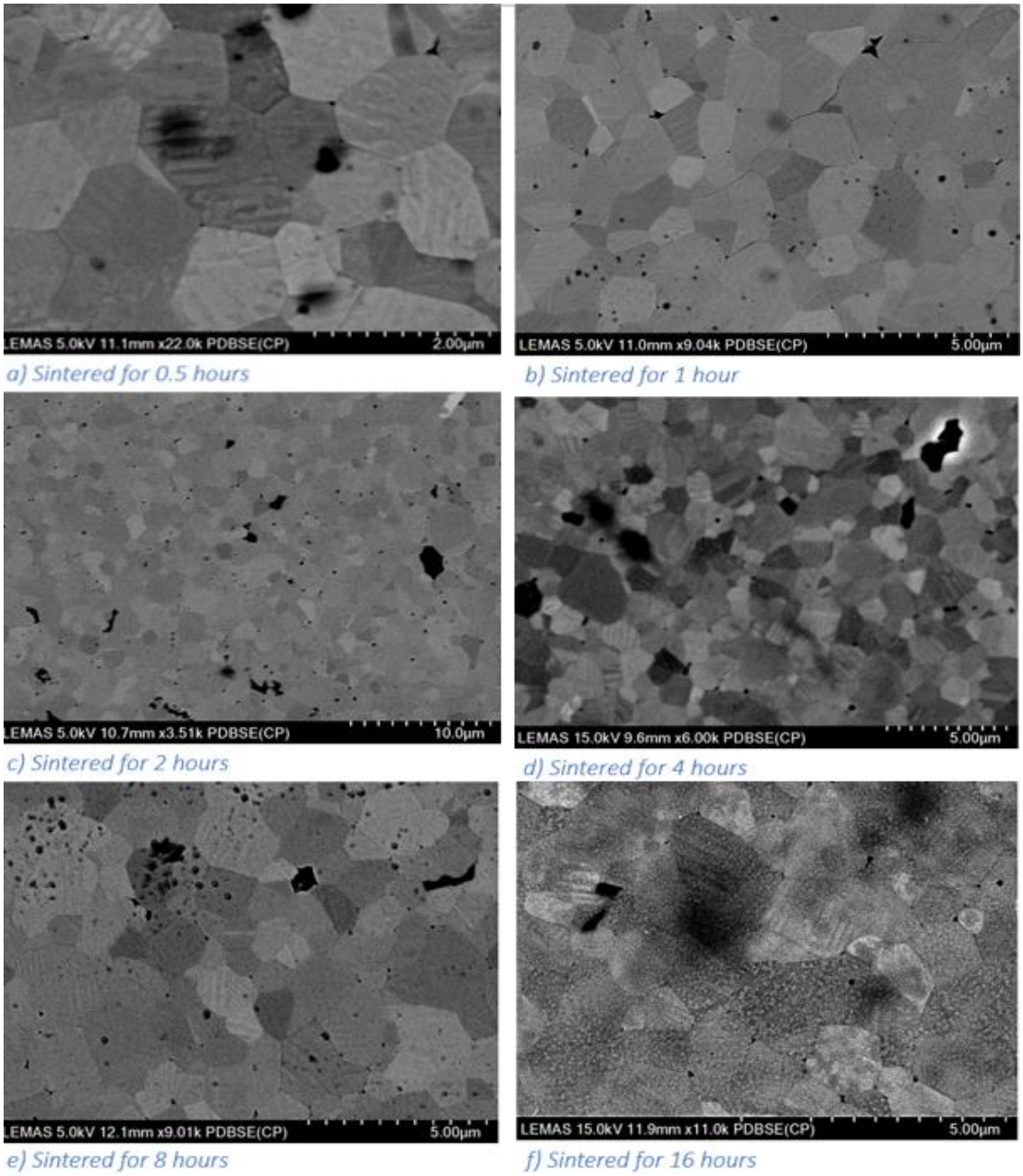

Figure 6. 34 Shows scanning electron micrographs of $Ba_{0.99}$ $(Ti_{0.995},Nb_{0.005})O_3$ sintered at 1340°C for various lengths of time.

The micrographs of $Ba(Ti_{0.9925},Nb_{0.0075})O_3$ are shown below in Figure 6.35. This sample had the second smallest average grain size. There is evidence of intergranular porosity in this sample, although unlike the $BaTiO_3$ samples there is limited evidence of intragranular porosity.

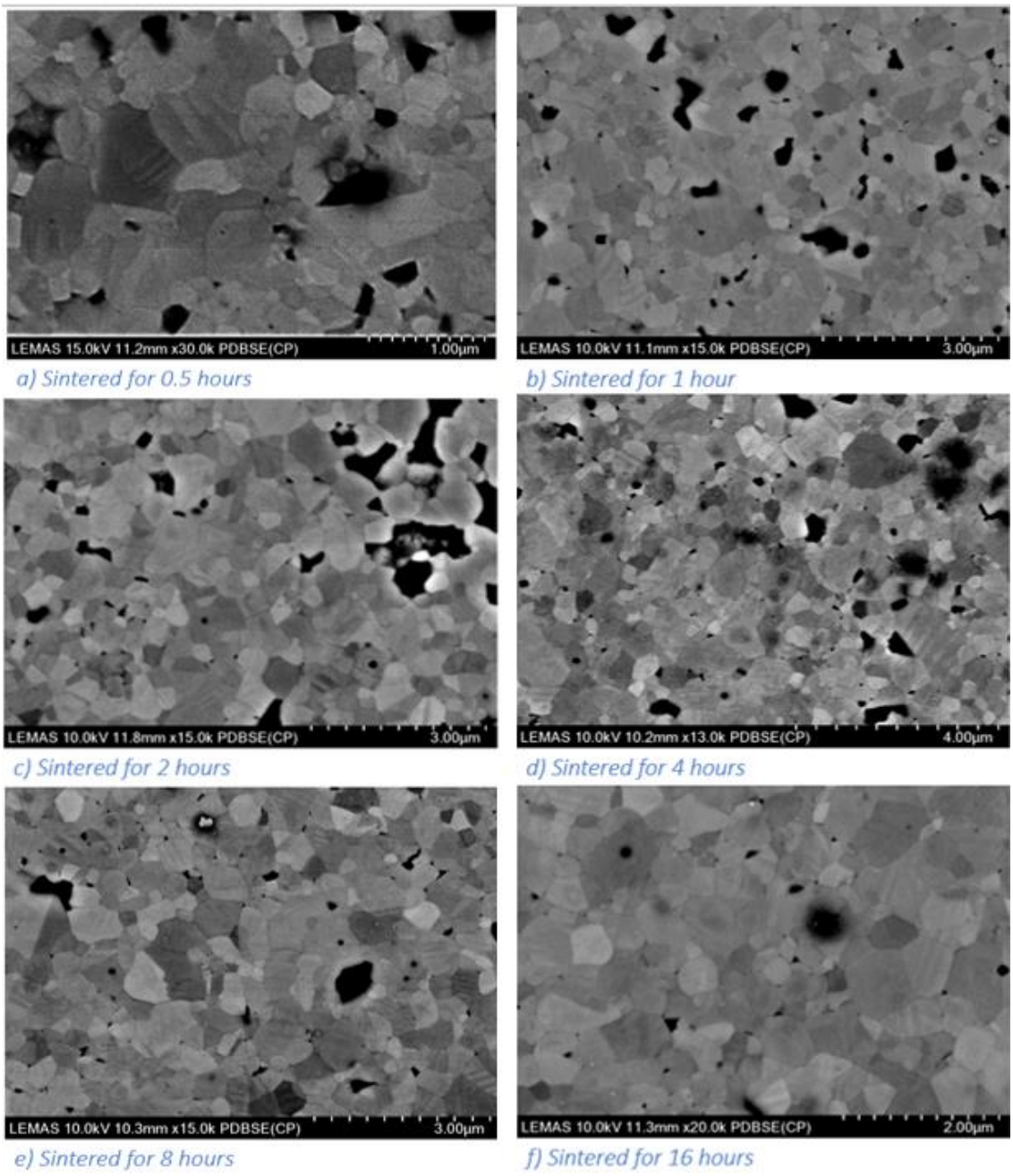

Figure 6. 35 Shows scanning electron micrographs of Ba $(Ti_{0.9925},Nb_{0.0075})O_3$ sintered at 1340°C for various lengths of time.

The sample with the second largest average grain size was $Ba_{0.99}$ ($Ti_{0.9925}$,$Nb_{0.0075}$)O_3 (shown in Figure 6.36). This sample had much less porosity than the Nb_2O_5 equivalent sample.

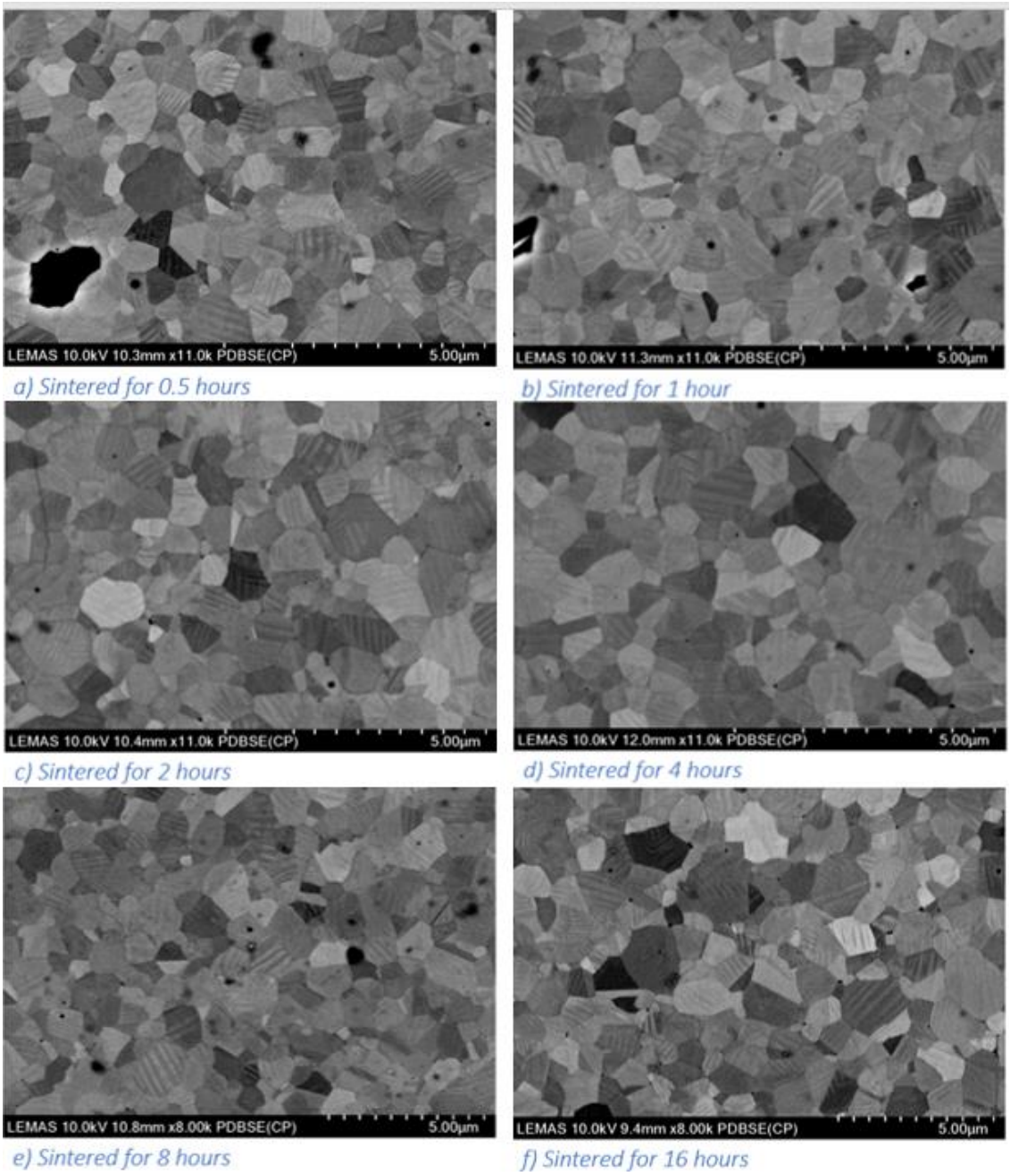

Figure 6. 36 Shows scanning electron micrographs of $Ba_{0.99}$ ($Ti_{0.9925}$,$Nb_{0.0075}$)O_3 sintered at 1340°C for various lengths of time.

Figure 6.37 Shows micrographs of Ba $(Ti_{0.99},Nb_{0.01})O_3$, this sample has the highest Nb_2O_5 concentration and in the absence of excess TiO_2 the smallest average grain size. Some of the images shown also illustrate some porosity between grain boundaries.

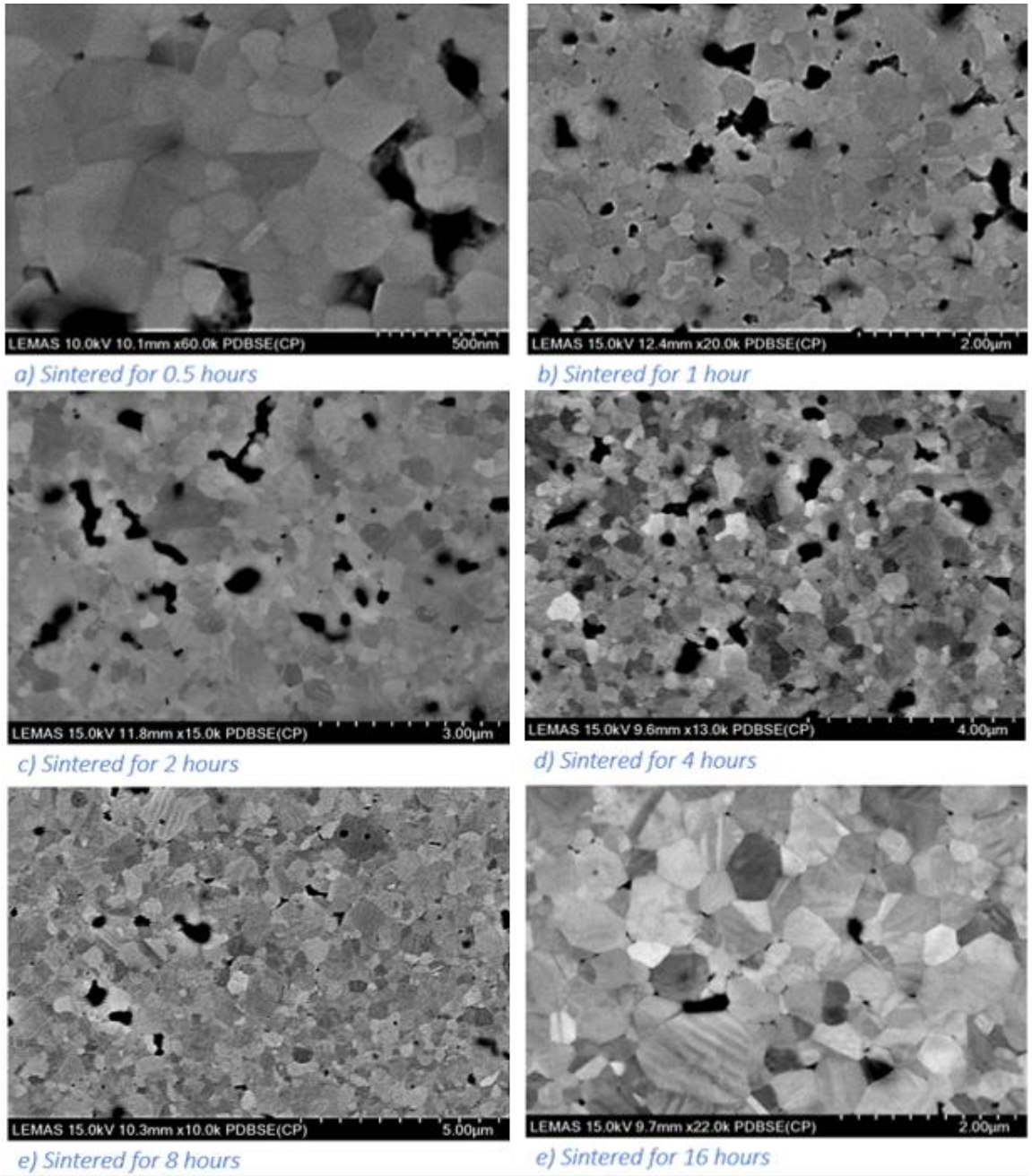

Figure 6. 37 Shows scanning electron micrographs of Ba $(Ti_{0.99},Nb_{0.01})O_3$ sintered at 1340°C for various lengths of time.

Figure 6.38 Shows images taken by SEM of $Ba_{0.99}$ $(Ti_{0.99},Nb_{0.01})O_3$. As this sample has the largest concentration of Nb_2O_5 alongside a Ba/Ti ratio of 0.99 it has the third largest average grain size. Grains are larger than in the samples with a Ba/Ti ratio of 1 but smaller than the samples containing excess TiO_2 but a smaller Nb_2O_5 concentration. Again, the addition of TiO_2 correlates with a reduction in intergranular porosity.

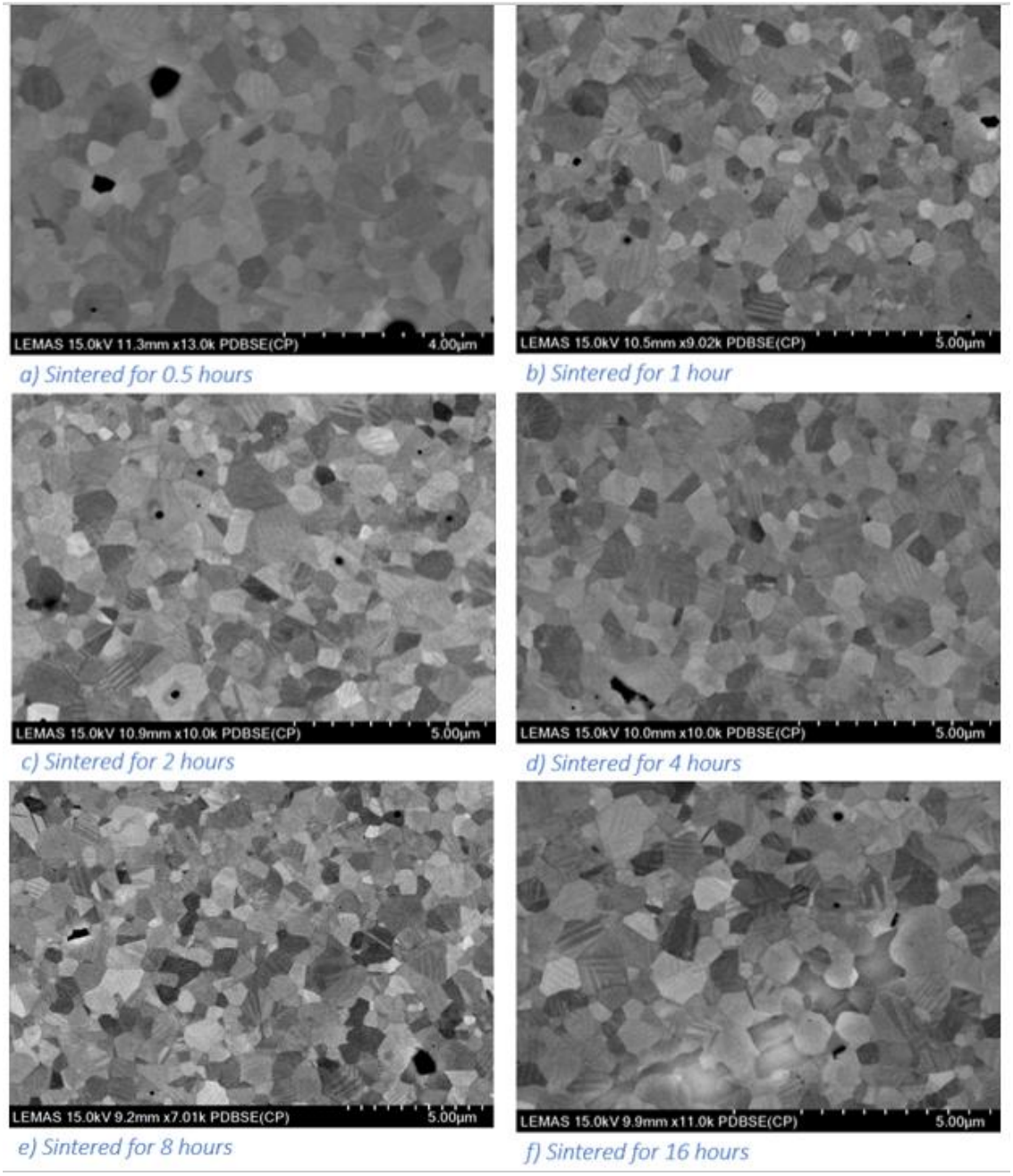

Figure 6. 38 Shows scanning electron micrographs of $Ba_{0.99}$ $(Ti_{0.99},Nb_{0.01})O_3$ sintered at 1340°C for various lengths of time.

6.2.3 Solid state crystal growth in $Ba_{0.99}(Ti_{0.995},Nb_{0.005})O_3$

As evidenced by the grain growth studies Nb_2O_5 addition caused significant changes to the microstructure of $BaTiO_3$. The decrease in grain size and reduction of porosity could be beneficial during SSCG by preventing large grains developing in the bulk, that could prevent crystal growth and to reduce porosity in the crystal. One issue with using a Nb doped $BaTiO_3$ however, is that the solute drag mechanism responsible for reducing grain size in the bulk would also restrict crystal growth. For this reason it was decided that an experiment would be conducted using a layer $BaTiO_3$ with 1 mol% excess TiO_2 on top of Nb_2O_5 doped $BaTiO_3$. This would mean that the seed crystal would be pressed In TiO_2 rich $BaTiO_3$ and could begin growth before reaching the Nb layer where grain growth would be reduced. 0.2g of $BaTiO_3$ with 1 mol% excess TiO_2 and 0.5g of $Ba_{0.99}(Ti_{0.995},Nb_{0.005})O_3$ were used. This composition was chosen as it would likely be the least restrictive to crystal growth whilst still producing a fine grained microstructure. The seeded pellet was then sintered for 72 hours at 1340°C. The sample can be viewed in Figure 6.39 and 6.40 and the compositional layers are evident. The blue/grey layer is the $Ba_{0.99}(Ti_{0.995},Nb_{0.005})O_3$ and the brown/gold layer is the $BaTiO_3$ with excess TiO_2.

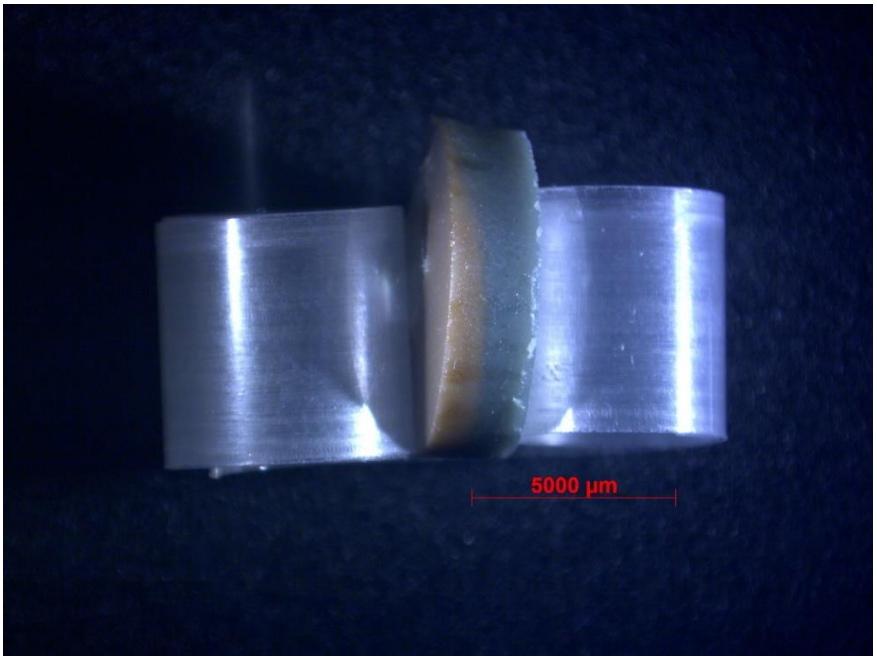

Figure 6. 39 Showing the sample containing a seed crystal pressed into $BaTiO_3$ with 1mol% excess TiO_2 on top of a layer of $Ba_{0.99}(Ti_{0.995},Nb_{0.005})O_3$ sintered at 1340°C for 72 hours. This image was taken at 0.75x magnification and the pellet is being held in a clip.

Figure 6. 40 Showing a cross section of the sample containing a seed crystal pressed into $BaTiO_3$ with 1mol% excess TiO_2 on top of a layer of $Ba_{0.99}(Ti_{0.995},Nb_{0.005})O_3$ sintered at 1340°C for 72 hours. This image was taken at 5x magnification and the pellet is being held in a clip.

Figure 6.41 shows microscope images of the same sample. The compositional difference can be seen clearly here as a drastic difference in grain size. There is evidence of some SSCG in these images although only a small amount. The crystal has not grown into the Nb_2O_5 doped region suggesting the restriction of grain growth has also prevented crystal growth. The maximum growth length of this crystal was found to be ~182µm giving it a growth rate of 2.5µm/hr.

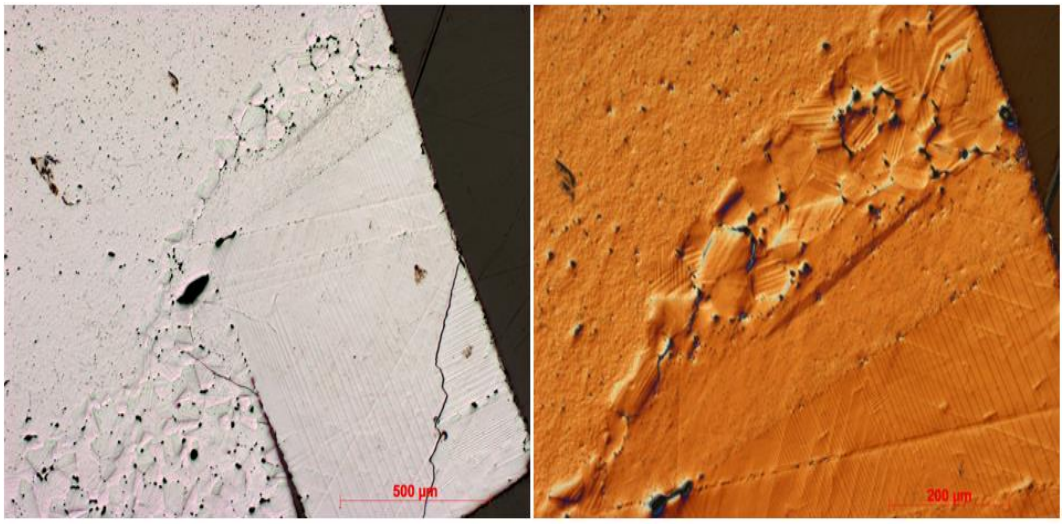

Figure 6. 41 a (left) and b (right) Showing a cross section of the sample containing a seed crystal pressed into $BaTiO_3$ with 1mol% excess TiO_2 on top of a layer of $Ba_{0.99}(Ti_{0.995},Nb_{0.005})O_3$ sintered at 1340°C for 72 hours. Image a was taken in bright field at 5x magnification and image b is taken at 10x magnification in bright field using polarised light and differential interference contrast.

6.2.4 Discussion

6.2.4.1 Grain growth in $Ba(Ti_x,Nb_{1-x})O_3$ and $Ba_{0.99}(Ti_x,Nb_{1-x})O_3$.

It is known that Nb doping can affect the grain structure of $BaTiO_3$ by reducing grain growth rate [14]. The mechanism by which this occurs is known as solute drag. Solute drag is caused by the diffusion of impurities of dopants, in this case Nb atoms, toward the grain boundary region which provides them with a low energy site. This diffusion of solutes occurs at a slower rate than diffusion across the grain boundary. This results in longer range diffusions to maintain equilibrium concentration distributions and thus becomes the rate limiting step [81]. Although grain boundary mobility is reduced during this process densification is not therefore microstructures with less porosity than in undoped $BaTiO_3$ were observed and can be seen in Figure 6.38. The reduction in grain size due to solute drag was evident in all the Nb doped concentrations with this effect increasing with Nb concentration. The presence of a TiO_2 excess did result in slightly larger grains although the effect of any liquid phase enhancement on grain growth was minor and the largest observed grain size was 3.5um in $Ba_{0.99}$ $(Ti_{0.995},Nb_{0.005})O_3$ sintered at 1340°C for 16 hours.

6.2.4.2 Solid state crystal growth in $Ba(Ti_x,Nb_{1-x})O_3$ and $Ba_{0.99}(Ti_x,Nb_{1-x})O_3$

When compositional interlayers of Nb doped $BaTiO_3$ were used for SSCG experiments only a small amount of crystal growth was observed and crystal growth stopped when it reached the Nb doped layer.

6.3 Barium Zirconate Titanate ($Ba(Zr_{x,}Ti_{1-x})O_3$)

After performing grain growth studies on $BaTiO_3$ and Nb doped $BaTiO_3$, BZT was the next material chosen in order to give perspective on the effect of Zr on the microstructure. The compositions made were $Ba(Zr_{0.01,}Ti_{0.99})O_3$, $Ba_{0.99}(Zr_{0.01,}Ti_{0.99})O_{3,}$ $Ba(Zr_{0.02,}Ti_{0.98})O_3$ and $Ba_{0.99}(Zr_{0.02,}Ti_{0.98})O_{3.}$ These compositions were chosen so that the effects of both ZrO_2 and TiO_2 could be examined. These samples were sintered at a range of temperatures (1360°C, 1380°C, 1400°C, 1420°C, 1440°C and 1460°C) for 8 hours.

6.3.1 X-ray Diffraction of $Ba(Zr_{x,}Ti_{1-x})O_3$ and $Ba_{99}(Zr_{x,}Ti_{1-x})O_3$

After sintering at 1400°C for 8 hours the pellets were all analysed using a Bruker D8 diffractometer with scans ranging from 20° to 80° 2θ with a step size of 0.033 at a rate of 0.5s/step.

All of the spectra were matched with ICDD files corresponding with tetragonal $BaTiO_3$. These spectra can be seen in Figure 6.42. No impurity peaks were noted for any of the spectra produced.

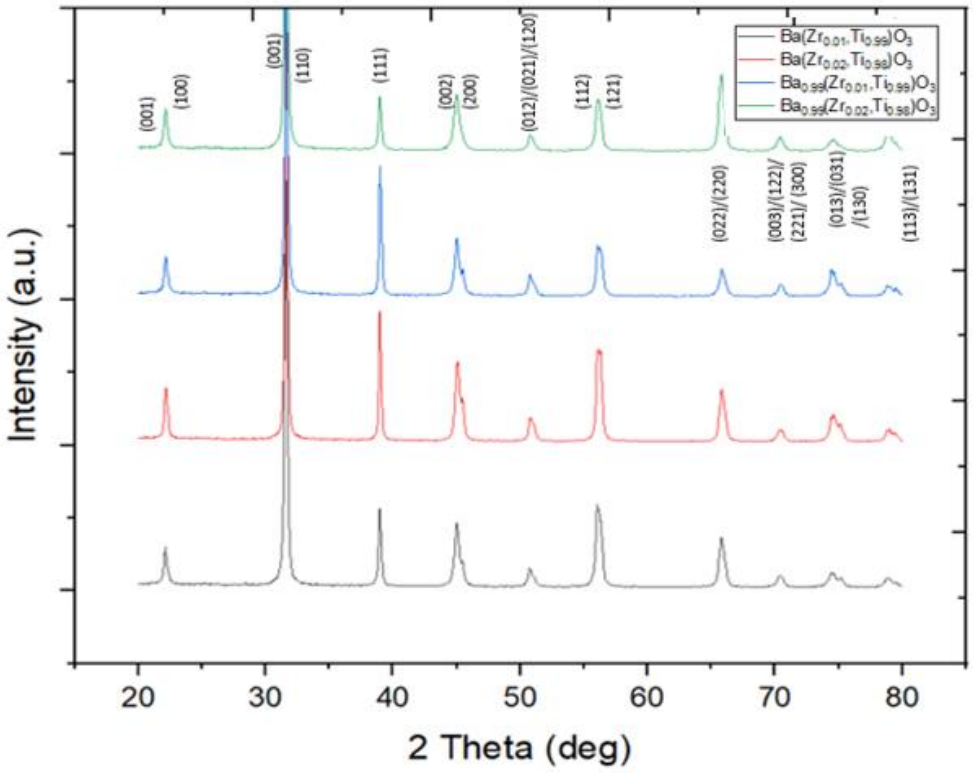

Figure 6. 42 XRD spectra of all the BZT compositions produced after sintering for 8 hours at 1400°C.

6.3.2 Grain Growth in $Ba(Zr_{x,}Ti_{1-x})O_3$

Average grain size at each temperature can be seen in Table 6.2, from the table it is evident that both ZrO_2 and TiO_2 promote grain growth and that ZrO_2 does not cause solute drag and reduced grain size. The largest grains by a considerable amount were found in $Ba_{0.99}(Zr_{0.02,}Ti_{0.98})O_{3.}$ This composition also produced less porosity than its counterparts. Another observation is that abnormal grain growth is prominent in the samples containing no excess TiO_2.

Table 6. 2 Showing the average grain sizes for all of the BZT compositions produced and sintered for 8 hours.

	$Ba(Zr_{0.01},Ti_{0.99})O_3$		$Ba(Zr_{0.02,}Ti_{0.98})O_3$		$Ba_{0.99}(Zr_{0.01},Ti_{0.99})O_3$	$Ba_{0.99}(Zr_{0.02},Ti_{0.98})O_3$
Sintering Temperature (°C)	Average size of smaller grains (µm)	Average size of larger grains (µm)	Average size of smaller grains (µm)	Average size of larger grains (µm)	Average grain size (µm)	Average grain size (µm)
1360	N/A	103.41	8.8	N/A	53.9	259
1380	11.89	110.43	10	N/A	73.6	255.2
1400	22.5	312.3	13.1	N/A	93.8	232
1420	17	193.4	7.5	126	99.3	233
1440	12.7	131	8.9	104	139.3	237.58
1460	N/A	95	16.4	139	148	258

As there was no bimodal grain growth in the compositions containing excess TiO_2 a plot of average grain size vs temperature can be seen for these compositions in Figure 6.43. Unusually in $Ba_{0.99}(Zr_{0.02,}Ti_{0.98})O_3$ the sintering temperature had little effect on the grain size. Where as in $Ba_{0.99}(Zr_{0.01,}Ti_{0.99})O_3$ grain size steadily increased with temperature.

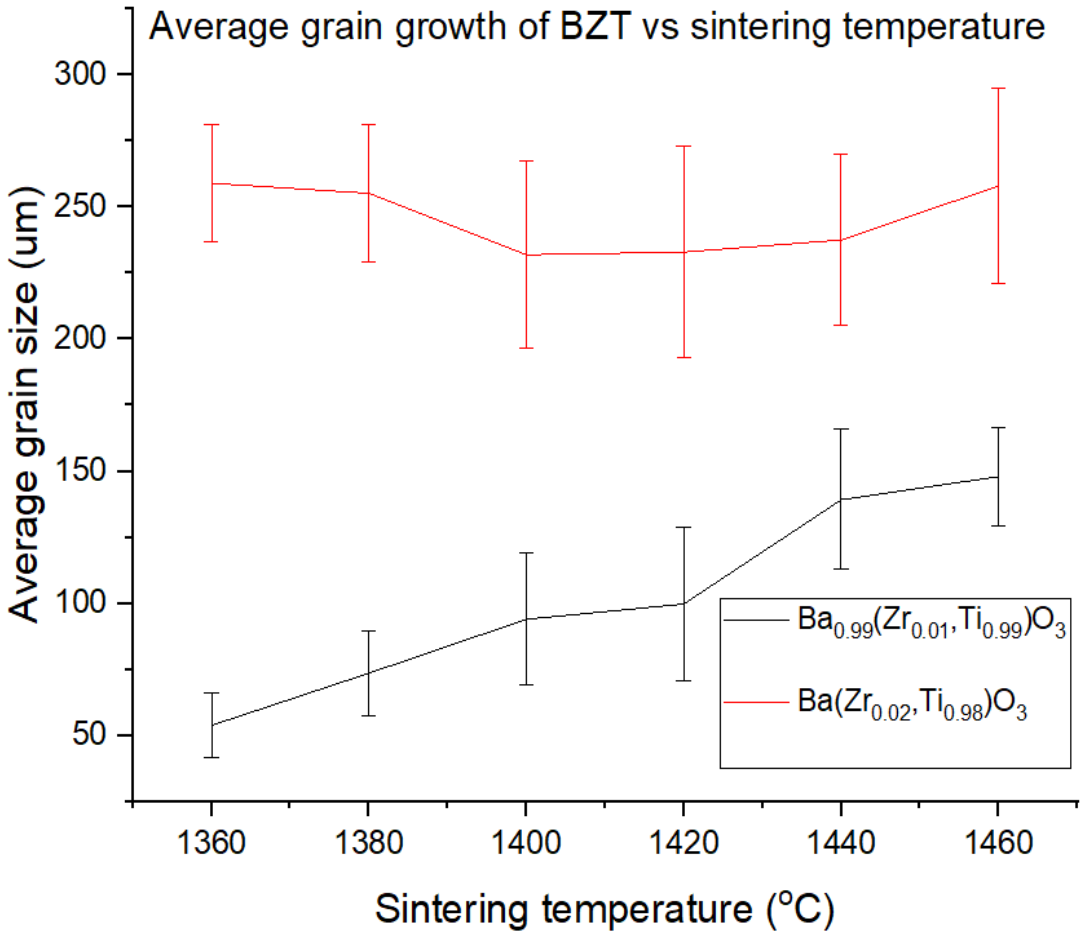

Figure 6. 43 A plot of average grain size vs temperature for the BZT samples containing excess TiO_2 and sintered for 8 hours. The error bars represent the standard deviation of the measured grain sizes.

Figure 6.44 shows scanning electron micrographs of all the BZT samples when sintered at 1460°C.From these images it is clear that BZT composition drastically effects the resulting microstructure in terms of grain size porosity and grain structure.

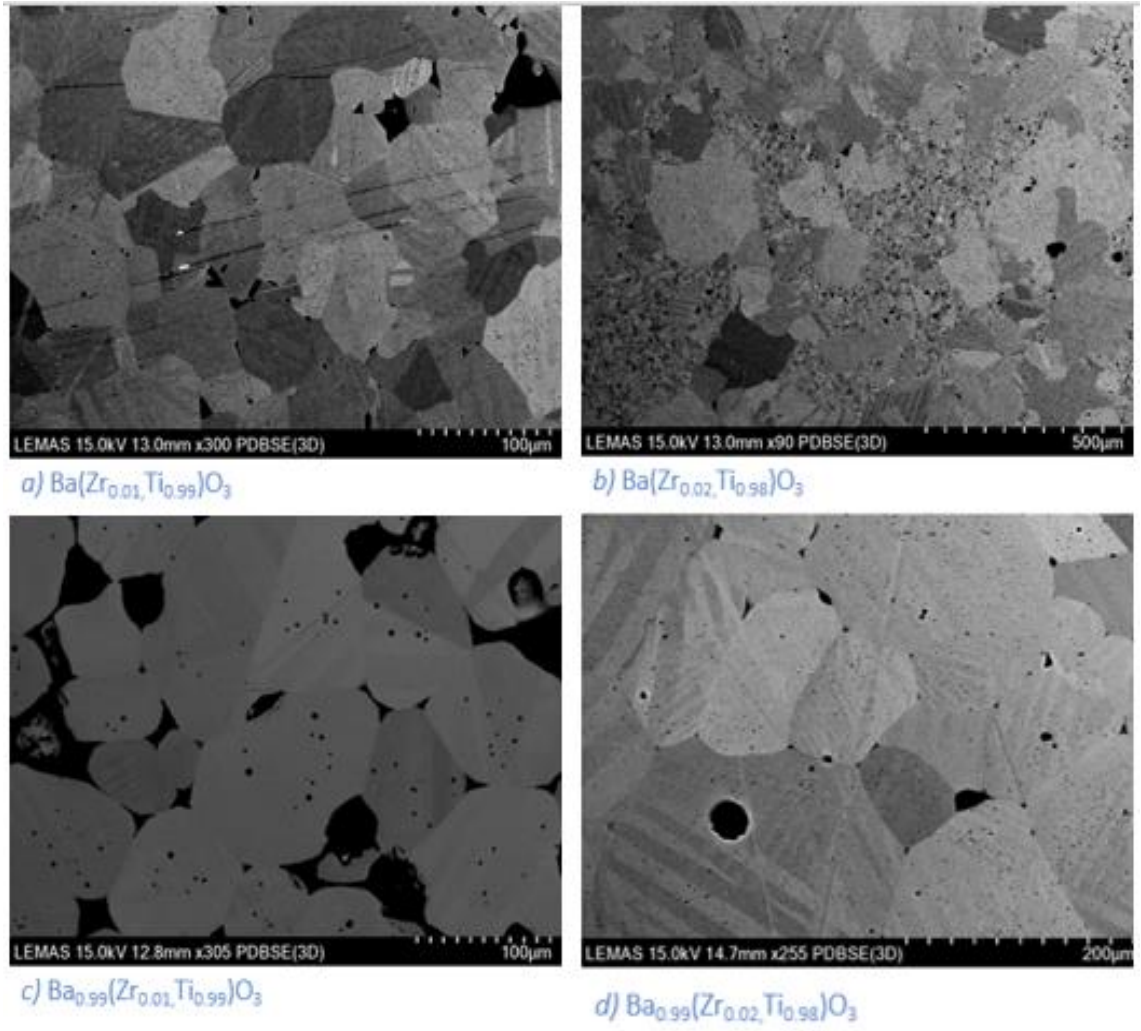

Figure 6. 44 Scanning electron micrographs of the BZT compositions produced and sintered at 1460°C for 8 hours.

Micrographs of $Ba(Zr_{0.01,}Ti_{0.99})O_3$ can be seen in Figure 6.45. From the micrographs it can be seen that at the four middle sintering temperatures abnormal grain growth occurs with normal grain growth at 1360°C and 1460°C. Intragranular porosity is present throughout this sample at all temperature and intergranular porosity can be seen between the smaller grains where bimodal grain growth had occurred. The sintering temperature at which the least porosity occurred was 1460°C.

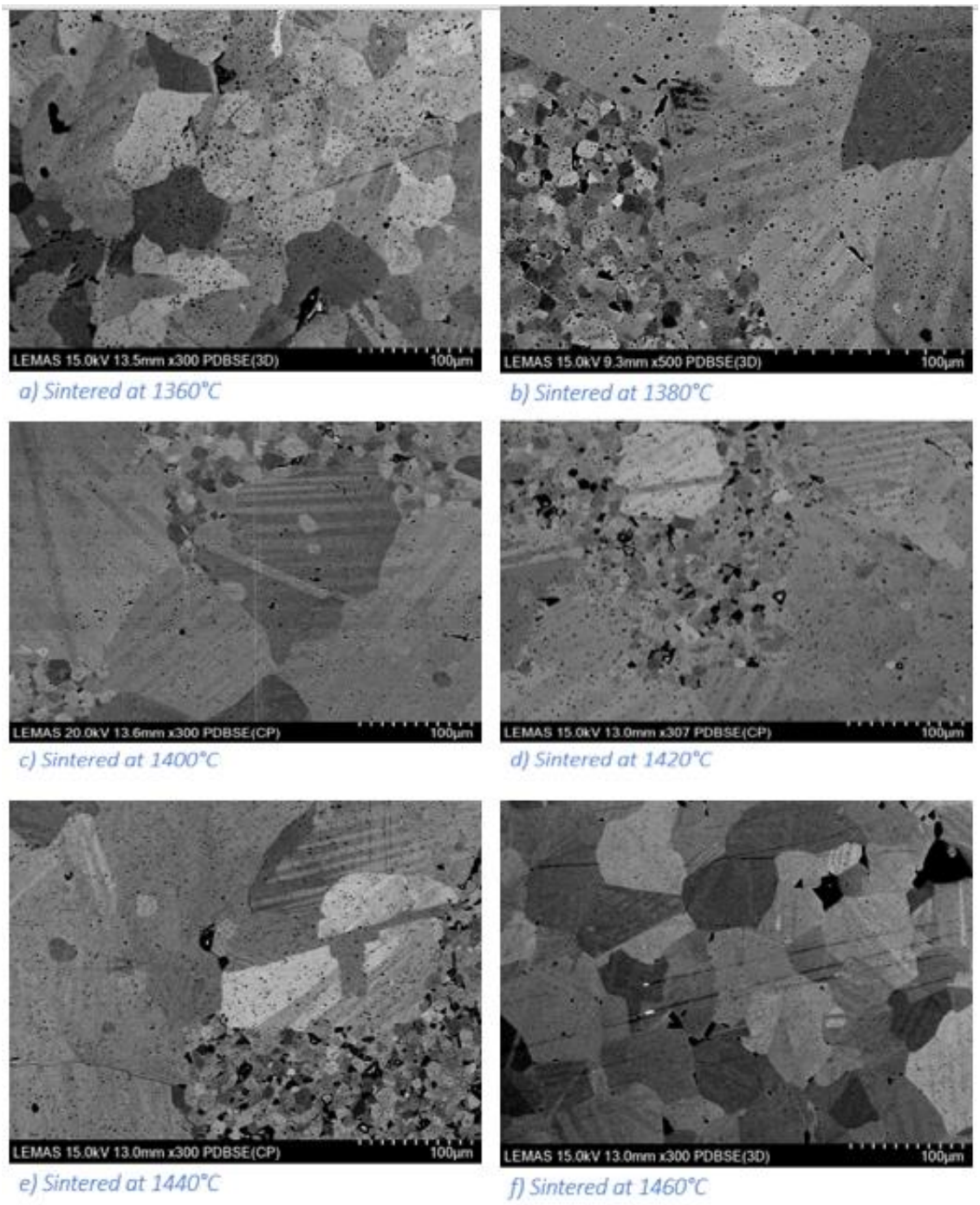

Figure 6. 45 Scanning electron micrographs of $Ba(Zr_{0.01,}Ti_{0.99})O_3$ sintered for 8 hours.

$Ba(Zr_{0.02,}Ti_{0.98})O_3$ had a fine grained microstructure where no abnormal grain growth had occurred with a microstructure similar to TiO_2 deficient $BaTiO_3$. Porosity within both grains and grain boundaries was prevalent in this composition at all sintering temperatures. Figure 6.46 shows scanning electron micrographs of this composition at the various temperatures.

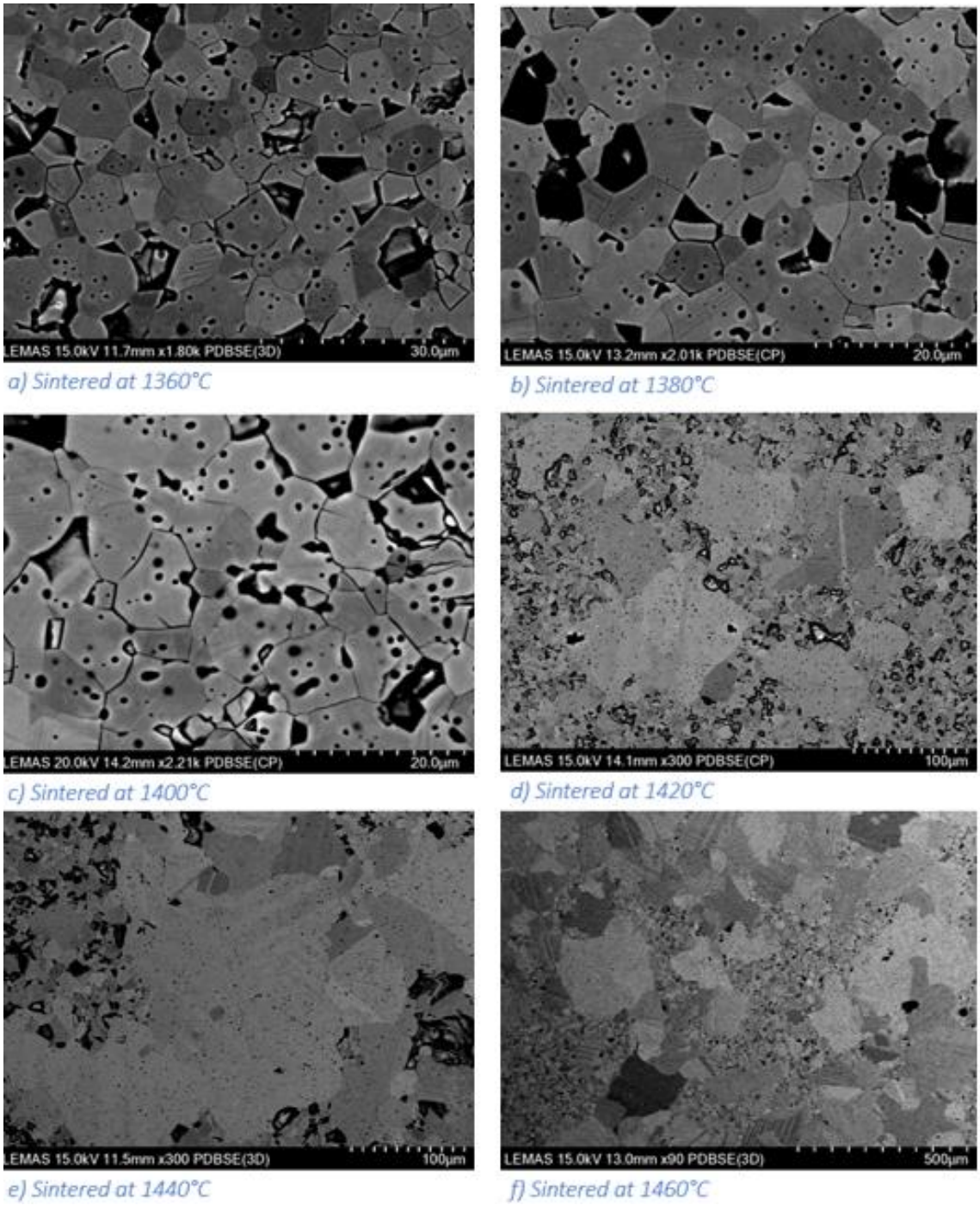

Figure 6. 46 Scanning electron micrographs of $Ba(Zr_{0.02,}Ti_{0.98})O_3$ sintered for 8 hours at various sintering temperatures.

Figure 6.47 shows SEM images of $Ba_{0.99}(Zr_{0.01,}Ti_{0.99})O_3$ sintered at the different sintering temperatures. Porosity was again prevalent in this composition across the range of sintering temperatures. Unlike the samples containing no excess $TiO_{2,}$ grains in this sample were all large and of a more uniform size.

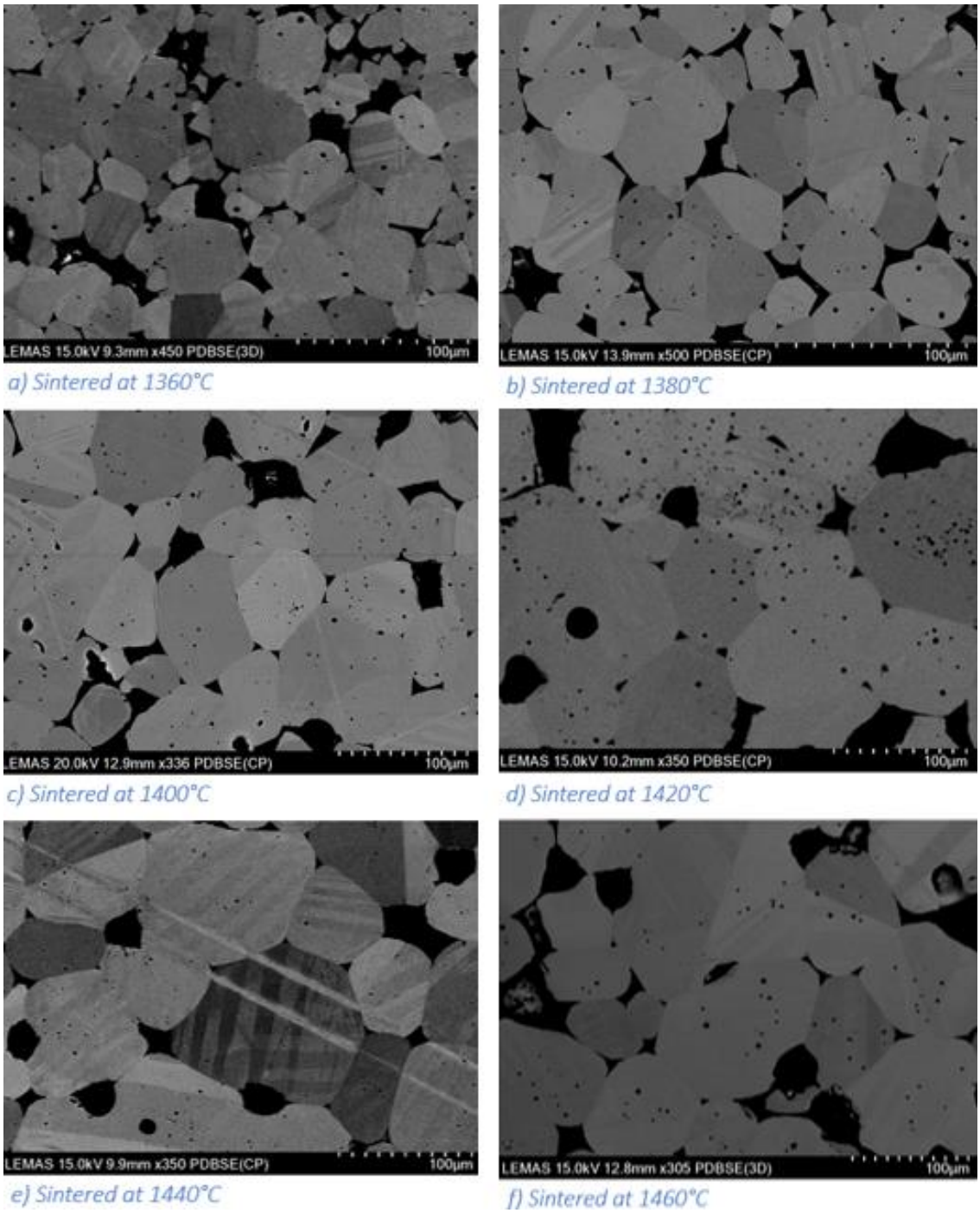

Figure 6. 47 Scanning electron micrographs of $Ba_{0.99}(Zr_{0.01,}Ti_{0.99})O_3$ sintered for 8 hours at various sintering temperatures.

The largest grain sizes along with the least porosity were seen in $Ba_{0.99}(Zr_{0.02,}Ti_{0.98})O_3$. SEM images of this composition can be seen in Figure 6.48.

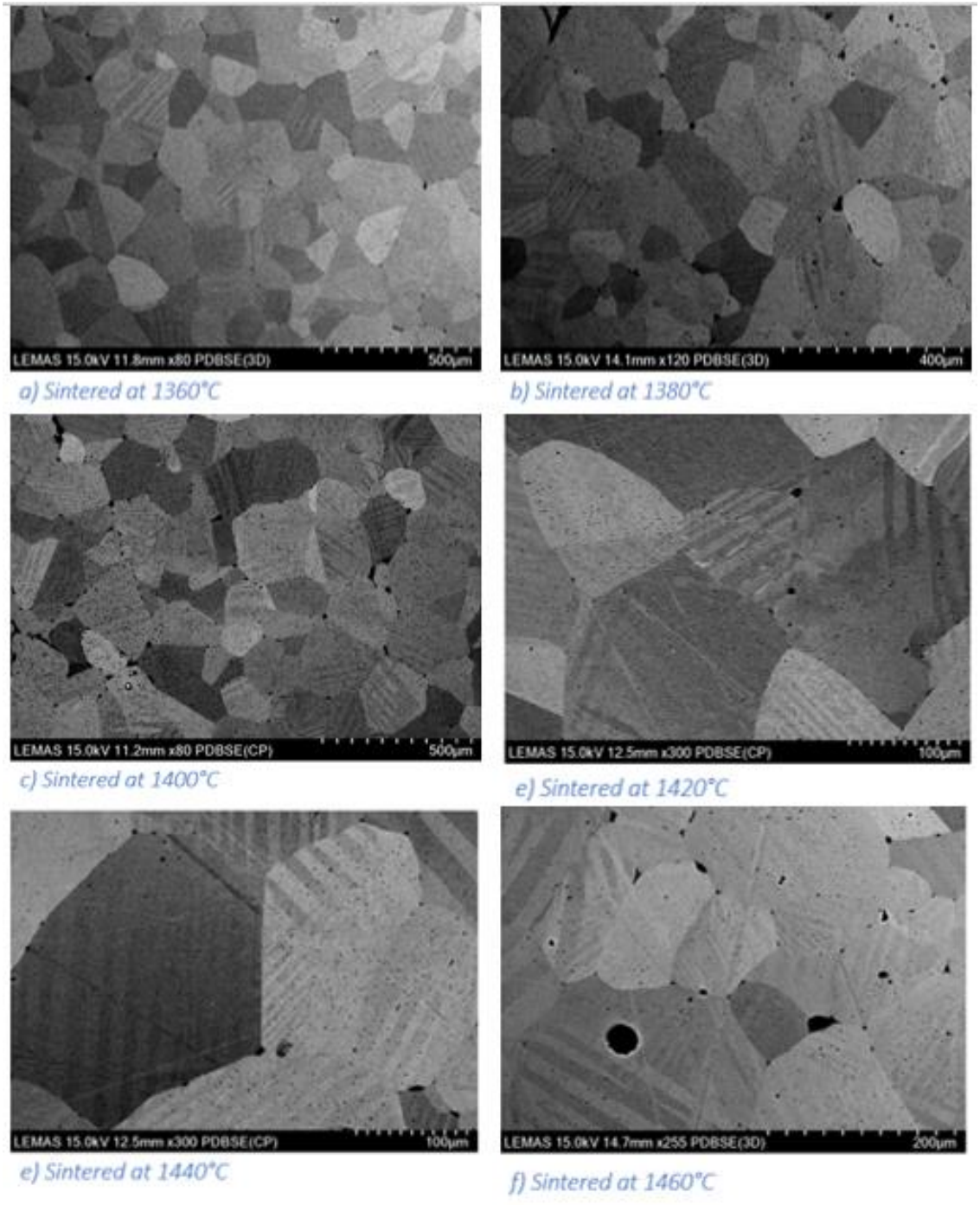

Figure 6. 48 Scanning electron micrographs of $Ba_{0.99}(Zr_{0.02,}Ti_{0.98})O_3$ sintered for 8 hours at various temperatures.

6.3.3 Solid state crystal growth in $Ba(Zr_{x,}Ti_{1-x})O_3$

After conclusion of the grain growth studies solid state crystal growth experiments began. For these experiments the compositions containing excess TiO_2 were initially chosen. After securing a $BaTiO_3$ seed crystal these samples were sintered at 1460°C for 72 hours.

6.3.3.1 Solid state crystal growth in $Ba_{0.99}(Zr_{0.01,}Ti_{0.99})O_3$

After sintering the $Ba_{0.99}(Zr_{0.01,}Ti_{0.99})O_3$ containing the seed crystal, large grains were visible in the sample when viewed with the stereo microscope. There was a small area around the seed crystal where it looked possible that crystal growth had occurred. A stereo microscope image can be seen in Figure 6.49.

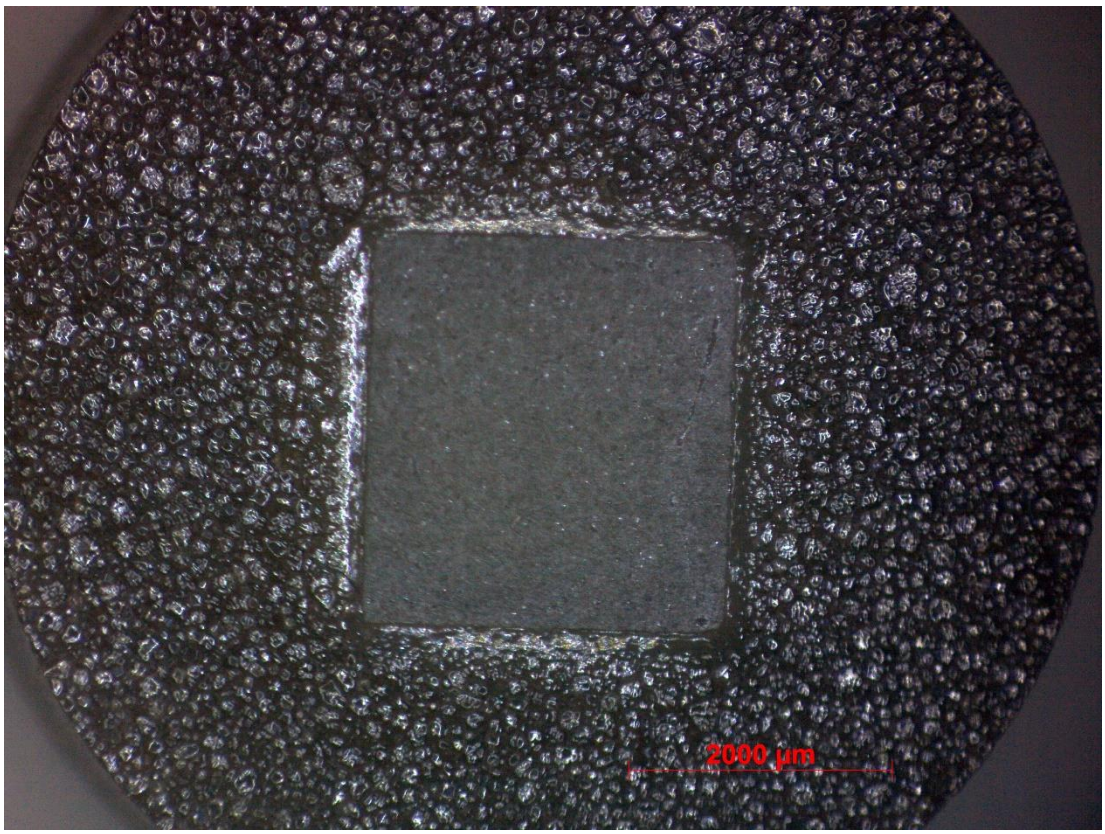

Figure 6. 49 A microscope image taken at 2x magnification of the $Ba_{0.99}(Zr_{0.01,}Ti_{0.99})O_3$ and $BaTiO_3$ single crystal seed after sintering at 1460°C for 72 hours.

Scanning electron microscopy was then performed and it was clear that some solid state crystal growth had taken place. Figure 6.50 shows an SEM image of the seed crystal and grown single crystal. The maximum growth length of the crystal was approximately 452.5µm with a growth rate of ~6.28µm. Unfortunately, the seed crystal was ground down during polishing but the outline of the seed crystal could be determined by the edges of the cross section and the underlying porosity pattern. The pore dense area can be seen in Figure 5.50, this area can be observed in several of the SSCG experiments performed and are likely due to higher growth rate occurring whilst the matrix grains are smaller.

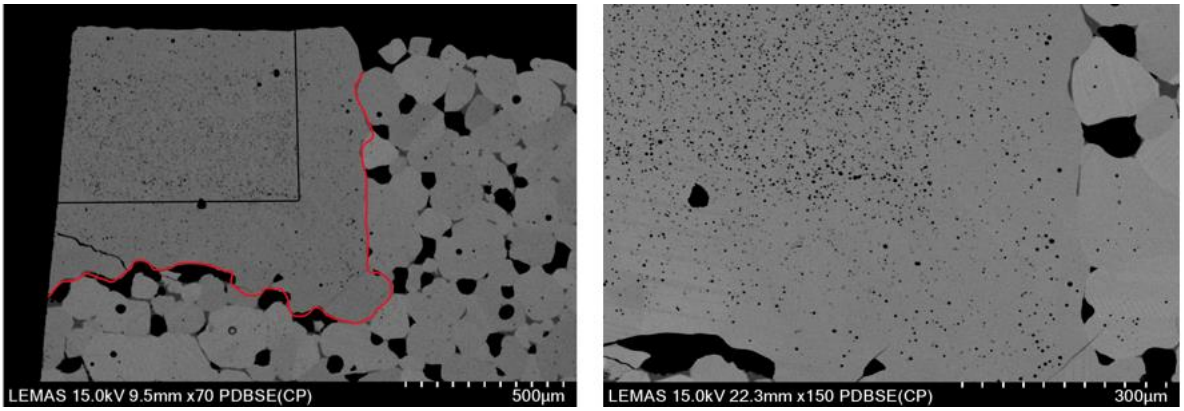

Figure 6. 50 Scanning electron micrographs a (left) and b (right) showing the $Ba_{0.99}(Zr_{0.01,}Ti_{0.99})O_3$ crystal grown. The black line outlines where the $BaTiO_3$ was positioned and the red line outlines the crystal grown.

EDX imaging (Figure 6.51) did not detect any changes in composition, no Zr was detected throughout the sample due to the low amounts added. It should be noted that this sample was coated using carbon.

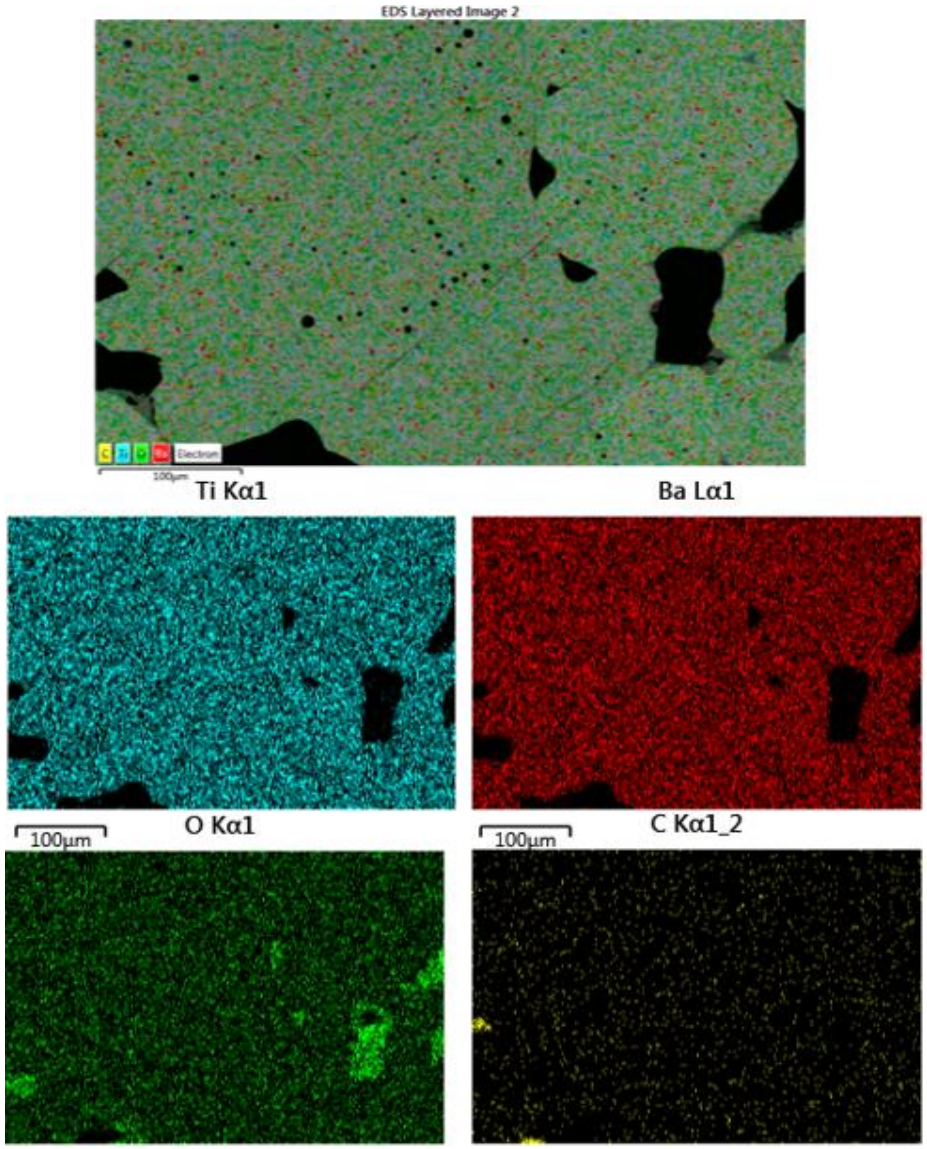

Figure 6. 51 A compositional map of the $Ba_{0.99}(Zr_{0.01,}Ti_{0.99})O_3$ crystal grown and surrounding microstructure.

6.3.3.2 Solid state crystal growth in $Ba_{0.99}(Zr_{0.02,}Ti_{0.98})O_3$.

After sintering at 72 hours with a crystal seed, large grains were visible throughout the pellet when examined using the stereo microscope as shown in Figure 6.52. There was no evidence that any crystal growth had occurred.

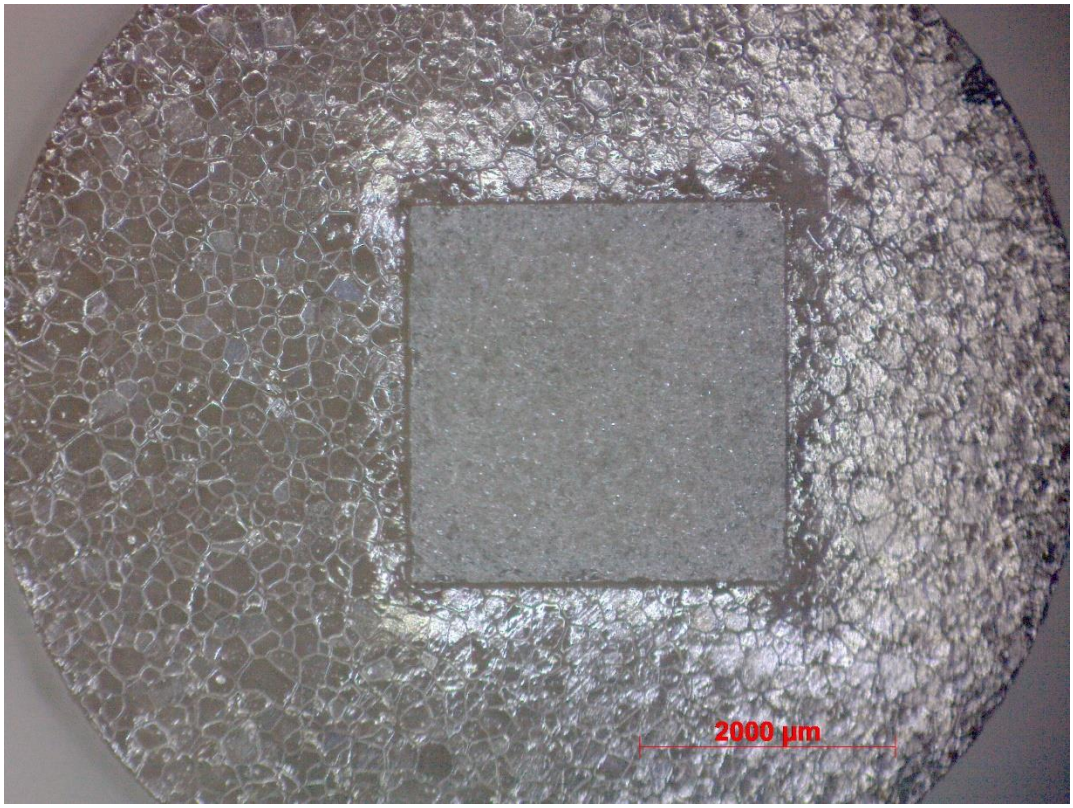

Figure 6. 52 A microscope image taken at 2x magnification. Showing the $BaTiO_3$ crystal seed implanted in $Ba_{0.99}(Zr_{0.02,}Ti_{0.98})O_3$ after sintering at 1460°C for 72 hours.

When a cross section of this sample was taken a limited amount of crystal growth could be seen using SEM. Figure 6.53 shows a scanning electron micrograph of this sample. The maximum growth length of this crystal was found to be ~390µm with an approximate growth rate of 5.49µm. The crystal grown was again found to be porous, this porosity can be viewed in Figure 6.53 b.

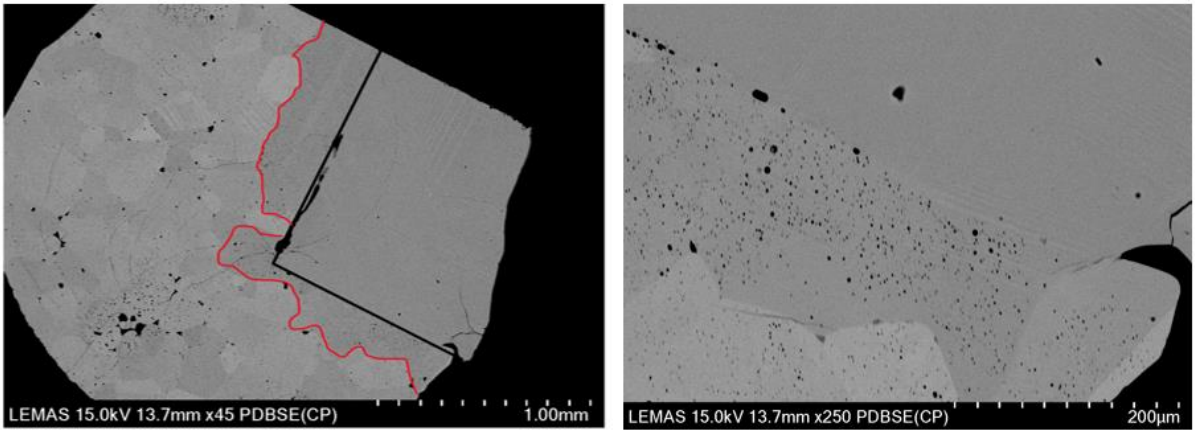

Figure 6. 53 Scanning electron micrographs a (left) and b (right) showing the $Ba_{0.99}(Zr_{0.02,}Ti_{0.98})O_3$ crystal grown. The black line outlines the $BaTiO_3$ seed crystal and the red line outlines the crystal grown.

EDX mapping can be viewed in Figure 6.54, again no Zr was detected. It should be noted that this sample was coated using carbon.

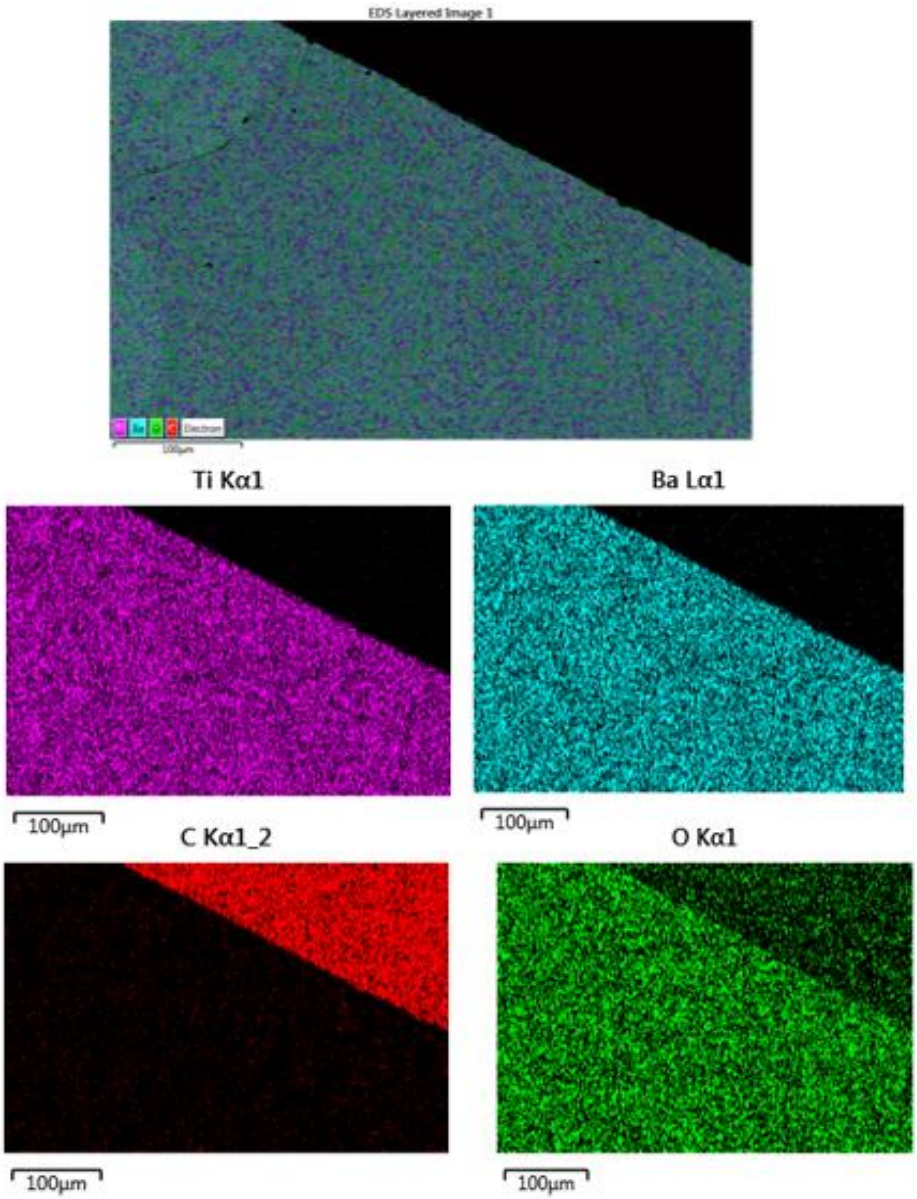

Figure 6. 54 A compositional map of the $BaTiO_3$ crystal seed and the $Ba_{0.99}(Zr_{0.02,}Ti_{0.98})O_3$ crystal grown.

6.3.4 Discussion

6.3.4.1 Grain growth in $Ba(Zr_xTi_{1-x})O_3$ and $Ba_{99}(Zr_xTi_{1-x})O_3$

Abnormal grain growth has previously been reported in BZT [58] and large grain size has been reported in several studied [56], [62] when sintered at either high temperature or for longer lengths of time (4-8 hour). Rehrig et al also reported an increase in grain size with increasing Zr concentrations [57] this is in agreement with the results presented here where abnormal grain growth was present at 1 and 2 mol% Zr concentrations. When excess TiO_2 was also introduced to these compositions grain size was found to be very large. Grain size increased steadily with sintering time in the sample $Ba_{0.99}(Zr_{0.01,}Ti_{0.99})O_3$. Whereas grain size appeared to be independent of sintering temperature in the $Ba_{0.99}(Zr_{0.02,}Ti_{0.99})O_3$.

6.3.4.2 Solid state crystal growth in $Ba(Zr_xTi_{1-x})O_3$ and $Ba_{99}(Zr_xTi_{1-x})O_3$

SSCG experiments were performed using $Ba_{0.99}(Zr_{0.01,}Ti_{0.99})O_3$ and $Ba_{0.99}(Zr_{0.02,}Ti_{0.99})O_3$. Some crystal growth had occurred however the crystal growth was relatively small when compared to other samples and porosity was again an issue.

6.4 Barium calcium zirconate titanate $(Ba_{0.85},Ca_{0.15})(Ti_{0.9},Zr_{0.1})O_3$.

As discussed in Chapter 4 BCTZ is a promising lead-free piezoelectric based on $BaTiO_3$. After single crystals had been successfully grown using SSCG in $BaTiO_3$, it was decided experiments would begin to determine whether BCTZ had similar microstructural properties and if it would be possible to use the addition of TiO_2 or other sintering aids in order to grow a BCTZ single crystal.

$(Ba_{0.85},Ca_{0.15})(Ti_{0.9},Zr_{0.1})O_3$ was decided on as the initial composition and then Ba/Ti ratio was adjusted to include 1 and 2 mol% excess TiO_2 in order to introduce a small amount of intergranular liquid phase to the system. As ZnO is a known BCTZ sintering aid and SiO_2 forms a eutectic liquid with $BaTiO_3$ 1 wt% of each was also added to stoichiometric $(Ba_{0.85},Ca_{0.15})(Ti_{0.9},Zr_{0.1})O_3$ after calcination. 1 and 2 wt% of $BaTi_2O_5$ were also added to $(Ba_{0.85},Ca_{0.15})(Ti_{0.9},Zr_{0.1})O_3$ in order to promote the formation of the intergranular liquid phase

as $BaTi_2O_5$ is found directly below the eutectic liquid phase in the BaO-TiO_2 phase diagram. All of these compositions were sintered for 8 hours at 1420°C, 1440°C, 1460°C, 1480°C and 1500°C.

6.4.1 X-ray Diffraction of $(Ba_{0.85},Ca_{0.15})(Ti_{0.9},Zr_{0.1})O_3$.

After sintering at 1440°C for 8 hours the pellets were all analysed using a Bruker D8 diffractometer with scans ranging from 20° to 80° 2θ with a step size of 0.033 at a rate of 0.5s/step.

All of the spectra were matched with ICDD files corresponding with tetragonal BCTZ. These spectra can be seen in Figures 6.55 and 6.58.

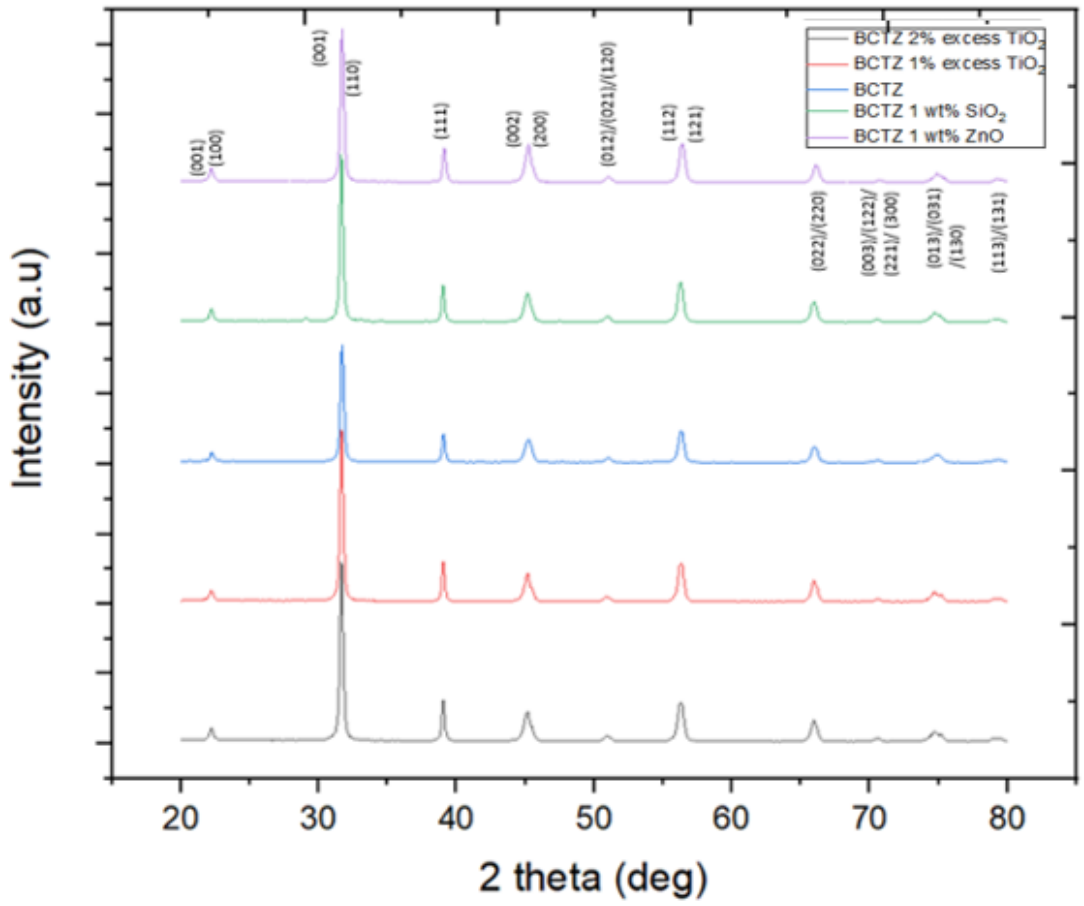

Figure 6. 55 Showing the XRD spectra for some of the BCTZ compositions after sintering for 8 hours at 1440°C.

From Figure 6.55 a small impurity peak can be seen in the spectrum for the BCTZ containing 1wt% SiO_2. Figure 5.66 shows the spectrum in more detail. The impurity peaks were matched with the ICDD files for SiO_2 (file number 04-015-7163) and BaO (file number 01-080-3938).

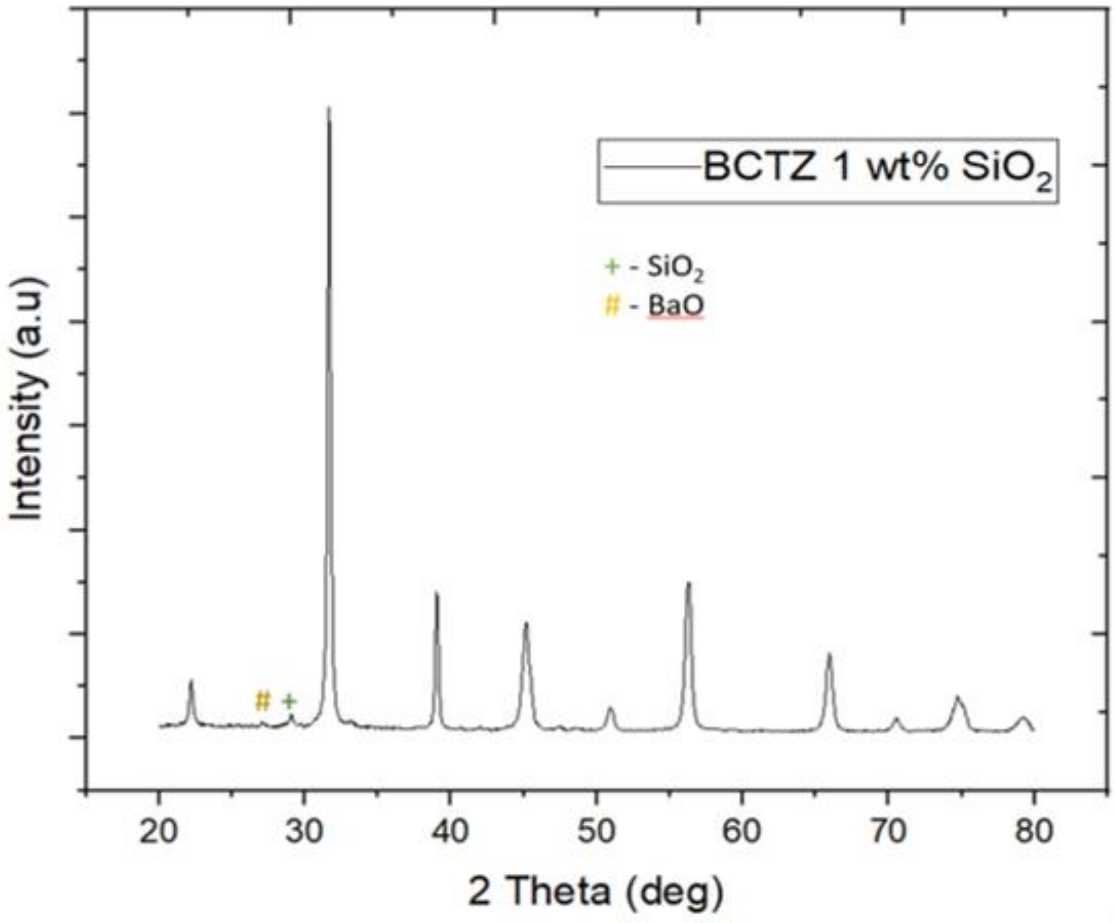

Figure 6. 56 Showing the XRD spectrum of BCTZ with 1 wt% SiO_2.

$BaTi_2O_5$ was prepared by the mixed oxide method described in Chapter 4. After calcination at 1100°C for 4 hours XRD was carried out on the powder prior to the powder being added to BCTZ. The spectrum of this powder is shown below in Figure 5.57. This spectrum matched with ICDD file 04-009-3293 corresponding to $BaTi_2O_4$.

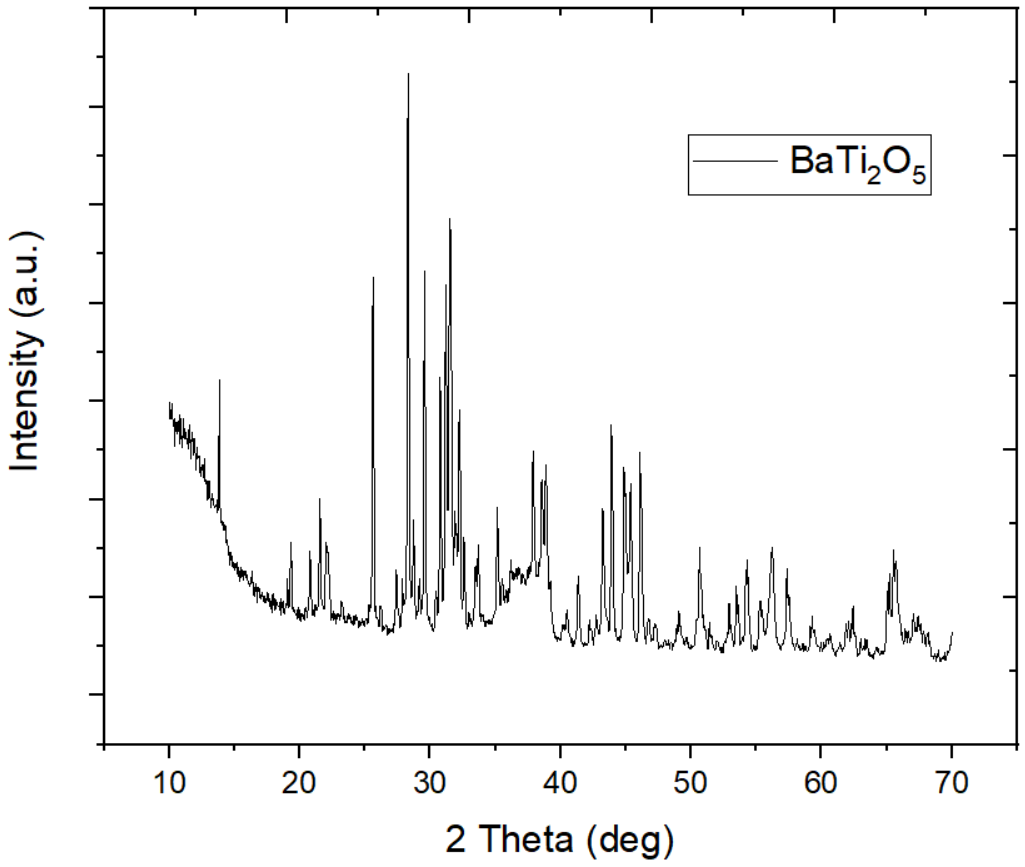

Figure 6. 57 Showing the XRD spectrum of $BaTi_2O_5$.

The XRD spectra for BCTZ with $BaTi_2O_5$ addition can be seen in Figure 6.58. Again, these samples matched with ICDD data for tetragonal BCTZ. There is a small impurity at around 35 2θ in the spectrum containing 1 wt % $BaTi_2O_5$. This peak was identified as $BaTiO_3$ corresponding to ICDD file 01-083-8303.

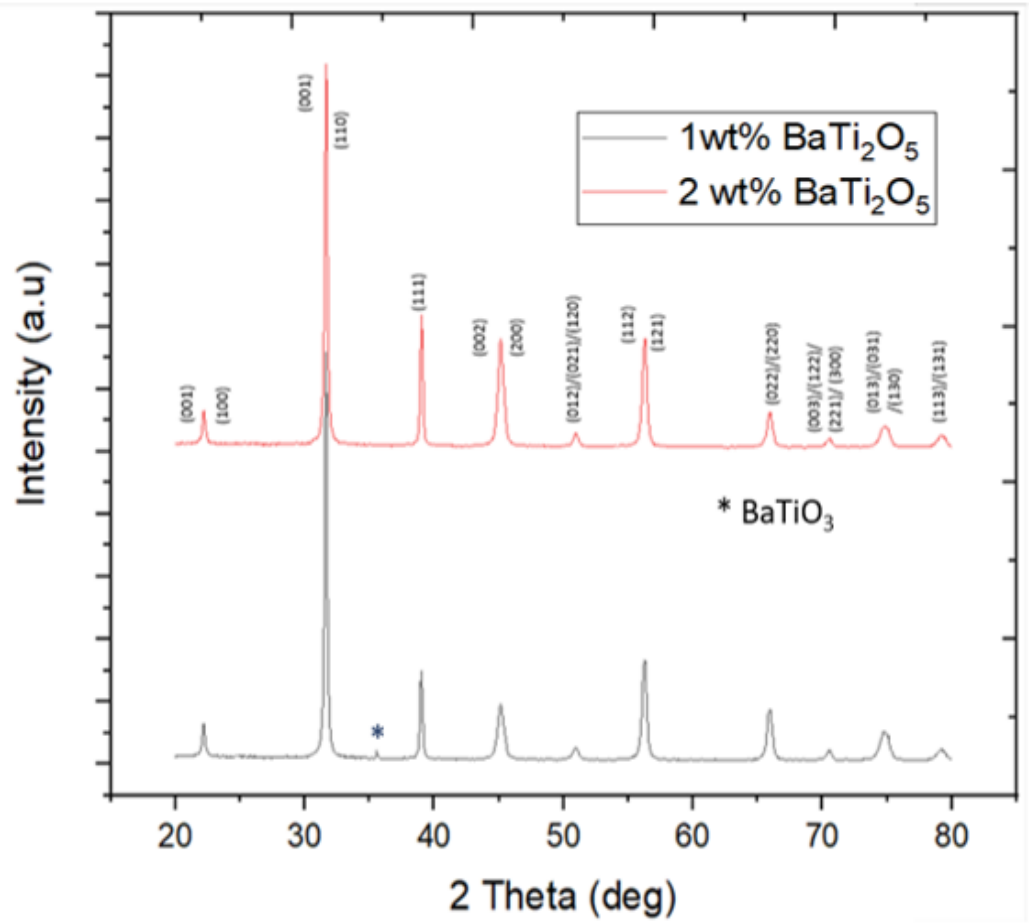

Figure 6. 58 Showing the XRD spectra for the BCTZ containing $BaTi_2O_5$ after sintering for 8 hours at 1440°C.

6.4.2 Grain Growth in $(Ba_{0.85},Ca_{0.15})(Ti_{0.9},Zr_{0.1})O_3$.

After sintering at 1420°C, 1440°C, 1460°C, 1480°C or 1500°C pellets were examined using scanning electron microscopy in order to determine grain growth rates and possible viability for SSCG experiments. Grain size across these temperatures can be seen for the BCTZ samples containing excess TiO_2 and with the addition of ZnO in Figure 6.59. Due to bimodal grain growth in SiO_2 these samples were not plotted as there was a large variation between the smaller matrix grains and large abnormally grown grains.

Figure 6.59 shows that the largest observed average grain size was found in the samples containing 1 wt% ZnO. This was followed by the samples containing excess TiO_2. Similarly, to $BaTiO_3$, addition of 1 mol% excess TiO_2 resulted in larger average grain size compared to 2

mol% excess TiO_2, although the difference in grain size was only slight. Stoichiometric BCTZ had the smallest average grain size. SEM images taken at 1420°C of all the BCTZ compositions can be seen in Figure 6.60.

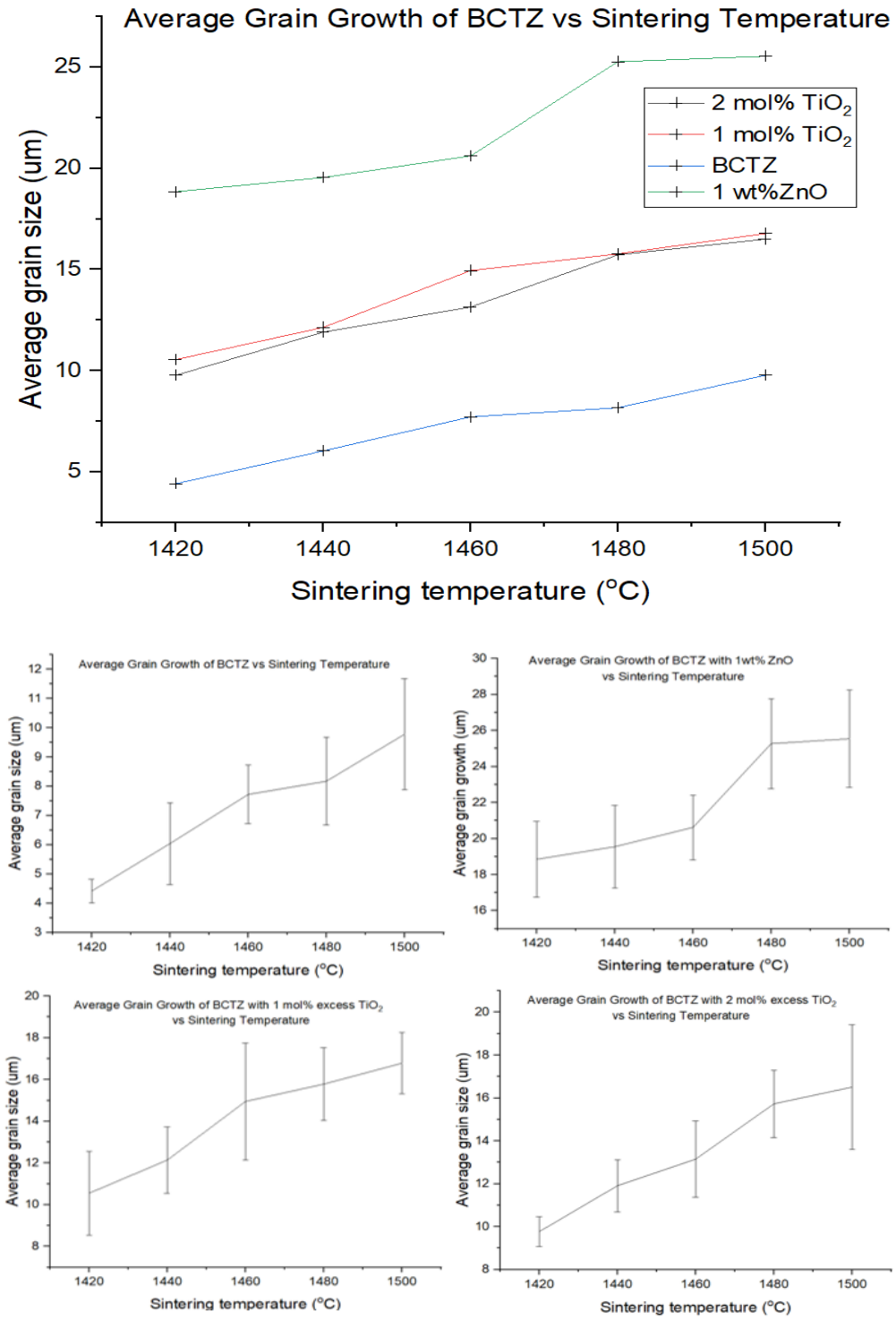

Figure 6. 59 A plot of average grain size vs sintering times for some of the BCTZ compositions. The smaller graphs show the individual data along with error bars displaying the standard deviation of the grain growth measurements.

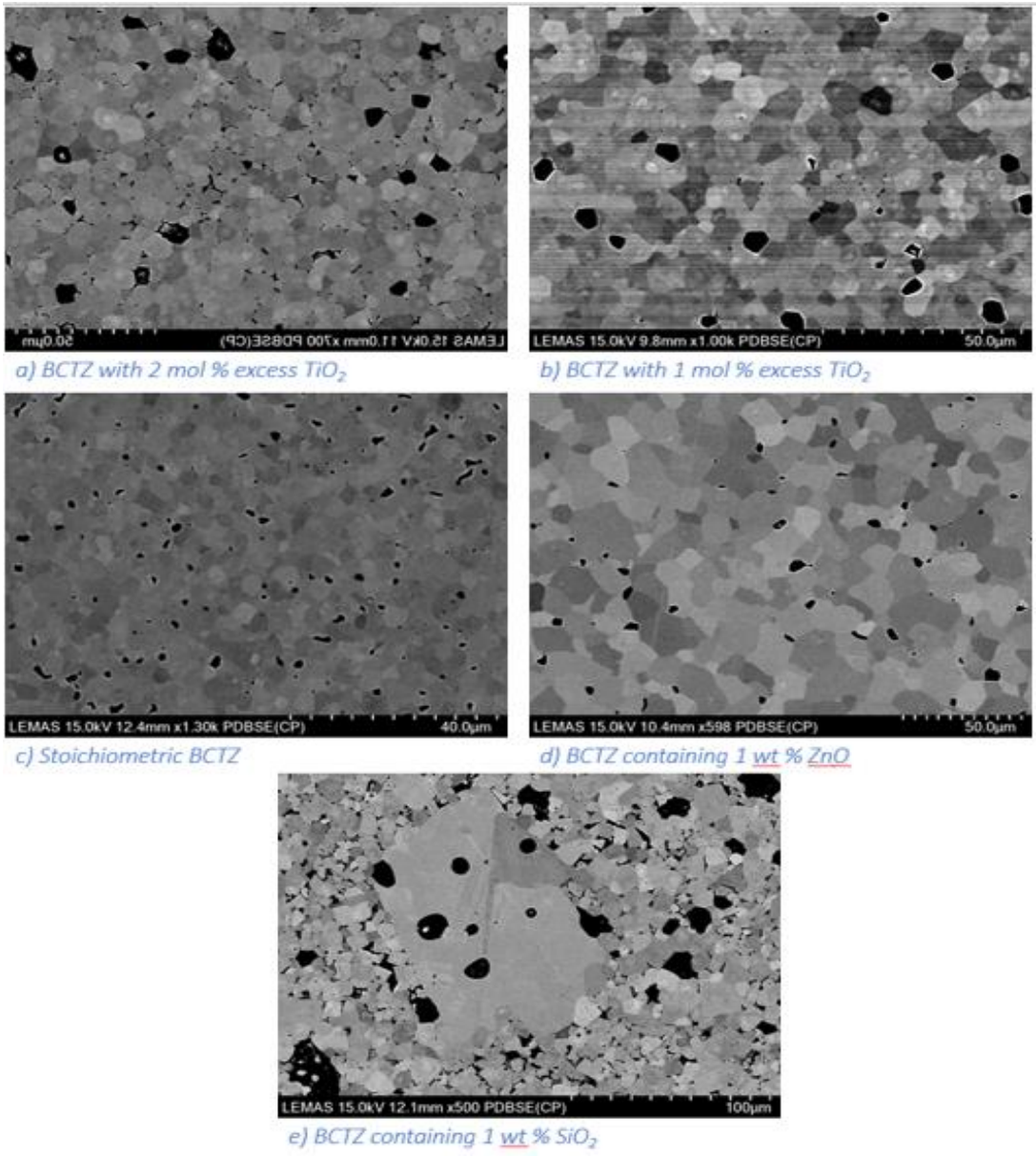

Figure 6. 60 Showing scanning electron micrographs of the various compositions of BCTZ sintered at 1420°C.

The average grain sizes of BCTZ containing 1 wt% SiO_2 is shown below in Table 6.3.There is no clear correlation between sintering temperature and grain size in this samples. All the samples sintered at and above 1420°C displayed bimodal grain growth to varying degrees. Many of these larger grains were faceted and/or twinned grains. The sample with the largest grains was the sample sintered at 1420°C. It was decided to also sinter this composition at lower temperatures (1300 and 1350°C) as it has been reported that SiO_2 reduces sintering temperature in BCTZ [65]. No abnormal grain growth was observed at these two lower sintering temperatures. Another notable feature of this composition is that all the microstructures were very porous compared to the other compositions. Figure 6.61 Shows the microstructures of BCTZ with 1 wt% SiO_2 sintered at the various temperatures mentioned above.

Table 6. 3 Showing the average grain sizes for BCTZ containing 1 wt% SiO_2 showing the sizes of both the large abnormal grains and the finer grains within the matrix.

Sintering Temperature (°C)	Average size of smaller grains (µm)	Average size of larger grains (µm)
1300	8	N/A
1350	10	N/A
1420	12.5	136.6
1440	9.7	23.9
1460	10	38.5
1480	7.9	60.96
1500	5.9	22.5

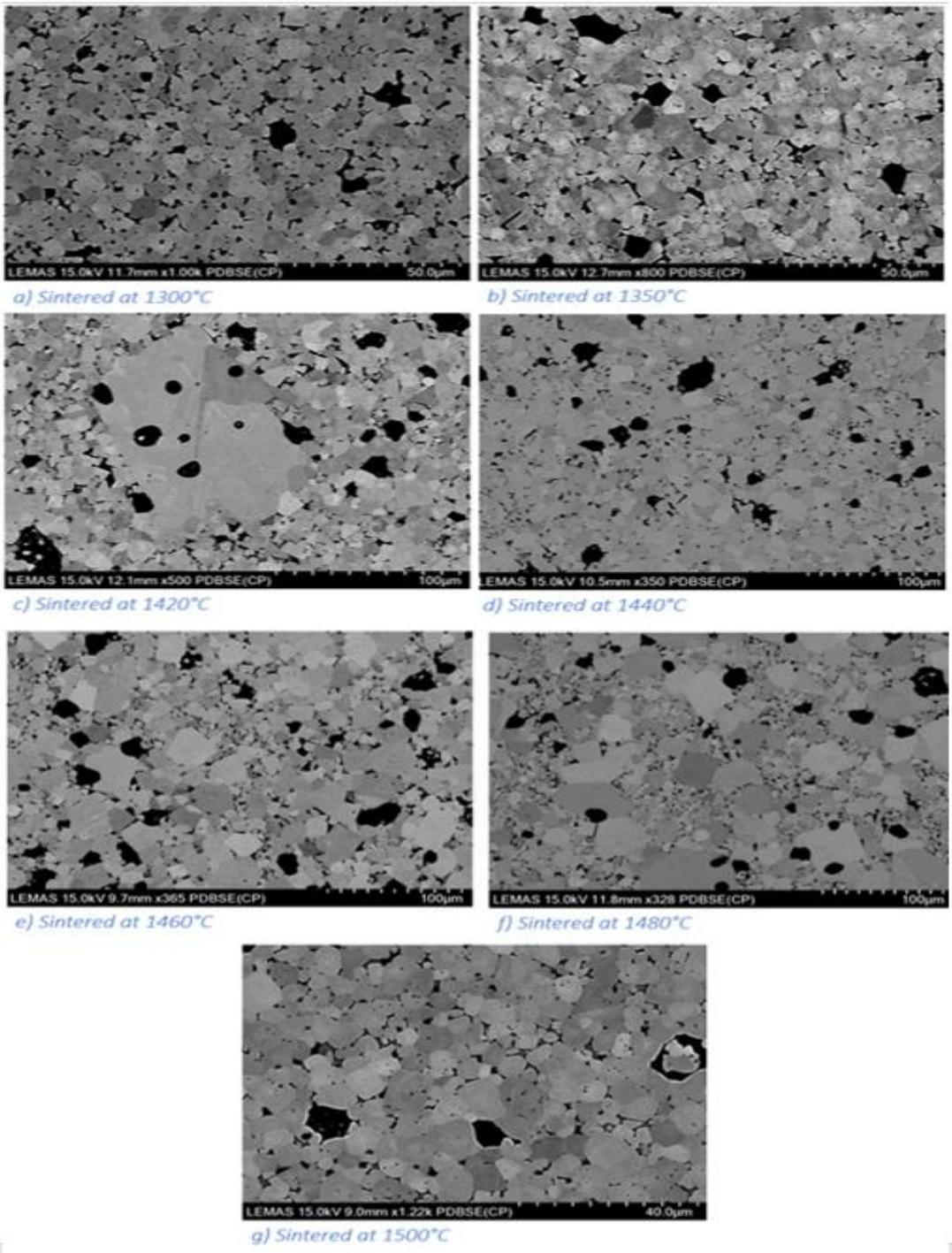

Figure 6. 61 Showing scanning electron micrographs of BCTZ containing 1 wt% SiO_2 sintered at various temperatures.

Interestingly EDX analysis on BCTZ containing 1 wt% SiO_2 (Figure 6.62) sintered at 1460°C displayed evidence of a Si rich intergranular second phase. It is likely that the detectable levels of intergranular liquid formed was contributing to porosity. All of the BCTZ samples were coated using carbon therefore carbon can be seen in all of the EDX maps and spectra.

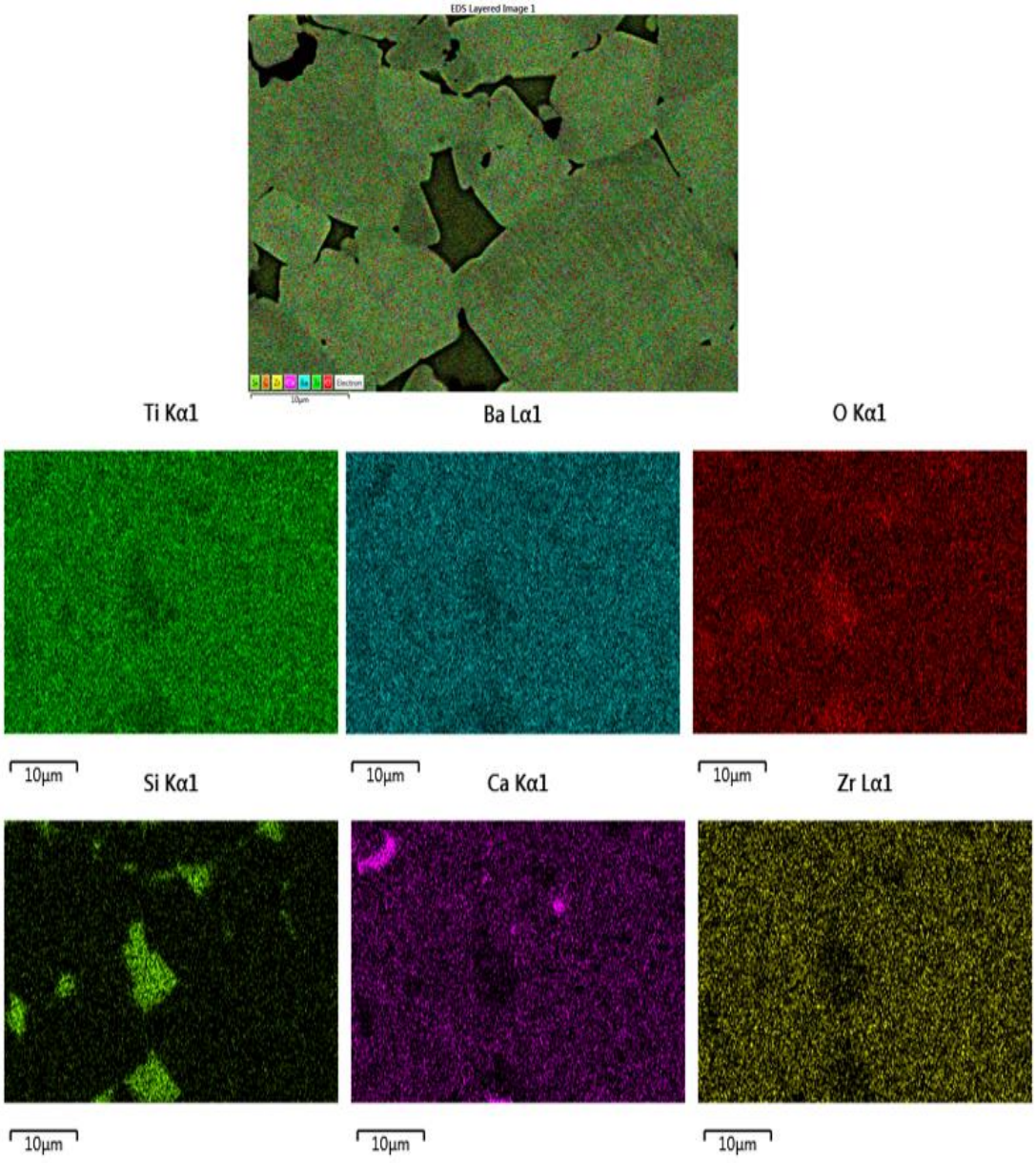

Figure 6. 62 Shows EDX mapping of BCTZ with 1 wt% SiO_2 sintered for 8 hours at 1460°C.

The BCTZ with the largest average grain size was determined to be the sample with 1 wt% of ZnO addition. Scanning electron micrographs of this composition sintered at times ranging from 1420°C to 1500° can be seen below in Figure 6.63. There was no bimodal grain growth in the samples and less porosity than the samples in the BCTZ containing SiO_2.

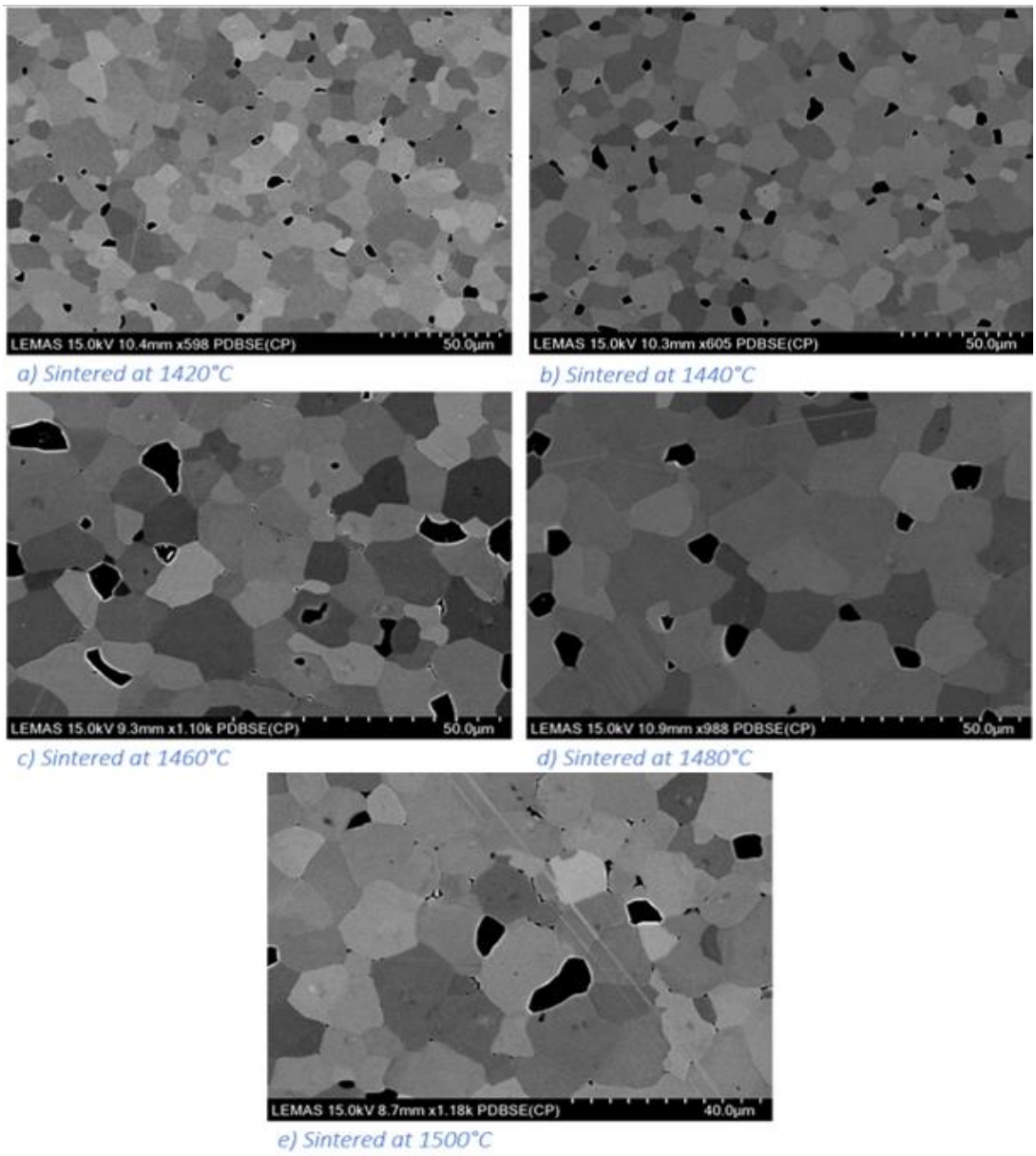

Figure 6. 63 Showing Scanning electron micrographs of BCTZ containing 1 wt% ZnO sintered at various temperatures.

The composition with second largest average grain size was the BCTZ containing 1 mol% excess TiO_2. Micrographs of this sample when sintered at various temperatures can be seen in Figure 6.64.

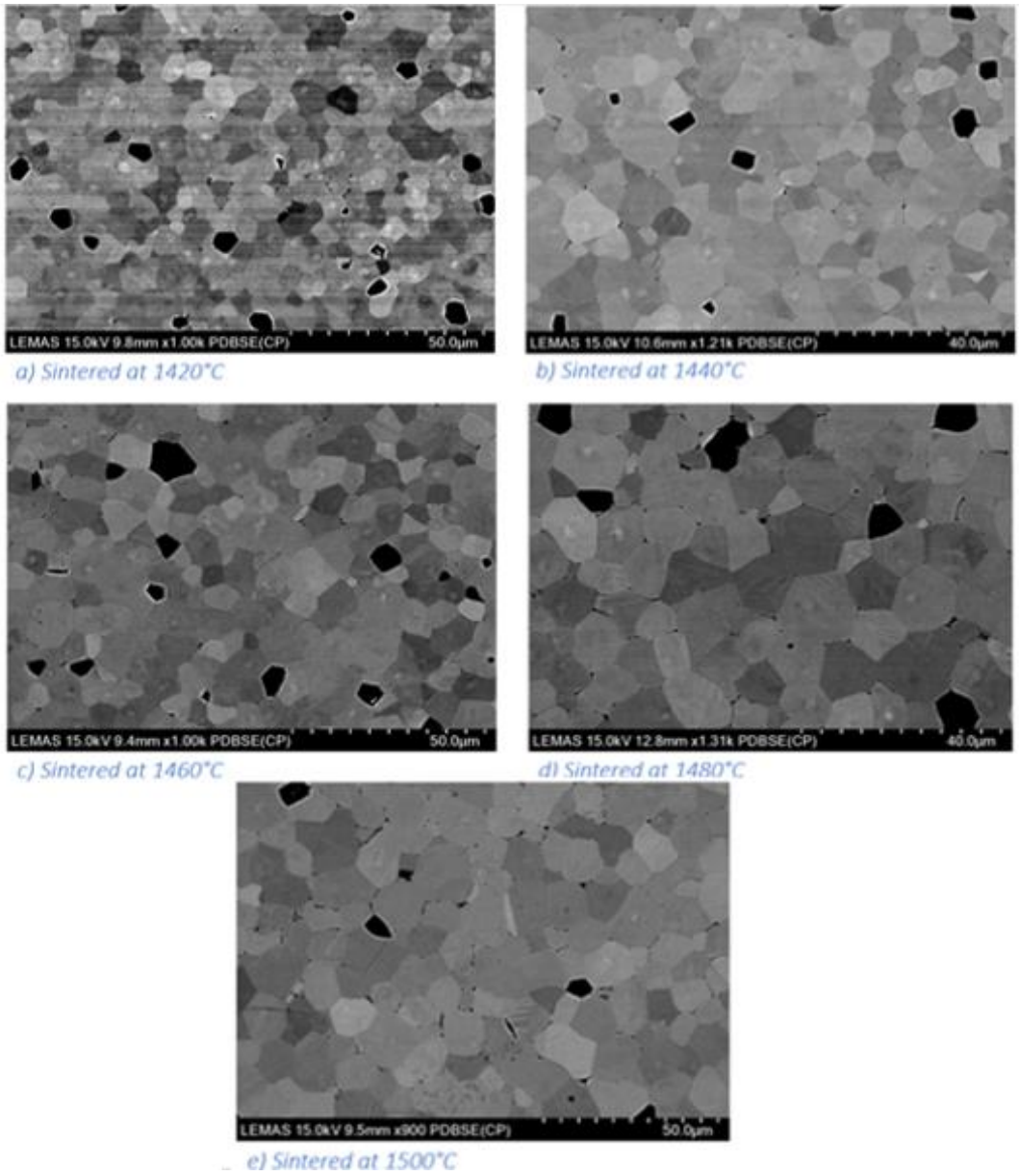

Figure 6. 64 Showing scanning electron micrographs of BCTZ containing 1 mol% excess TiO_2 sintered at various temperatures.

When 2 mol% excess TiO_2 was added, grain size decreased slightly again. Images of BCTZ with 2 mol% excess TiO_2 sintered at the same temperatures can be seen below in Figure 6.65.

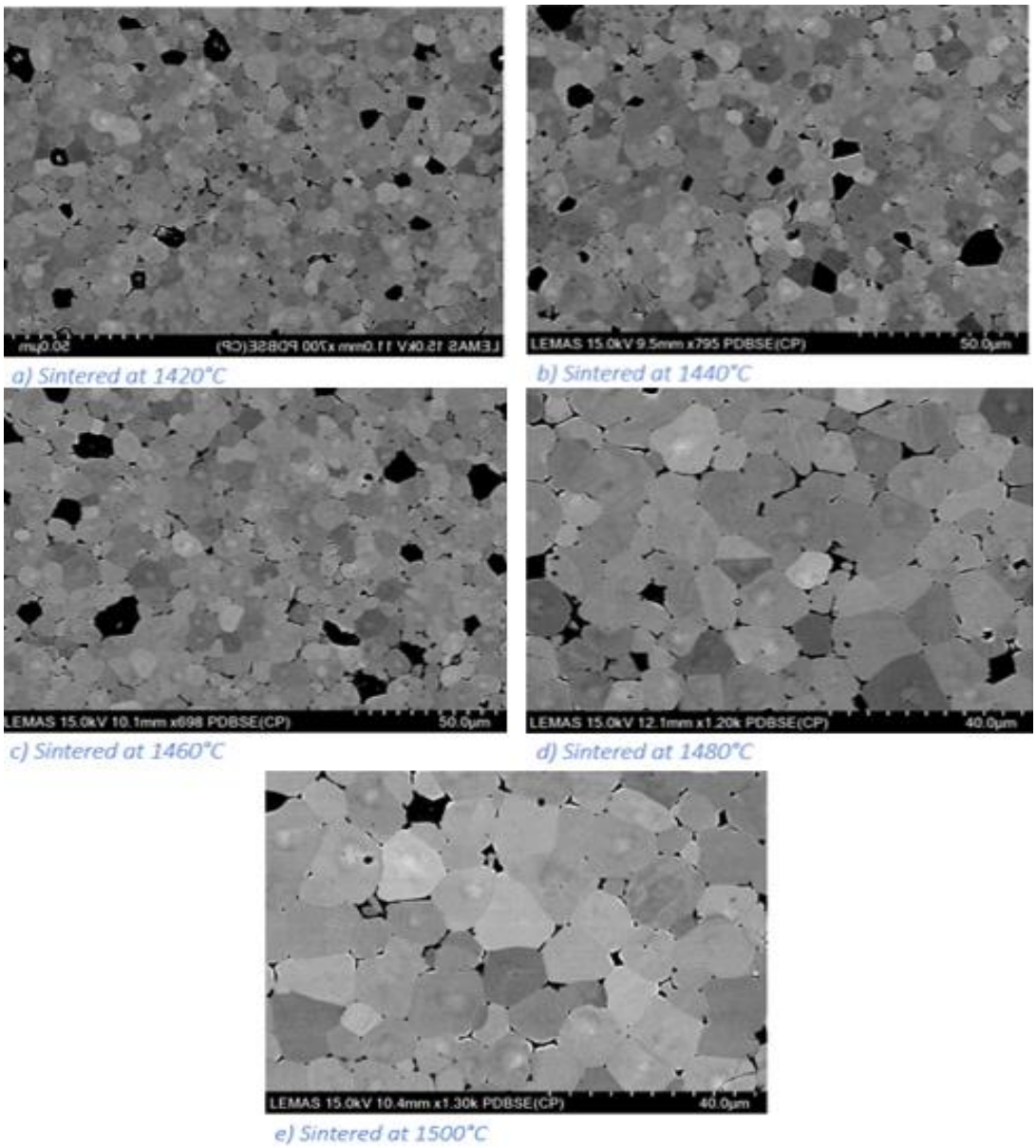

Figure 6. 65 Showing scanning electron micrographs of BCTZ containing 2 mol% excess TiO_2 sintered at various temperatures.

A notable feature of the BCTZ containing excess TiO_2 was the apparent appearance of core-shell structures. These structures are known to occur in $BaTiO_3$ based materials in the presence of an intergranular liquid phase. The mechanism by which these structures occur is due to solution and precipitation from the liquid phase onto the outer 'shell' portion of the grain. This leads to a compositional inhomogeneity between the core which has the original composition and the shell which has the composition of the more recently formed solid solution [82]. Compositional maps were generated for both of these compositions and can be seen below in Figures 6.66 and 6.67. The composition maps did not detect any obvious compositional differences between these regions.

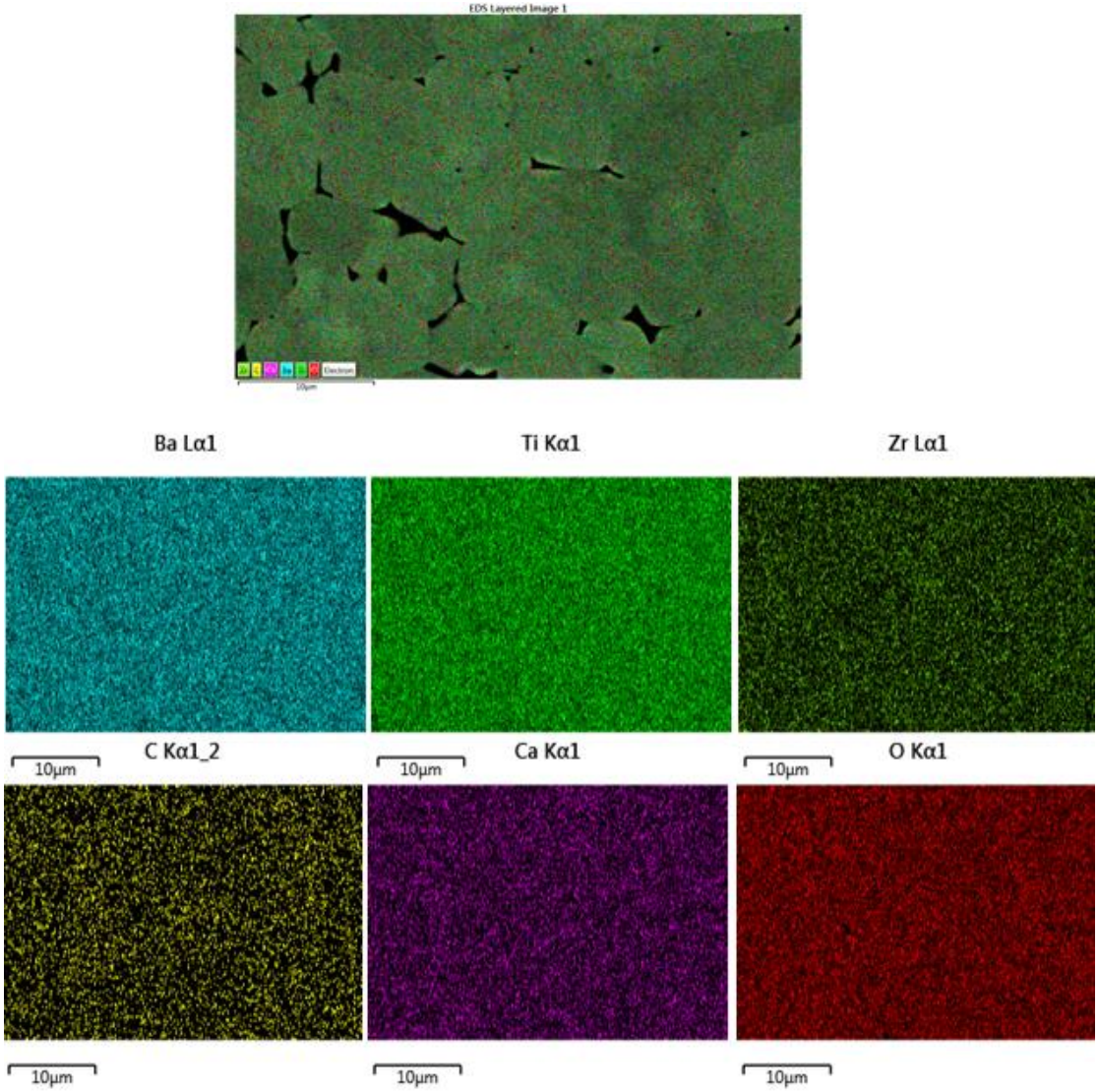

Figure 6. 66 Showing a composition map of BCTZ containing 2 mol% excess TiO_2 sintered at 1460°C.

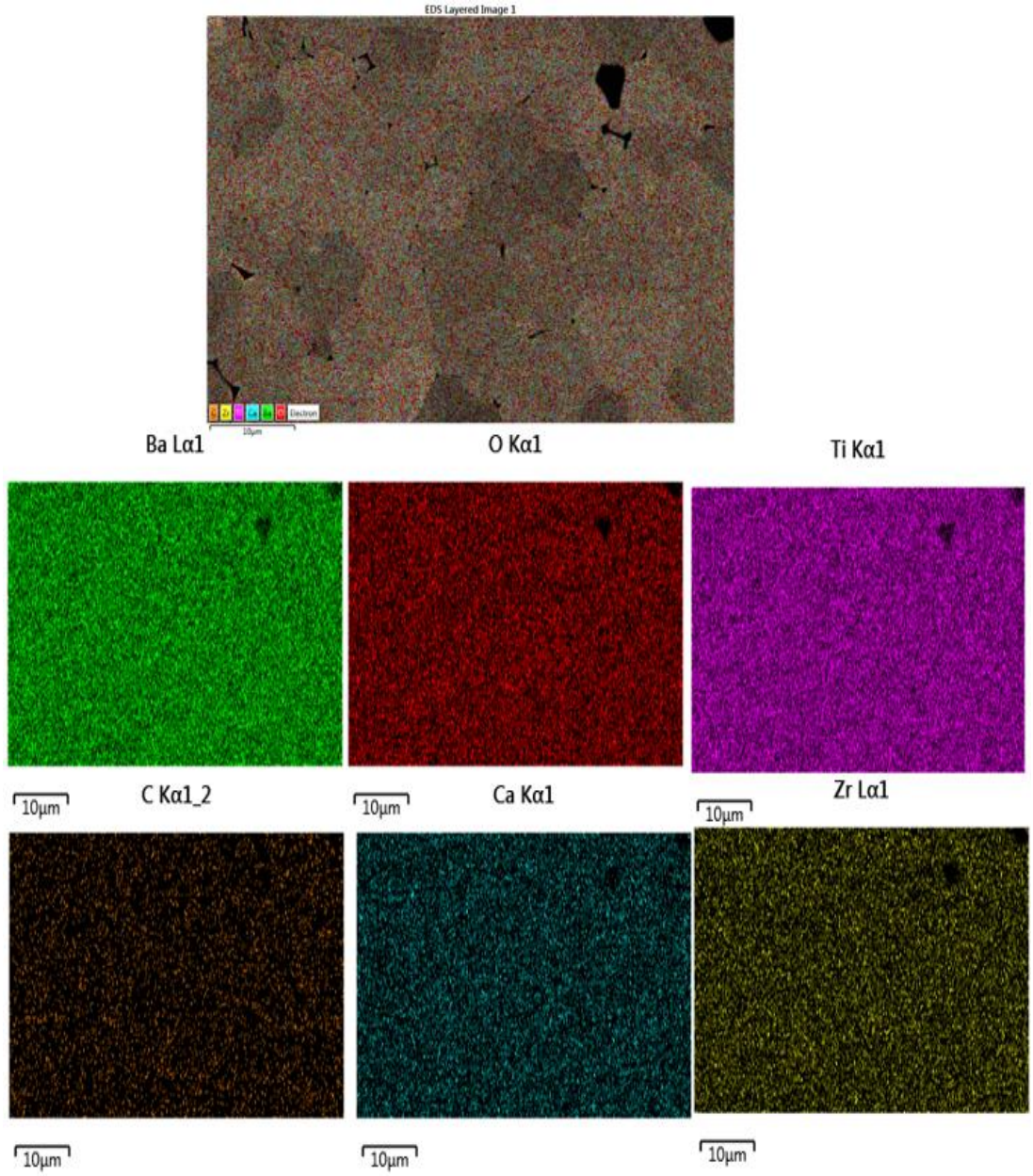

Figure 6.67 Showing a composition map of BCTZ containing 1 mol% excess TiO_2 sintered at 1460°C.

The Stoichiometric BCTZ containing no sintering aids was, unsurprisingly, found to have the smallest average grain size of all the BCTZ samples. The scanning electron micrographs for this sample sintered at temperatures ranging from 1420°C to 1500°C can be found below in Figure 6.68.

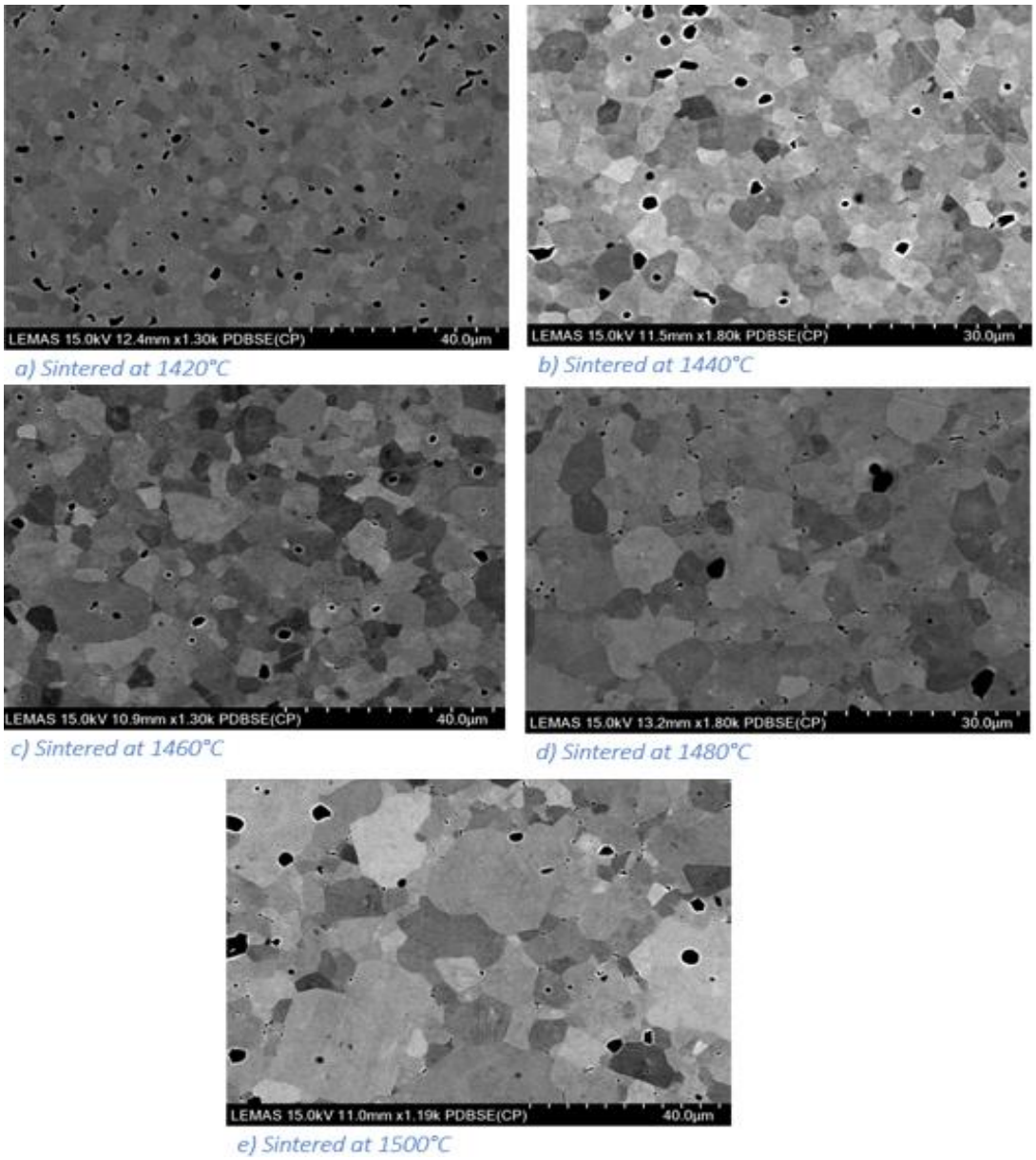

Figure 6. 68Scanning electron micrographs of the BCTZ with no sintering aids sintered at various temperatures.

After the initial compositions were examined, it was decided to study the effects of adding $BaTi_2O_5$, which is the composition directly below the eutectic liquid phase in the BaO-TiO_2 phase diagram, to the BCTZ as a sintering aid. These were added after calcination on a weight % basis. 1 and 2 wt % of $BaTi_2O_5$ were used. As with the other BCTZ samples these were sintered at temperatures ranging from 1420°C to 1500°C for 8 hours. Both of these samples displayed bimodal grain growth with large grains accompanied by clusters of smaller grains. For this reason, the large and small grains were measured separately and can be seen in Figure 6.69. Although grain size in 1wt% $BaTi_2O_5$ is slighter larger grains at 1420°C and 1440°C, it can be seen that grain size does not differ significantly between the two compositions until 1480°C. At sintering temperatures above 1480°C the samples containing 1 wt% $BaTi_2O_5$ had the largest grains along with the smallest.

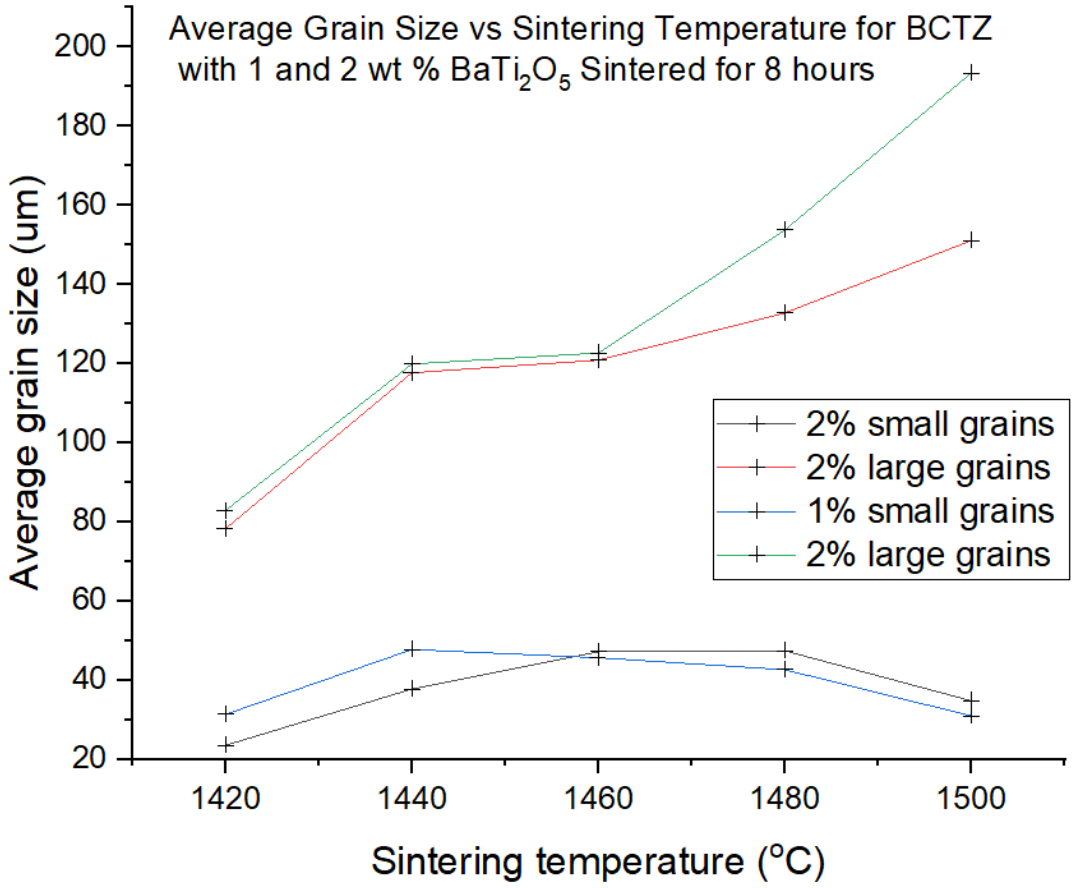

Figure 6. 69 Showing average grain sizes vs sintering temperature for the samples containing $BaTi_2O_5$.

Figure 6.70 shows the BCTZ containing 1 wt % $BaTi_2O_5$. The larger and smaller size grains can be seen. Another noteworthy feature of these samples is the presence of intragranular pores. It would be likely any crystal growth experiments using these samples would lead to a porous crystal as with the $BaTiO_3$ containing excess TiO_2.

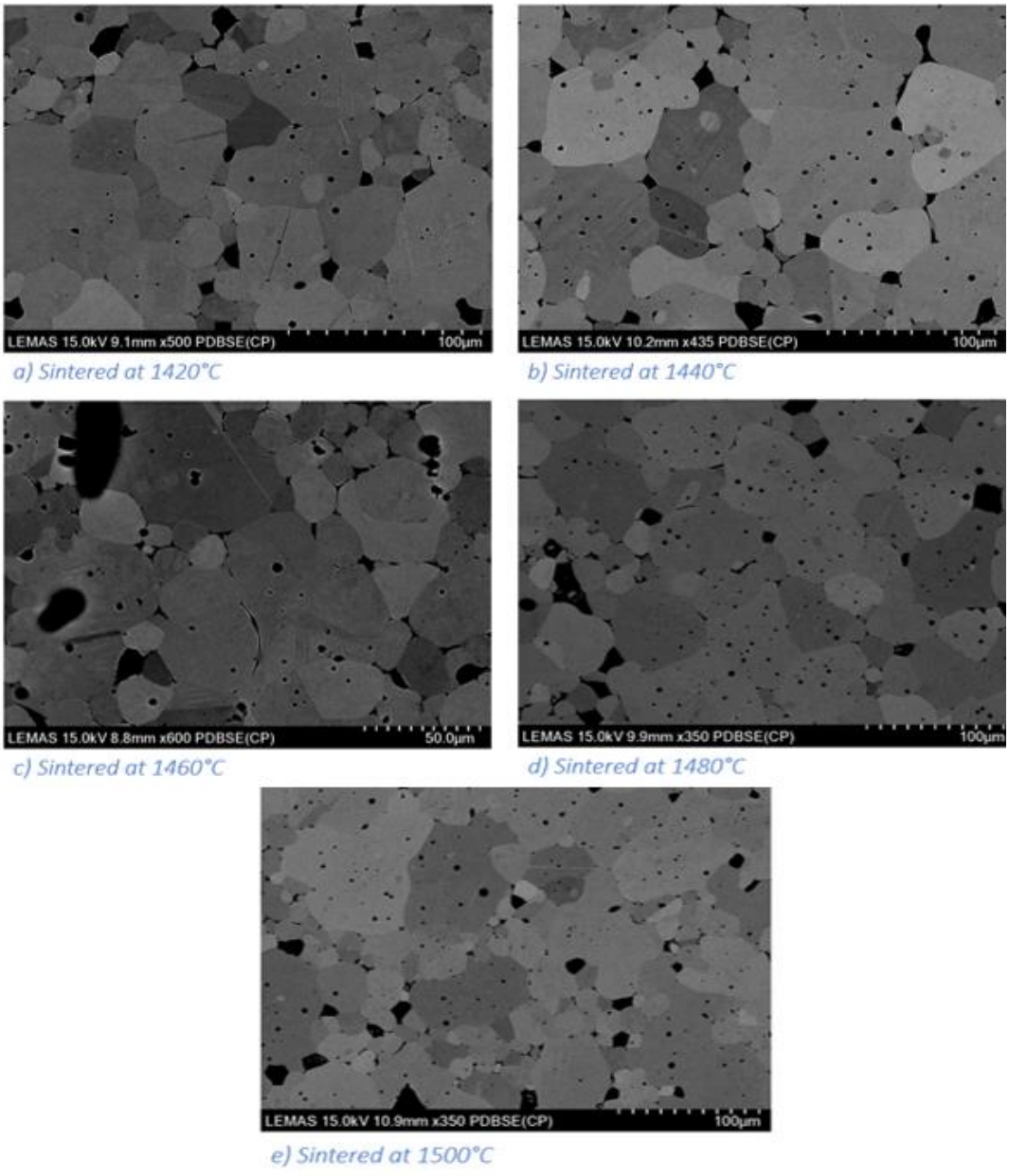

Figure 6. 70 Scanning electron micrographs of BCTZ containing 1 wt% $BaTi_2O_5$ sintered at various temperatures for 8 hours.

Figure 6.71 shows scanning electron micrographs of BCTZ containing 2 wt % $BaTi_2O_5$. The samples containing 1 and 2 wt% of the eutectic composition display very similar microstructures with the intragranular pores apparent in both compositions.

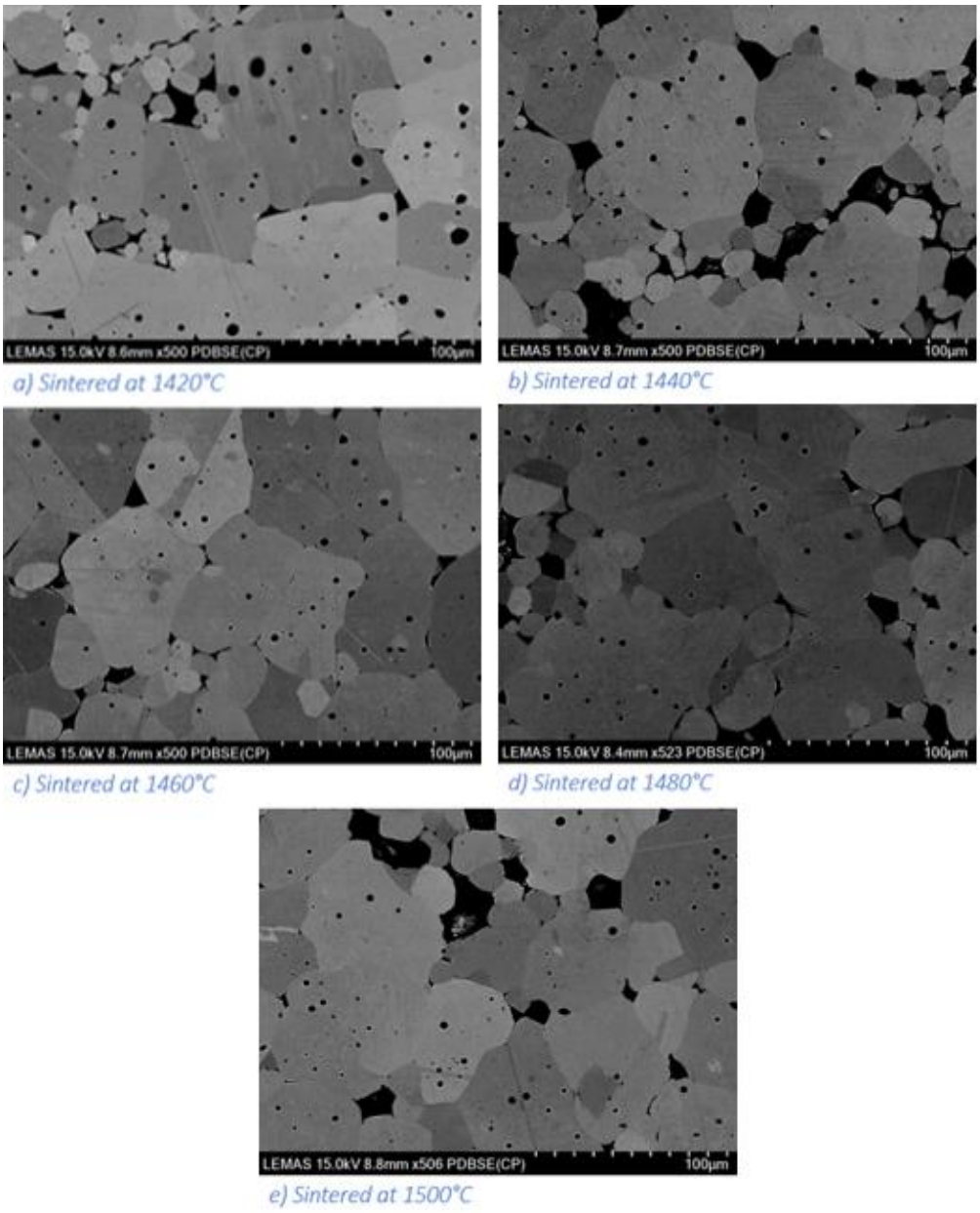

Figure 6.71 Scanning electron micrographs of BCTZ containing 2 wt% $BaTi_2O_5$ sintered at various temperatures for 8 hours.

6.4.3 Solid State Crystal Growth in $(Ba_{0.85},Ca_{0.15})(Ti_{0.9},Zr_{0.1})O_3$.

6.4.3.1 Solid state crystal growth in BCTZ containing 1 wt % ZnO.

As BCTZ containing ZnO had the largest average grain size it was decided to begin SSCG experiments using this powder. A $BaTiO_3$ crystal seed was used and the sample was sintered for 72 hours at 1500°C. After sintering there was no crystal visible to the naked eye, Figure 6.72 shows the sample immediately after sintering.

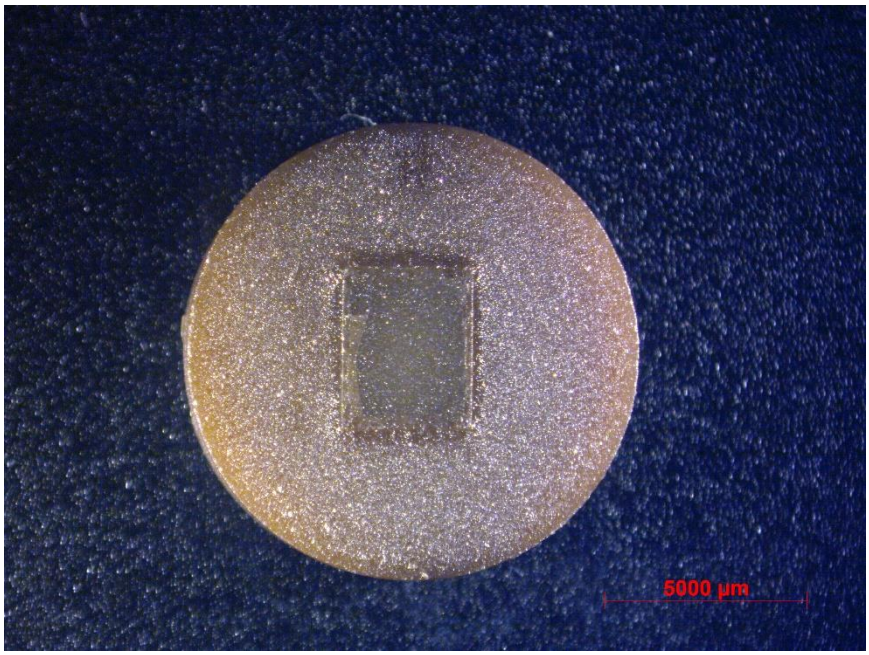

Figure 6. 72 An image taken at 1x magnification of the BCTZ containing 1 wt % ZnO pellet and $BaTiO_3$ seed crystal sintered for 72 hours at 1500°C.

The pellet shown in Figure 6.72 was then cut into cross sections and prepared as discussed in Chapter 5. Optical microscopy proved that some crystal growth has occurred in this sample which can be seen in Figure 6.73. The maximum growth length of the single crystal was approximately 1250µm with a growth rate of ~ 17.4 µm/hour.

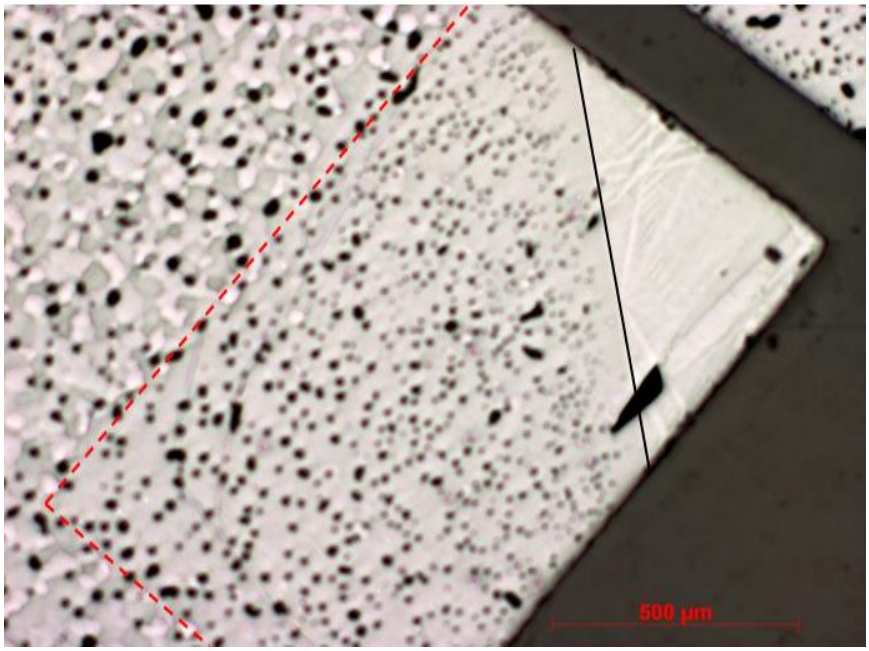

Figure 6. 73 An optical micrograph taken at 5x magnification in bright field of the single crystal grown using BCTZ with 1 wt% of ZnO. The black line outlines the seed crystal and the red lines outline the grown single crystal.

Further examination of the crystal grown was performed using SEM as shown in Figure 6.74. Although there is obvious evidence of porosity in the single crystal, the crystal shown here appears to be more dense than the $BaTiO_3$ single crystals discussed earlier in this chapter.

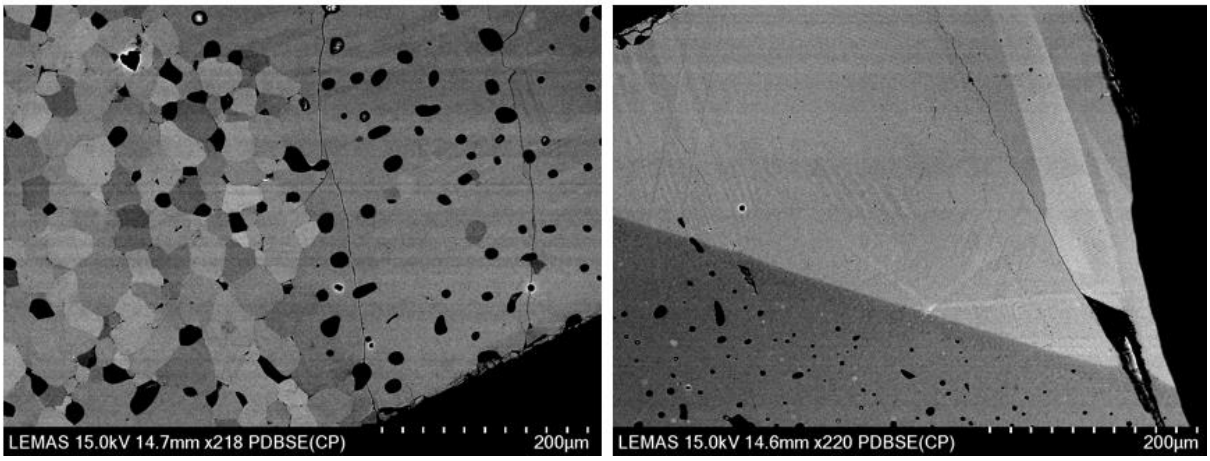

Figure 6. 74 Showing scanning electron micrographs of the seed single crystal and the single crystal grown using BCTZ with 1 wt% ZnO.

Figure 6.75 shows EDX mapping of the seed crystal and grown single crystal. A clear compositional difference between the $BaTiO_3$ seed crystal and the BCTZ crystal grown can be seen.

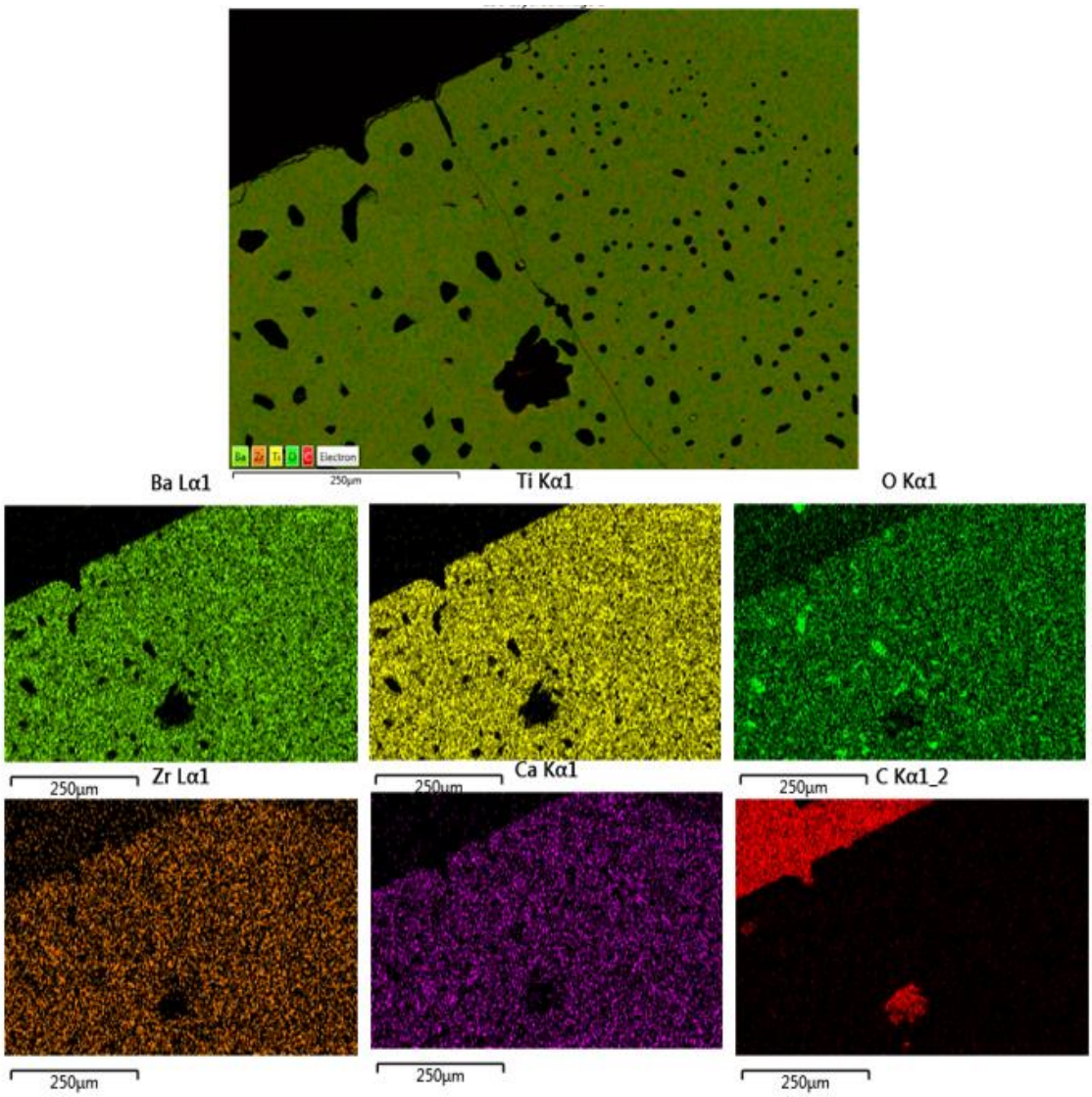

Figure 6. 75 Shows a compositional map produced by EDX. The top right of the images show the seed crystal and a clear line between the seed crystal and grown single crystal can be seen in the Zr and Ca maps.

6.4.3.2 Solid state crystal growth in BCTZ containing 1 wt % SiO_2.

Initial SSCG studies using BCTZ containing 1 wt% SiO_2 were conducted, using a $BaTiO_3$ crystal seed and sintering at 1500°C for 72 hours. Upon removing this sample from the furnace there was no evidence that any crystal growth had occurred as can be seen in Figure 6.76 taken using the Motic SMZ-168.

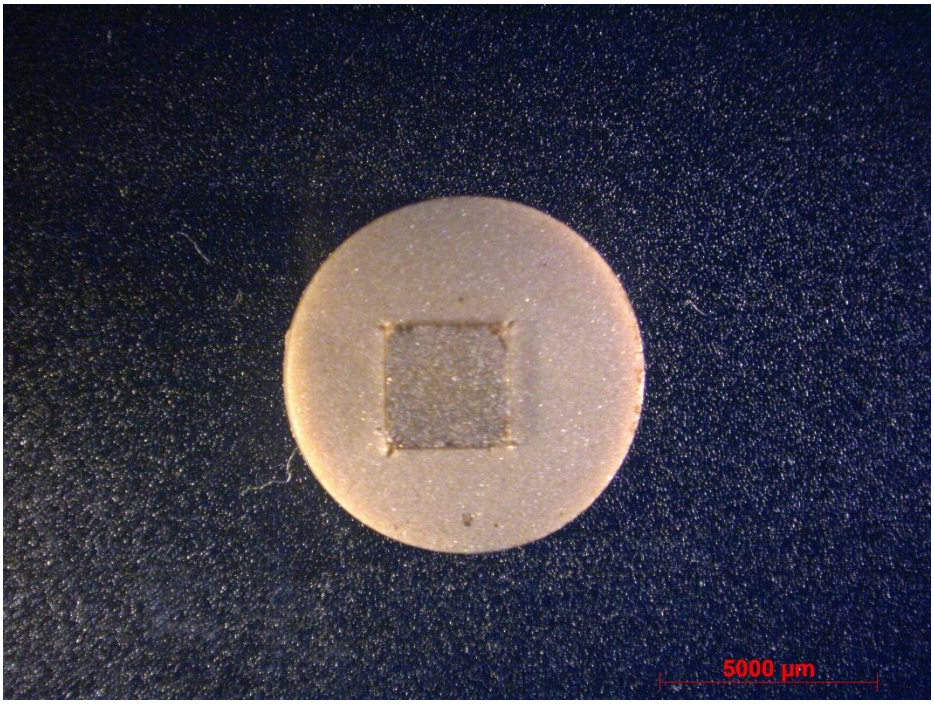

Figure 6. 76 taken at 1x showing the sintered $BaTiO_3$ crystal seed and BCTZ containing 1 wt% SiO_2. Sintered at 1500°C for 72 hours.

This sample was then cross sectioned and examined again using the Olympus BX-51 (Figure 6.77) A small amount of crystal growth was present. The maximum growth length was found to be ~100.5µm with an approximate growth length of 1.4µm/hour.

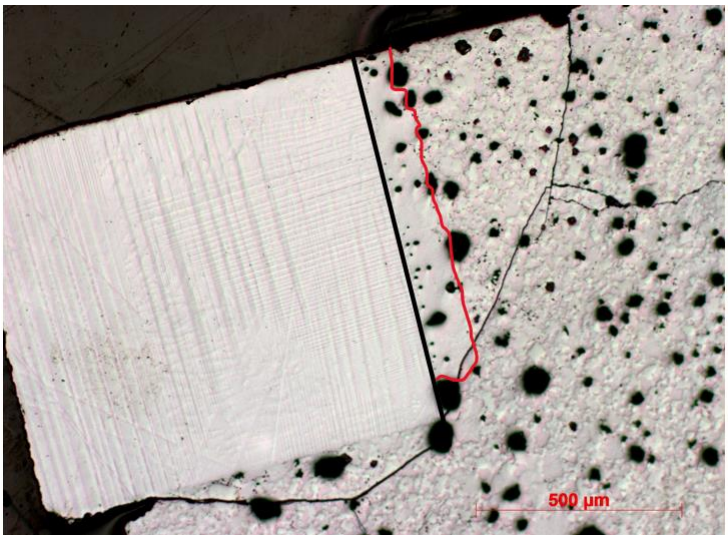

Figure 6. 77 An optical micrograph taken at 5x magnification in bright field of the seed crystal outlined by the black line and the grown single crystal. After sintering at 1500°C for 72 hours.

This sample was then analysed by SEM and EDX as shown in Figures 6.80 and 6.81. Only a small amount of crystal growth was observed indicating a slow growth rate at this temperature. The sample had several large pores as did the surrounding microstructure, however, apart from these pores was relatively dense. A second phase was again present on the micrographs, although, none of this phase was found to be in contact with the growing single crystal. The matrix grains were found to be faceted and grain size was found to be bimodal. These features can be found in Figure 6.78.

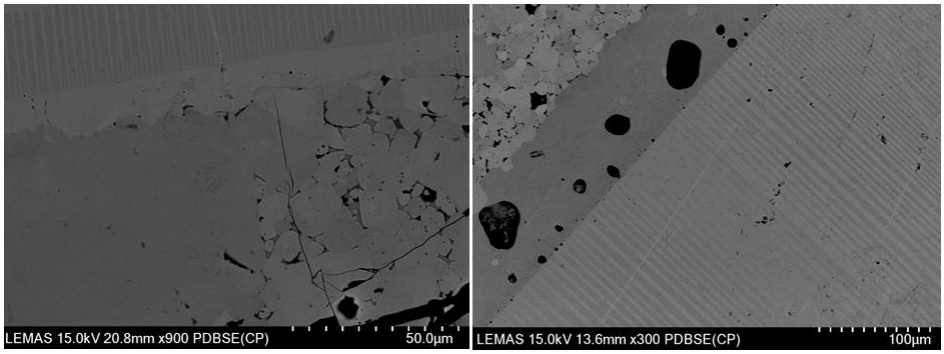

Figure 6. 78 SEM images of the seed single crystal, grown single crystal and surrounding matrix.

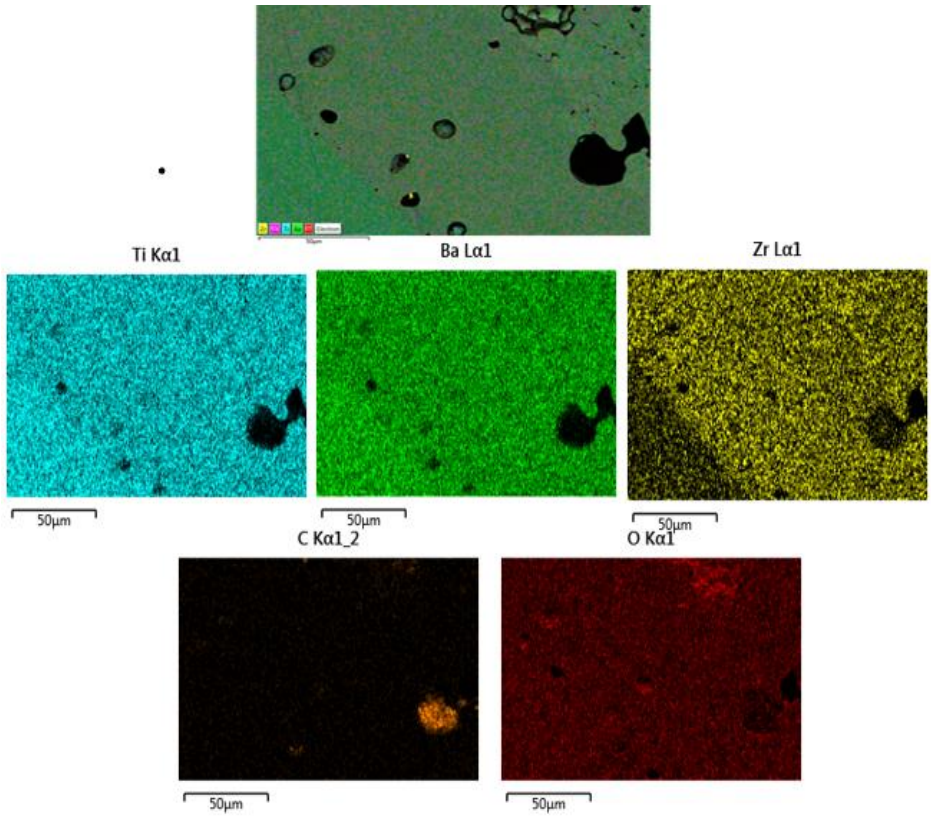

Figure 6. 79 Showing EDX mapping of the crystal seed, grown crystal and surrounding matrix of the BCTZ sample sintered at 1500°C for 72 hours.

The grain growth study conducted demonstrated that the addition of SiO_2 could lead to large abnormal grains, particularly at 1420°C. To determine if this quality was beneficial and could increase the growth rate the BCTZ containing 1 wt % SiO_2 was used for further crystal growth experiments. Again, a $BaTiO_3$ seed single crystal was used however, this sample was sintered at 1420°C for 72hours.

After sintering it was clear from the stereo microscope images that large grains had grown sporadically throughout the matrix and there was some evidence that a small amount of crystal growth had taken place. An image of this sample prior to cutting and polishing can be seen in Figure 6.80.

.

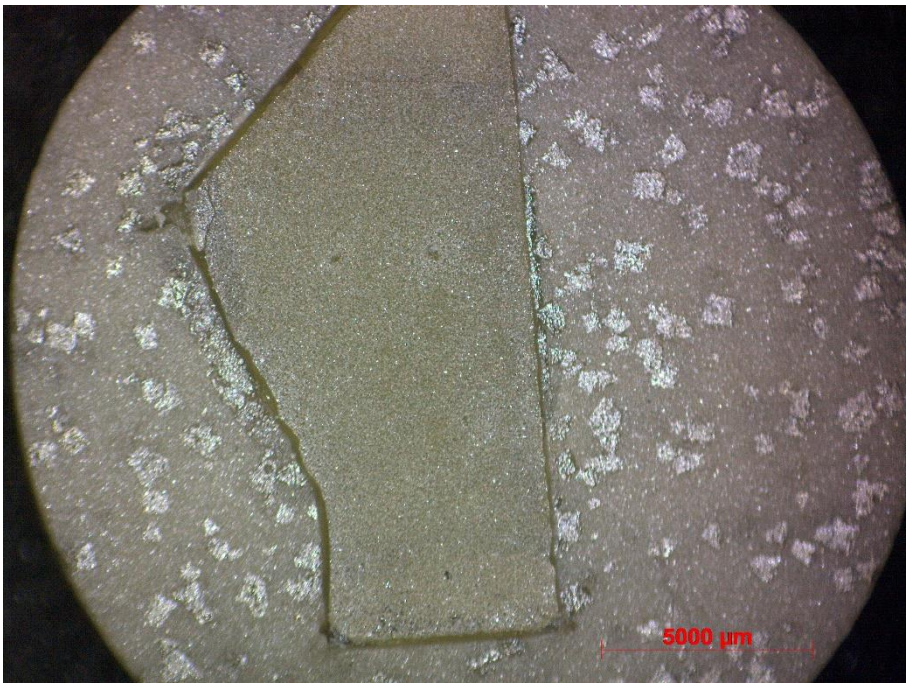

Figure 6. 80 Showing a microscope image taken at 2x magnification of BCTZ with 1 wt% SiO_2 containing a $BaTiO_3$ seed single crystal after sintering at 1420°C for 72 hours.

After the sample has been cross sectioned and polished further optical microscopy was performed (Figure 6.81), It was evident that some crystal growth had occurred. Although this was not as successful as the BCTZ containing ZnO. The maximum growth length was found to be ~260µm with a growth rate of ~3.6µm/hour.

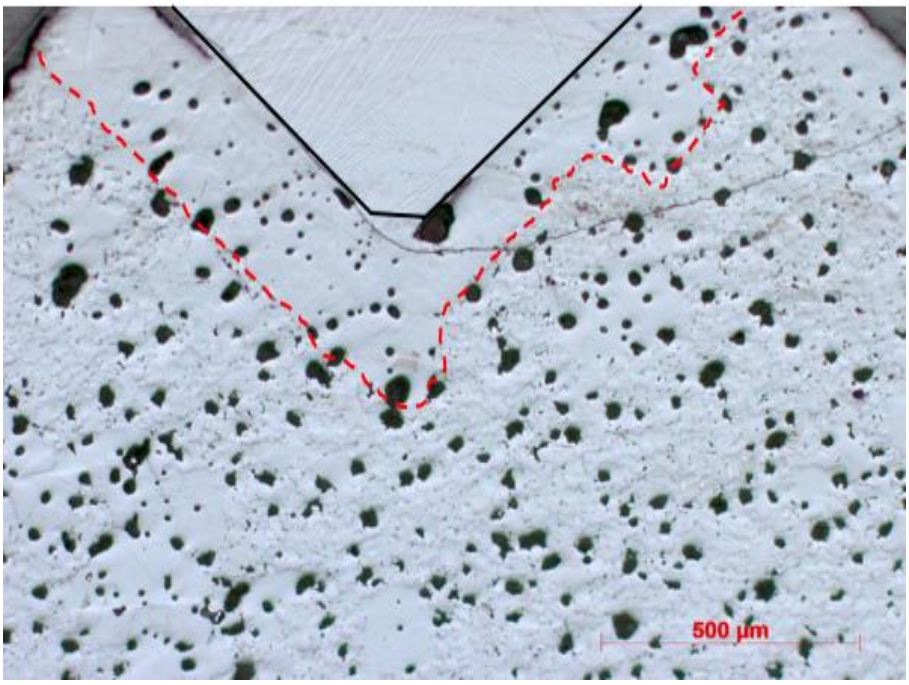

Figure 6. 81 An optical micrograph taken at 5x magnification in bright field of the single crystal grown using BCTZ with 1 wt% of SiO_2 sintered at 1420°C for 72 hours. The black line outlines the seed crystal and the red lines outline the grown single crystal.

Scanning electron microscopy was also performed on this sample (Figure 6.82) and the large matrix grains were found to be impinging on the small amount of crystal growth.

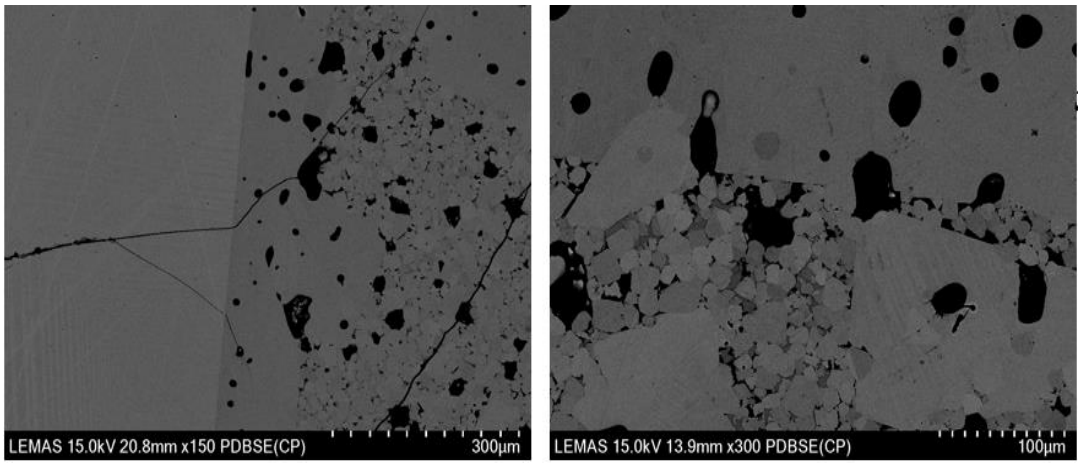

Figure 6. 82 Showing scanning electron micrographs of the seed single crystal and the single crystal grown using BCTZ with 1 wt% SiO_2.

EDX mapping was also performed and there was found to be a clear compositional difference between the $BaTiO_3$ seed crystal and the BCTZ crystal grown. In this example however, EDX did not detect any Zr in the sample. Similarly, to the EDX performed on the BCTZ with added SiO_2 in the grain growth study, an Si rich intergranular phase was detected. The compositional map of this sample can be viewed in Figure *6.83*.

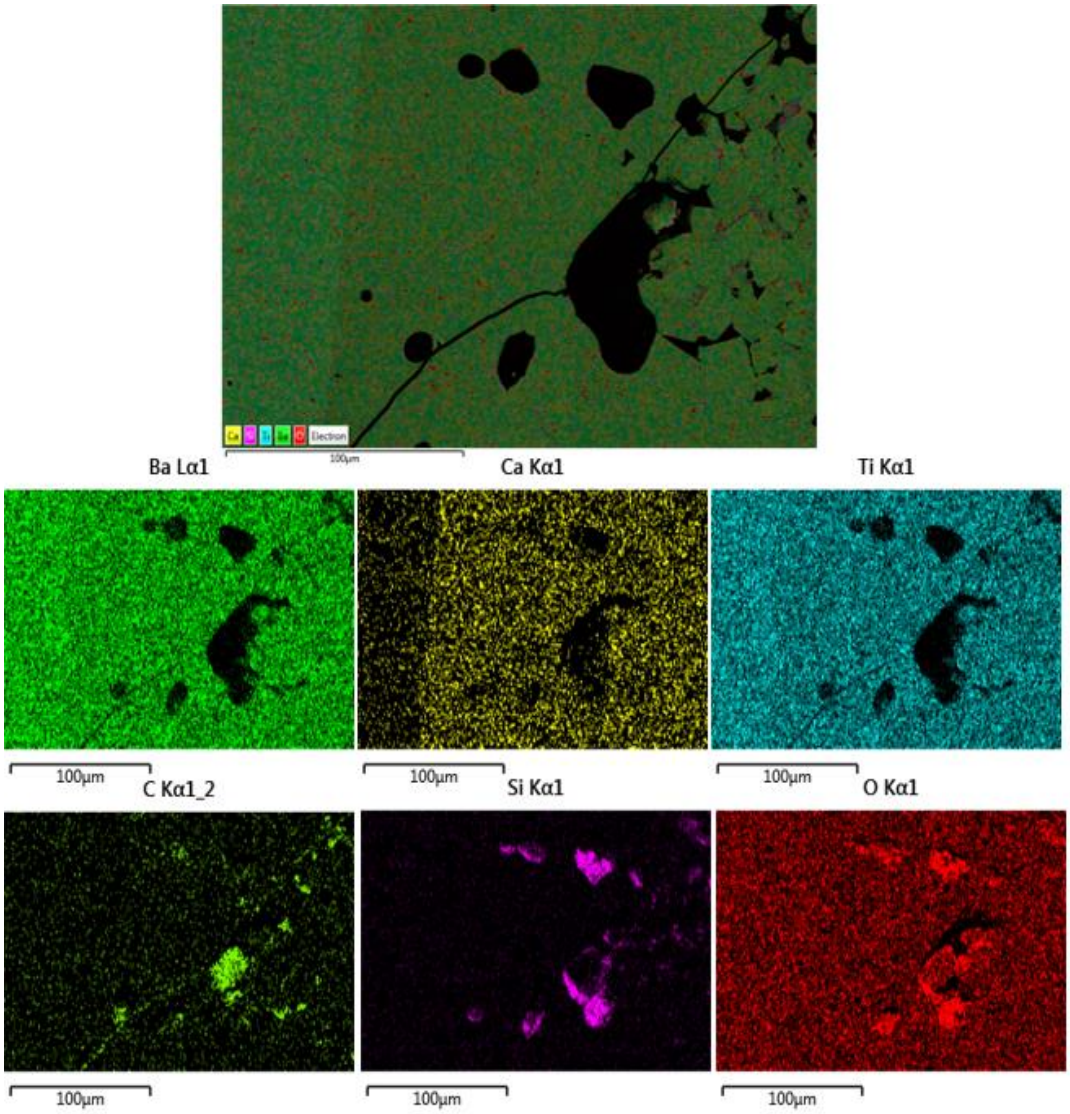

Figure 6. 83 Shows a compositional map produced by EDX of the $BaTiO_3$ seed crystal and the crystal grown using BCTZ with 1 wt % SiO_2. This sample was sintered for 72hours at 1420°C.

6.4.3.3 Solid state crystal growth in BCTZ with a 1 mol % TiO_2 excess

SSCG experiments were also performed using BCTZ with a 1 mol % TiO_2 excess in order to determine if like in $BaTiO_3$, excess TiO_2 would be beneficial to crystal growth. A $BaTiO_3$ crystal seed was used and this sample was sintered at 1440°C for 72 hours. There was no obvious crystal growth when the sample was viewed visually or when using the stereo microscope. Figure 6.84 shows the sample, prior to cross sections being taken.

Figure 6. 84 showing an image of the BCTZ with 1 mol% excess TiO_2 and $BaTiO_3$ crystal seed after sintering for 72 hours at 1440°C.

After inspecting the cross sectioned sample, it was evident a small amount of crystal growth had occurred. The maximum growth length was found to be ~60µm with a growth rate of ~0.83µm/hour. Due to the small size of the single crystal grown this sample was viewed in more detail using SEM. Figure 6.85 is an SEM image showing this small amount of crystal growth.

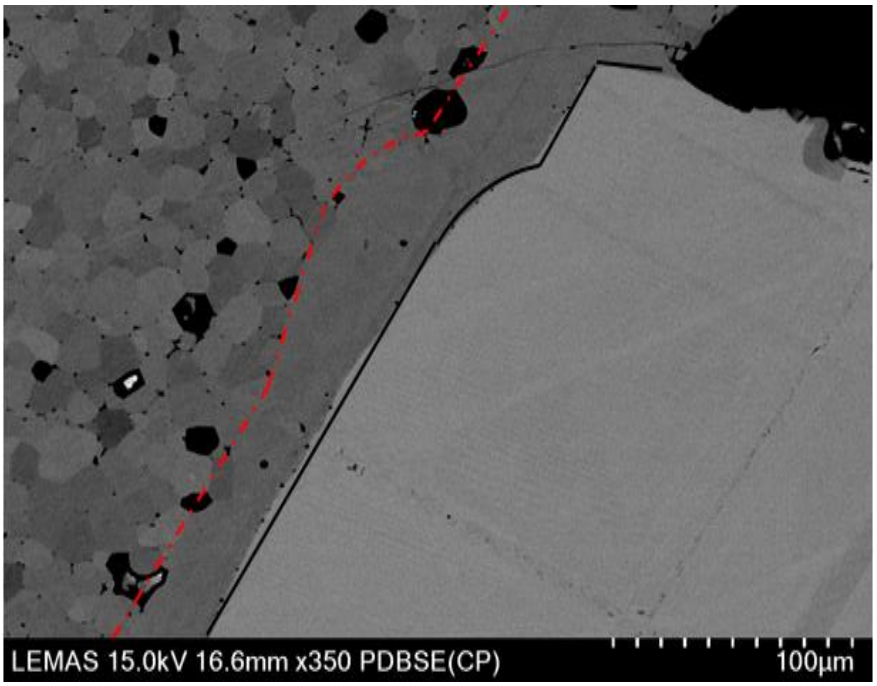

Figure 6. 85 A scanning electron micrograph of a $BaTiO_3$ crystal seed and the single crystal grown using 1 mol% excess TiO_2 BCTZ. This sample was sintered for 72 hours at 1440°C. The black line highlights the edge of the seed single crystal and the red lines outline the single crystal grown.

EDX was also performed and the compositional difference between the seed and grown single crystals was clear. EDX mapping can be seen in Figure 6.86.

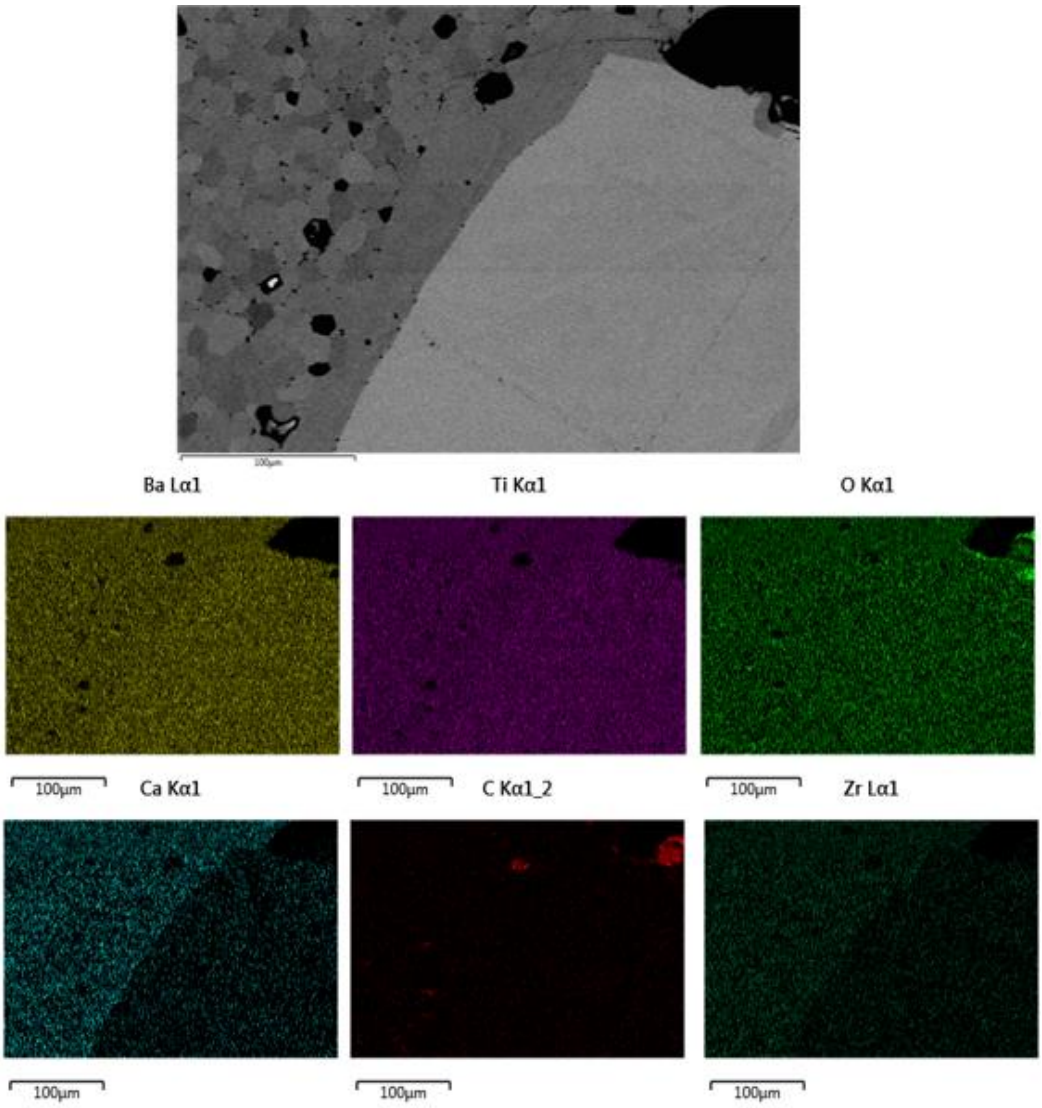

Figure 6. 86 A compositional map of a $BaTiO_3$ crystal seed and the single crystal grown using 1 mol% excess TiO_2 BCTZ. This sample was sintered for 72 hours at 1440°C.

6.4.4 Discussion

6.4.4.1 Grain growth in $(Ba_{0.85},Ca_{0.15})(Ti_{0.9},Zr_{0.1})O_3$.

Grain growth in BCTZ was found to increase with increasing sintering temperature across all of the compositions made with the exception of BCZT containing 1 wt% SiO_2. This sample displayed anomalous grain growth when sintered at temperatures above 1400°C where large twinned grains grew at the expense of smaller matrix grains due to the twin re-entrant edge mechanism in conjunction with $BaTiSiO_5$ liquid phase enhanced grain growth. Despite the temperature required for the formation of this liquid phase being 1260°C no large grains were observed in temperatures lower than 1400°C. This is likely in part to the addition of Zr increasing the necessary sintering temperature. Grains became faceted in the presence of SiO_2 which is another prerequisite for the occurrence of large abnormal grains. A large effect of second phase was also discovered by EDX analysis which is unsurprising but perhaps, like with TiO_2 addition in $BaTiO_3$, grain size may be larger in the presence of a thinner liquid film.

ZnO addition to BCTZ produced the largest grains across all temperatures, this is due to ZnO having a lower melting point than BCTZ [64]. TiO_2 excess also had the effect of increasing grain size when compared to BCTZ with no additions but this effect was not as pronounced as in $BaTiO_3$. Very large grains however were observed with addition of $BaTi_2O_5$. Bimodal grain growth was displayed in these samples with clusters of smaller grains remaining in the microstructure.

6.4.4.2 Solid state crystal growth in $(Ba_{0.85},Ca_{0.15})(Ti_{0.9},Zr_{0.1})O_3$.

Several SSCG experiments were performed using BCTZ in contact with a $BaTiO_3$ crystal seed. The most successful in terms of size was performed using BCTZ with 1 wt% ZnO. However, there was a significant amount of porosity within the grown single crystal. In contrast to this when single crystal growth experiments were performed using 1 mol% TiO_2 excess low porosity was achieved this was unfortunately at the expense of crystal growth rate.

6.5 Solid state crystal growth in $(Pb(Zr_{(1-x)}Ti_{(X)})O_3$

A preliminary crystal growth experiment was performed using PZT. This was performed using PZT 5 from Morgan Advanced Materials. A $BaTiO_3$ crystal seed was used and sintering was at 1200°C for 72 hours. Due to the volatility of PbO, atmosphere powder of the same composition as the sample was used to bury the pellet inside a sealed alumina crucible set-up.

When viewing the sample with the Motic SMZ-168 there was some small evidence of crystal growth at the edge of the $BaTiO_3$ seed crystal as can be seen in Figure 6.87.

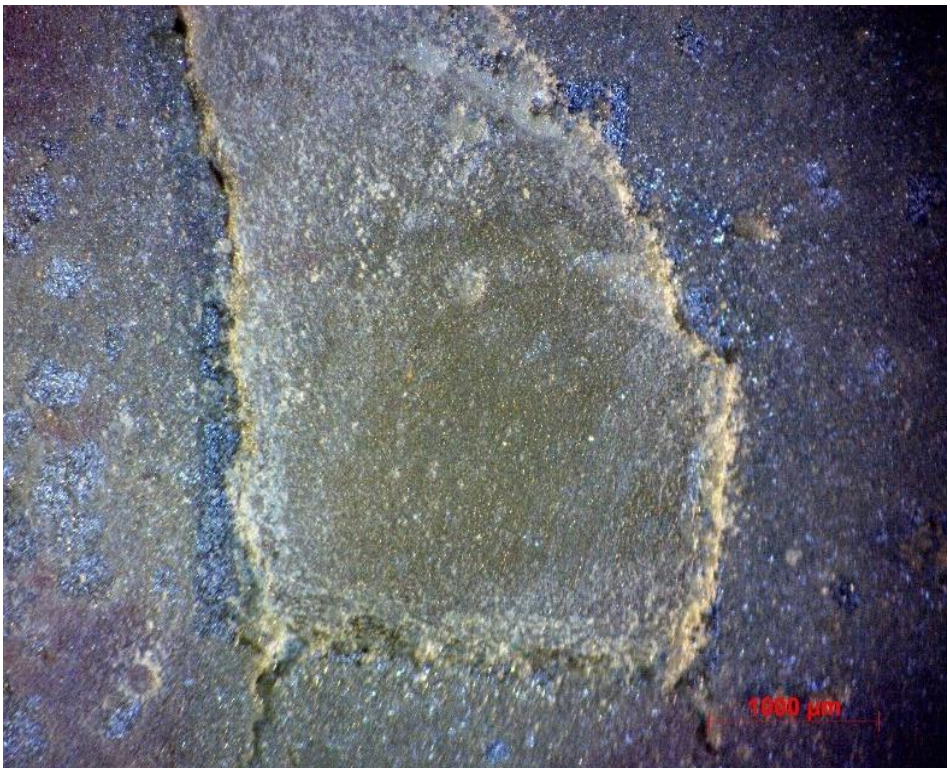

Figure 6. 87 Optical micrograph taken at 3x magnification of PZT containing a $BaTiO_3$ single crystal seed after sintering at 1200°C for 72 hours.

From Figure 6.87 it is also evident that large, faceted PZT grains had formed in the matrix. These grains can again be viewed in Figure 6.88 taken using the Olympus BX51. Some of these large grains were impinging on a region of the crystal seed which had prevented any crystal growth in that area.

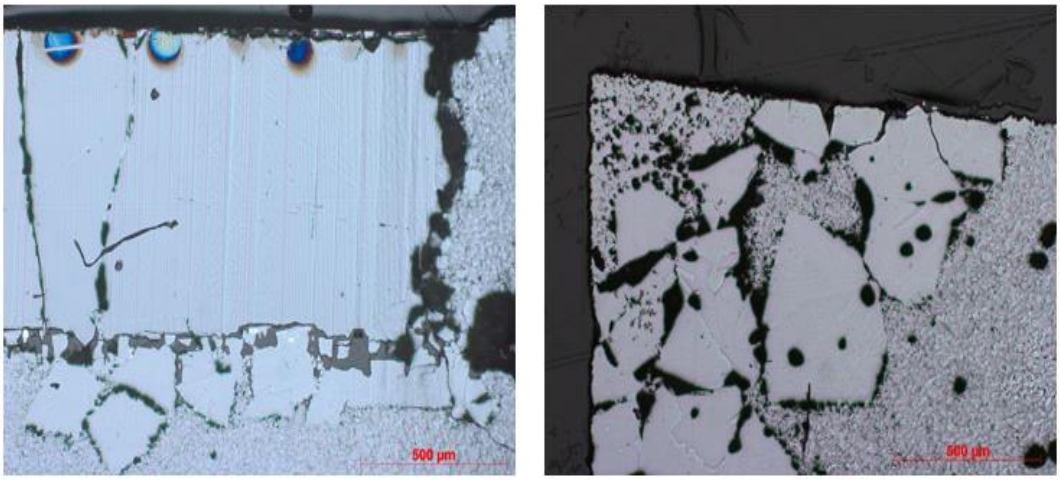

Figure 6. 88 Optical micrographs taken at 5x magnification in bright field of PZT sintered at 1200°C for 72hours.

.

When the cross sections had been taken of this sample it was evident that a small amount of crystal growth had occurred. This crystal growth had very limited porosity but like with the BCTZ containing 1 mol% excess TiO_2 this reduction in porosity occurred at the expense of growth rate. The maximum growth length observed in this sample was 200µm with a growth rate of 2.77µm/hour. An area of the single crystal growth can be seen in Figure 6.89.

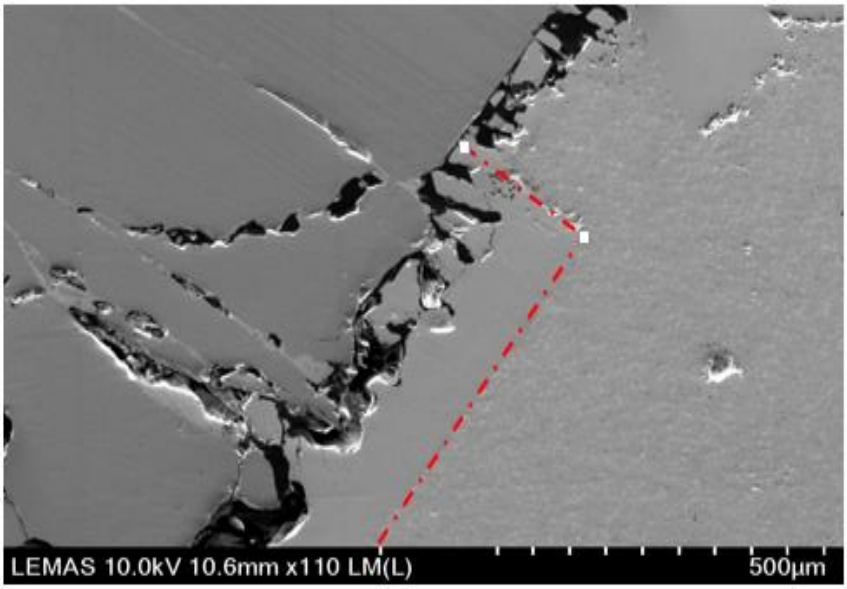

Figure 6. 89 A scanning electron micrograph showing the $BaTiO_3$ crystal seed and the PZT crystal grown. The red line outlines the PZT crystal growth.

The crystal seed in Figure 6.89 has separated from the bulk. This is likely due to the rate of shrinkage in PZT, this did not however prevent crystal growth occurring.

EDX analysis was also performed and can be viewed in Figure 6.90, where there is a clear compositional difference between the seed crystal and the PZT bulk.

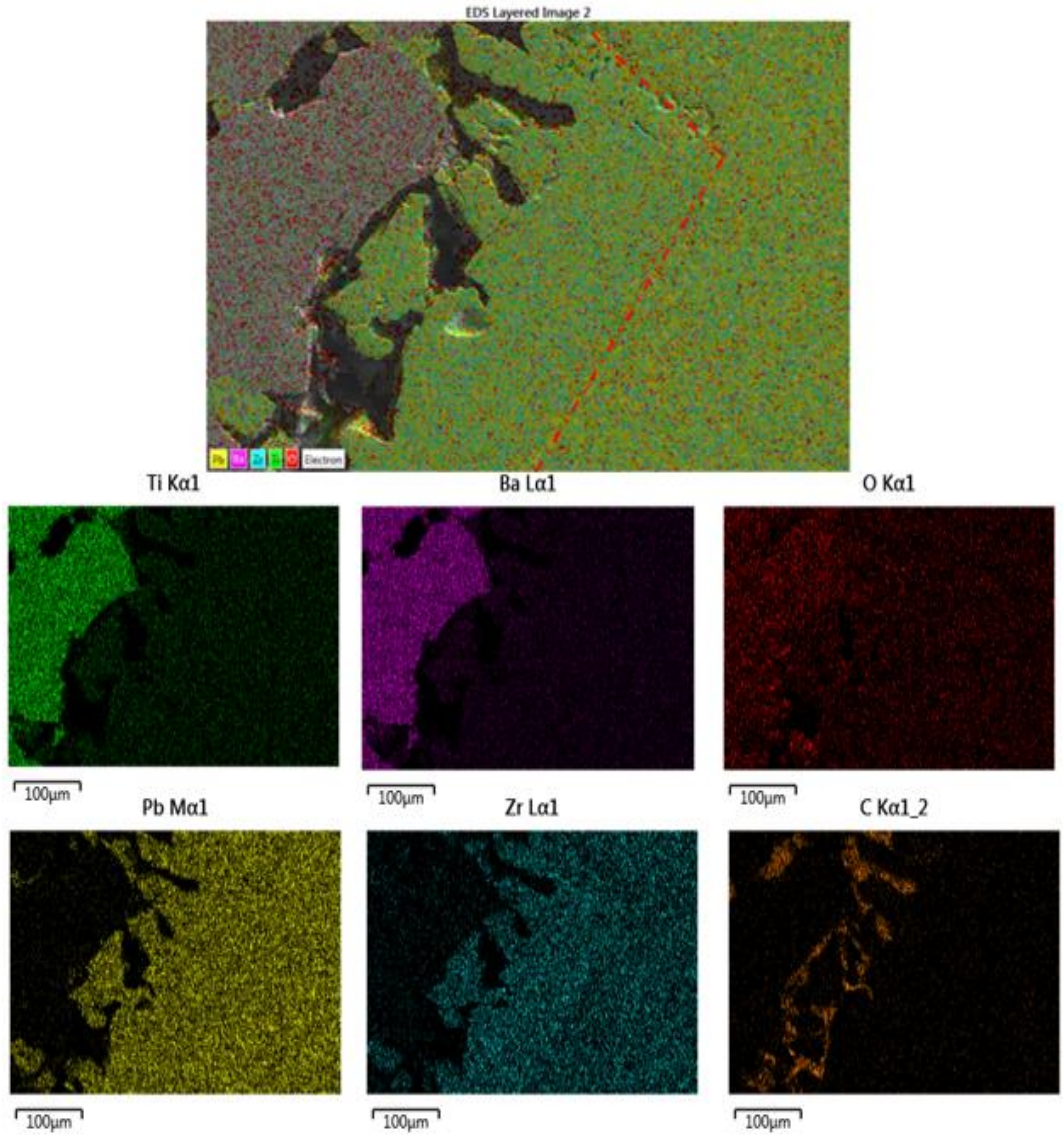

Figure 6. 90 A compositional map generated by EDX showing a $BaTiO_3$ single crystal seed, PZT crystal growth (outlined by the red line) and the PZT bulk.

The microstructure of the bulk was examined by SEM and an intergranular second phase was detected. An SEM micrograph of this second phase can be seen in Figure 6.91.

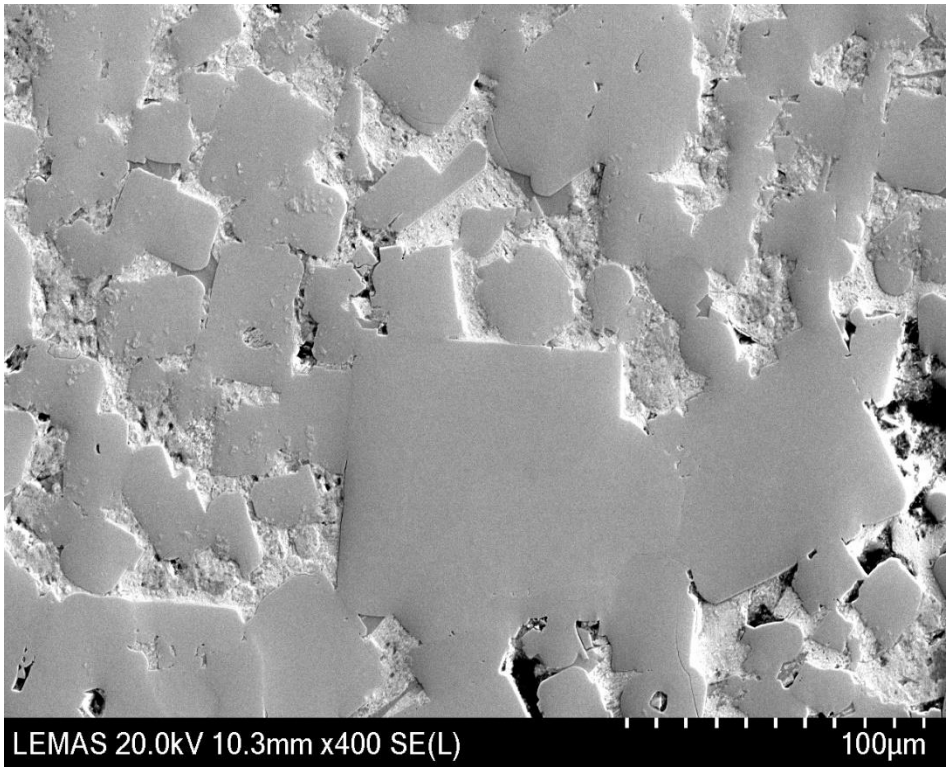

Figure 6. 91 The matrix grains of PZT sintered at 1200°C for 72 hours.

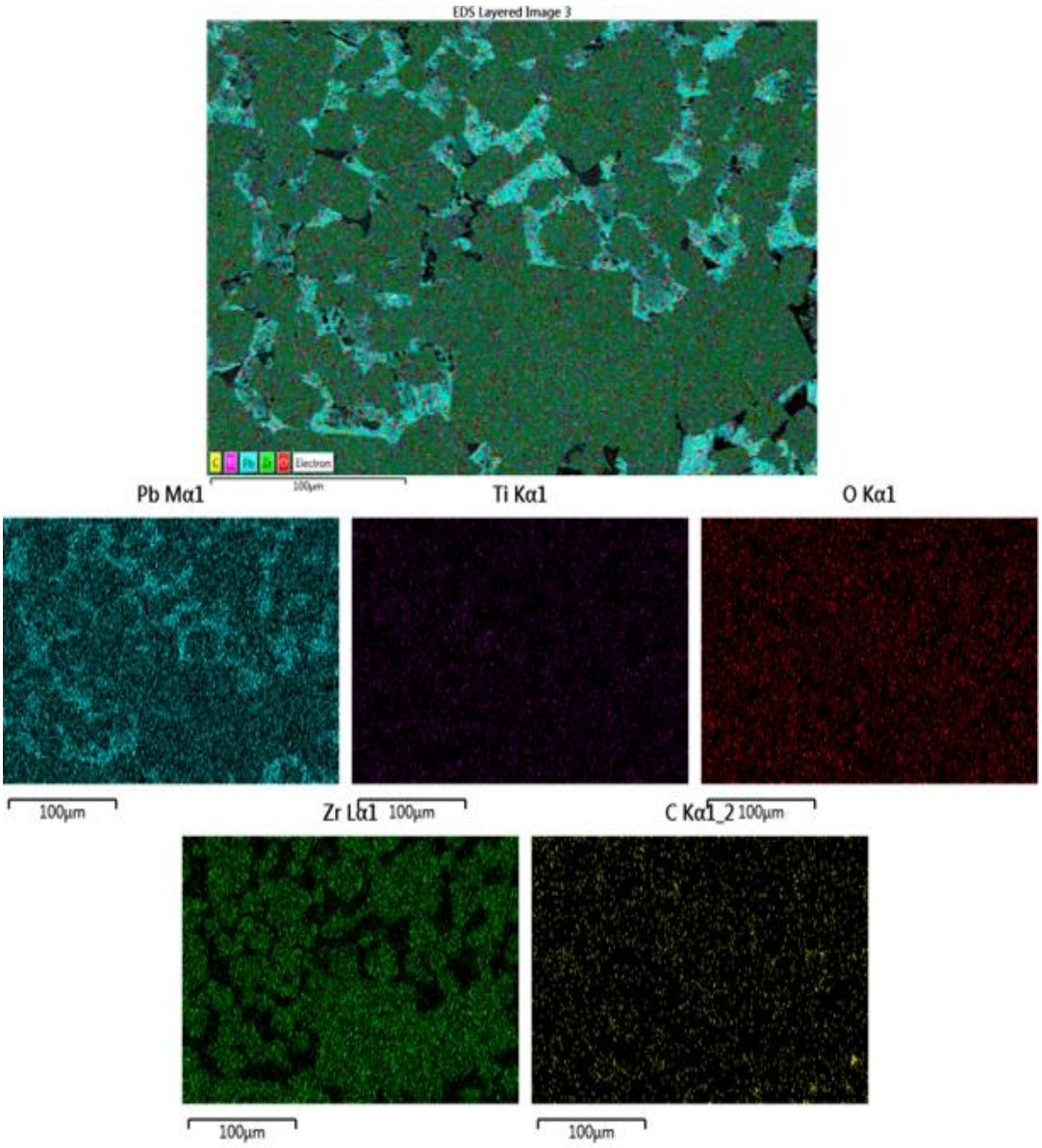

Figure 6. 92 EDX mapping of the PZT bulk after sintering for 72 hours at 1200°C.

EDX imagery was obtained for this area and the presence of a Pb rich second phase was confirmed, as shown in Figure 6.92.

6.5.1 Discussion

It is clear that it is possible to grow PZT single crystals by the SSCG method however more work is needed in order to determine the best conditions. The full composition of the PZT used here is unknown as it was acquired pre-made by Morgan Advanced Materials. In order to understand the crystal and grain growth mechanisms it is essential that any additives are known. The small amount of crystal growth observed was non-porous however similarly to BCZT this came at the expense of growth rate. Large abnormally grown grains were observed and some were found to be impinging on the crystal seed resulting in regions where no crystal growth could occur. Further work is needed for this material in order to better understand the microstructure and prevent growth of these large grains.

Chapter 7 Summary and Conclusions

Currently used methods for obtaining single crystals from the melt, for example the Bridgman method have several drawbacks. These include costly growth methods, concentration gradients in the produced single crystals, being incompatible with materials that display incongruent melting (such as PZT) and long periods of time to obtain just one single crystal. SSCG is a promising alternative to such methods that this work has proven to be compatible with a range of materials including the incongruently melting PZT. The growths rates in the crystals produced by SSCG in these experiments was determined to be reduced in comparison to the growth rates of Bridgman grown crystals. For example, the growth rate of $BaTiO_3$ with 1 mol% excess TiO_2 single crystals grown in this study were approximately 962µm/day whereas Bridgman grown crystals have a growth rate of approximately 4.8mm/day [36]. However, with the Bridgman method only one crystal can be produced in one specialised crystal furnace at a time whereas with the SSCG method multiple crystals can be grown in one standard box furnace. In addition to this the concentration gradient found in Bridgman produced single crystals means that only two thirds of the crystal is usable.

One obvious downfall of the SSCG process is porosity inclusion in the single crystals produced. As evidenced by single crystal growth in BCTZ containing 1 mol% excess TiO_2 (presented in Chapter 6) porosity can be eliminated from these crystals, however this comes at the expense of growth rate.

Another issue with the SSCG process is the appearance of large anomalous grains arising in the matrix and impinging on the growing single crystal. Several examples of this have been observed in work in the experiments using compositions $BaTiO_3$ with excess TiO_2, BCTZ with addition of SiO_2 and PZT. These grains would be even more problematic when growing larger single crystals as there would be more time allowed for them to proliferate around the edges of the compact. It has been evidenced by this work that small compositional changes can prevent formation of these grains and more recommendations can be found in the Further Work section below. With matrix grains that grow normally their increase in size also has an effect on crystal growth rate, this is evidenced by gradients in the volume of porosity, particularly in the $BaTiO_3$ samples.

One of the various reasons this work has focused on $BaTiO_3$ based crystals is due to the fact they can be used as seed crystals to obtain single crystals of other materials such as PMN-PT and PMN-PZT [3], [83]. From the work presented here, single crystals of composition $Ba_{0.99}(Zr_{0.01,}Ti_{0.99})O_{3,}$ would be a viable option for this application, as they offer a good compromise between porosity and growth rate. However, further optimisation would be necessary to further reduce porosity by for example hot-pressing the compacts prior to SSCG.

To conclude SSCG method has proven viability as a method for growth of single crystals of various materials. However, some further optimisation of this process is needed in order to control porosity whilst maintaining growth rate. Table 7.1 shows the growth rates and growth lengths of the single crystals produced in this thesis.

Table 7. 1 Showing the results of all the SSCG experiments presented in this work.

Material	Additions	~ Growth rate	Comments
$BaTiO_3$	none	7.3 µm/hr 183 µm/day Max growth length 550µm	Porous, however not as porous as when 1 mol% TiO_2 is present No abnormal grains observed in the bulk
$BaTiO_3$	1 mol% TiO_2	29 µm/hr 696 µm/day Max growth length of 2075µm/hr	High porosity Large anomalous grains in the bulk, preventing further growth
$BaTiO_3$	1 mol% TiO_2	38.1 µm/hr 961.5 µm/day Max growth length 2750µm	Highest growth rate High porosity No anomalous grains
$BaTiO_3$	Nano layer TiO_2	11 µm/hr 264µm/day Max growth length 790µm	Grains have impinged on growing crystal High porosity
$Ba_{0.99}(Ti_{0.995},Nb_{0.005})$ O3	With layer of $Ba_{0.99}TiO_3$	2.1µm/hr 50µm/day Max growth length 150µm	Similar levels of porosity to the stoichiometric sample
$(Ba_{0.85},Ca_{0.15})(Ti_{0.9},Zr_{0.1})O_3$	1 mol% TiO_2	0.83 µm/hr 20 µm/day Max growth length 60µm	Very low porosity Slow growth rate
$(Ba_{0.85},Ca_{0.15})(Ti_{0.9},Zr_{0.1})O_3$	1 wt% SiO_2	3.6 µm/hr 86.66 µm/day Max growth length 260µm	Fewer but much larger pores compared to $BaTiO_3$ Large anomalous grains , preventing further crystal growth
$(Ba_{0.85},Ca_{0.15})(Ti_{0.9},Zr_{0.1})O_3$	1 wt% ZnO	17.4 µm/hr 416.6 µm/day Max growth length 1250µm	Fewer but much larger pores compared to $BaTiO_3$
PZT		2.8 µm/hr 66.6 µm/day Max growth length 200µm	Low porosity Large anomalous grains , preventing further crystal growth
$Ba_{0.99}(Zr_{0.01},Ti_{0.99})O_3$		6.3µm/hr 150.8µm/hr Max growth length 452.5µm	Less porosity than in the $BaTiO_3$ samples Smaller sized pores than in the BCTZ samples
$Ba_{0.99}(Zr_{0.02},Ti_{0.99})O_3$		5.4µm/hr 130µm/day Max growth length 390µm	Less porosity than in the $BaTiO_3$ samples Smaller sized pores than in the BCTZ samples Very large matrix grains

Further Work

Several opportunities for further work arise from this research. Firstly, as previously mentioned, continued experiments are necessary in order to reduce porosity in the grown single crystals whilst maintaining crystal growth rates. One suggestion would involve the use of a hot-press which would aid densification and pore removal whilst promoting a fine-grained microstructure. This would allow subsequent crystal growth to progress at a high rate without pores becoming inclusions in the produced crystal.

Interlayers could also be used in order to promote crystal growth whilst matrix grain growth could be limited by composition (e.g. not including excess TiO_2 in $BaTiO_3$). A technique such as pulsed laser deposition would be recommended to achieve a thin film on the single crystal seed prior to SSCG [36], [84].

Experiments investigating the growth rates of crystals grown by SSCG over time should be performed. This would provide an insight into how the matrix grain size affects the growth rate of the single crystal and could be used to determine the time it would take to grow larger single crystals. If the increase in matrix grain size caused issues after a certain length of time, crystals could be removed, cut, polished and placed into a new green compact.

As PZT crystal growth has been shown to be possible in this work, further experiments are needed to optimise crystal growth parameters, starting with a grain growth study.

Finally, as relaxor-PT such as PMN-PT single crystals are widely used in piezoelectric applications, further experiments should focus on obtaining reproducible crystal growth parameters for these materials.

Bibliography

[1] E. Sun and W. Cao, "Relaxor-based ferroelectric single crystals: Growth, domain engineering, characterization and applications," *Prog. Mater. Sci.*, vol. 65, pp. 124–210, 2014, doi: 10.1016/j.pmatsci.2014.03.006.

[2] S. Zhang and F. Li, "High performance ferroelectric relaxor-PbTiO 3 single crystals: Status and perspective," *J. Appl. Phys.*, vol. 111, no. 3, 2012, doi: 10.1063/1.3679521.

[3] Ceracomp, "Ceracomp website," 2008. http://ceracomp.com/ (accessed Apr. 10, 2017).

[4] B. JAFFE, W. R. COOK, and H. JAFFE, *Piezoelectric Ceramics*. Academic Press London and New York, 1971.

[5] W. G. Cady, *Piezoelectricity: An Introduction to the Theory and Applications of Electro-mechanical Phenomena in Crystals*, vol. 1. McGraw-Hill, 1946.

[6] K. Uchino, "Glory of piezoelectric perovskites," *Sci. Technol. Adv. Mater.*, vol. 16, no. 4, p. 46001, 2015, doi: 10.1088/1468-6996/16/4/046001.

[7] M. S. Vijaya, *Piezoelectric Materials and Devices: Applications in Engineering and Medical Sciences*, 1st ed. CRC Press, 2013.

[8] C. Hammond, *The Basics of Crystallography and Diffraction*, 4th ed. Oxford university press, 2015.

[9] A. J. Moulson and J. M. Herbert, "Electroceramics: Materials, Properties, Applications," in *Electroceramics*, 2nd ed., Chichester: Wiley, 2003, pp. 95–134.

[10] M. P. Marder, *Condensed matter physics*, 2nd ed. Wiley - Blackwell, 2010.

[11] K. Uchino, *Ferroelectric Devices*. 2018.

[12] B. Jaffe, R. . Cook, and H. Jaffe, *Piezoelectric Ceramics*. Academic press London and New York, 1971.

[13] D. Vatansever, E. Siores, R. L., and T. Shah, "Smart Woven Fabrics In Renewable Energy Generation," *Adv. Mod. Woven Fabr. Technol.*, no. July, 2011, doi: 10.5772/24790.

[14] Y.-M. Chiang, D. P. Birnie, and W. D. Kingery, *Physical Ceramics*. 1997.

[15] Y. S. Yoo, H. Kim, and D. Y. Kim, "Effect of SiO2 and TiO2 addition on the exaggerated grain growth of BaTiO3," *J. Eur. Ceram. Soc.*, vol. 17, no. 6, pp. 805–811, 1997, doi: 10.1016/s0955-2219(96)00134-3.

[16] H. Y. Lee *et al.*, "Method for single crystal growth of barium titanate solid solution," US 6,758,898,B2, 2009.

[17] J. P. Remeika, "A method for growing Barium Titanate single crystals," *J. Am. Ceram. Soc.*, vol. 76, no. 10, pp. 940–941, 1953.

[18] H. Sasaki, " Growth of BaTiO 3 Crystals from TiO 2 -Rich Melt ," *Jpn. J. Appl. Phys.*, vol. 4, no. 1, pp. 24–27, 1965, doi: 10.1143/jjap.4.24.

[19] T. Yamamoto and T. Sakuma, “Fabrication of Barium Titanate Single Crystals by Solid-State Grain Growth,” *J. Am. Ceram. Soc.*, vol. 77, no. 4, pp. 1107–1109, 1994, doi: 10.1111/j.1151-2916.1994.tb07281.x.

[20] A. J. Bell, “Grain size property relationships in Barium Titanate,” University of leeds, 1984.

[21] A. J. Bell and O. Deubzer, “Lead-free piezoelectrics - The environmental and regulatory issues,” *MRS Bull.*, vol. 43, no. 8, pp. 581–587, 2018, doi: 10.1557/mrs.2018.154.

[22] S. W. Zhang, H. Zhang, B. P. Zhang, and S. Yang, “Phase-transition behavior and piezoelectric properties of lead-free (Ba0.95Ca0.05)(Ti1-xZrx)O 3 ceramics,” *J. Alloys Compd.*, vol. 506, no. 1, pp. 131–135, 2010, doi: 10.1016/j.jallcom.2010.06.157.

[23] P. Wang, Y. Li, and Y. Lu, “Enhanced piezoelectric properties of (Ba0.85Ca0.15)(Ti0.9Zr0.1)O3 lead-free ceramics by optimizing calcination and sintering temperature,” *J. Eur. Ceram. Soc.*, vol. 31, no. 11, pp. 2005–2012, 2011, doi: 10.1016/j.jeurceramsoc.2011.04.023.

[24] J. J. Fisher, A. Bencian, M. Kosec, S. Vernay, and D. Rytz, “Growth of potassium sodium niobate single crystals by solid state crystal growth,” *J. Cryst. Growth*, vol. 303, pp. 487–492, 2008.

[25] T. Ibn-Mohammed *et al.*, “Are lead-free piezoelectrics more environmentally friendly?,” *MRS Commun.*, vol. 7, no. 1, pp. 1–7, 2017, doi: 10.1557/mrc.2017.10.

[26] T. Ibn-Mohammed *et al.*, “Life cycle assessment and environmental profile evaluation of lead-free piezoelectrics in comparison with lead zirconate titanate,” *J. Eur. Ceram. Soc.*, vol. 38, no. 15, pp. 4922–4938, 2018, doi: 10.1016/j.jeurceramsoc.2018.06.044.

[27] S. J. Parry, “KN-based Lead-free Ferroelectric Materials for SONAR applications,” no. March, 2019, [Online]. Available: http://etheses.whiterose.ac.uk/24245/.

[28] M. Acosta *et al.*, “BaTiO3-based piezoelectrics: Fundamentals, current status, and perspectives,” *Appl. Phys. Rev.*, vol. 4, no. 4, 2017, doi: 10.1063/1.4990046.

[29] S. Butee, K. R. Kambale, A. Ghorpade, A. Halikar, R. Gaikwad, and H. Panda, “Significant improvement in Curie temperature and piezoelectric properties of BaTiO3 with minimum Pb addition,” *J. Asian Ceram. Soc.*, vol. 7, no. 4, pp. 407–416, 2019, doi: 10.1080/21870764.2019.1656359.

[30] S. E. Park and T. R. Shrout, “Ultrahigh strain and piezoelectric behavior in relaxor based ferroelectric single crystals,” *J. Appl. Phys.*, vol. 82, no. 4, pp. 1804–1811, 1997, doi: 10.1063/1.365983.

[31] X. Li and H. Luo, “The growth and properties of relaxor-based ferroelectric single crystals,” *J. Am. Ceram. Soc.*, vol. 93, no. 10, pp. 2915–2928, 2010, doi: 10.1111/j.1551-2916.2010.04107.x.

[32] A. K. Batra, A. Alomari, A. K. Batra, and A. Alomari, “Processing Important Piezoelectric Materials,” *Power Harvest. via Smart Mater.*, pp. 233–255, 2017, doi: 10.1117/3.2268643.ch9.

[33] P. W. Bridgman, “Certain Physical Properties of Single Crystals of Tungsten , Antimony , Bismuth , Tellurium , Cadmium , Zinc , and Tin Author (s): P . W . Bridgman Source : Proceedings of the American Academy of Arts and Sciences , Vol . 60 , No . 6 (Oct .,

Published," vol. 60, no. 6, pp. 305–383, 1924.

[34] D. C. Stockbarger, "The production of large single crystals of Lithium Flouride," *Rev. Sci. Instrum.*, vol. 7, p. 133, 1935, doi: 10.1063/1.1751759.

[35] P. Capper, "Springer Handbook of Electronic and Photonic Materials," *Springer Handb. Electron. Photonic Mater.*, pp. 269–292, 2017, doi: 10.1007/978-3-319-48933-9.

[36] L. A. Stoica, "processing , growth and characterisation The University of Leeds School of Chemical and Process Engineering Faculty of Engineering September 2016," no. September, 2016.

[37] T. Kobayashi, S. Shimanuki, S. Saitoh, and Y. Yamashita, "Improved growth of large lead zinc niobate titanate piezoelectric single crystals for medical ultrasonic transducers," *Japanese J. Appl. Physics, Part 1 Regul. Pap. Short Notes Rev. Pap.*, vol. 36, no. 9 SUPPL. B, pp. 6035–6038, 1997, doi: 10.1143/jjap.36.6035.

[38] K. Harada, S. Shimanuki, T. Kobayashi, S. Saitoh, and Y. Yamashita, "Crystal Growth and Electrical Properties of Pb(Zn1/3Nb2/3)0.91Ti0.0903 Single Crystals Produced by Solution Bridgman Method," vol. 81, no. 11, pp. 2785–2788, 1998.

[39] W. Chen and Z. G. Ye, "Top seeded solution growth and characterisation of piezo/ferroelectric (1 - x) Pb (Zn 1/3 Nb 2/3) O3-x PbTiO3 single crystals." Journal of Crystal growth 223, pp. 503–511, 2001.

[40] S. J. L. Kang, J. H. Park, S. Y. Ko, and H. Y. Lee, "Solid-state conversion of single crystals: The principle and the state-of-the-art," *J. Am. Ceram. Soc.*, vol. 98, no. 2, pp. 347–360, 2015, doi: 10.1111/jace.13420.

[41] D. F. K. HENNINGS, R. JANSSEN, and P. J. L. REYNEN, "Control of Liquid-Phase-Enhanced Discontinuous Grain Growth in Barium Titanate," *J. Am. Ceram. Soc.*, vol. 70, no. 1, pp. 23–27, 1987, doi: 10.1111/j.1151-2916.1987.tb04847.x.

[42] S. J. L. Kang, S. Y. Ko, and S. Y. Moon, "Mixed control of boundary migration and the principle of microstructural evolution," *J. Ceram. Soc. Japan*, vol. 124, no. 4, pp. 259–267, 2016, doi: 10.2109/jcersj2.15262.

[43] P. R. Rios, T. Yamamoto, T. Kondo, and T. Sakuma, "Abnormal grain growth kinetics of BaTiO3 with an excess TiO2," *Acta Mater.*, vol. 46, no. 5, pp. 1617–1623, 1998, doi: 10.1016/S1359-6454(97)00340-6.

[44] S. Lee, C. A. Randall, and Z. K. Liu, "Factors limiting equilibrium in fabricating a simple ferroelectric oxide: BaTiO3," *J. Am. Ceram. Soc.*, vol. 92, no. 1, pp. 222–228, 2009, doi: 10.1111/j.1551-2916.2008.02859.x.

[45] B. K. Lee, S. Y. Chung, and S. J. L. Kang, "Grain boundary faceting and abnormal grain growth in BaTiO3," *Acta Mater.*, vol. 48, pp. 1575–1580, 2000.

[46] S. Y. Choi, S. J. L. Kang, S. Y. Chung, T. Yamamoto, and Y. Ikuhara, "Change in cation nonstoichiometry at interfaces during crystal growth in polycrystalline BaTiO3," *Appl. Phys. Lett.*, vol. 88, p. 011909, 2006.

[47] Y. I. Jung, S. Y. Choi, and S. J. L. Kang, "Grain growth behaviour during stepwise sintering of barium titante in hydrogen gas and air," *J. Am. Ceram. Soc.*, vol. 86, no. 12, pp. 2228–2230, 2003.

[48] H. OPPOLZER and H. SCHMELZ, “Investigation of Twin Lamellae in BaTiO3 Ceramics,” *J. Am. Ceram. Soc.*, vol. 66, no. 6, pp. 444–446, 1983, doi: 10.1111/j.1151-2916.1983.tb10078.x.

[49] O. Eibl, P. Pongratz, P. Skalicky, and H. Schmelz, “Formation of (111) twins in BaTiO3 caramics,” *J. Am. Ceram. Soc.*, vol. 70, no. 8, pp. 195–197, 1987.

[50] H. Y. Lee, J. S. Kim, N. M. Hwang, and D. Y. Kim, “Effect of sintering temperature on the secondary abnormal grain growth of BaTiO3,” *J. Eur. Ceram. Soc.*, vol. 20, pp. 731–737, 2000.

[51] Y. S. Yoo, M. K. Kang, J. H. Han, H. Kim, and D. Y. Kim, “Fabrication of BaTiO3 single crystals by using the exaggerated grain growth method,” *J. Eur. Ceram. Soc.*, vol. 17, no. 14, pp. 1725–1727, 1997, doi: 10.1016/s0955-2219(97)00017-4.

[52] H. Y. Lee, J. S. Kim, and D. Y. Kim, “Fabrication of BaTiO3 single crystals using secondary abnormal grain growth,” *J. Eur. Ceram. Soc.*, vol. 20, no. 10, pp. 1595–1597, 2000, doi: 10.1016/s0955-2219(00)00030-3.

[53] S. Y. Choi, S. Y. Moon, and S. J. L. Kang, “Kinetic formation and thickening of intergranular amorphus films in barium titanate,” *Acta Mater.*, vol. 52, pp. 3721–3726, 2004.

[54] H.-Y. Lee, J.-B. Lee, T. Hur, and D. Kim, “Method for solid state crystal growth,” EP1549786A1, 2004.

[55] M. L. V Mahesh, V. V Bhanu Prasad, and A. R. James, “Effect of sintering temperature on the microstructure and electrical properties of zirconium doped barium titanate ceramics,” vol. 24, no. 12, pp. 4684–4692, 2013, doi: 10.1007/s10854-013-1460-3.

[56] W. Cai, C. Fu, J. Gao, and H. Chen, “Effects of grain size on domain structure and ferroelectric properties of barium zirconate titanate ceramics,” vol. 480, pp. 870–873, 2009, doi: 10.1016/j.jallcom.2009.02.049.

[57] P. W. Rehrig *et al.*, “Piezoelectric properties of zirconium-doped barium titanate single crystals grown by templated grain growth grown by templated grain growth,” vol. 1657, no. April 1999, pp. 1–6, 2017.

[58] P. Zheng, J. L. Zhang, S. F. Shao, and E. Al, “Piezoelectric properties and stabilities of CuO modified Ba(Ti,Zr)O3 ceramics,” *Appl. Phys. Lett.*, vol. 032902, no. December 2008, pp. 92–95, 2008, doi: 10.1063/1.3072347.

[59] D. Liang, X. Zhu, J. Zhu, J. Zhu, and D. Xiao, “Effects of CuO addition on the structure and electrical properties of low temperature sintered Ba (Zr , Ti) O 3 lead-free piezoelectric ceramics,” *Ceram. Int.*, vol. 40, no. 2, pp. 2585–2592, 2014, doi: 10.1016/j.ceramint.2013.10.084.

[60] W. Liu and X. Ren, “Large piezoelectric effect in Pb-free ceramics,” *Phys. Rev. Lett.*, vol. 103, no. 25, pp. 1–4, 2009, doi: 10.1103/PhysRevLett.103.257602.

[61] W. Li, Z. Xu, R. Chu, P. Fu, and G. Zang, “Piezoelectric and dielectric properties of (Ba1-xCa x)(Ti0.95Zr0.05)O3 lead-free ceramics,” *J. Am. Ceram. Soc.*, vol. 93, no. 10, pp. 2942–2944, 2010, doi: 10.1111/j.1551-2916.2010.03907.x.

[62] H. L. Sun *et al.*, “Correlation of grain size, phase transition and piezoelectric properties in Ba0.85Ca0.15Ti0.90Zr0.10O3 ceramics,” *J. Mater. Sci. Mater. Electron.*, vol. 26, no. 7, pp. 5270–5278, 2015, doi: 10.1007/s10854-015-3063-7.

[63] J. Wu *et al.*, "Sintering temperature-induced electrical properties of (Ba 0.90Ca 0.10)(Ti 0.85Zr 0.15)O 3 lead-free ceramics," *Mater. Res. Bull.*, vol. 47, no. 5, pp. 1281–1284, 2012, doi: 10.1016/j.materresbull.2012.01.032.

[64] S. H. Shin and J. Yoo, "Effect of ZnO addition on dielectric and piezoelectric properties of (Ba0.85Ca0.15)(Ti0.915Zr0.085)O3 ceramics," *Ferroelectr. Lett. Sect.*, vol. 42, no. 1–3, pp. 43–50, 2015, doi: 10.1080/07315171.2015.1007803.

[65] Y. C. Lee, C. W. Lin, W. H. Lu, W. J. Chen, and W. H. Lee, "Influence of SiO2 addition on the dielectric properties and microstructure of (Ba0.96Ca0.04)(Ti0.85 Zr0.15)O3 ceramics," *Int. J. Appl. Ceram. Technol.*, vol. 6, no. 6, pp. 692–701, 2009, doi: 10.1111/j.1744-7402.2009.02379.x.

[66] T. Chen, T. Wang, G. Zhou, J. Zhang, and Y. Lui, "Effects of CuO on the microstructure and electrical properties of Ba0.85 Ca0.15 Ti 0.90 Zr0.10 03 piezoceramics," *J. Mater. Sci.*, vol. 47, pp. 4612–4619, 2012.

[67] A. I. Kingon and J. B. Clark, "Sintering of PZT ceramics: 11 effect of PbO content on densification kinetics," *J. Am. Ceram. Soc.*, vol. 66, pp. 256–260, 1983.

[68] D. E. WITTMER and R. C. BUCHANAN, "Low-Temperature Densification of Lead Zirconate-Titanate with Vanadium Pentoxide Additive," *J. Am. Ceram. Soc.*, vol. 64, no. 8, pp. 485–490, 1981, doi: 10.1111/j.1151-2916.1981.tb09902.x.

[69] K. W. Kim, W. Jo, H. R. Jin, N. M. Hwang, and D. Y. Kim, "Abnormal grain growth of lead zirconium titanate (PZT) ceramics induced by the penetration twin," *J. Am. Ceram. Soc.*, vol. 89, no. 5, pp. 1530–1533, 2006, doi: 10.1111/j.1551-2916.2006.00934.x.

[70] A. Khan, F. A. Meschke, T. Li, A. M. Scotch, H. M. Chan, and M. P. Harmer, "Growth of PMN-PT single crystals from (111) substrates by seeded polycrystal conversion," *J. Am. Ceram. Soc.*, vol. 82, no. 11, pp. 2958–2962, 1999.

[71] P. T. King, E. P. Gorzkowski, A. M. Scotch, D. J. Rockosi, H. M. Chan, and M. P. Harmer, "Grown by Seeded Polycrystal Conversion," *Growth (Lakeland)*, vol. 87, pp. 2182–2187, 2003.

[72] M. S. Kim, J. G. Fisher, S. J. L. Kang, and H. Y. Lee, "Grain growth control and solid-state crystal growth by Li 2O/PbO addition and dislocation introduction in the PMN-35PT system," *J. Am. Ceram. Soc.*, vol. 89, no. 4, pp. 1237–1243, 2006, doi: 10.1111/j.1551-2916.2005.00883.x.

[73] H. Yamada, "The growth of PMN-PT single crystals via the solid-state conversion method," *Ferroelectrics*, vol. 355, no. 1 PART 1, pp. 231–239, 2007, doi: 10.1080/00150190701522242.

[74] H. Yamada, "Pressureless sintering of PMN-PT ceramics," *J. Eur. Ceram. Soc.*, vol. 19, no. 6–7, pp. 1053–1056, 1999, doi: 10.1016/s0955-2219(98)00372-0.

[75] J. J. Fisher, A. Bencian, M. Kosec, S. Vernay, and D. Rytz, "Growth of dense single crystals of potassium niobate by a combination of solid state crystal growth and hot-pressing," *J. Am. Ceram. Soc.*, vol. 91, pp. 1503–1507, 2008.

[76] PANanalytical, "PANalytical website," 2013. http://www.panalytical.com/Technology-background/Phase-quantification.htm (accessed Aug. 01, 2017).

[77] T. Fellers and M. Davidson, “Olympus Microscopy Website,” 2012. http://www.olympusmicro.com/primer/index.html (accessed Aug. 09, 2017).

[78] J. Kuo, *Electron Microscopy*, 2nd ed. New Jersey: Humana Press, 2007.

[79] M. I. MENDELSON, “Average Grain Size in Polycrystalline Ceramics,” *J. Am. Ceram. Soc.*, vol. 52, no. 8, pp. 443–446, 1969, doi: 10.1111/j.1151-2916.1969.tb11975.x.

[80] D. F. K. HENNINGS, R. JANSSEN, and P. J. L. REYNEN, “Control of liquid phase enhanced discontinuous grain growth in barium titanate,” *J. Am. Ceram. Soc.*, vol. 70, no. 1, pp. 23–27, 1987.

[81] S. J. L. Kang, *Sintering*, 1st ed. Daejeon: Elsevier Ltd, 2005.

[82] S. H. Yoon, J. H. Lee, D. Y. Kim, and N. M. Hwang, “Core-shell structure of acceptor-rich, coarse barium titanate grains,” *J. Am. Ceram. Soc.*, vol. 85, no. 12, pp. 3111–3113, 2002, doi: 10.1111/j.1151-2916.2002.tb00593.x.

[83] I. Milisavljevic and Y. Wu, “Current status of solid-state single crystal growth,” *BMC Mater.*, vol. 2, no. 1, pp. 1–26, 2020, doi: 10.1186/s42833-020-0008-0.

[84] J. Jiang, H. J. Jung, and S. G. Yoon, “Epitaxial PMN-PT thin films grown on buffered Si substrates using ceramic and single-crystal targets,” *J. Alloys Compd.*, vol. 509, no. 24, pp. 6924–6929, 2011, doi: 10.1016/j.jallcom.2011.04.002.